



Conductive nitrides: Growth principles, optical and electronic properties, and their perspectives in photonics and plasmonics



P. Patsalas^{a,*}, N. Kalfagiannis^b, S. Kassavetis^a, G. Abadias^c, D.V. Bellas^d, Ch. Lekka^d, E. Lidorikis^d

^a Department of Physics, Aristotle University of Thessaloniki, Thessaloniki, GR-54124, Greece

^b School of Science and Technology, Nottingham Trent University, Nottingham, NG11 8NS, United Kingdom

^c Institut Prime, Université de Poitiers-CNRS-ENSMA, Département Physique et Mécanique des Matériaux, 86962 Chasseneuil-Futuroscope, France

^d Department of Materials Science and Engineering, University of Ioannina, GR-45110 Ioannina, Greece

ARTICLE INFO

Article history:

Received 22 June 2017

Received in revised form 18 October 2017

Accepted 13 November 2017

Keywords:

Transition metal nitrides

Thin film growth

Optical properties

Surface plasmon-polariton

Localized surface plasmon resonance

Photothermal properties

ABSTRACT

The nitrides of most of the group IVb-Vb-VIb transition metals (TiN, ZrN, HfN, VN, NbN, TaN, MoN, WN) constitute the unique category of conductive ceramics. Having substantial electronic conductivity, exceptionally high melting points and covering a wide range of work function values, they were considered for a variety of electronic applications, which include diffusion barriers in metallizations of integrated circuits, Ohmic contacts on compound semiconductors, and thin film resistors, since early eighties. Among them, TiN and ZrN are recently emerging as significant candidates for plasmonic applications. So the possible plasmonic activity of the rest of transition metal nitrides (TMN) emerges as an important open question. In this work, we exhaustively review the experimental and computational (mostly *ab initio*) works in the literature dealing with the optical properties and electronic structure of TMN spanning over three decades of time and employing all the available growth techniques. We critically evaluate the optical properties of all TMN and we model their predicted plasmonic response. Hence, we provide a solid understanding of the intrinsic (e.g. the valence electron configuration of the constituent metal) and extrinsic (e.g. point defects and microstructure) factors that dictate the plasmonic performance. Based on the reported optical spectra, we evaluate the quality factors for surface plasmon polariton and localized surface plasmon for various TMN and critically compare them to each other. We demonstrate that, indeed TiN and ZrN along with HfN are the most well-performing plasmonic materials in the visible range, while VN and NbN may be viable alternatives for plasmonic devices in the blue, violet and near UV ranges, albeit in expense of increased electronic loss. Furthermore, we consider the alloyed ternary TMN and by critical evaluation and comparison of the reported experimental and computational works, we identify the emerging optimal tunable plasmonic conductors among the immense number of alloying combinations.

© 2017 Elsevier B.V. All rights reserved.

Contents

1. Introduction	2
2. TMN continuous films	3
2.1. Fundamental features and growth	3
2.1.1. Fundamental features	3
2.1.2. Growth mechanisms, structural defects and stress, strain development	5
2.2. Optical and electronic properties of continuous films	11
2.2.1. The work function of B1 transition metal nitrides	11
2.2.2. The importance of B1 transition metal nitrides as optical conductors	11
2.2.3. Electronic structure calculations	12
2.2.4. Experimental dielectric function spectra of binary nitrides	17
2.2.5. Experimental dielectric function spectra of ternary nitrides	26

* Corresponding author.

E-mail address: ppats@physics.auth.gr (P. Patsalas).

3.	TMN nanostructures and plasmonic applications	32
3.1.	Quality factors of plasmonic resonances	32
3.2.	SPP performance at TMN/dielectric interfaces	38
3.3.	LSPR performance of TMN nanoparticles	41
3.3.1.	Far field properties	41
3.3.2.	Near field properties	44
3.3.3.	Photothermal properties	45
4.	Conclusions and outlook	48
	Acknowledgements	48
	References	48

1. Introduction

The recent emergence of plasmonics, the science and technology of metallic nanostructures interacting with light, is based upon the surface plasmon polariton (SPP) modes in planar surfaces and localized surface plasmon resonance (LSPR) in metallic nanoparticles [1–14], two unique phenomena that manifest exclusively at the nanoscale. As a result, plasmonics is one of the most characteristic examples of what is called ‘nanotechnology’ nowadays, despite being manifested since antiquity and theoretically explained since the early twentieth century [15,16]. Thus, plasmonics promise radical breakthroughs in electronic devices [17–24], biosensing [25–35], catalysis and photochemistry [36–45], solar energy harvesting [46–64], photodetection [65–74], optical storage of information [75–84], telecommunications [85–94] and metamaterials [95–99]. These applications are, in their turn, based on the high spatial resolution of SPP and LSPR, which is below the diffraction limit of light [7,82,100–103], the ultra-fast response of plasmonic systems [104–107], the maximized absorption and scattering of light [1,108], the elevation of the metal’s electrons to a hot state [109–113], and more importantly the creation of extreme near-fields [114–119] that result in enhanced Raman and fluorescence signals of adjacent molecules [28,120–128] and the increased electron field emission probability [129,130] at the resonance wavelengths.

The most popular plasmonic metals are gold and silver due to their high conductivity and low dielectric losses (especially for Ag); the former due to its chemical inertness and stability and its facile surface functionalization by thiolates [131] and the later due to the absence of interband transitions in the visible spectral range rendering stronger and tunable LSPR throughout the visible spectral range, yet in expense of the feature size resolution (i.e. for Ag nanoparticles with LSPR in red the particles should exceed 100 nm [132]). However, their spectral tunability is limited (LSPR of Au or Ag nanoparticles cannot be extended to UV, and extension to IR would dictate size and shape compromises), their melting point is low, especially when in nanoparticle form [133,134], making them unstable for photothermal and hot electron devices, their conduction electron mobility is very low, and consequently they exhibit high conduction electron losses [135–137] and they both exhibit relatively high work function [138] minimizing the electron emission probabilities. Copper combines the drawbacks of gold (interband absorption and dielectric losses in the visible) and silver (reactivity), its plasmonic behavior is inferior [139] and, consequently, studies on its plasmonic response are less frequent [140–143].

In order to tackle the aforementioned obstacles of gold, silver and copper, a quest for alternative plasmonic conductors is taking place recently [136,137,144–176]. Group-III metals (aluminum, gallium and indium) have been investigated for extending the plasmonic devices to the UV range [148–157]; however they suffer from fast oxidation resulting in a metal/oxide core/shell structures, which eventually operate in the visible spectral range [148]. In addition, they have exceptionally low melting temperatures (Ga nanoparticles melt even below room temperature) and high diffusivities that compromise

their long-term stability. On the other hand, for extending the operation of plasmonic devices to IR, transparent conductors, such as indium tin oxide (ITO), aluminum-doped zinc oxide (AZO) and gallium-doped zinc oxide (GZO) have been implemented [158–169].

An emerging category of alternative plasmonic materials is the conductive transition metal nitrides (TMN), such as TiN, ZrN and TaN [169–183]. Going beyond the three aforementioned nitrides, of significant technological importance are all the nitrides of the transition metals of the group IVb–Vb–VIb (4–6 IUPAC) of the periodic table of elements, as shown in the reduced periodic table of elements in Fig. 1 (data taken from [184–187]); these nitrides can form cubic rocksalt-type crystals (B1-structure, Fm3m symmetry) and constitute a category of very important technological materials due to their exceptional mechanical properties, high melting point, refractory character and chemical stability over hostile environments. Thus, TMN are widely studied and used for a variety of applications, such as decorative coatings, protective and anti-corrosive coatings, in cutting tools and machining equipment; therefore, the works dealing with comparisons on their growth and properties are numerous and well-established [184,188–200]. They also exhibit electronic conductivity due to the partially filled valence *d* orbitals that are not completely hybridized with the N-2p electrons, as we will show below. The unique combination of their electronic properties with their stability and refractory character resulted in TMN being used also for applications in electronics, such as diffusion barriers [201–210], Schottky contacts [211–213], superconducting devices [214–219], conductive growth templates for wide bandgap semiconductors [220–222], field emission cathodes [223], and Ohmic contacts for optoelectronic devices [176,184,224] or other types of metallizations [225–231]. Finally, an exceptional asset is their compatibility with CMOS technology, due to their high electron mobility and refractory character [232–235], which enables their easy integration and upscaling in realistic, mainstream electronic devices. In this respect, TMN would boost the integration of plasmonics into CMOS technology for optical communications by replacing the incompatible Au [236] and Ag [237]. Alloying elements to form conductive ternary compounds in the B1 rocksalt structure include the elements of the groups II, IIIa, and IIIb (mostly Al).

In this work we review the fundamental properties (phases, microstructure, growth techniques) of the TMN, as well as their electronic structure via detailed *ab-initio* and semi-empirical computational methods, their dielectric function spectra extracted from an extended literature survey of reported ellipsometry and optical reflectivity spectra. As a result, we critically compare the reported electronic properties (such as resistivity/conductivity, conduction electron density-via the unscreened plasma energy, the spectral position of their interband transitions and their work-function). We also consider the effect of grain size to the optical and electronic properties of TMN.

Furthermore we consider the successful alloying of TMN to form ternary TMN (or more accurately pseudobinary nitrides, because the B1 structure is retained in the entire compositional range and the nitrogen sublattice of the B1 structure remains intact during

II						IIIa	Va
Be						B	N $2s^2 2p^3$
Mg						Al $3s^2 3p^1$ AlN: w, zb $E_g=6.3$ eV	P
		IIIb	IVb	Vb	VIIb		
Ca	Sc $3d^1 4s^2$ ScN: rs a=0.442 nm $E_g=1.58$ eV	Ti $3d^2 4s^2$ TiN: rs a=0.424 nm $E_{pu}=7.8$ eV	V $3d^3 4s^2$ VN: rs a=0.414 nm	Cr $3d^4 4s^2$ CrN: rs a=0.416 nm $E_{pu}=0$ eV		Ga $4s^2 4p^1$ GaN: w, zb $E_g=3.4$ eV	As
Sr	Y $4d^1 5s^2$ YN: rs a=0.487 nm $E_g=0.85$ eV	Zr $4d^2 5s^2$ ZrN: rs a=0.461 nm $E_{pu}=6.98$ eV	Nb $4d^4 5s^1$ NbN: rs a=0.439 nm $E_{pu}=8.93$ eV	Mo $5d^5 4s^1$ MoN: rs a=0.424 nm $E_{pu}=9.57$ eV		In $5s^2 5p^1$ InN: w, zb $E_g=0.7$ eV	Sb
Ba	La $5d^1 6s^2$ LaN: rs a=0.530 nm $E_g=0.75$ eV	Hf $5d^2 6s^2$ HfN: rs a=0.452 nm $E_{pu}=7.95$ eV	Ta $5d^3 6s^2$ TaN: rs a=0.439 nm $E_{pu}=9.33$ eV	W $5d^4 6s^2$ WN: rs a=0.421 nm $E_{pu}=10.5$ eV		Tl	Bi

rs: Rock salt
zb: Zinc blende
w: Wurtzite

E_{pu} : Unscreened Plasma Energy of a Conductor
 E_g : Bandgap of a Semiconductor

Fig. 1. An excerpt of the periodic table of elements where the usual constituents of the various conductive binary and ternary transition metal nitrides are shown (blue and green are the usual constituent of the conductive nitrides of B1 structure, magenta are the elements that can be potentially used as dopants in order to control the conductivity and the LSPR spectral position and red are elements that are not recommended for electronic applications); data taken from [184–187]. The colors of the cells are a graphic indication of the color of light where LSPR can occur for nanoparticles of a ternary nitride of the form $B1-Ti_xE_{1-x}N$, where E is the corresponding element (dark wine color stands for infrared). (For interpretation of the references to colour in this figure legend, the reader is referred to the web version of this article.)

alloying) with tuned electronic properties [238–253]. We demonstrate that these ternary systems provide exceptional flexibility, vast range for the values of the main electronic properties, thus offering immense potential for applications in plasmonics.

Finally and most importantly, we evaluate the potential use of binary and ternary TMN as core components for plasmonics by providing the LSPR performance of TMN nanoparticles through detailed Maxwell–Garnett effective medium approximation calculations and accurate Finite Difference Time Domain (FDTD) calculations. We demonstrate that the plasmonic response of nanoparticles of TMN is equivalent of that of nanoparticles of noble metals. In addition, we show that TMN can be active and stable plasmonic materials with LSPR ranging from the UV (using TaN and Ta-rich $Ti_xTa_{1-x}N$) to IR (using ternary $Ti_xSc_{1-x}N$ and $Ti_xAl_{1-x}N$) and combining additional assets such as refractory character, which makes them suitable for high temperature/high power plasmonics [182,183,254], photothermal applications [255], and low work function that makes them suitable for plasmon-enhanced electron emitters.

2. TMN continuous films

2.1. Fundamental features and growth

2.1.1. Fundamental features

2.1.1.1. Nitrides of group IVb elements (TiN, ZrN, HfN). The metals of the group IVb of the periodic table of elements have four valence

electrons with a configuration of d^2s^2 for all the three metals ($[Ar]3d^2 4s^2$, $[Kr]4d^2 5s^2$ and $[Xe]4f^{14} 5d^2 6s^2$ for Ti, Zr, and Hf, respectively) and they form bonds with N atoms (valence electronic configuration $2s^2 2p^3$). While various nitride phases such as the Me_2N [256,257] and Me_3N_4 (Me = Ti, Zr, Hf) [258,259] were reported, the most stable and durable nitrides of these metals are those in the cubic rocksalt B1–MeN arrangement or also called δ -MeN (Me = Ti, Zr, Hf). The B1 TiN, ZrN and HfN are characterized by gold-like yellow color (bright yellow for TiN and becoming gradually paler for ZrN and HfN [184,190]), high hardness [188,196], electrical conductivity [184,226] and refractory character [198].

B1–TiN is the archetypical example of the conductive nitrides. It has been studied since the early 1930s and B1–TiN films have been systematically grown and studied since the mid-1970s [260]. B1–TiN is considered nowadays as one of the most technologically important materials. A wide variety of fabrication techniques have been used for the growth of B1–TiN films, such as Magnetron Sputtering (MS) [261–268], Cathodic Vacuum Arc (CVA) [269–271], Chemical Vapor Deposition (CVD) [272,273], Atomic Layer Deposition (ALD) [189], Pulsed Laser Deposition (PLD) [184,274], Ion Beam Assisted Deposition (IBAD) [275], Dual Ion Beam Sputtering (DIBS) [276], and High Power Impulse Magnetron Sputtering (HIPIMS) [277]. The numerous works on the growth of B1–TiN led to an unprecedented understanding and control of its microstructural features, such as the grain size, orientation, columnar or globular type of growth, etc [276,278–282], and

epitaxial growth of TiN on MgO, GaN, AlN, and Si has been achieved [283], even at low temperature [284], as shown in the high-resolution transmission electron microscopy images of Fig. 2 for the cases of MgO (Fig. 2a) and GaN (Fig. 2b) substrates images from Refs. [224,284]. Therefore, it is evident that with the appropriate substrate selection both TiN(100) and TiN(111) films can be grown. The optical properties of B1-TiN, which are relevant to plasmonic applications, have been also a subject of intense experimental research [170,172–174,176,184,190,195,200,224,226,239,246,249,251,285–295]. The optical properties and the electronic structure reported in the aforementioned references [170,172–174,176,184,190,195,200,224,226,239,246,249,251,285–295] will be thoroughly reviewed in the following paragraphs.

B1-ZrN is another widely studied material, which finds a wide spectrum of applications such as superconductors [296], protective coatings [297], diffusion barrier layers [206], and IR reflectors [298]. The most popular technique for the growth of B1-ZrN is MS [229,297,299–303], however, CVA [304–306], ALD [307], PLD [296], and IBAD [308] were also successfully implemented. ZrN usually contains a higher amount of intrinsic stress and structural defects than TiN grown with similar conditions, mostly for kinetic reasons [309,310]. Consequently, the heteroepitaxy of ZrN on Si was not successful so far, as only local epitaxial domains were achieved [311], and the ZrN heteroepitaxy on MgO was achieved much later than for TiN and HfN [312].

Finally, B1-HfN is the less frequently studied compound of the group-IVb nitrides, possibly due to the scarcity of Hf and the difficulty of purifying metallic Hf from Zr impurities, despite of B1-HfN films' receiving attention since the early 1970s [313]. Sputter deposition is the most widely used deposition method for B1-HfN [314–317], as well, while alternative deposition techniques include ALD [318], CVD [319], IBAD [320] and Molecular Beam Epitaxy (MBE) [321]. The heteroepitaxy of HfN films was achieved on Si and MgO [322,323].

The dielectric function spectra and the optical reflectivity spectra of B1-ZrN [184,190,195,200,244,251,285–287,308,311,324–326] and B1-HfN [184,190,200,285–287,327–329] were studied and reported by many groups and are critically compared to those of B1-TiN in this work.

2.1.1.2. Nitrides of group Vb elements (VN, NbN, TaN). V, Nb and Ta have one more valence electron than Ti, Zr, and Hf, respectively, consequently they have five valence electrons and their valence electron configurations are [Ar]3d³4s², [Kr]4d⁴5s¹, and [Xe]5d³6s², respectively. VN and NbN can form easily the B1 nitride phase while B1-TaN is metastable. Several techniques were used for their growth, such as reactive sputter deposition (VN [330–333], NbN [334], TaN [335–340]), CVA (NbN [341–343], TaN [344]), PLD (VN [345], NbN [184,200,346,347], TaN [184,200,274]), ALD (VN [348,349], NbN [188,350], TaN [188,351,352]), CVD (VN [353], NbN [191], TaN [191,353]), and IBAD (VN [354], NbN [355], TaN

[356]). The epitaxial growth of B1-VN, B1-NbN and less frequently of B1-TaN, mostly on MgO, was also achieved successfully [333,357–360].

According to Papaconstantopoulos et al. [361] B1-VN, B1-NbN, B1-TaN are paramagnetic, while they all have been reported to be superconductors [347,362]. Especially NbN is a well known superconductor whose superconducting properties have been under investigation since the early 1980s [216–218,363–368]. B1-VN, B1-NbN, B1-TaN have also remarkable mechanical properties and stability and were studied accordingly [188,369–376], though not so intensively as B1-TiN and B1-ZrN.

Among them, TaN was more intensively studied, especially regarding its electrical properties, which are relevant to applications as diffusion barrier [202–205,209,377] and metallizations [196,225,228,233,378,379] where TaN is becoming an industry-standard material. B1-TaN has a colorless grayish appearance and its optical properties have been thoroughly investigated [168,169,174,184,200,242,246,248,251,380–383] and can be tuned by alloying with TiN, [184,246,248,251] or ZrN [242]; due to its remarkable optical properties, it was proposed as a promising alternative plasmonic material [168,169,174]. Note however, that TaN is very hardly stabilized in the B1 phase [376,384], although high quality B1-TaN has been achieved by few authors [381,385,386], and it has been recently suggested that the point defects, which are undesirable for the electrical conductivity, are playing a crucial role towards the stability of B1-TaN [387]. Studies on the optical properties of VN [238,328,380,388] and NbN do exist [184,200,389–391] but they are far more rare.

2.1.1.3. Nitrides of group Vlb elements (CrN, MoN, WN). Cr, Mo and W have one more electron than V, Nb, and Ta, respectively, consequently they have six valence electrons and their valence electron configurations are [Ar]3d⁴4s², [Kr]4d⁵5s¹, and [Xe]5d⁴6s², respectively. Cr can easily form the B1 nitride phase by conventional sputtering [392–395], HIPIMS [277,396,397], MBE [398], and CVD [399]. The attention that B1-CrN received was due to its superior wear and anti-corrosion performance compared to B1-TiN [400–408]. The magnetic properties of CrN are unique among all the TMN, as implied since the pioneering work of Papaconstantopoulos [361] where the paramagnetic state of CrN was questioned, and clearly proven by Filipetti et al. who performed spin polarized calculations and predicted its semi-conductive character when in anti-ferromagnetic state [409]. The interplay between the magnetic properties of CrN and its semiconductive behavior was experimentally confirmed by several groups [408,410–412] and disregard it as a candidate plasmonic conductor; therefore, the study of its electronic structure and dielectric function spectra is excluded from this work.

B1-MoN and B1-WN are the less studied among all TMN. MoN has been studied since early 1980s [413]. It is hardly stabilized in the

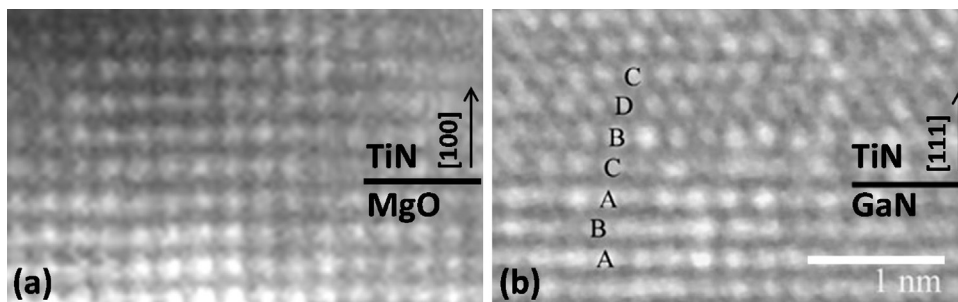


Fig. 2. High-resolution transmission electron microscopy images of epitaxial TiN grown by magnetron sputtering on (a) MgO, and (b) GaN/Al₂O₃. The horizontal black lines indicate the interfaces; lettering in (b) defines the stacking of crystal planes, which is different for the hexagonal w-GaN and the cubic B1-TiN according to [224]; the scale bar applies to both images. Images from [224,284].

B1 structure and competitive hexagonal MoN phases exist [414,415]. MoN is also paramagnetic [361] and superconducting [416–418]. B1-MoN has been reported to be grown by sputtering [414,419], PLD [184,200], CVA [420], IBAD [421], CVD [422,423], and ALD [424]. WN was considered mostly as a diffusion barrier [425] and despite of being desposited by a variety of techniques, such as sputtering [211,370,426,427], CVD [422,428], and ALD [429,430] its B1 phase in epitaxial form on MgO and sapphire has been very recently achieved [187]. Consequently, the studies of their optical properties are extremely rare [184,200,431], while until recently [184,432] the optical properties of B1-WN were missing from the literature, since most of the reported works dealing with WN referred to other phases.

Both MoN and WN are unstable in the B1 cubic structure [186,387,433] and it was recently revealed that the existence of point defects (metal and ligand vacancies) play a crucial role for their stabilization [186,387,433].

2.1.1.4. Ternary conductive nitrides. Alloying the aforementioned TMN to form ternary (or more accurately pseudo-binary) films is an effective pathway to controlling their mechanical, optical and electronic properties. The similar crystal structure (rocksalt), local symmetry (octahedral) and the similar bonding to N (via hybridization of the metal's *d* electrons with the nitrogen's *2p* electrons) [187], make all the nitrides of the group IVb, Vb, and VIb metals completely soluble to each other in the B1 phase and in the entire compositional range [184,249,250]; in fact, such alloying may result in more stable films with less structural defects compared to some metastable binary nitrides, with the most prominent example being the stable Ta-rich B1-Ti_xTa_{1-x}N and the metastable B1-TaN [376]. The most widely used alloying phase for electronic applications is the B1-TiN, which is implemented as the basis for the formation of Ti_xZr_{1-x}N [251,305,376], Ti_xHf_{1-x}N [184,249], Ti_xV_{1-x}N [238,247,253], Ti_xNb_{1-x}N [184,249,250], Ti_xTa_{1-x}N [376,434], Ti_xCr_{1-x}N [241], Ti_xMo_{1-x}N [184,239,241,249,250,435,436], and Ti_xW_{1-x}N [184,437,438]. Electronics-relevant Ta-based (Ta_xZr_{1-x}N and Ta_xW_{1-x}N) [184,242,244,249,250,439], Zr-based (Zr_xHf_{1-x}N, Zr_xNb_{1-x}N, Zr_xCr_{1-x}N, Zr_xY_{1-x}N,) [243,245,440,441], and V-based (V_xW_{1-x}N) [370] ternary nitrides were also reported.

Apart from the structural stability, the driving force for alloying and forming ternary conductive nitrides is the tailoring of key properties, such as the resistance against oxidation that enhances the stability and lifetime of the films [442], the diffusion barrier capability [443], the electrical resistivity [248,251,444], the work function [184,445], the superconductivity [446,447], the optical reflectivity edge, which defines the color and brightness of optical films [184,448], and more recently the conduction electron density, which defines the plasmonic response of nanoparticles of these nitrides [439].

Ti, Zr, and Hf share the same valence electron configuration of the constituent metal (*d²s²*) and they form bonds with nitrogen atoms (valence electron configuration *2s²2p³*). Their electrical conductivity is due to the excess of *d* electrons of the metal. By substituting any of these metal atoms by atoms of a group Vb (V, Nb, Ta) or group VIb (Mo, W) element, the cubic ternary structure is enriched with conduction electrons [184], thus increasing the resistivity [248], and blueshifting the reflectivity edge [184,200,434] and the localized surface plasmon resonance of the corresponding nanoparticles [439].

It is clear that such alloying cannot reduce the conduction electron density below that of B1-TiN, B1-ZrN, and B1-HfN. In order to reduce their conduction electron density, and shift their optical and plasmonic performance towards the infrared, B1-TiN and B1-ZrN should be alloyed with group III or II elements. Among the group IIIa elements the only efficient candidate for alloying with B1-TiN and B1-ZrN is Al (valence electron configuration *3s²3p¹*).

Despite of AlN being mostly crystallized in the wurtzite-type hexagonal phase w-AlN and being a well-known extremely wide band gap semiconductor (*E_g* = 6.2 eV) [449–452], Al can be incorporated as an alloying element into Ti substitutional positions in B1-TiN and form the pseudobinary alloy B1-Ti_xAl_{1-x}N [198,439,453–457]. The B1-Ti_xAl_{1-x}N phase is electrically conductive and stable only in the range 0.55 < *x* < 1; its electrical and optical properties are apparently varying with *x* [453,457–460]. Electronic and photonic applications of the Ti_xAl_{1-x}N system include decorative colored coatings [453], plasmonic conductors operating in the deep red [439] and solar selective absorbers [461]. For the time being, the rest of the group IIIa elements are not efficient in alloying with B1-TiN. Ti-B-N films tend to be nanocomposite, and not ternary or pseudo-binary compounds, due to the competition of the rocksalt TiN and the hexagonal TiB₂ phases [462,463] and resemble more the properties of the Ti-Si-N nanocomposites [464]. Ti_xGa_{1-x}N is extremely scarce [461] due to the incompatibility of the sputtering process used for the TiN growth and the MBE process used for the GaN growth [465]; note that gallium targets cannot endure the plasma in the sputtering process and liquefy due the exceptional low melting point of gallium [466]; the emergence of the ALD technology for the growth of both TiN and GaN [467,468] can overcome the process incompatibility and might enable in the future the elaboration and the more careful investigation of this compound. Finally, indium combines the drawbacks of gallium in alloying with B1-TiN with the large mismatch of the atomic radii of titanium and indium, which are expected to induce severe stress and a strong driving force for decomposition; consequently, there is no report for the formation of Ti_xIn_{1-x}N.

As Al is not soluble in B1-TiN in the entire compositional range, other candidate substitution elements with three or two valence electrons, such as the rare earth elements (Sc, Y, La) of group IIIb and the alkaline earth elements (Mg, Ca) of group II have been considered, and Ti_xSc_{1-x}N, Ti_xY_{1-x}N, Zr_xY_{1-x}N, Ti-La-N (amorphous), Ti_xMg_{1-x}N and Ti_xCa_{1-x}N films were reported [441,469–472]. Among them, the most promising in terms of its electronic and optical properties, as well as of its stability, is Ti_xSc_{1-x}N [441,469,471]. This is mostly due to the valence electron configuration (*3d¹4s²*) of Sc, and the B1 crystal structure being the most stable phase of ScN, which is, however, an intermediate bandgap semiconductor (*E_g* = 1.30–1.58 eV) [473–476]. As a direct consequence of the similar crystal structure (B1) and valence electron configuration (partially filled *d*-band and filled *s*-band) of ScN and TiN, the pseudobinary B1-Ti_xSc_{1-x}N is stable in the B1 structure in the entire compositional range (0 < *x* < 1) and films of exceptionally high crystallinity and outstanding optical performance can be achieved [441,469–471].

2.1.2. Growth mechanisms, structural defects and stress, strain development

The high melting point of TMN has the direct consequence of their usual fine crystal structure and the ability of growing high crystalline quality TMN has been a subject of intense research for several years. In addition, it has been recently suggested [439,441] that the crystallinity of such films is of paramount importance for their plasmonic behavior. As a result, reviewing the growth mechanisms, microstructure and stress development during physical vapor deposition (PVD) of TMN thin films is very important for the understanding of TMN and for their critical evaluation for realistic applications in photonics and plasmonics. A special emphasis is given to TiN, which is the most widely studied binary compound among conductive TMN. We discuss the origin of stress evolution in binary and ternary compounds, based on recent kinetic stress models, as well as the growth-induced structural defects due to energetic particles impingement of the film surface/

subsurface that takes place under energetic deposition conditions, such as MS, DIBS, CVA, and HiPIMS. We will also illustrate the interplay between growth morphology, phase formation, texture and stress development for the case of ternary nitrides, for which a large variety of microstructures can be formed. Such microstructural attributes, in terms of grain size, preferential orientation and stress levels can deeply influence the TMN optical properties. The knowledge of these ‘extrinsic’ effects is as crucial as the ground electronic features of TMN for the quest in the design of conductive TMN for photonic and plasmonic applications.

2.1.2.1. Microstructural development during TiN film growth. A general development of film microstructure with respect to various growth conditions is commonly represented by diagrams called structure zone models (SZM) [477], which tend to relate the effects of the process parameters on the resulting microstructure of polycrystalline thin film materials. These diagrams are usually compiled as a function of the homologous temperature, $T_h = T_s/T_M$, where T_s is the substrate temperature and T_M is the melting point of the deposited material ($T_M = 3222$ K for TiN). For the case of sputter-deposition, it also necessary to take into account the working pressure [478], and more generally the energy deposited per incident particle, E_d [479]. Typical deposition conditions to

obtain stoichiometric TiN films with a relatively dense microstructure require sufficient adatom mobility, *i.e.* operating at T_s in the 550–800 K range, resulting in $T_h \sim 0.17$ – 0.25 , which corresponds to microstructures of ‘Zone T’-type of SZM [480]. The microstructure of polycrystalline TiN films grown under Zone T consists of V-shaped columns [184,481] see Fig. 3a, characteristic of an evolutionary microstructure throughout the film thickness, *i.e.* the columns become larger at larger film thickness; such features are limited for films thinner than 100 nm, which are usually employed in photonic and plasmonic devices [224]. The bright contrast between columns in the cross-sectional TEM image of Fig. 3a corresponds to voided grain boundaries, and this effect is also more pronounced with increasing film thickness. These columns emerge at the surface forming facets, corresponding to crystallographic planes of low surface energy γ , resulting in rough surface morphologies. The planes of lowest γ correspond to the planes with the largest lateral growth rate, in other words to the lowest perpendicular crystallographic growth rate. The formation of V-shaped columns is the result of a kinetically-limited competitive columnar growth, due to anisotropy in adatom surface diffusion: after random nucleation of grains [480], some column/grain orientations survive, while other disappear, and the film microstructure shown in Fig. 3a testifies that overgrowth has

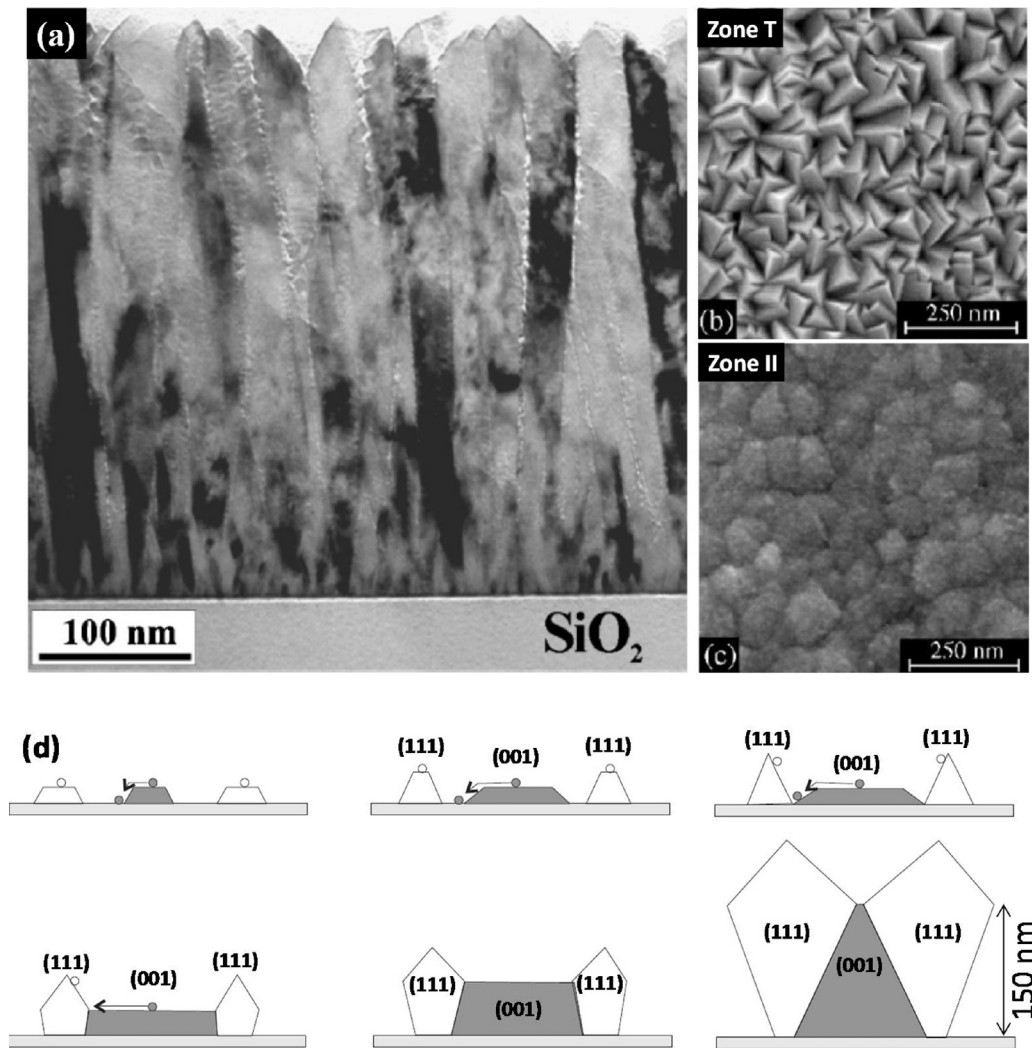


Fig. 3. a) Bright-field cross-section TEM micrograph of a TiN sputter-deposited film at 573 K and $P_{\text{tot}} = 0.66$ Pa and ion energy $E_i = 20$ eV, from Ref. [481] b) and c) Plan-view SEM surface morphology of TiN films sputter-deposited at 5 (b) and 20 sccm N_2 at, characteristic of Zone T and Zone II regions of SZM, respectively, from Ref. [477], d) the evolution of the competitive of the (111) and (200) crystals of TiN-based on sketch from Ref. [482], the differences are mostly due to the perpendicular and lateral surface diffusion of the deposited species.

occurred during film thickening. Mahieu et al. [477] have shown that the preferred orientation of TiN films grown under Zone-T corresponds to the geometrically fastest growing direction perpendicular to the substrate, *i.e.* the texture that develops corresponds to the [hkl]-oriented columns that gradually envelop and overgrow the other out-of-plane oriented grains. In this temperature range, the mobility is high enough to allow for surface diffusion as well as intergrain diffusion (mass transport from one grain to another), but not for bulk diffusion (grain boundary are immobile) so that restructuring is prohibited. The preferred orientation depends on the nature of the reactive gas species (either atomic N or N₂ molecule) and incoming adparticles (either Ti or TiN), which dictates the crystallographic orientation which forms the facets [480]. For conditions at which the formed facets are {100}, the fastest geometric growth direction is [111], and TiN films will have a [111] out-of-plane preferred orientation. The corresponding surface morphology consists of nicely faceted grains of tetrahedron shape, pointing with a corner upward (see Fig. 3b), typically obtained for MS at low N₂ partial pressure for which the state of reactive gas is molecular and the incoming flux is composed of Ti atoms. However, in the presence of atomic N, which is the case of MS at higher N₂ flow, faceting results in {111} crystal habits, so that the preferential out-of-plane orientation is along [001]. In this case, the characteristic surface morphology consists of square-base pyramids (shown in Fig. 3d [482]). Therefore, for certain applications (*i.e.* plasmonic nanoparticles) that are based on isolated self-assembled TiN islands the different growth behavior of the [001] and [111] oriented grains, depicted in Fig. 3d, should be taken into account.

Let us mention that TiN films grown under Zone T conditions can develop also an in-plane preferential orientation in addition to their out-of-plane orientation, often referred as a biaxial alignment, this is typically the case when the substrates are tilted with respect to the incoming material flux [477]. This is called glancing angle deposition (GLAD). Anisotropic in-plane growth rates (in terms of 2D capture length of diffusing particles) also govern the development of in-plane alignment similarly to the mechanism responsible for the out-of-plane orientation.

At higher homologous temperatures, typically for $T_h > 0.3$, TiN films can develop a Zone II-type microstructure, consisting of straight columns with constant column diameter throughout the entire film thickness. The column diameter in Zone II is much larger than that of Zone T, and the columns are not faceted, but rather exhibit a smooth morphology. This is illustrated in Fig. 3c, where it can be clearly seen that the TiN surface is more compact and grains have a rather rounded aspect; consequently, we might propose as a rule of thumb to select these conditions for the growth of TiN for plasmonic and photonic applications. The resulting out-of-plane preferred orientation corresponds to the plane of lowest surface energy. For TiN, the computed values of γ evidence a strong anisotropy: the planes of lowest surface energy being (001), with $\gamma_{001} \sim 1.3 \text{ J m}^{-2}$, much lower than the values for the (110) and (111) surfaces, with $\gamma_{110} \sim 2.6\text{--}2.9 \text{ J m}^{-2}$ and $\gamma_{111} \sim 4.5\text{--}5.0 \text{ J m}^{-2}$, respectively [281]. Note that the (111) surface of TiN is polar, so that the energy of N- and Ti-terminated (111) surfaces differ significantly [483].

For the TiN film morphology shown in Fig. 3c, the Zone II-type microstructure was not obtained by increasing T_s , compared to the Zone T case shown in Fig. 3b but rather by increasing the N/Ti flux (operating at higher N₂ flow rate), which contributes to increasing the energy flux E_{tot} towards the substrate [268]. Since the diffusion length of adatoms, L , is related to E_{tot} through $L \approx \sqrt{\frac{e^{-1/E_{\text{tot}}}}{J_{\text{Ti}}}}$, where J_{Ti} is the metallic Ti flux, increasing E_{tot} will increase the diffusion length, enabling to span different film microstructures from Zone Ic (small L values, corresponding to columnar growth with random orientation), to zone T and finally to Zone II. Mahieu and Depla

[268] suggested that the crossing from Zone T to Zone II involves recrystallization processes occurring through island ripening and island diffusion rather than by grain boundary migration. The close correlation between the magnitude of particle fluxes reaching the substrate, preferred orientation and microstructure is rationalized in terms of extended SZM [477] and also in line with the atomic N/Ti flux model of Gall et al. [281]. Using *ab initio* calculations, these authors reported that in the presence of excess atomic N, the diffusion length of Ti adatoms is significantly reduced on (001) planes, leading to a lower chemical potential for Ti adatoms on (001) than on (111), $\mu_{\text{Ti},001} < \mu_{\text{Ti},111}$, and consequently to a net atomic flux from 111- to 001-oriented grains. This latter grain orientation will therefore survive under high N/Ti flux conditions. This might be an important pathway for the growth of low electron loss TiN at moderate temperatures.

Ion bombardment can often be used to enhance film densification. Several processes take place, including biased surface diffusion by momentum transfer, but also creation of primary recoils, followed by knock-on atomic displacement events and eventually defect formation in the subsurface once the energy of incoming particles exceeds the energy threshold for atomic displacement, E_{dis} , which is typically around 25 eV for Ti. The use of such hyperthermal particle fluxes will favor renucleation and restructuring, leading to a more fine-grained microstructure, but can be highly detrimental in terms of compressive stress that is generated by subplantation mechanism [282], as it will be discussed below.

Finally, the use of pulsed particle fluxes, as generated by HiPIMS discharges, modifies both the plasma composition and ionization degree of the metallic species. At high discharge currents (20–30 A), a significant fraction of metallic Ti⁺ ($J_{\text{Ti}^+}/J_{\text{Ti}} > 1$) and Ti²⁺ ($J_{\text{Ti}^{2+}}/J_{\text{Ti}} \sim 0.5$) ions will reach the growing film surface, together with N₂⁺ and N⁺ ions coming from nitrogen dissociation in the plasma, thereby influencing nucleation, competitive columnar growth, column size, texture and stress state [442]. Note that N₂⁺ ions with energy above the binding energy of molecular N₂ (9.7 eV) [484] will dissociate upon collision with the film surface.

2.1.2.2. The effect of deposition parameters on stress evolution in TiN thin films. The origin of the residual stress is in general associated with structural changes occurring during film growth (*growth or intrinsic stress*), the effect of post-deposition temperature change (*thermal stress*) and effects following growth (*extrinsic stress*). Typical processes resulting in the development of either tensile or compressive *intrinsic stress* comprise coalescence of crystallite islands in the initial growth stages, grain growth and corresponding reduction of volume fraction of grain boundaries, shrinkage of grain boundary voids, grain boundary relaxation, defect annihilation, incorporation of adatoms into grains and grain boundaries and incorporation of additives/impurities. Consequently, minimizing the electron loss in conductive nitrides requires the elimination of such defects and of the stress, which is a strong indicator for their existence. An understanding of the origin and development of stresses in thin films grown under various process conditions was recently possible due to real-time and depth-resolved analytical methods applied to deduce relations between fundamental film-forming processes, structural development and stress generating mechanisms [267,309,442,484]. Fig. 4a shows the evolution of the stress-thickness product ($\sigma \times h$) for a series of TiN films deposited by MS at different N₂ flows. Depending on the N₂ flow, and therefore N/Ti flux, the stress that develops can be either tensile (at low N₂) or compressive (at high N₂). It can be clearly observed that the stress evolves with film thickness, attesting for the presence of stress gradients along the film thickness. No steady-state stress is reached in the investigated film thickness range and this is associated with an evolutionary microstructure following a Zone T regime: the incremental stress (given by the derivative of $\sigma \times h$

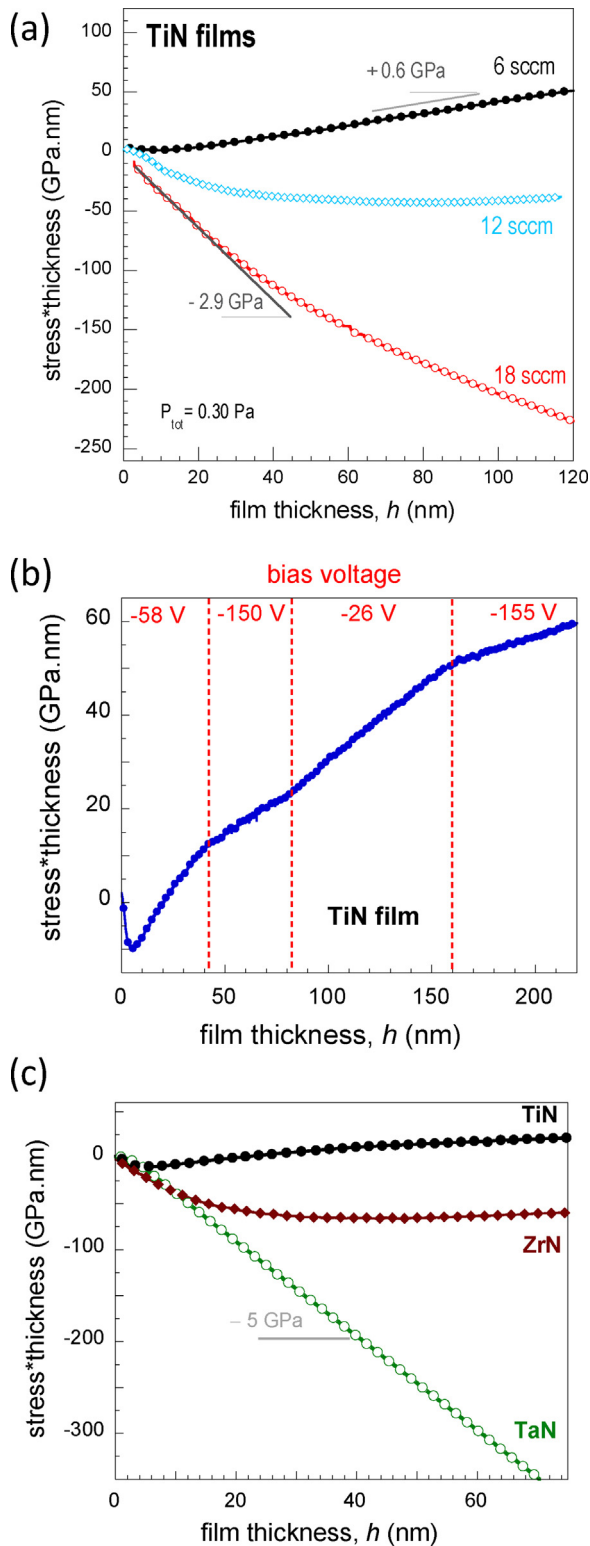


Fig. 4. Real-time stress evolution measured using MOSS during a) TiN sputter-deposition at different N_2 flow, b) TiN sputter-deposition with varying substrate bias voltage and c) TiN, ZrN and TaN sputter-deposition. All stress curves were recorded at the same $P_{tot} = 0.30$ Pa working pressure but with a target-to-substrate distance being either 18 cm (b) and (c) or 13 cm (a). The target makes an angle of 25° with respect to substrate normal.

with respect to film thickness h) is initially compressive, typically for $h < 10$ nm values of -3 GPa are obtained, and gradually levels off with increasing thickness or even becomes tensile (+0.6 Pa) for TiN films deposited at low N_2 flow. The change from compressive

towards tensile regime occurring in the early growth stages is more clearly seen in Fig. 4b, where the effect of varying substrate bias voltage is additionally reported. By changing the bias voltage during the course of deposition the slope of the stress-thickness curves is altered, the incremental stress becoming less tensile when larger bias voltages are applied. This evidences that the intrinsic stress that develops in TiN films with Zone T microstructures is the sum of two competing sources: a tensile stress source due to attraction between columns and a compressive stress source due to energetic bombardment of the growing film. This latter effect is known as the “atomic peening” process, in which defects are created by energetic species. This occurs typically in the sub-surface region, when the energy of incoming particles exceeds the *subplantation* energy threshold, which is ~ 50 eV for TiN [282,485]. Recent experimental findings have shown the importance of grain boundary on the mechanisms of defects incorporation during thin film growth [486,487]. The grain boundaries act as preferential sites for incorporation of excess atoms. Defects can also be created in the grain interior, in the form of vacancies, self-interstitials or substitutional atoms. The net result of the incorporation of interstitial-type defects or substitutional atoms with larger size than the host atoms is a volume expansion (associated with a hydrostatic stress field around the defect), which traduces by in-plane compressive stress state since the lateral dimensions of the film are fixed by those of the rigid substrate. Depending on the deposition rate, grain size, adatom surface diffusivity and energy of incoming species, complex stress variations are therefore anticipated. A kinetic stress model for PVD thin film growth under energetic conditions has been recently proposed [488,489], to which the interested reader can refer more details.

At constant deposition conditions, the energetic bombardment in the growing film remains the same throughout the whole deposition, so any stress evolution is related to a change in microstructure/texture. Typically, for Zone T, as the columns enlarge with film thickening, the stress turns from compressive to tensile, which is a direct consequence of evolutionary nature of the microstructure (the fraction of grain boundary decreases from the substrate interface towards the film surface, see Fig. 3a). The correlation between stress gradients and column/grain size variations has been evidenced recently by Daniel et al. [490,491] on TiN films using depth-sensitive X-ray nanodiffraction. By increasing the bias voltage during deposition, the energy of ions accelerated across the substrate sheath increases, which has the immediate consequence to increase the contribution of atomic peening, resulting in a less tensile incremental stress, as illustrated in Fig. 4b.

As discussed above, the degree of texture, grain size and surface morphology of TiN films grown by reactive MS can be tailored by appropriate choice of the deposition conditions, *i.e.* by monitoring the substrate temperature T_s , the N/Ti flux or the average energy per deposited particles, $\langle E_d \rangle$. These parameters will also strongly impact the resulting stress state. The energetic species contributing to E_d are the film-forming species, backscattered gas neutrals (gas ions that are neutralized and reflected at the sputtering target) and ions (from the plasma or an independent ion source, typically Ar^+ , N_2^+ , N^+), whose relative fraction depends on the plasma composition and discharge type (MS vs. HiPIMS) [442,492]. The film-forming species are either neutral, *i.e.* sputtered Ti^0 atoms from the target, or ionized metallic or nitrogen species, Ti^+ , Ti^{2+} , N^+ . The average energy per deposited metallic atoms can be expressed as

$\langle E_d \rangle = E_{sp} + E_i \times J_i/J_{Me} + E_b \times J_b/J_{Me}$, where E_{sp} is the average energy of sputtered metal atoms, J_i/J_{Me} is the ion-to-metal flux ratio, E_i is the average ion energy, E_b is the average energy of backscattered gas species, and J_b the flux of backscattered atoms.

The energy of sputtered Ti atoms and reflected Ar depends on the working pressure P_{tot} during deposition: these particles will experience collision in the gas phase during their transport from the target to the film surface. For target-to-substrate distance d_{TS} lower than the particle mean free path λ (λ is inversely proportional to P_{tot}), the particles will reach the substrate with the same nascent energy they had when leaving the target. However, operating at increasing P_{tot} can result in λ becoming significantly shorter than d_{TS} and particles can get thermalized before reaching the substrate. For example, for Ti atoms, λ decreases from 23 to 9 cm when P_{tot} increases from 0.2 to 0.5 Pa [309]. For the same pressure variation, E_{sp} decreases from 17 eV to 3 eV. The relative flux $J_{\text{b}}/J_{\text{Me}}$ of reflected gas atoms reaching the substrate depends on the metal target mass relative to that of the working gas, as well as and cathode geometry.

For reactive direct current MS (DCMS) in Ar+N₂ plasma discharges, the N₂ fraction in the sputtering gas mixture is typically several percent and sputtering often occurs under metal target mode. The dominant ion flux reaching the growing film surface is Ar⁺, with incident energy E_i depending on the applied substrate V_s , that is $E_i = n_i e (V_s - V_p)$, where V_p is the plasma potential (≈ 10 V) and n_i the charge state of the ion. The range of V_s widely used in conventional DCMS deposition of TiN films is 30–60 eV, which is enough to ensure film densification by enhancing adatom surface mobility but can also cause defect incorporation. Operating at higher V_s (>100 eV) will cause film re-sputtering (and consequently roughening) and entrapment of gas atoms (Ar) in the film. The fraction of Ar impurity in TiN films may in this case reach several atomic percent, at the origin of lattice expansion and compressive stresses, as reported by Petrov et al. [493].

Let us summarize the influence of main deposition parameters on the resulting stress state. Increasing P_{tot} will result to a net tensile stress increase [487]; increasing N/Ti flux will result to a net compressive stress increase, as seen in Fig. 4a for TiN films deposited at different N₂ flow, from 6 to 18 sccm, corresponding to N/Ti flux increase from 1 to 23 [487]. Changing the magnetron configuration or operating under rf discharges instead of dc will affect J_i/J_{Me} (e.g., J_i/J_{Me} will increase when unbalancing the magnetron, leading to more compressive stress). The influence of substrate temperature is more complex, as opposing effects can come into play. Increasing T_s will enhance surface diffusion, promoting incorporation of excess atoms at the grain boundary (compressive stress source), but also activating migration of defects and their annihilation at the film surface (stress relaxation). It can also favor grain growth (tensile stress source) and change in preferential orientation of grains (inducing a stress change for anisotropic elastic material).

The change of texture from [001] to [111] with increasing TiN film thickness (texture crossover) has initially been ascribed to an overall energy minimization, based on thermodynamics considerations that the stored elastic strain energy is lower for (111) planes compared to (002) planes for the same stress level due to elastic anisotropy of TiN crystals. However, there is a converging set of experimental and theoretical findings [268,276,281,282,484,494] which demonstrates that the texture crossover is driven by kinetic limitations intrinsic to the out-of-equilibrium nature of PVD processes, more precisely to anisotropy in surface diffusion.

2.1.2.3. Influence of chemical element and point defects. We briefly review here the variations in stress state of binary TMN, the case of chemical alloying for ternary TMN will be addressed below. The comparative evolution of the intrinsic stress during sputter-deposition of TiN, ZrN and TaN is shown in Fig. 4c, for exactly the same deposition conditions ($P_{\text{tot}} = 0.3$ Pa, $V_s = 50$ eV) and chamber geometry. One can see that for heavier metal targets ($M_{\text{Ta}} > M_{\text{Zr}} > M_{\text{Ti}}$) the stress becomes more compressive, evolving

from slightly tensile for TiN towards -5 GPa for TaN. For TaN, the stress rapidly reaches a steady-state, indicating that there is no significant microstructural change with increasing film thickness. This is related to a loss of columnar structure due to repeated nucleation, TaN films exhibiting a fine grained morphology. These differences can be explained by the contribution of backscattered gas (here Ar) neutrals, whose relative flux and energy increases with M_{Me} [495]. In particular, the average energy of backscattered Ar increases from ~ 5 eV to ~ 57 eV when changing Ti to Ta target. $J_{\text{Ar}}/J_{\text{Me}}$ is 0 for a lighter metal target (like Al), ~ 2 –3% for Ti target and around 30% for a heavier metal target (like Ta). The average energy of sputtered atoms also increases from ~ 14 eV for Ti to ~ 25 eV for Ta. Both sputtered metal atoms and reflected Ar will contribute to increase $\langle E_d \rangle$ and finally larger compressive stresses will develop as a consequence of defect creation by atomic peening. Changing to a heavier gas atom, like Xe, can be a suitable route to minimize the impact of energetic reflected atoms and reduce the level of compressive stress.

For TiN, Kamminga et al. [496] have shown that atomic peening induces incorporation of misfitting atoms in the TiN layer, causing an hydrostatic state of stress around the defects, and a net compression in the film plane. These authors concluded that approx. 1 at.% of Ti atoms on N sites can cause a compressive stress of around -5 GPa, while the contribution of Ar on N sites will result in lower compressive stress magnitudes (-2.2 GPa for 1 at.%).

As discussed above, grain boundaries play an important role on the resulting stress state. By varying P_{tot} during ZrN sputter-deposition, Koutsokeras and Abadias [310] evidenced that at low Ar pressure excess atoms can get trapped in the grain boundary, causing a compressive stress contribution to the total stress state, while at higher Ar pressure, the column/grain boundary are under-tensile and the stress due to grain boundary contribution is tensile. If, for the vast majority of cases, the presence of defects in the TMN films is detrimental for their physical properties, they usually contribute to render the material harder. For some TMN, such as MoN and TaN, the existence of point-defects (mainly metal vacancies) is beneficial in stabilizing the cubic structure, as reported recently by Koutna et al. using *ab initio* calculations [387].

2.1.2.4. Consideration for ternary nitrides: stress and microstructure evolution. For many applications, tailoring the physical properties through chemical alloying has become an important research strategy, together with interfacial design. Fig. 5 summarizes the microstructure and stress evolution for two ternary systems, namely Ti-Zr-N and Ti-Ta-N, as representative archetypes of iso-structural and non-isostructural pseudo-binary systems, respectively. It can be clearly seen that the degree of [002] texture, T_{002} , grain size $\langle D \rangle$, microstrain ϵ and stress magnitudes are correlated with the variations in $\langle E_d \rangle$ when spanning the whole composition range. By increasing the Zr or Ta content in Ti-Zr-N or Ti-Ta-N thin film alloys deposited by reactive DCMS, one can see that the film's microstructure evolves from [111]-oriented columns towards more fine-grained morphology with [002]-preferred orientation, while the stress becomes more compressive. If cubic $\text{Ti}_{1-x}\text{Zr}_x\text{N}$ solid solutions are obtained in the entire compositional range for the Ti-Zr-N system [497], this is no longer the case for the Ti-Ta-N system, as hexagonal phases form above a TaN fraction of $y \sim 0.7$. Above this elemental threshold, the value of $\langle E_d \rangle$ becomes relatively large, above 35 eV/at., and it is believed that the large ϵ values $>1\%$ are responsible for the destabilization of the cubic structure for TaN-rich ternary alloys. A similar behavior was observed for DCMS-deposited Ta-Zr-N alloy thin films [498].

By employing different deposition processes, namely MS, IBS and PLD, Koutsokeras et al. [384] have shown that texture evolution of ternary TiTa₂N as well as the microstructural features of such films can be well understood in the framework of the kinetic

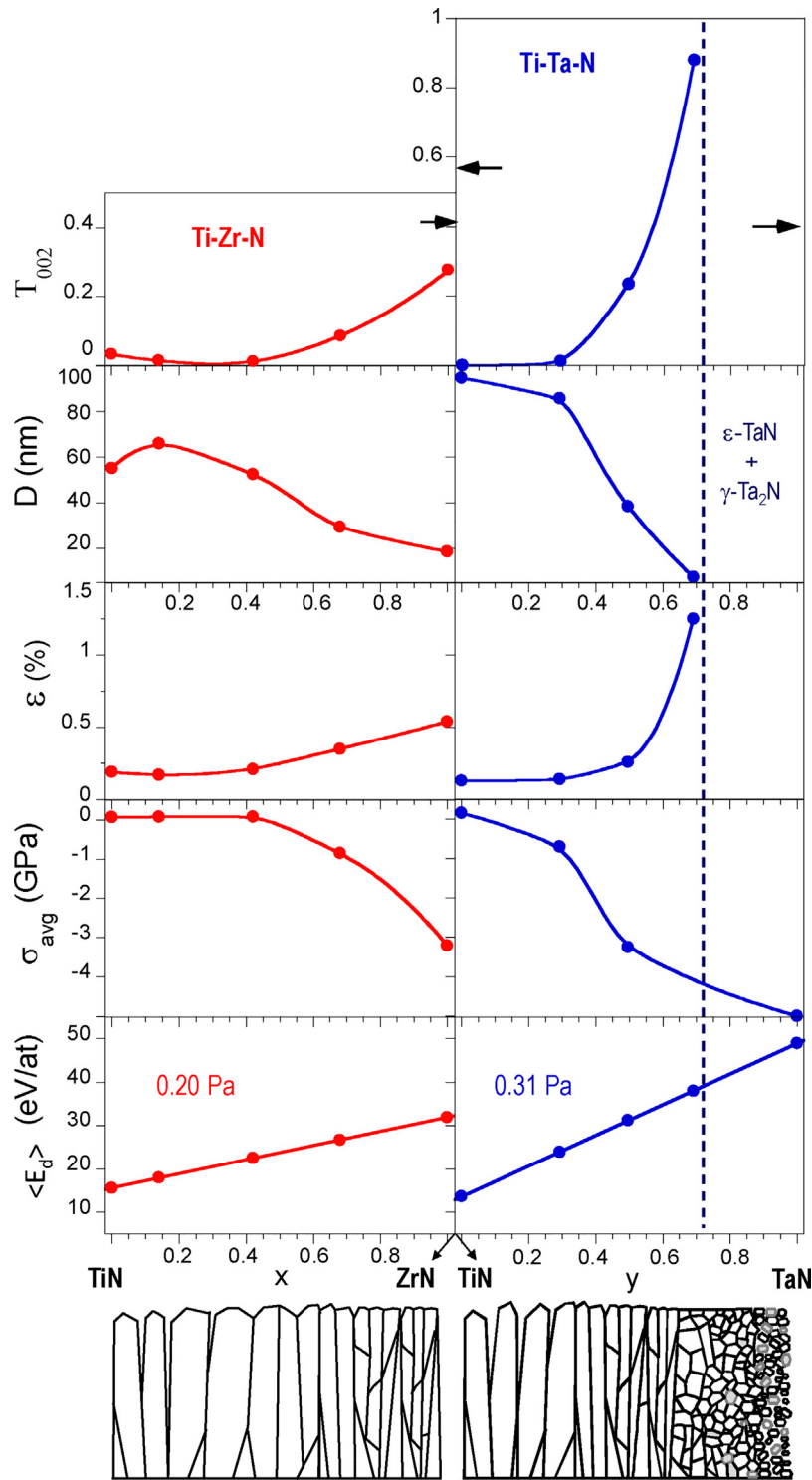


Fig. 5. Comparative evolution of a) preferred orientation (T_{002} ratio), b) vertical grain size (D), c) microstrain (ϵ), d) average stress (σ_{avg}) and e) deposited energy ($\langle E_d \rangle$) for $Ti_{1-x}Zr_xN$ (left) and $Ti_{1-y}Ta_yN$ (right) systems. The vertical dashed line marks the stability limit of the cubic $Ti_{1-y}Ta_yN$ lattice upon Ta incorporation. The arrows indicate the T_{002} ratio for binary powder compounds. The evolution of the microstructure with increasing x (or y) fraction is schematically shown at the bottom in terms of SZM, from Refs. [492,495].

mechanisms proposed for their binary counterparts, thus giving these mechanisms a global application. It was concluded that texture and microstructure are determined by the energetic and kinetic conditions rather by the composition of the film itself. Another system of practical interest is Ti-Al-N. The cubic phase is usually retained up to AlN fractions of 0.6–0.7 depending on the deposition process, while alloys with richer AlN content stabilize in

the wurtzite phase. The texture development is influenced by the Al content and deposition rate, but also by the film thickness [499,500]. By employing a hybrid Ti-DCMS/Al-HiPIMS deposition process, Greczynski et al. [501] were able to produce cubic $Ti_{1-x}Al_xN$ films with $x \sim 0.6$ and low stress state (less than 1 GPa) by synchronizing the substrate bias voltage to the metal-ion rich part of the HiPIMS pulse.

2.2. Optical and electronic properties of continuous films

2.2.1. The work function of B1 transition metal nitrides

The work function WF [184], which dictates the Ohmic or Schottky character of conductor/semiconductor junctions, as well as the potential for hot electron emission is of particular importance for a variety of applications [110,502–504]. In particular, the height of the Schottky barrier between a conductor and an n -type semiconductor is defined by the conductor's work function and the semiconductor's electron affinity [505], as it is presented in Fig. 6a. Thus, for an ideal Ohmic contact on an n -type semiconductor the metal's WF should be equal to the electron affinity of the semiconductor [505], while a tailored Schottky barrier that would fit certain hot electron applications [110,502–504] could be designed accordingly.

TMN exhibit a quite wide range of WF values, as shown in Fig. 6b. In particular, TMN exhibit WF values in the range of 3.56–5 eV [184,506–508] that coincides with the range of electron affinity values for most elemental and compound semiconductors (yellow shade region) with the major exception of Al-based compound semiconductors (pure AlN, AlP, AlAs). Therefore, by appropriate selection of the nitride conductor and the semiconductor, predesigned Schottky barriers or completely Ohmic contacts can be developed. In addition, good lattice match can be achieved in nitride conductors/nitride semiconductors that may enable epitaxial growth of such heterojunctions [224]. We note here that for simplicity the lattice constants of III-nitride semiconductors presented in Fig. 5 are for the zincblende polytypes; in the case of the wurtzite polytypes, the picture is similar for heteroepitaxy of the (111) rocksalt conductor nitride along the (0001) III-nitride semiconductor. Last but not least, it was reported [184] that the ternary $Ti_xZr_{1-x}N$ exhibits (red stars in Fig. 6b) intermediate WF values between those of the binary TiN and ZrN thus providing immense tailoring potential for designing hot electron devices with varying Schottky barriers.

2.2.2. The importance of B1 transition metal nitrides as optical conductors

Apart from the refractory character of the transition metal nitrides and their higher melting points compared to the

corresponding metals, which are more pronounced for the group IVb metals (as shown in Fig. 7a with data from Refs. [509–513]), and their improved thermal stability (e.g. pure titanium is transformed to anatase at 275 °C [514], while B1-TiN can endure up to 800 °C and is transformed directly to rutile [442]), their most important asset for the applications in photonics and plasmonics is their resemblance to an ideal optical conductor, in contrast to their metallic counterparts. The DC conductivity of transition metals is comparable or lower than that of the corresponding nitrides, as shown in Fig. 7b (with data from Ref. [311,366,432,515–517]), yet their optical behavior is inferior in terms of their plasmonic potential. Therefore, basic questions are risen, such as, what is the difference between an optical conductor and an electrical conductor, and what makes the transition metal nitrides in the B1 cubic structure better optical conductors than the corresponding metals?

In real conductors the measured optical performance is not dictated exclusively by the conduction electrons, in contrast to their DC and AC conductivity as in the case of ideal conductors often described in textbooks. The real permittivity is screened by the existence of interband transitions of bound electrons. A good optical conductor, which is intended to be used in near-infrared, visible and ultraviolet ranges, should exhibit negative real permittivity (real part of the dielectric function ϵ_1), with a clear and steep crossing to positive values at the wavelength region where the optimal plasmonic performance is desired to be, while its imaginary permittivity (imaginary part of the dielectric function ϵ_2) should have the smallest possible positive values in the entire spectrum, in order to minimize optical losses. A secondary concern is the actual slope of the ϵ_1 at the crossing point ($\epsilon_1 = 0$) and the absolute negative values of the conductor; Controlling the absolute negative values of ϵ_1 is highly desirable for several applications [518,519]. An exceptionally comprehensive discussion on this issue can be found in Ref. [135].

In Fig. 8 the real and imaginary permittivities of the group Vb metals (right panels) and their nitrides (left panels) are shown (data from Refs. [380,381,390,520–522]). VN and NbN are undoubtedly better optical conductors than V and Nb, despite of the nitrides having higher DC resistivity according to Fig. 7b, while TaN has a way shorter crossing wavelength than Ta, suggesting a

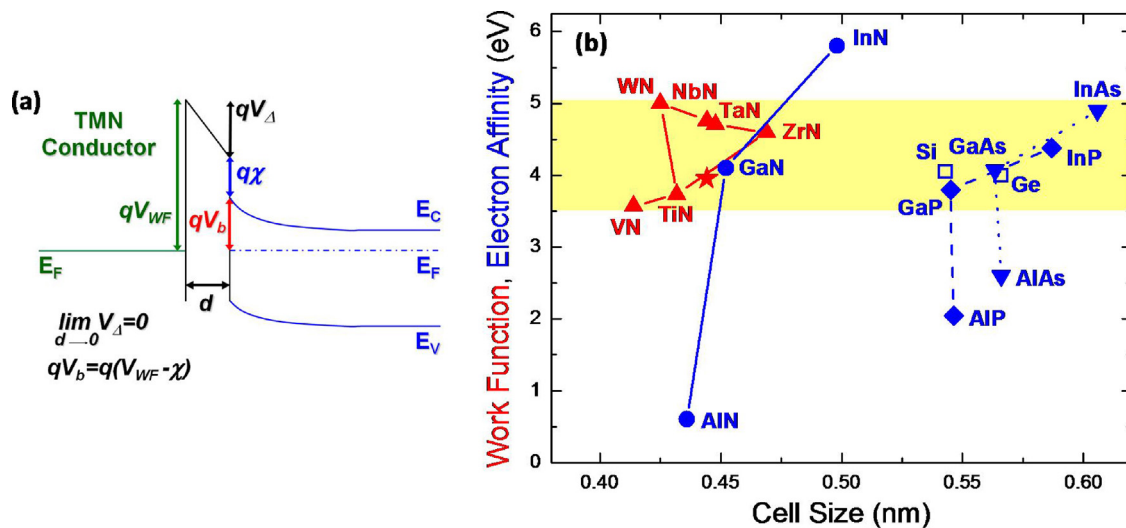


Fig. 6. (a) Band diagram of the emergence of a Schottky barrier between a conductor with a work function $WF = qV_{WF}$, and a semiconductor with electron affinity χ . (b) The variation of the WF of TMN with the nitride's cubic lattice constant in comparison with the electron affinities and the lattice constants of the major semiconductors (note that for the III-nitrides the lattice constant is for the cubic zincblende polytype and not of the most stable and usual hexagonal wurtzite polytype); star symbols represent ternary $Ti_xZr_{1-x}N$ [184]. Red triangles stand for the WF of TMN, while blue disks, diamonds and reversed triangles stand for III-nitrides, III-phosphides, and III-arsenides, respectively, and open squares stand for elemental IV semiconductors. (For interpretation of the references to colour in this figure legend, the reader is referred to the web version of this article.)

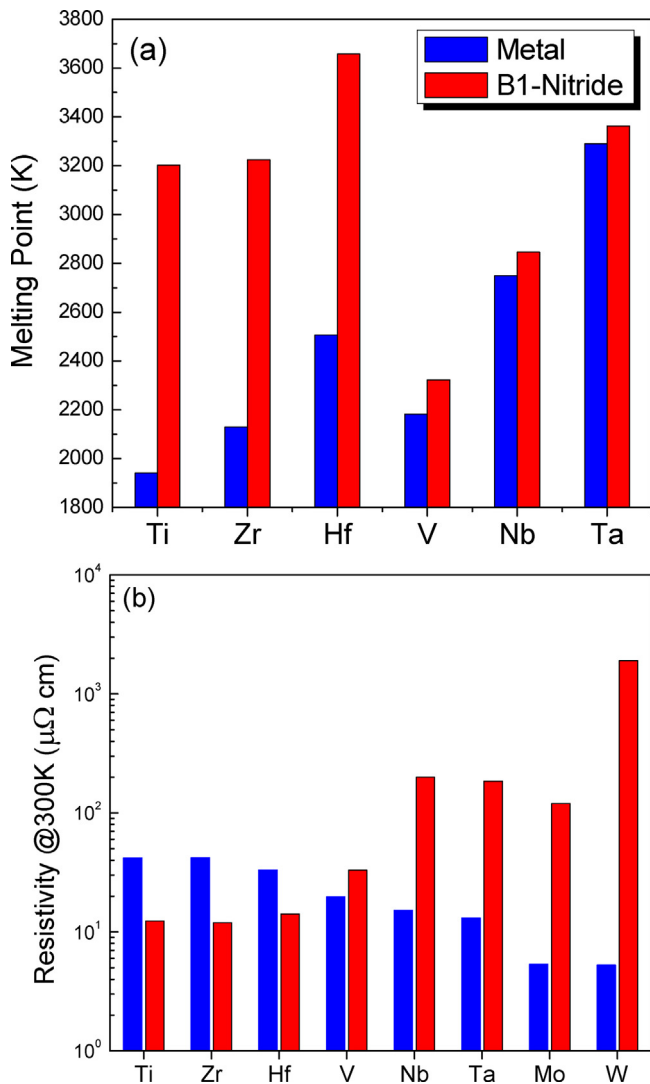


Fig. 7. (a) The melting points of the group IVb and Vb metals (blue bars) and their nitrides in the B1 structure (red bars); data from Refs. [509–513]; (b) Resistivity values of the group IVb, Vb–VIb metals (blue bars), and their corresponding nitrides in the B structure and epitaxial form on MgO (red bars); data from [311,366,432,515–517]. (For interpretation of the references to colour in this figure legend, the reader is referred to the web version of this article.)

plasmonic operation at a different spectral range. This contrasting behavior is, indeed, due to the co-existence of intraband (due to conduction electrons) and interband (due to bound electrons) absorption that may, or may not, spectrally overlap; any metal with small DC and AC resistivity may not necessarily be a good optical conductor due to this overlap that occurs exclusively in the range of optical frequencies. When there is strong spectral overlapping (e.g. the case of gold) the dielectric function is screened and the ϵ_1 gets negative values only for long wavelengths; on the contrary, when the interband and intraband absorption are not overlapping (i.e. if the valence electrons are strongly bound and having energy quite deep compared to the Fermi level, e.g. the case of silver), the conduction electrons are interacting with the light without such screening and the range of negative ϵ_1 values extends to shorter wavelengths.

The interplay between the intraband and interband absorption and its consequences to the optical spectra, are clearly illustrated in Fig. 9 for the Ti–N system (data from Refs. [176,259,523–526]; note that the ϵ_2 spectrum of ϵ -Ti₂N is not reported in Ref. [523]). Fig. 9a,b shows the dielectric function spectra for pure metallic

hcp-Ti, the hexagonal ϵ -Ti₂N, which are both conductors, the B1-TiN, and of the hypothetical Ti₃N₄, which is a semiconductor. It is clear that the *hcp*-Ti and the hexagonal ϵ -Ti₂N do not fulfill the criteria of a good optical conductor, despite of their significant DC and AC conductivity. On the contrary B1-TiN behaves like an ideal optical conductor with a very clear and steep crossing of the real permittivity to positive values, an almost featureless lineshape of the corresponding spectra, and very low values of imaginary permittivity. These variations can be well understood, if we take into account the electronic structure via the calculated electron density of states (EDOS) of the relevant compounds. Fig. 9c shows the EDOS of *hcp*-Ti and B1-TiN calculated by the linear augmented plane wave (LAPW) method. The emergence of the Ti3d–N2p bonds, via the hybridization of the corresponding valence electrons, shifts the majority of the Ti3d states from 0.5–3 eV below the Fermi level for *hcp*-Ti to 3–6 eV below the Fermi level for B1-TiN; this shift of the Ti3d states is the origin of the spectral separation of interband and intraband absorption in B1-TiN and the B1-TiN behaving like an ideal optical conductor. The LAPW calculations are in excellent agreement with detailed photoemission experiments, which are presented in Fig. 9d. These experiments clearly show the gradual depletion of the Ti3d states, which are located 0.5 eV below the Fermi level, upon incorporation of nitrogen and the emergence of the hybridized Ti3d–N2p deeper below the Fermi level. Note that in the photoemission experiments the unoccupied states cannot be probed, hence the differences between calculations (Fig. 9c) and experiments (Fig. 9d) above the Fermi level. Overstoichiometric TiN_{1.12} can be still stabilized in the B1 structure, it is still a conductor [176] but it exhibits smaller concentration of conduction electrons compared to stoichiometric TiN [226], and thus it further proves the association of N with the reduction of Ti3d states close to the Fermi level; finally, for Ti₃N₄ (i.e. TiN_{1.33}) the Ti3d states close to the Fermi level are completely depleted and Ti₃N₄ is predicted to be a semiconductor [259].

In order to have a more clear view of the effect of the overlapping of interband and intraband transitions, we show the experimental dielectric function spectra of an opaque B1-TiN film (Fig. 10, red solid lines), which may be analyzed to contributions due to intraband (magenta line) and interband absorption (red dotted line), which were calculated following the procedures described in Ref. [176]; the collective interband absorption (which consists of two Lorentzians) has a maximum at 5.3 eV. Then we calculated two hypothetical nitrides with exactly the same intraband contribution, and the interband contributions red-shifted by one (blue lines) or two eV (green lines). When the overlapping of interband and intraband absorption increases (i.e. the interband absorption occurs at lower photon energy) the ϵ_1 spectra cross the zero line with a less steep slope (if any at all), resembling the optical behavior of Ti and Ti₂N in Fig. 9a, and the ϵ_2 spectra exhibit higher values in the visible range, indicating also higher optical losses. This unequivocally demonstrates the optimal optical behavior of B1-TiN compared to metallic Ti and to all the other phases of the Ti–N system, and we can safely anticipate that this is the origin of the excellent optical behavior of most of the B1 nitrides compared to their metallic counterparts.

2.2.3. Electronic structure calculations

2.2.3.1. Binary nitrides. The origin of electronic conductivity and the spectral position of the interband transitions are closely associated with the bonding configuration of the valence electrons of the constituent metal and nitrogen atoms. Therefore, detailed band structure calculations can shed some light on the correlation between chemical bonding and electronic conductivity in TMN, and they can identify all the features in the reported optical spectra of TMN. Consequently, many groups have performed relevant

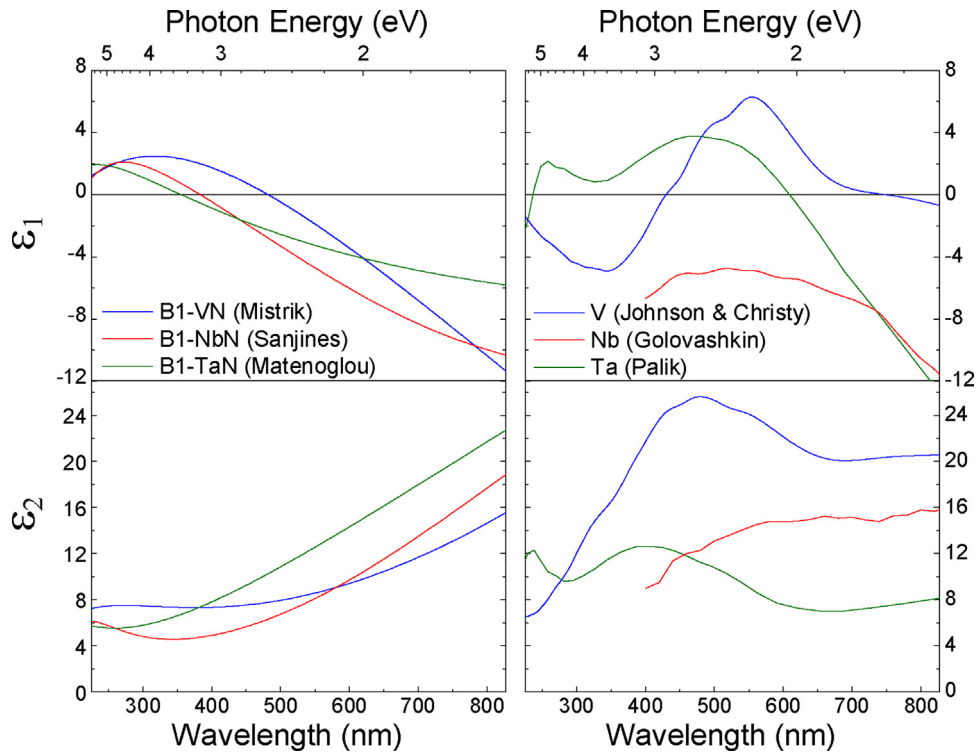


Fig. 8. The dielectric function spectra of the group Vb metals (right panels) and of their B1 nitrides (left panels); data from Refs. [380,381,390,520–522].

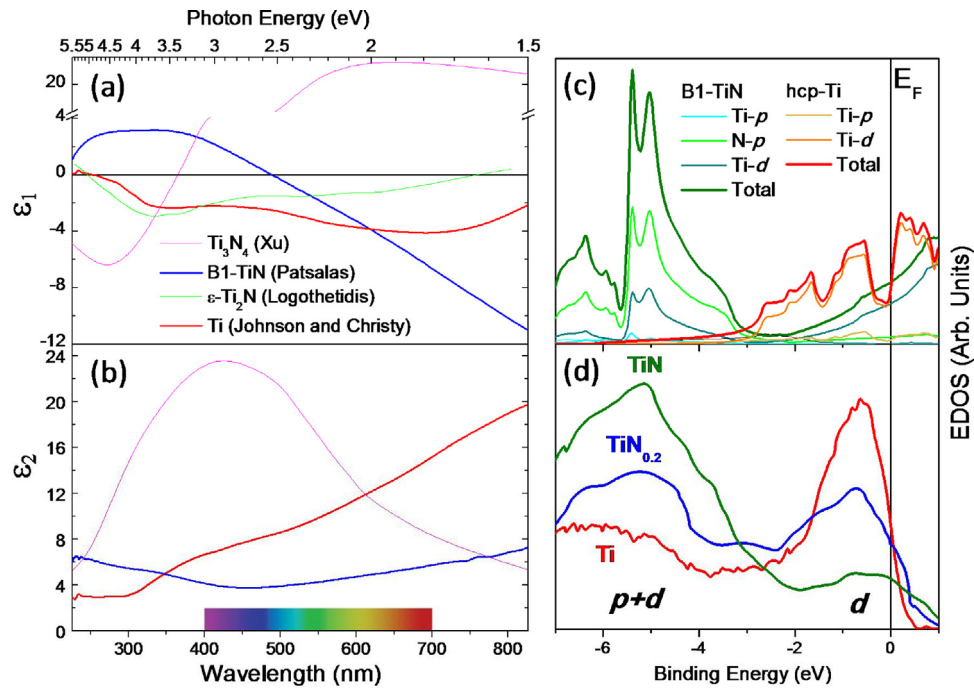


Fig. 9. Spectra of the (a) real, and (b) imaginary parts of the dielectric function for metallic *hcp*-Ti, ϵ -Ti₂N, B1-TiN, and the hypothetical calculated Ti₃N₄ (data from Refs. [176,259,523,524]); (c) linear augmented plane wave calculations of EDOS for *hcp*-Ti and B1-TiN; (d) valence band spectra acquired by photoemission experiments (data from Refs. [525,526]), the vertical line indicates the Fermi level.

detailed calculations of the EDOS for most TMN using various methods and computational packages as demonstrated in Table 1 and the references therein. All these computational works create a consensus that the chemical bonding in TMN is based on the hybridization of the nitrogen's *p* electrons with the metal's *d* electrons and that the electronic conductivity of TMN is due to the excess *d* electrons of the metal.

As most of the works in the literature are dealing with some or one of the TMN, in this work, the total ground energy, the lattice parameter and the electron density of states (EDOS) of all the nitrides of the transition metals of the groups IVb-Vb-VIb in the B1 structure (except CrN) have been calculated with the linear augmented plane wave (LAPW) method within the density functional theory using the Wien2k software [527], in order to

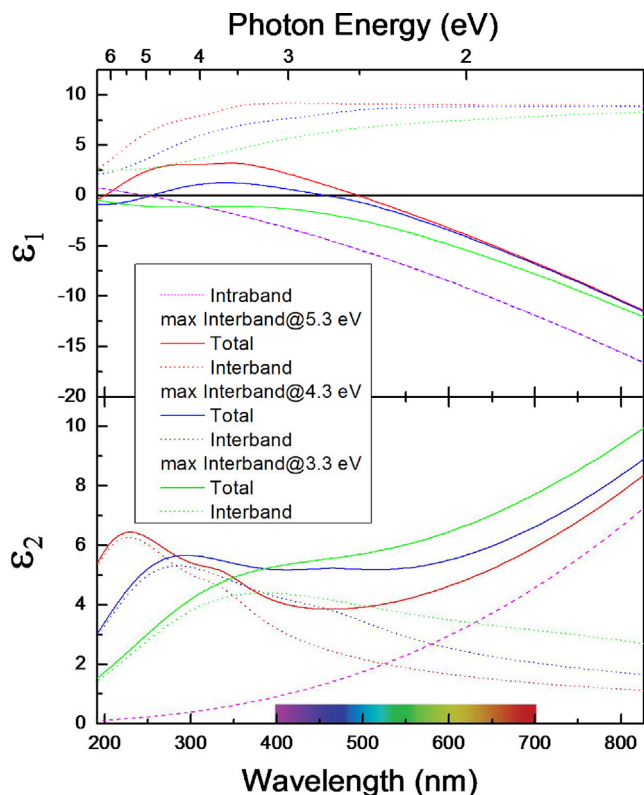


Fig. 10. Simulations demonstrating the effect of overlap of the intraband and interband absorption to the real and imaginary parts of the dielectric function of TiN; the less overlap (red lines) results in a clear crossing of ϵ_1 through zero and less optical losses in the visible range. (For interpretation of the references to colour in this figure legend, the reader is referred to the web version of this article.)

deal with all of them using exactly the same computational details and thus being able to compare their differences quantitatively. The LAPW method, which is the most widely used method for the EDOS calculations of TMN, according to Table 1, expands the Kohn-Sham in atomic-like orbitals inside the atomic (Muffin Tin (MT)) spheres and plane waves in the interstitial region. The calculations have been performed with the exchange-correlation functional being treated using the Generalized Gradient Approximation (GGA) in the form given by Perdew, Burke and Ernzerhof (PBE96) [528]. The joined density of states (JDOS) has been also calculated from the EDOS. JDOS was used to determine the spectral dependence of the imaginary part of the dielectric function (ϵ_2) [529].

The EDOS and its breakdown to contributions of individual electrons can enlighten the chemical bonding and the optical properties of the B1 TMN. Inspecting Fig. 11 we can distinguish two energy regions of occupied states for all TMN: a) from -10 eV to around -4 eV, and b) from around -4 eV up to Fermi level (E_F). The first region is characterized by the strong hybridization of the d -electrons of the metals with the p -electrons of nitrogen, which is in the origin of the partial covalent bonding in these materials, and of the experimentally observed interband transitions [177,184]. In particular, the fine structure of the EDOS below -4 eV manifests in the optical absorption spectra measured either by ellipsometry or reflectivity measurements as two distinct absorption bands, which originate from the shoulder and the peak of the EDOS located at around -3.5 eV and -5.5 eV for TiN and denoted in Fig. 11 as E_{01} and E_{02} , respectively, to unoccupied states above E_F ; the exact spectral positions of these absorption bands vary for the various TMN. The unoccupied states above E_F correspond to metal- d states and, therefore, in all TMN the interband transitions are of the form

$N-p \rightarrow \text{Metal-}d$, in accordance with the selection rules for photonic excitation ($\Delta l = 0, \pm 1$). The cut-off energy (the maximum energy below E_F , where the partial EDOS of the $N-p$ states gets non-zero values) is also of substantial importance, as it defines the threshold at which the dielectric losses contribute to the optical response of TMN (it is denoted in Fig. 11 for the case of TiN).

At the second region (above -4 eV) and up to the Fermi level, the energy states are filled mainly by the d -electrons of the metals and a small contribution of the nitrogen's p -electrons. Above the Fermi level, the unoccupied states are mostly of metal's d character. The Fermi level intercepts this d -electron band, giving rise to the electronic conductivity of TMN. The intuitive conclusion is that the conduction electron density would increase with the number of the metal's d -electrons (*i.e.* with the group numbering); indeed, this is confirmed both computationally (Fig. 12) and experimentally (Refs. [184,200]).

Fig. 13 summarizes the variations of the EDOS at E_F (which determines the conduction electron density), the wavelengths corresponding to the E_{01} interband transition (λ_{01}), defined previously in Fig. 11, and the cut-off energy ($\lambda_{\text{cut-off}}$). Some general trends can be identified; in particular, with increasing group numbering of the constituent metal there is an increase of the EDOS value at E_F , which is associated with the unscreened plasma energy E_{pu} that depends on the concentration of the conduction electrons of the TMN and is defined by the relation [184,200,550]:

$$E_{pu} = \hbar\omega_{pu}, \omega_{pu} = \sqrt{\frac{Ne^2}{\epsilon_0 m^*}}, \quad (1)$$

where N is the conduction electron density, e is the electron charge, ϵ_0 is the permittivity of free space and m^* is the electron effective mass, in SI units. Since E_{pu} is directly correlated with the conduction electron density, it can be used to determine the metallic character of the TMN and it has severe effect on the plasmonic performance of TMN, as we will discuss in the following sections.

The enhancement of the EDOS values at the Fermi level with the group numbering of the constituent metal is accompanied by substantial blue shift of λ_{01} and λ_{cutoff} with the numbering of both the group and period of the constituent metal (Fig. 13). Note that the E_{01} interband transition is the major source of dielectric losses of all TMN and its spectral location is critical for their plasmonic performance. Therefore, the collective effects of enhancement of the EDOS value at E_F and the reduced dielectric losses at visible wavelengths with increasing group numbering shift the optical absorption and the plasmonic activity of TMN towards the UV. These considerations are vividly illustrated in the spectra of the imaginary part of the dielectric function ϵ_2 calculated from the JDOS [529] and presented in Fig. 14 vs. the wavelength of light, which is more suitable than the photon energy for designing photonic and plasmonic devices. For wavelengths below 500 nm (2.48 eV) the ϵ_2 spectra are dominated by the interband absorption due to bound electrons (Fig. 14a,c,e) and the optical absorption is mostly due to the $N-p \rightarrow \text{Metal-}d$ interband transition in all cases, while at longer wavelengths (Fig. 14b,d,f) the spectra are dominated by the intraband absorption of conduction electrons. Special care should be taken, when we compare computational and experimental ϵ_2 spectra. The computed ϵ_2 spectra correspond to perfect single-crystals at 0 K and, therefore, take into account only the electron-electron scattering and neglect all the other scattering mechanisms, such as scattering of electrons by phonons, point defects and surfaces (grain boundaries) that do contribute to the experimental spectra of polycrystalline films. For these reasons all the features in the computed ϵ_2 spectra are exceptionally sharp and there is a clear discrimination between the contributions of the

Table 1

A review of the computational studies of EDOS of various binary TMN.

	Reference	Material	Method	Functional	Code	Quantity	Calculated Property-Application
10	[244]	ZrN, TaN, Ta _x Zr _{1-x} N	LAPW	GGA (PW)	CASTEP	EDOS	Complex refractive index
11	[248]	TiN, TaN, Ti _x Ta _{1-x} N	LAPW	GGA (PBE) and LDA	WIEN2k	EDOS, lattice constant	Dielectric function
21	[252]	TiN, TaN, Ti _x Ta _{1-x} N	PP	GGA (PBE)	ABINIT	EDOS, lattice constant	Elastic constants, Young's modulus
1	[361]	VN, NbN, TaN, CrN, MoN, WN	SAPW	LDA	N/A	EDOS, lattice constant	Carrier density, electron-ion interaction constant, electron phonon coupling
6	[473]	TiN, VN, CrN	FLAPW	LDA	N/A	Lattice constant	Magnetic moment
7	[485]	TiN	LAPW	GGA (PW) and GGA (PBE)	CASTEP	EDOS, lattice constant	Elastic constants, Bulk modulus, surface energies
13	[486]	ZrN, NbN	LAPW	LDA	WIEN2k	EDOS, lattice constant	Elastic constants, Bulk modulus
14	[488]	ZrN, NbN, MoN	LAPW	GGA (PBE)	CASTEP	EDOS, lattice constant	Elastic constants, Bulk modulus
15	[490]	TiN, ZrN	LAPW	GGA (PBE)	VASP	EDOS, lattice constant	Dielectric function, optical reflectivity
8	[492]	TiN, VN, ZrN, NbN, HfN, TaN	FLAPW	GGA (PW) and LDA	N/A	EDOS, lattice constant	Cohesive energy, Bulk modulus, Energy gaps
19	[497]	TiN, ZrN, Ti _x Zr _{1-x} N	LAPW	GGA (PBE)	Quantum ESPRESSO	EDOS, Lattice constant	Elastic constants
2	[530]	TiN, VN	LMTO	LDA	N/A	EDOS, lattice constant	Bulk modulus
3	[531]	TiN, VN, CrN	LMTO	LDA	N/A	EDOS	Cohesive energy
4	[531]	HfN, TaN, WN	LMTO	LDA	N/A	EDOS	Cohesive energy
5	[532]	TiN, ZrN, HfN	FLMTO	LDA	N/A	EDOS	Optical reflectivity
9	[533]	TiN, HfN	LAPW	LDA and GGA (PBE)	WIEN2k	EDOS, lattice constant	Elastic constants, Bulk modulus
12	[534]	ZrN, NbN, MoN, HfN, TaN, WN	PP	GGA and LDA	CASTEP	EDOS, lattice constant	Elastic constants, cohesive energy
16	[535]	TiN	LAPW	GGA (PBE)	CASTEP	EDOS, lattice constant	Dielectric function, loss function, optical reflectivity and absorbance
17	[535]	TiN, VN	LAPW	GGA (PW)	VASP	EDOS, lattice constant	Elastic constants, Bulk modulus, hardness
18	[536]	TiN, VN, CrN, ZrN, NbN	FLAPW	GGA (PBE) and LDA	CASTEP	EDOS, Lattice constant	Electronic and magnetic properties, Elastic constants
20	[537]	TiN	LAPW	LDA	Quantum ESPRESSO	EDOS, lattice constant	Bulk modulus, Electron-phonon coupling constant, phonon band structure
22	[538]	WN, TaN	FLMTO	LDA	N/A	EDOS, lattice constant	Elastic constants, Bulk modulus
23	[539]	TiN, ZrN, HfN	FLAPW and PP	GGA (PBE)	WIEN2k & SIESTA	EDOS, lattice constant	Bulk, Shear and Young's moduli, Debye temperature
24	[540]	TiN, VN	LAPW	GGA (PW) and LDA	VASP	EDOS, lattice constant	Elastic constants, Bulk modulus
25	[541]	TiN, VN, CrN	PWSCF	GGA	N/A	EDOS, lattice constant	Bulk modulus, interband transitions, carrier density, electron-phonon coupling
26	[542]	TiN, ZrN, HfN, TaN, WN	IPA	GGA (PBE)	WIEN2k	EDOS	Dielectric function spectra

LAPW: Linearized augmented plane-wave.

FLAPW: Full-potential linearized augmented plane-wave.

SAPW: Semirelativistic augmented plane-wave.

PWSCF: Plane-wave self-consistent field.

LMTO: Linear muffin-tin orbital.

FLMTO: Full-potential linear muffin-tin orbital.

IPA: Independent Particle Approximation.

PP: Pseudo-potential.

GGA: Generalized Gradient Approximation.

LDA: Local Density Approximation.

PBE: Perdew–Burke–Ernzerhof, Ref. [528].

PBES: Modified PBE for solids and surfaces, Ref. [543].

PW: Perdew–Wang, Ref. [544].

Quantum ESPRESSO: Ref. [545].

CASTEP: Ref. [546].

ABINIT: Ref. [547].

WIEN2k: Ref. [527].

VASP: Ref. [548].

SIESTA: Ref. [549].

SIESTA.

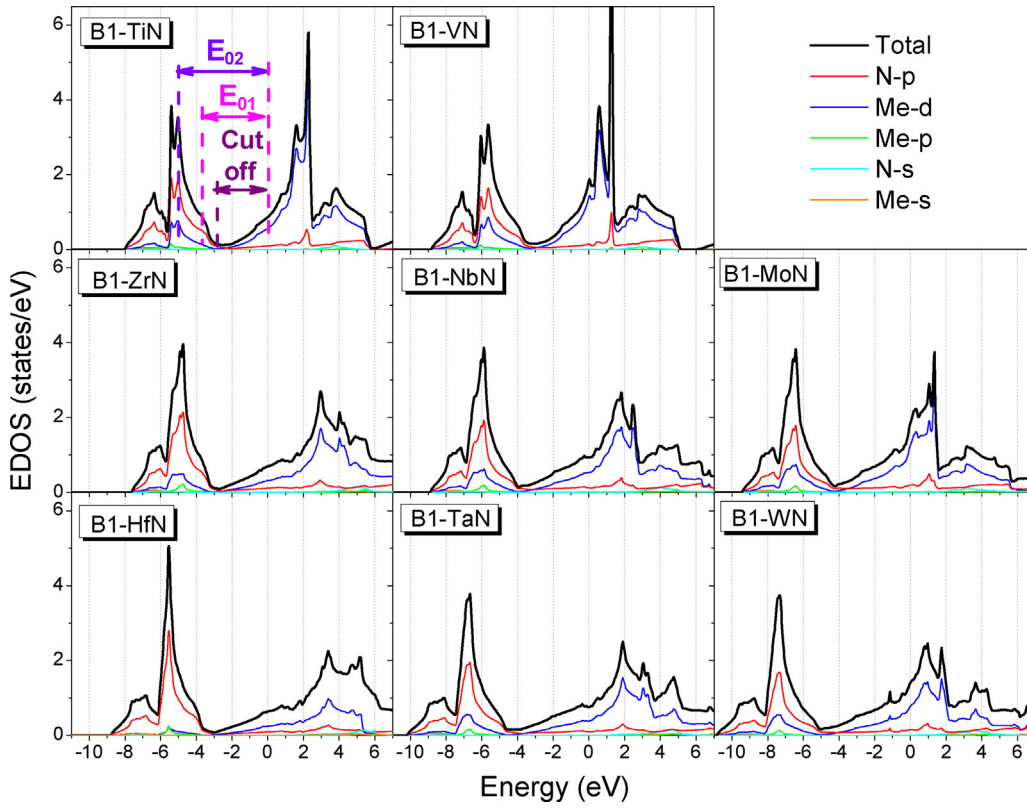


Fig. 11. (Color online): EDOS for the various nitrides of the IVb-Vb-VIb transition metals in the B1 structure. Zero energy stands for the Fermi level. The total EDOS (black lines) is deconvoluted to contributions from individual electron states (s, p of N and metal and d of metal).

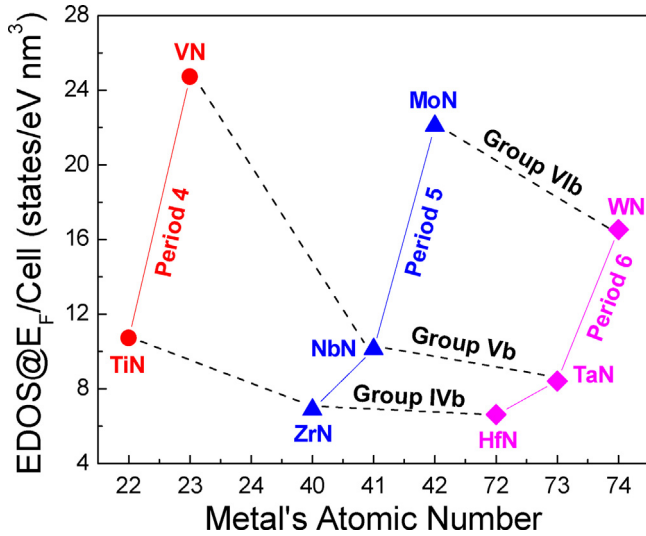


Fig. 12. (color online): The variation of the density of electrons at the Fermi level for the TMN in the B1 structure vs. the atomic number of the constituent metal calculated using LAPW-GGA. The values are rationally grouped according to the groups and periods of the periodic table of elements where the constituent metals belong.

interband transitions (Fig. 14a,c,e) and of the conduction electrons (Fig. 14b,d,f). The computed ϵ_2 spectra at the conduction electron regime (Fig. 14b,d,f) were fitted by the formula of optical dispersion of the Drude theory of metals [550]:

$$\tilde{\epsilon}(\omega) = \epsilon_1 + \epsilon_2 = 1 - \frac{\omega_{pu}^2}{\omega^2 - i\Gamma_D\omega}, \quad (2)$$

in order to evaluate the intrinsic electron-electron scattering, which is accountable for the electronic losses, of TMN, through the broadening parameter Γ_D . Γ_D is associated with the conduction electron relaxation time τ_D [529] as:

$$\Gamma_D(\text{eV}) = \frac{\hbar}{\tau_D(\text{s})}, \quad (3)$$

and affects both the material's resistivity [551]:

$$\rho = \left(\frac{1}{\epsilon_0}\right) \frac{\hbar^2 \cdot \Gamma_D}{E_{pu}^2} \quad (4)$$

and the mean free path MFP of conduction electrons [551]:

$$\text{MFP} = \left(\frac{0.75\pi}{(m^*e)^2}\right)^{1/3} \cdot \frac{\hbar^2 \omega_{pu}^{2/3}}{\Gamma_D} \quad (5)$$

Note that the spikes observed in the ϵ_2 spectra in the conduction electron regime (Fig. 14a,c,e) originate from the fine structure of the metal's *d*-band and can be reasonably neglected as they do not correspond to allowed optical transitions according to the relevant selection rules ($\Delta l = \pm 1$). Fig. 15 shows the variation of intrinsic electron scattering parameter Γ_D evaluated from the computed ϵ_2 spectra for the various TMN. The Γ_D values are increasing with increasing group number of the constituent metal, due to the observed enhancement of conduction electron density (see also Fig. 12). This is more clearly illustrated in Fig. 16, where the mean free path of conduction electrons (Fig. 16a) and the resistivity (Fig. 16b) of the various B1 nitrides are displayed; these values were determined from Eqs. (4) and (5) by using the E_{pu} and Γ_D values extracted from fitting the spectra shown in Fig. 14 and they provide a clear and quantitative view of the inherent electron losses for the perfect single-crystalline materials at 0 K. Indeed, it is evident that group IVb nitrides are the less lossy, with B1-ZrN having the best performance,

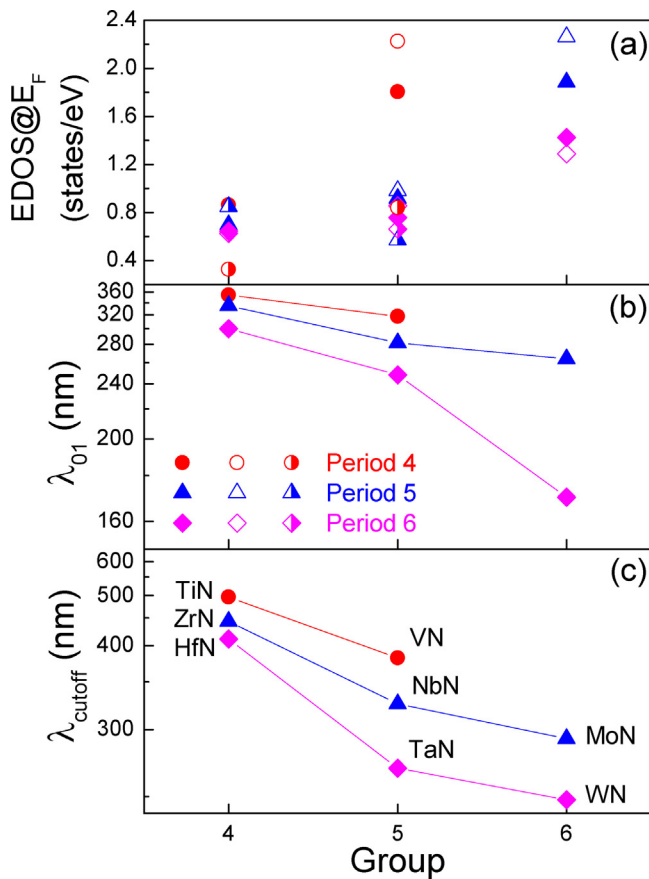


Fig. 13. The variations of (a) the electron density of states at the Fermi level (which affects the conduction electron density), (b) the wavelength (λ_{01}) where the first interband transition occurs; note that the first interband transition is the major source of dielectric losses of TMN, and (c) the cut off wavelength where dielectric losses emerge, vs. the group and period of the constituent metal in the periodic table of elements; solid symbols from this work (LAPW), open symbols from Papaconstantopoulos et al. [361], and composite symbols from Stampfl et al. [492].

while the group VIb nitrides are excessively lossy even in their ideal, defect-free, single-crystalline form; the losses of the latter are further increased by the existence of thermodynamically-favourable point defects [186,387]. Among the group Vb nitrides B1-VN is inferior to B1-NbN and B1-TaN.

Overall, the blueshift of interband transitions of TMN, and consequently of the dielectric losses as well, towards the UV with increasing group number of the constituent metal comes in expense of the intrinsic electronic losses, which are concurrently enhanced. Therefore, this interplay should be taken into account when designing optoelectronic or plasmonic components based on TMN. The combined trends, revealed by analyzing the computed EDOS and ϵ_2 spectra, clearly demonstrate that the overall less lossy TMN (those that exhibit the best compromise of less electronic and dielectric loss) are B1-ZrN and B1-HfN and not the most widely studied B1-TiN. These predicted trends are, indeed, confirmed by the experimental results that will follow.

2.2.3.2. Ternary nitrides. Computational studies on ternary TMN are more recent (references shown in Table 2) and they are mostly concentrated on the stability of the various systems, thus a very common calculation is that of the mixing enthalpy, and on using the EDOS as a means of understanding the chemical bonding, and through it of understanding the deformation mechanisms and the mechanical performance of such systems. The most popular conductive ternary nitrides, in terms of the computational studies,

include $\text{Ti}_x\text{Zr}_{1-x}\text{N}$ [249,558], $\text{Ti}_x\text{Ta}_{1-x}\text{N}$ [248,249,252,562], $\text{Ti}_x\text{Al}_{1-x}\text{N}$ [198,554,555], and $\text{Ti}_x\text{W}_{1-x}\text{N}$ [535,557,563], among others.

Among these studies, the optical and electrical properties of the ternary TMN are scarcely reported [248,564,565]. In particular, it has been demonstrated by detailed calculations that the B1- $\text{Ti}_x\text{Ta}_{1-x}\text{N}$ [248] and B1- $\text{Ti}_x\text{Zr}_{1-x}\text{N}$ [565] constitute efficient material platforms with tunable optical properties. The EDOS of the various B1- $\text{Ti}_x\text{Ta}_{1-x}\text{N}$ crystals are demonstrated in Fig. 17; it is clearly shown that the incorporation of Ta into TiN to form B1- $\text{Ti}_x\text{Ta}_{1-x}\text{N}$ results in a gradual blueshift of the dielectric losses that originate from the N-Metal bonds via the hybridization of N 2p-Metal d electrons. This is accompanied by the increase of the density of metal's d states close to the Fermi level, which is expected to result in the increase of electron losses, according to the previous discussion and the data of Fig. 9c,d. The corresponding EDOS of the B1- $\text{Ti}_x\text{Zr}_{1-x}\text{N}$ system presented in Ref. [565] shows also a blueshift of the dielectric losses upon incorporation of Zr into TiN (though not as pronounced as for the B1- $\text{Ti}_x\text{Ta}_{1-x}\text{N}$), which is accompanied by reduced density of d electrons close to the Fermi level, and thus resulting in an overall optimal combination of dielectric and electronic losses, while being tunable at the same time.

In Ref. [248] the ϵ_2 spectra of various $\text{Ti}_x\text{Ta}_{1-x}\text{N}$ have been calculated from the joined density of states (JDOS) determined by LAPW, while the ϵ_1 spectra were calculated from ϵ_2 using Kramers-Kronig integration. The calculated dielectric function spectra are presented in Fig. 18. The optical properties of $\text{Ti}_x\text{Ta}_{1-x}\text{N}$ films are that of typical conductors exhibiting a strong intraband absorption, which quantitatively varies with the composition x. The interband absorption emerges from about 3 eV. The exact spectral position of the interband absorption due to the N-p \rightarrow Metal-d transitions depends on x due to the gradual spectral shift of the N-p states with respect to the Fermi level (Fig. 17); similar behavior but with variations in a narrower range are also observed for the B1- $\text{Ti}_x\text{Zr}_{1-x}\text{N}$ system [565]. The electronic characteristics of the ideal, defect-free B1- $\text{Ti}_x\text{Ta}_{1-x}\text{N}$ at 0 K are quantified by fitting the computational spectra of Fig. 18 by Eq. (2) and determining E_{pu} , Γ_D , MFP and the resistivity (ρ) via Eqs. (4) and (5). The aforementioned quantities vs. x are summarized in the insets of Fig. 18. The ternary B1- $\text{Ti}_x\text{Ta}_{1-x}\text{N}$ system exhibits intermediate E_{pu} and Γ_D values between those of B1-TiN and B1-TaN, which, however, do not follow a linear relation with x. The determined MFP and resistivity indicate that for these systems there is no substantial contribution from alloying scattering [444], and thus the dominant factors for the experimentally observed inferior conductivity of such ternary nitrides, that will be reviewed in the following sections, is mostly due to the microstructural variations upon alloying as described in Fig. 5. This clearly dictates that the improvement of the existing growth technology of ternary TMN is of utmost importance for their implementation in realistic applications in photonics and plasmonics.

Finally, some less studied, emerging systems, such as B1- $\text{Ti}_x\text{Mg}_{1-x}\text{N}$ [560], seem particularly interesting. In particular, B1- $\text{Ti}_x\text{Mg}_{1-x}\text{N}$ exhibits a conductor-semiconductor transition for $x=0.5$ and substantial reduction of conduction electron density for small amounts of Mg; the later is very important for applications in infrared optics and plasmonics [441]. In addition, B1- $\text{Ti}_x\text{Mg}_{1-x}\text{N}$ is a stable compound as it has a negative enthalpy of mixing for $0.625 < x < 1$ [560]. The competing B1- $\text{Ti}_x\text{Sc}_{1-x}\text{N}$ system is stable in the entire compositional range [559], however, for the time being there is no report of a computational study of its optical properties.

2.2.4. Experimental dielectric function spectra of binary nitrides

There are numerous studies of the optical properties of the nitrides of the group IV_b-V_b-VI_b transition metals (see Table 3), albeit in most cases these were not the core subject of research. In

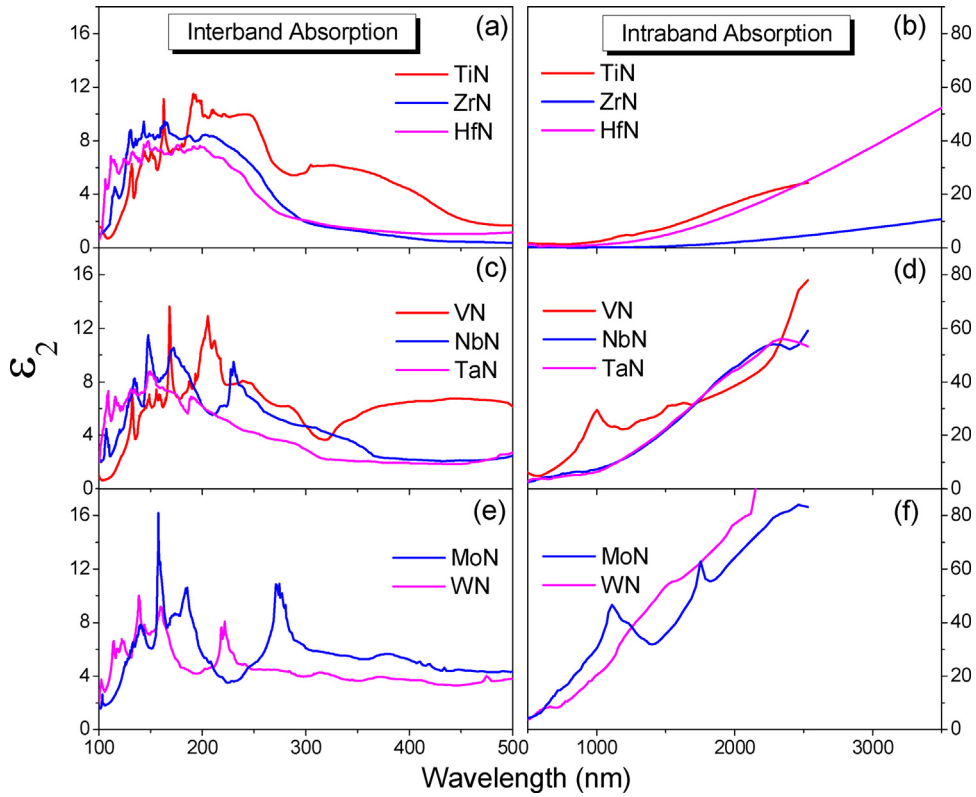


Fig. 14. Spectra of the imaginary part ϵ_2 of the dielectric function spectra of (a), (b) Group IVb, (c), (d) Group Vb, and (e)(f) VIb nitrides in the B1 structure.

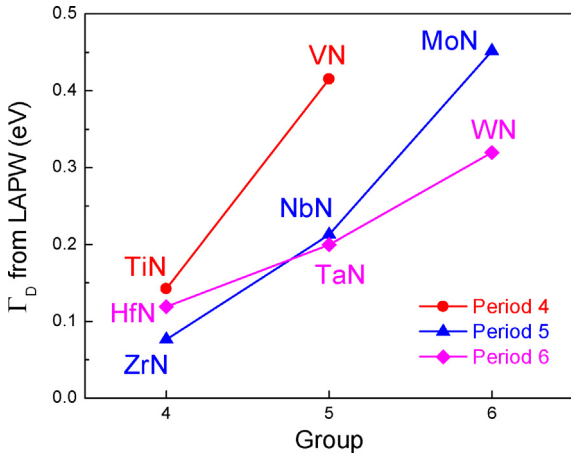


Fig. 15. The variation of the intrinsic electron scattering parameter evaluated from the computed ϵ_2 spectra for the various binary TMN.

these studies two experimental methods of measuring the optical response of the materials were used, namely, spectroscopic ellipsometry (SE), in all of its varieties (variable angle, phase modulated *etc*), and optical reflectivity spectroscopy (ORS) at near-normal incidence. SE measures the so-called ellipsometric angles Ψ – Δ . The amplitude ratio Ψ and the phase difference Δ between p - and s - polarizations are representing the refractive index n and the extinction coefficient k , respectively. These two ellipsometric parameters are associated with the ratio ρ_f of the Fresnel reflection coefficients for s - and p -polarization through the relationship [569]:

$$\rho_f = \tan\psi \cdot e^{i\Delta} = \frac{r_p}{r_s}. \quad (6)$$

Then, the real and imaginary parts of the dielectric function $\tilde{\epsilon} = \epsilon_1 + i\epsilon_2$ can be analytically calculated from ρ_f and the angle of incidence ϕ (usually in the range 55–75°) as [569]:

$$\tilde{\epsilon} = \sin^2\phi \cdot \left[1 + \tan^2\phi \left(\frac{1 - \rho_f}{1 + \rho_f} \right)^2 \right]. \quad (7)$$

On the other hand, the real and imaginary parts of the complex refractive index $\tilde{n} = n + ik$ can be extracted from the spectral reflectivity measurements at normal incidence R via the relations [570]:

$$n = \frac{1 - R}{1 + R - 2\cos\theta\sqrt{R}}, \quad (8-1)$$

$$k = \frac{-2\sin\theta\sqrt{R}}{1 + R - 2\cos\theta\sqrt{R}}, \quad (8-2)$$

where θ is the phase change due to reflectivity, which is determined by Kramers-Kronig integration [570]:

$$\theta(\omega_0) = \frac{1}{\pi} \int_0^{\infty} \ln \left| \frac{\omega + \omega_0}{\omega - \omega_0} \right| \frac{d \ln \sqrt{R(\omega)}}{d\omega} d\omega. \quad (9)$$

Alternatively, the n , k can be also determined by fitting the spectral reflectivity curves using specific dispersion models [248]. The complex dielectric function and the complex refractive index are equivalent and interchangeable quantities, as they are analytically correlated [571]:

$$\epsilon_1 = n^2 - k^2, \quad (10-1)$$

$$\epsilon_2 = 2nk. \quad (10-2)$$

In the case of a thin film grown on a bulk substrate the measured spectra by SE or spectral reflectivity accounts the effect of the substrate and film's thickness, in addition to the film's optical

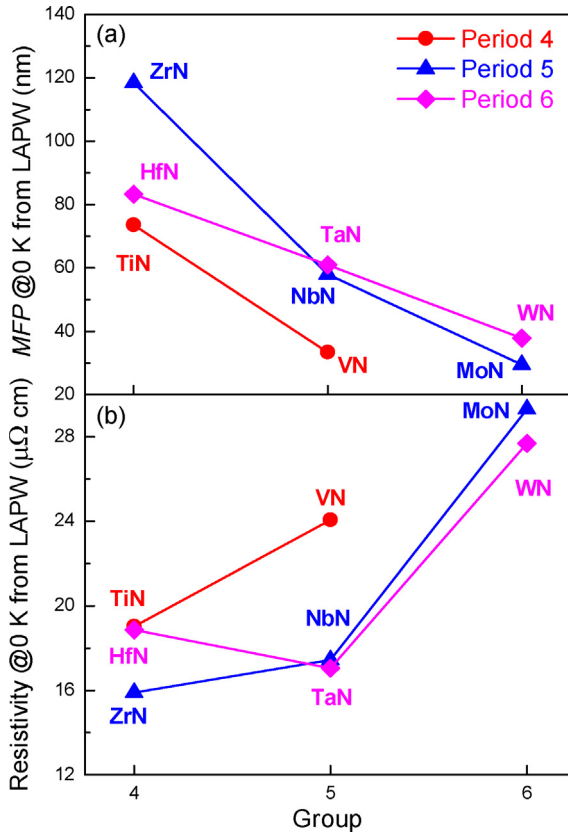


Fig. 16. The variation of the (a) resistivity, and (b) the conduction electron mean free path for single crystals at 0 K calculated from E_{pu} and Γ_D values resulted from fitting the computed ϵ_2 spectra for the various binary TMN.

properties. Opaque TMN films should be thicker than 100 nm in order to measure directly the complex dielectric function, without any contribution from the substrate; otherwise, a three-phase geometrical model (air/homogeneous film/semi-infinite substrate) [572] and knowledge of the substrate’s optical response are required to determine the complex dielectric function of TMN.

In this work, we retrieved and critically review the optical data of TMN from all the references shown in Table 2. We selected these works out of the entirety of the relevant literature because they are reporting directly ϵ_1 , ϵ_2 or n , k spectra and not just optical reflectivity or transmission values, as the rest of the papers in the literature do. Thus, we can review safely their raw data without any further data handling (e.g. by Eqs. (8) and (9)). Table 3 summarizes the samples grown and the spectra measured by numerous groups worldwide regarding the optical properties of TMN and reviewed in this work. It includes information relevant to the growth conditions, morphology, and the conditions of optical measurements, as well as the corresponding references of Table 3. In order to provide a unified picture and compare all the available data in the literature in a self-consistent manner, we calculated the ϵ_1 , ϵ_2 values using Eq. (9) when the n , k values are reported in the original references.

The experimental spectra of TMN in most cases are coming from polycrystalline films and they were measured at RT; as a result, the various absorption bands (intraband and interband absorptions) are substantially wider than those of single-crystal materials measured at cryogenic temperatures (which would be directly comparable with the calculated spectra presented in Figs. 14 and 18) and, thus they are overlapping each other. Consequently, it is not possible to spectrally discriminate the intraband and interband absorptions, as we did for the case of the LAPW computational

spectra, and a combined Drude-Lorentz model is required for the analysis of the dielectric function spectra [176]:

$$\tilde{\epsilon}(\omega) = \epsilon_\infty - \frac{\omega_{pu}^2}{\omega^2 - i\Gamma_D\omega} + \sum_{j=1}^2 \frac{f_j \cdot \omega_{0j}^2}{\omega_{0j}^2 - \omega^2 + i\gamma_j\omega}, \quad (11)$$

In Eq. (11) ϵ_∞ is a background constant, larger than unity, which accounts the high-energy contributions (beyond the experimental spectral range) due to transitions that are not taken into account by the Lorentz term(s). Each of the Lorentz oscillators ($n = 1$ or 2) is located at an energy position $E_j = \hbar\omega_{0j}$, with strength f_j and damping (broadening) factor g_j . The Drude term is characterized by the unscreened plasma energy $E_{pu} = \hbar\omega_{pu}$ and the damping factor Γ_D as mentioned previously. All the ϵ_1 , ϵ_2 spectra retrieved from the works summarized in Table 3 were fitted by a least-square regression algorithm using Eq. (11) with mostly two Lorentz oscillators ($n = 2$) within the Horiba Jobin-Yvon Delta-Psi[®] software. The use of two Lorentz oscillators physically describes the absorption bands E_{01} and E_{02} as identified by the LAPW data in Fig. 11. In the cases where the second Lorentz oscillator was far beyond the experimental spectral range, or the fitting process had substantial uncertainties [by means of the least square values when using two oscillators ($n = 2$), or the fitting rendered values with no physical meaning for the second oscillator (e.g. coinciding spectral energy of the two oscillators, strength or broadening parameters close to zero, etc)] we utilized Eq. (11) with only one Lorentz oscillator ($n = 1$). In the rare cases of spectra corresponding to non-opaque (thickness <100 nm) films, the least-square regression fit was combining Eq. (11) with a three-phase geometrical model (air/film/substrate) [573]; note that for these cases, we did not have accurate knowledge of the ϵ_1 , ϵ_2 spectra of the substrates, and therefore, our corresponding fitting might be of questionable accuracy. Finally, we did not manage to fit adequately the data presented in Ref. [285], so in the following text wherever Ref. [285] is mentioned, its raw data are used, albeit without too much compromise, since the thickness of the films reported where above 100 nm and so any contribution from the substrate would be negligible.

The quantitative results of the fits are summarized in Table 4. Representative experimental spectra from various opaque TMN films from Refs. [197,303,380] along with the corresponding fit results and the deconvolutions to the individual contributions of the Drude term (intraband absorption) and the two Lorentz terms (interband absorptions E_{01} and E_{02}) are presented in Fig. 19 (note that the wavelength of the x-axis is in reciprocal scale to resemble the variation of photon energy). Based on the excellent fit quality in most cases, we extrapolated the ϵ_1 , ϵ_2 spectra using the values of the parameters of the best fit listed in Table 4 in the spectral range 200–1300 nm as presented in Fig. 19, in order all the spectra to be comparable to each other. The extrapolated spectra of the real and imaginary parts of the dielectric function (or equivalently of the real and imaginary permittivity) for all the studied samples listed in Table 3 are presented in Figs. 20 and 21, respectively.

In particular for Fig. 20, the typical metallic and featureless lineshape of negative ϵ_1 for long wavelengths (>450 nm) is observed only for group IVb nitrides (TiN, ZrN, HfN) and VN. This spectral region is characterized by negative values of ϵ_1 due to the interaction of light with the conduction electrons of the corresponding nitrides, i.e. due to intraband absorption.

Among the group IVb nitrides (TiN, ZrN, HfN), TiN is the most widely studied so far and exhibits the wider range of absolute values of ϵ_1 vs. the wavelength compared to the most well-reproducible ZrN; HfN exhibits an intermediate scattering of ϵ_1 values. The absolute values of ϵ_1 at long wavelengths are affected by both the electron density and the electron losses, and thus

Table 2

A review of the computational studies of EDOS of various ternary TMN.

	Reference	Material	Method	Functional	Code	Quantity	Calculated Property-Application
7	[248]	Ti _x Ta _{1-x} N	LAPW	GGA (PBE)	Wien2k	EDOS, lattice constant	Dielectric function spectra, resistivity
6	[249]	Ti _x Ta _{1-x} N, Ti _x Zr _{1-x} N	LAPW	GGA (PBE)	Wien2k	EDOS, lattice constant	
11	[252]	Ti _x Ta _{1-x} N	LAPW	GGA (PBE)	ABINIT	EDOS, lattice constant	Bulk modulus, elastic constants
14	[498]	Ta _x Zr _{1-x} N	LAPW	GGA (PBE)	VASP	EDOS, lattice constant	
9	[535]	Ti _x V _{1-x} N, Ti _x Nb _{1-x} N, Ti _x Ta _{1-x} N, Ti _x W _{1-x} N, V _x Nb _{1-x} N, V _x Ta _{1-x} N, V _x W _{1-x} N	PAW	GGA (PW)	VASP	EDOS, lattice constant	Bulk modulus, elastic constants
1	[552]	Ti _x Al _{1-x} N	PAW	GGA	VASP	EDOS, lattice constant	Bulk modulus, elastic constants, energy of formation
2	[553]	Ta _x Zr _{1-x} N	PP	GGA (PW)	CASTEP	EDOS, lattice constant	
3	[554]	Ti _x Al _{1-x} N	PAW	GGA	VASP	EDOS, lattice constant	
4	[555]	Ti _x Al _{1-x} N, Hf _x Al _{1-x} N	PAW	GGA	VASP	EDOS, lattice constant	Mixing enthalpy
5	[556]	Ti _x Zr _{1-x} N, Ti _x Al _{1-x} N	FLMTO	HL	N/A		Mixing enthalpy, bulk modulus
8	[557]	Ti _x Mo _{1-x} N, Ti _x W _{1-x} N	PAW	GGA (PW)	VASP	EDOS, lattice constant	Bulk modulus, elastic constants
10	[558]	Ti _x Zr _{1-x} N	LAPW	GGA (PBE)	ABINIT		Bulk modulus, elastic constants
12	[559]	Ti _x Sc _{1-x} N, Zr _x Sc _{1-x} N, Hf _x Sc _{1-x} N, V _x Sc _{1-x} N, Nb _x Sc _{1-x} N, Ta _x Sc _{1-x} N	PAW	GGA (PBE)	VASP		Mixing enthalpy
13	[560]	Ti _x Mg _{1-x} N	PAW	GGA	VASP	EDOS, lattice constant	Mixing enthalpy, energy of vacancy formation
15	[561]	Ti _x Mo _{1-x} N, Ta _x W _{1-x} N	LAPW	GGA (PBE)	ABINIT	EDOS, lattice constant	
16	[562]	Ti _x Y _{1-x} N, Ti _x Zr _{1-x} N, Ti _x Hf _{1-x} N, Ti _x Nb _{1-x} N, Ti _x Ta _{1-x} N	PAW	GGA (PBE)	VASP		Mixing enthalpy, elastic constants
17	[563]	Ti _x W _{1-x} N	PAW	GGA (PW)	VASP		bulk modulus, deformation
18	[564]	Ta _x Hf _{1-x} N	N/A	N/A	N/A	EDOS	
19	[565]	Ti _x Zr _{1-x} N	PAW	GGA (PBE)	VASP	EDOS	Dielectric function spectra, reflectivity, loss function, plasmonic field enhancement
20	[566]	V _x Al _{1-x} N	PAW	GGA (PBE)	VASP		
21	[567]	Ti _x Zr _{1-x} N, Ti _x Hf _{1-x} N, Zr _x Hf _{1-x} N	PAW	GGA (PBE)	VASP	EDOS, lattice constant	Mixing Enthalpy

LAPW: Linearized augmented plane-wave.

PAW: Projected Augmented Wave.

FLMTO: Full-potential linear muffin-tin orbital.

PP: Pseudo-potential.

GGA: Generalized Gradient Approximation.

PBE: Perdew–Burke–Ernzerhof, Ref. [528].

PW: Perdew–Wang, Ref. [544].

HL: Hedin–Lundqvist, Ref. [568].

CASTEP: Ref. [546].

ABINIT: Ref. [547].

WIEN2k: Ref. [527].

VASP: Ref. [548].

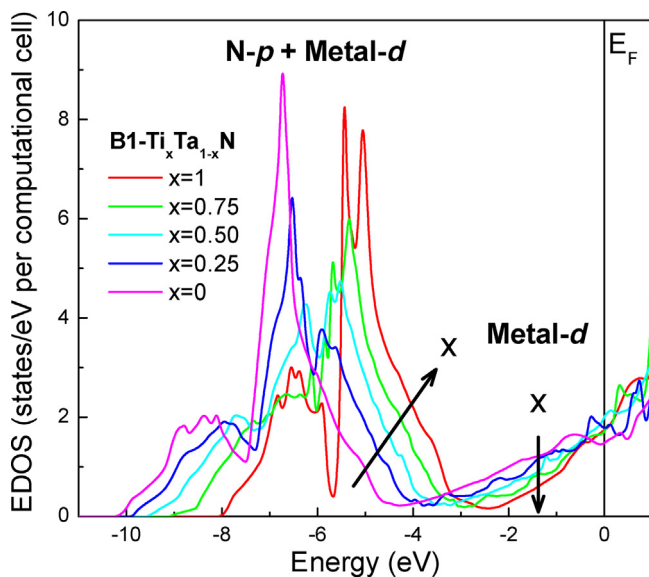


Fig. 17. EDOS of the B1-Ti_xTa_{1-x}N system calculated by LAPW in Ref. [248]. The composition x affects both the conduction d electron density (vertical arrow) and the range of the dielectric losses (diagonal arrow).

indirectly by the film's composition and stoichiometry, respectively. The scattering of the ϵ_1 experimental values reported by various groups using various growth techniques indicate that TiN is the nitride with the highest tailoring potential (possibly due to

its ability to accommodate excess nitrogen and form over-stoichiometric films [176], as well as the large variety of microstructural features observed in TiN films as we have previously shown in Section 2.1.2), while ZrN is best in terms of stability and reproducibility of its optical performance.

NbN and MoN exhibit also negative ϵ_1 values for long wavelengths, but lower absolute values than what is observed for TiN, ZrN, HfN, and VN. This is due to high values of electronic losses (characterized by higher values of the Γ_D parameter), which are an inherent characteristic of NbN and MoN, as mentioned previously when discussing Figs. 15 and 16, and further enhanced by the poor crystalline quality of the corresponding studied MoN samples. Finally, TaN and WN are more complicated cases, as most of their spectra do not exhibit the simplified metallic lineshape. For TaN, this is due to the coexistence of two or more crystal phases [384] (i.e. the films do not consist exclusively of the B1 phase as stated in the comments of Table 3), the existence of high density of point defects in TaN [387] and the ultrafine grain sizes, as presented in Fig. 5, which further increase the scattering of electrons and the relevant electronic losses beyond the level of the rest of the studied nitrides. These inherent drawbacks of B1-TaN can be overcome by alloying with a small concentration of Ti to form B1-Ti_xTa_{1-x}N, as we will discuss later in more detail. Finally, the WN are so lossy, due to the excessive incorporation of point defects [432,574], so as their ϵ_1 do not have negative values in the visible and near infrared ranges at all. In fact, the high electron losses of B1-WN cause the ϵ_1 to remain positive up to very long wavelengths in the infrared region, becoming negative only above

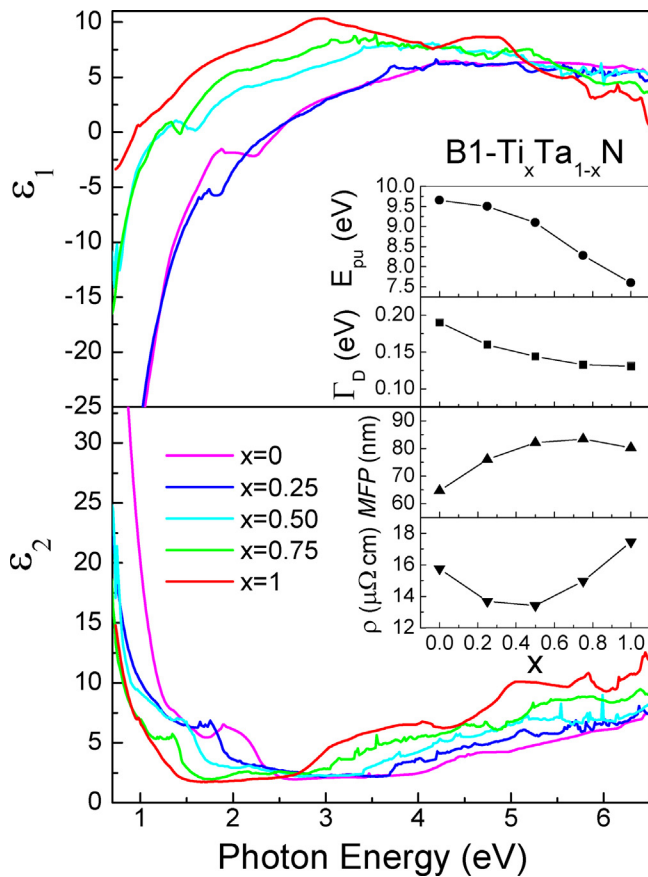


Fig. 18. Dielectric function spectra for the B1-Ti_xTa_{1-x}N system determined from the EDOS calculated by LAPW in Ref. [248]. The insets show the variation of E_{ps} , Γ_D , MFP and resistivity vs. x determined from the spectra using Eqs. (2), (4), (5).

22 μm [432]. This challenges the perspectives of B1-WN for applications in mainstream plasmonics contrary to what has recently been proposed [542]. On the contrary, WN may be promising as high electron loss was recently proposed as a pathway for implementing localized plasmon-enhanced photothermal processes such as photothermal therapy [575], and as a potential tunable epsilon-near-zero (ENZ) material [576] due to the varying moderate slope of the ϵ_1 spectrum vs. photon wavelength that results in wide wavelength regions where ϵ_1 is nearly zero.

Of particular importance is the energy that corresponds to the wavelength of light where $\epsilon_1 = 0$. This energy is defined as the screened plasma energy $E_{ps} = \hbar\omega_{ps} = hc/\lambda_{ps}$, and is affected by both the intraband and interband characteristics. In the case of the non-existent ideal conductor where there are no bound electrons $E_{ps} = E_{pu}$. As an example, E_{ps} and E_{pu} for NbN are indicated by vertical arrows in Fig. 19b and their physical interpretations are clearly distinguished. E_{ps} and/or λ_{ps} separate the dielectric function spectra into two regions; the one is for long wavelengths ($\lambda > \lambda_{ps}$) where the light is reflected by the conductor due to conduction electrons, and the other is for short wavelengths ($\lambda < \lambda_{ps}$) where the conductor is semitransparent and exhibits moderate light attenuation exclusively due to interband absorption. When λ_{ps} lies into the visible spectral range, it actually defines the color of the conductor, as it is shown for representative nitrides in Fig. 22; thus λ_{ps} defines the reflectivity edge. When λ_{ps} lies into the visible range, then it also defines the color of the conductor. E_{ps} and/or λ_{ps} was also introduced as an indicator of the stoichiometry of TiN_x (E_{ps} gets the value 2.65 eV for $x = 1$) [572]; consequently, the actual visual appearance and the color is a safe indicator for TiN and other

TMN. Thus, high-quality stoichiometric TiN is bright yellow, overstoichiometric lossy TiN is reddish brown, ZrN and HfN are pale yellow, NbN is greenish extra-pale yellow, and TaN in the B1 structure is dim grey (dim due to the high electron loss resulting in low reflectivity as it is shown in Fig. 22, and grey because its λ_{ps} is at the verge of the visible range, thus reflecting the entire visible spectrum). A wider color palette can be achieved by ternary nitrides [471].

Although E_{ps} does not have any clear physical meaning other than that $\epsilon_1 = 0$ for real conductors, it was found to indicate, but not to coincide with, the spectral position of SPP and LSPR in TiN [177] and in ternary nitride nanostructures [439,441], and therefore, it has major practical importance for plasmonics.

Below E_{ps} (i.e. for longer wavelengths) the negative values of ϵ_1 , in combination with positive values of ϵ_2 , imply that the light propagation is not allowed through the conductor and the corresponding skin depth is infinitesimal small. Beyond E_{ps} (i.e. for shorter wavelengths) positive values of ϵ_1 are observed, which are associated with the interband absorption and the dielectric losses. In this range the nitride conductors are semitransparent to light, which can pass through them with a moderate attenuation due to the dielectric losses. The interband transitions can be more clearly seen in Fig. 21, where we present the extrapolated ϵ_2 values for all binary nitrides, and in particular they are indicated by the diagonal arrow in Fig. 21a for the case of TiN. The scaling of ϵ_2 values in the y-axis is the same in all graphs, in order to make them comparable. The corresponding dielectric losses are minimized for ZrN and NbN among the nitrides of IVb and Vb group elements, respectively, suggesting these nitrides as the most promising in terms of the lack of contribution of dielectric losses in their optical spectra and plasmonic properties. From the structural point of view, which affects mostly the electron losses [176], the growth of ZrN is usually accompanied by a substantial amount of structural defects [441,471]. Indeed, sputtered ZrN films deposited at the same growth conditions (pressure, substrate bias and target power) with TiN, exhibited substantially higher compressive intrinsic stress [309] due to the backscattered Ar⁺ ions from the Zr target, the reduced thermalization of Zr atoms in the gas phase and the reduced mobility of Zr adatoms on the active growing surface [309,310], all of them due to the higher atomic mass of Zr compared to Ti as also presented in Section 2.1.2.3 of this work; for all these reasons the growth of pure epitaxial ZrN films was achieved quite recently [311], despite of the growth of ZrN films, which include some epitaxial domains since the late eighties [312]. On the contrary, the epitaxial growth of NbN is quite usual on various substrates [581–584].

Coming back to E_{ps} , and in an effort to predict the spectral range of plasmonic effects in TMN, it is important to investigate the potential correlation of it with the effective number of valence electrons N_{eff} of the constituent metals (4, 5, 6 for IVb, Vb, VIb metals, respectively) of conductive nitrides. Fig. 23 displays this correlation. Despite of the wide scattering of experimental points, there is an identifiable trend of increasing the E_{ps} on the average when N_{eff} increases from 4 (TiN, ZrN, HfN) to 5 (VN, NbN, TaN) suggesting that VN, NbN and TaN would exhibit blueshifted plasmonic features compared to TiN, ZrN, HfN. This behavior is assigned to the increased conduction electron density of the nitrides of the group Vb metals. On the contrary, the nitrides of the group VIb metals (MoN, WN) exhibit reduced E_{ps} values compared to the group Vb nitrides despite their expected increased conduction electron density. This is accompanied by excessive electron losses [184,432], which are responsible for this phenomenological behavior. As a result, an E_{ps} spectral range of 1.99–3.51 eV (equivalent to wavelengths 623–353 nm) can be covered by binary TMN. The spectral range of E_{ps} cannot be used on its own merit as a benchmark for the plasmonic performance of conductive

Table 3
Summary of the experimental studies of the optical properties of various TMN reviewed in this work.

No	Reference	First Author	Growth Technique	Film Material	Substrate	Thickness (nm)	Morphology	Measurement Technique ^a	Instrument ^b	Experimental spectral range (nm)	Comments ^c
1	[286]	Edlou	Magnetron Sputtering	TiN, HfN	Fused Silica	Opaque	N/A	VASE	N/A	240–1660	Stoichiometry determined by RBS
2	[240]	Gall	UHV Sputtering	TiN	MgO(100)	200	Epitaxial	ORS	Perkin Elmer	413–2400	(100) Oriented identified by XRD; composition determined by RBS and XPS; ORS measurements acquired using an integrating sphere; ORS normalization was performed via a Si(100) wafer.
3	[292]	Huber	Me-PIII	TiN	Si(100)	100–500	Polycrystalline	SE	RAE	248–826	Stoichiometry $x=0.95$ determined by ERDA; crystal structure identified by XRD
4	[291]	Humlicek	IBAD	TiN	Si(100)	50–100	Polycrystalline	VASE	RAE	350–1650	Stoichiometry determined by XPS and RBS; crystal structure identified by XRD
5	[285]	Karlsson	CVD	TiN, ZrN, HfN	Polished Mo	~1000	Polycrystalline	ORS	Perkin Elmer	200–4900	Used halide precursors; Stoichiometry close to 1 determined by EPMA and by the cubic lattice size (0.424 nm) determined by XRD; no Cl impurities; C impurities <0.2% wt.
6	[434]	Koutsokeras	DIBS	TiN	Si(100)	>300	Globular polycrystalline	VASE	RPE by SOPRA	200–1200	Stoichiometry $x=1$ determined by AES and XPS; crystal structure identified by XRD
7	[294]	Langereis	ALD	TiN	H-terminated Si	>100	Polycrystalline	<i>in situ</i> SE	RCE by J.A. Woolam	250–1650	Used TiCl ₄ , H ₂ , and N ₂ precursors; $x < 1$
8	[170]	Naik	Magnetron Sputtering	TiN	c-Sapphire	30	Epitaxial	VASE	RCE by J.A. Woolam	250–2000	The TiN[111]/Al ₂ O ₃ [0006] epitaxy was confirmed by XRD
9	[176]	Patsalas	Magnetron Sputtering	TiN	Si(100)	>100	Polycrystalline	<i>in situ</i> SE	PME by JY-Horiba	225–826	Growth at 400 °C and Bias voltage of –100 V; Stoichiometry close to 1 confirmed by XPS; crystal structure and (100) texture identified by XRD
10	[176]	Patsalas	Magnetron Sputtering	TiN	Si(100)	>100	Polycrystalline	<i>in situ</i> SE	PME by JY-Horiba	225–826	Growth at RT and Bias voltage of –120 V; Stoichiometry $x=1$ determined by XPS; crystal structure and (100) texture identified by XRD
11	[176]	Patsalas	Magnetron Sputtering	TiN	Si(100)	>100	Columnar Polycrystalline	<i>in situ</i> SE	PME by JY-Horiba	225–826	Growth at RT and Bias voltage of –20 V; Stoichiometry $x=1.12$ determined by XPS; crystal structure and (111) texture identified by XRD

Table 3 (Continued)

No	Reference	First Author	Growth Technique	Film Material	Substrate	Thickness (nm)	Morphology	Measurement Technique ^a	Instrument ^b	Experimental spectral range (nm)	Comments ^c
12	[177]	Patsalas	PLD	TiN	Si(100)	>100	Polycrystalline	VASE	PME by JY-Horiba	191–826	Growth at RT; Stoichiometry $x=1$ determined by <i>in situ</i> XPS; crystal structure and (111) texture identified by XRD
13	[321]	Postava	Sputtering	TiN	Thick thermal SiO ₂	107.1	N/A	ORS	Shimadzu	225–826	Spectral normalization was performed via a Si wafer
14	[295]	Van Bui	ALD	TiN	100 nm SiO ₂ /Si	10	N/A	<i>in situ</i> SE	RCE by J.A. Woolam	250–1650	Used TiCl ₄ and NH ₃ precursors; Overstoichiometry determined by XPS; Existent Cl-impurities
15	[238]	Wiemer	Magnetron Sputtering	TiN	Si(100)	400	Polycrystalline	SE	PME by JY-Horiba	413–826	Stoichiometry $1.03 > x > 1$ determined by ERDA; crystal structure identified by XRD
16	[244]	Aouadi	Magnetron Sputtering	ZrN	Si(111)	1500	Polycrystalline	VUV-VASE	RAE by J.A. Woolam	150–600	Stoichiometry equals to 1 confirmed by RBS
17	[326]	Camelio	DIBS	ZrN	Si(100)	100	Polycrystalline	VASE	RPE by SOPRA	200–1200	Growth at 600 °C; Stoichiometry determined by RBS; a cubic lattice size (0.460 nm) determined by XRD; the chemical and structural data were reported in Ref. [528]
18	[303]	Mei	Magnetron Sputtering	ZrN	MgO(100)	830	Epitaxial	VASE	RCE by J.A. Woolam	240–1200	Stoichiometry equals to 1 confirmed by RBS; density 7.32 gr/cm ³ equals to that of bulk ZrN; a cubic lattice size (0.4575 nm) determined by XRD
19	[174]	Naik	Magnetron Sputtering	ZrN, HfN, TaN	c-Sapphire	30–50	N/A	SE	RCE by J.A. Woolam	250–2000	
20	[324]	Pilloud	Magnetron Sputtering	ZrN	Stainless steel	3000	Polycrystalline	VASE	RPE by SOPRA	200–1200	Growth at 150 °C; Stoichiometry determined by EPMA; a cubic lattice size (0.462 nm) determined by XRD
21	[325]	Veszelei	Magnetron Sputtering	ZrN	SiO ₂ /Si	Opaque	N/A	SE	RCE by J.A. Woolam	250–2500	
22	[328]	Gueddaoui	Magnetron Sputtering	HfN	Si(100)	50	Polycrystalline	ORS	Perkin Elmer	250–2500	Stoichiometry determined by WDS; the B1 structure identified by XRD
23	[577]	Hu	Magnetron Sputtering	HfN	Si(100)	614	Polycrystalline	ORS	Perkin Elmer	250–2500	Stoichiometry HfN _{0.989} determined by XPS; the B1 structure identified by XRD and HRTEM
24	[327]	Stromme	Magnetron Sputtering	HfN	Hf/borosilicate glass	53	N/A	ORS	Monolight OSA	230–2000	
25	[380]	Mistik	Magnetron Sputtering	VN, TaN	Fused Silica	100	N/A	Null Ellipsometry	N/A	248–826	Composition determined by AES; VN is stoichiometric; TaN _x is understoichiometric and likely includes the Ta ₂ N phase.

Table 3 (Continued)

No	Reference	First Author	Growth Technique	Film Material	Substrate	Thickness (nm)	Morphology	Measurement Technique ^a	Instrument ^b	Experimental spectral range (nm)	Comments ^c
26	[391]	Konevecki	Magnetron Sputtering	NbN	Borosilicate Glass	110	Columnar Polycrystalline	SE	RAE	248–826	Stoichiometry determined by XPS; XRD identified the B1 phase
27	[390]	Sanjines	Magnetron Sputtering	NbN	Si wafer	N/A	N/A	SE	PME by JY-Horiba	250–1650	Stoichiometry NbN _{1.06} determined by EPMA and RBS; XRD identified the B1 phase
28	[389]	Tanabe	Magnetron Sputtering	NbN	SiO ₂ /Si	200–300	Polycrystalline	ORS	N/A	200–1000	Stoichiometry NbN _{1.08} determined by AES; XRD identified the B1 phase
29	[578]	Aouadi	Magnetron Sputtering	TaN	Si(100)	Opaque	Nanocrystalline	VASE	RCE by J.A. Woolam	150–600	Stoichiometry TaN _{1.03} determined by XPS; XRD identified just one broad peak that may correspond to the (111) of B1-TaN or the (0002) of h-TaN
30	[579]	Bousquet	Magnetron Sputtering	TaN	Vitreous carbon	N/A	Mixed Phase Polycrystalline	SE	PME by JY-Horiba	261–1653	Overstoichiometric mixed phase films studied by RBS and XRD
31	[382]	Langereis	ALD	TaN	p-Si wafer	52	Polycrystalline	<i>In situ</i> SE	RCE by J.A. Woolam	250–1650	PDMAT precursor used; stoichiometry equals to unity determined by RBS; the B1 phase identified by XRD
32	[381]	Matenoglou	PLD	TaN	Si(100)	300	Nanocrystalline	VASE	RPE by SOPRA	200–1200	Film slightly underdense; Stoichiometry TaN _{1.02} determined by AES; the B1 structure identified by XRD
33	[580]	Waechtler	Magnetron Sputtering	TaN	Si wafer	380	N/A	SE	RAE by SENTECH	250–2500	Mixed B1-TaN and h-TaN phases
34	[184]	Matenoglou	PLD	MoN, WN	Si(100)	300	Nanocrystalline	ORS	Avantes	250–780	Stoichiometry [N]/[Me]=0.98 was determined by AES, B1 phase identified by XRD; experimental spectra restricted to $\lambda > 275$ nm
35	[431]	Parreira	Magnetron Sputtering	WN	Si wafer	N/A	Nanocrystalline	SE	PME by JY-Horiba	275–826	Stoichiometry not available; most likely a mixed phase film
36	[432]	Metaxa	UHV Sputtering	WN	MgO(111)	2500	Epitaxial	ORS	Avantes, OceanOptics, Bruker	193–100000	Epitaxial B1-WN(111)/MgO(111) testified by XRD and HRTEM; Stoichiometry [N]/[W]=0.87 was determined by XPS.

^a SE= Spectroscopic Ellipsometry, VASE= Variable-Angle Spectroscopic Ellipsometry, ORS= Normal-Incidence Optical Reflectivity Spectroscopy, VUV= Vacuum UV.

^b RAE= Rotating Analyzer Ellipsometer, RCE= Rotating Compensator Ellipsometer, RPE= Rotating Polarizer Ellipsometer, PME= Phase-Modulated Ellipsometer.

^c RBS= Rutherford Backscattering, ERDA= Elastic Recoil Detection Analysis, XPS= X-Ray Photoelectron Spectroscopy, AES= Auger Electron Spectroscopy, EPMA= Electron Probe Microanalysis, WDS= Wavelength-Dispersive Spectroscopy, XRD= X-Ray Diffraction, HRTEM= High-Resolution Transmission Electron Microscopy.

Table 4

Summary of the values of the fit parameters of the dielectric function spectra presented in Figs. 20 and 21 from samples listed in Table 3.

Material	Spectra from Ref.	First Author	ϵ_{∞}	E_{pu} (eV)	Γ_D (eV)	f_1	E_1 (eV)	γ_1 (eV)	f_2	E_2 (eV)	γ_2 (eV)	E_{ps} (eV)	ρ ($\mu\Omega$ cm)	
1	TiN	[286]	Edlou	2.35	7.25	0.64	0.23	2.07	0.54	4.04	5.65	3.62	2.75	94
2		[240]	Gall	8.78	9.77	0.35	0.40	2.20	0.82	5.28	8.23	4.04	2.59	28
3		[292]	Huber	3.00	8.08	0.86	3.54	5.14	3.04	N/A	N/A	N/A	2.90	102
4		[291]	Humlíček	3.84	6.42	0.86	3.12	3.77	1.55	N/A	N/A	N/A	2.15	161
5		[285]	Karlsson	N/A	N/A	N/A	N/A	N/A	N/A	N/A	N/A	N/A	N/A	N/A
6		[434]	Koutsokeras	2.13	7.05	0.63	0.38	3.71	1.33	4.35	5.88	4.28	2.55	98
7		[294]	Langereis	3.87	7.21	0.81	2.69	4.48	2.64	1.27	5.36	0.88	2.32	120
8		[170]	Naik	2.67	5.71	0.17	0.20	2.26	0.72	2.31	4.89	3.88	1.99	39
9		[176]	Patsalas, 400 °C, $V_b=-100$ V	1.85	7.75	0.35	0.10	3.68	0.71	5.62	6.26	3.88	2.67	45
10		[176]	Patsalas, RT, $V_b=-120$ V	1.87	6.93	0.59	0.18	3.69	0.94	4.88	5.97	4.88	2.65	95
11		[176]	Patsalas, RT, $V_b=-40$ V	1.20	4.49	1.38	0.55	3.76	2.08	1.64	6.67	5.55	1.98	527
12		[177]	Patsalas, PLD	1.20	6.94	0.73	3.96	5.52	4.12	1.04	7.82	2.20	2.64	116
13		[293]	Postava	1.96	6.36	0.74	0.15	3.48	0.76	7.01	5.79	5.93	1.99	141
14		[295]	Van Bui	3.18	8.05	0.95	1.47	3.99	2.54	2.51	5.34	2.26	2.66	109
15		[238]	Wiemer	3.24	7.07	0.44	4.22	5.08	3.35	N/A	N/A	N/A	2.48	68
16	ZrN	[244]	Aouadi	1.38	8.08	0.41	5.11	7.98	5.91	N/A	N/A	N/A	3.07	48
17		[326]	Carmelio	1.79	7.11	0.51	3.41	6.29	3.15	N/A	N/A	N/A	2.91	78
18		[303]	Mei	2.99	8.07	0.18	2.57	5.83	1.54	N/A	N/A	N/A	3.16	21
19		[285]	Karlsson	3.22	7.35	0.40	2.34	6.51	2.73	N/A	N/A	N/A	2.97	57
20		[174]	Naik	5.41	8.16	0.47	0.82	4.52	1.25	N/A	N/A	N/A	3.10	54
21		[324]	Pilloud	2.44	7.02	0.73	3.97	6.33	4.34	N/A	N/A	N/A	2.61	114
22		[325]	Veszelei	2.90	7.66	0.33	1.92	5.27	1.51	N/A	N/A	N/A	3.19	43
23	HfN	[286]	Edlou	1.74	8.09	0.92	3.41	6.48	3.32	N/A	N/A	N/A	3.23	108
24		[328]	Gueddaoui	1.30	7.30	0.12	3.97	4.44	2.62	N/A	N/A	N/A	2.97	17
25		[577]	Hu	2.09	5.33	0.53	0.35	3.96	1.40	N/A	N/A	N/A	3.21	144
26		[174]	Naik	4.32	5.20	0.47	61.25	0.70	0.86	1.83	4.77	1.52	2.83	134
27		[327]	Stromme	6.58	8.01	0.36	0.04	6.05	16.77	N/A	N/A	N/A	3.09	43
28	VN	[380]	Mistrik	1.47	8.04	0.91	8.75	6.63	9.50	N/A	N/A	N/A	2.57	109
29	NbN	[391]	Konevicki	1.92	7.17	2.42	1.47	5.32	3.56	N/A	N/A	N/A	2.92	363
30		[390]	Sanjines	2.93	9.15	1.81	2.22	5.33	2.39	N/A	N/A	N/A	3.29	167
31		[389]	Tanabe	2.69	8.89	1.97	2.74	6.19	4.43	N/A	N/A	N/A	3.17	192
32	TaN	[578]	Aouadi	1.54	3.41	0.99	26.70	1.80	4.30	4.85	7.50	7.60	N/A	657
33		[579]	Bousquet	3.49	2.88	1.12	13.49	1.63	1.65	3.88	5.42	3.68	N/A	1042
34		[382]	Langereis	1.80	3.92	1.88	8.96	1.92	2.55	4.63	7.42	6.38	N/A	944
35		[577]	Mistrik	2.32	5.55	0.80	31.22	1.45	2.25	3.73	6.47	4.54	3.51	200
36		[174]	Naik	1.53	3.29	0.31	42.69	1.55	3.23	4.23	6.27	2.28	2.67	221
37		[381]	Matenogou	2.10	9.45	2.85	3.65	7.24	5.61	N/A	N/A	N/A	3.49	182
38		[580]	Waechter	1.68	3.48	1.02	25.85	1.80	4.21	4.78	7.01	6.95	N/A	650
39	MoN	[200]	Matenoglou	1.75	9.69	2.76	5.49	5.18	2.10	N/A	N/A	N/A	2.91	244
40	WN	[200]	Matenoglou	1.00	10.49	3.19	7.78	5.40	2.45	N/A	N/A	N/A	0.87	252
41		[431]	Parreira	1.75	8.15	6.80	16.95	3.78	13.37	0.83	5.85	1.92	N/A	790

TMN; in order a conductor to be a viable candidate for plasmonics, it has to exhibit as low electron loss as possible. Consequently, it is very important to correlate the parameter Γ_D , which is associated with the electron loss, with E_{ps} or its equivalent wavelength λ_{ps} in order to evaluate the expected electron losses at various operational wavelengths for plasmonic devices. Such a correlation is presented in Fig. 24. Nitrides of the group IVB metals (TiN, ZrN, HfN) combine low electron losses (as low as 0.12 eV in exceptional cases, and typically around 0.3 eV for epitaxial and/or fully dense and low defect films) with an operational spectral range 390–620 nm that covers most of the visible range. Viable extension towards the red and infrared cannot be achieved with binary TMN, while extension towards UV (350 nm) can be done by mostly NbN and TaN, albeit in expense of the increasing electron loss.

In order to interpret the variations of the conduction electron density, via E_{pu} and Eq. (1), and the conduction electron loss, via Γ_D and Eq. (3), the resistivity via Eq. (4) and MFP we correlate them with the atomic number of the constituent metal. In the case of polycrystalline material for the accurate determination of the MFP Eq. (5) should be modified as [177]:

$$MFP = \left(\frac{0.75\pi}{(m^*e)^2} \right)^{1/3} \cdot \frac{\hbar^2 \omega_{pu}^{2/3}}{\Gamma_D - \Gamma_D^{bulk}} \quad (12)$$

where Γ_D^{bulk} is the Drude broadening of the single-crystal nitride. However, for our analysis we are using Eq. (5) instead of Eq. (12)

because Γ_D^{bulk} values are not readily available, and thus, we are underestimating the actual MFP . These correlations are presented in Fig. 25. E_{pu} and Γ_D values exhibit broad scattering, mostly for TiN and TaN. The scattering for TiN is due to the variations of stoichiometry and grain morphology as noted in Table 3; indeed, values for fully dense stoichiometric TiN and fibrous overstoichiometric $TiN_{1.1}$ from Ref. [176] are included in Fig. 25, and constitute marginal cases of high and low quality TiN. On the other hand, the scattering for TaN is due to its metastable nature and the difficulty of producing pure B1-TaN [381,386,410,498], so most of the reported dielectric function spectra in literature are originating from mixed B1 and hexagonal phases of TaN. Consequently, in Fig. 25 and for the case of TaN the points corresponding to B1-TaN are distinguished from those for mixed phase samples by horizontal dotted lines. The magenta lines in Fig. 25 are guides to the eye drawn through the average values of each quantity for every nitride. E_{pu} and Γ_D values are rationally grouped according to the metal's period and group (i.e. to the principal quantum number and number of valence electrons, respectively). Nitrides of metals of the same group (e.g. TiN, ZrN and HfN, whose metals share the same d^2s^2 valence electron configuration) exhibit similar values, while E_{pu} increases with increasing number of valence electrons, confirming qualitatively the computational predictions presented in Figs. 13a, 15, 16a and b. This is quite reasonable if we take into account that part of the metal's valence charge are hybridized to form the covalent bonding with N and the excess of the metal's

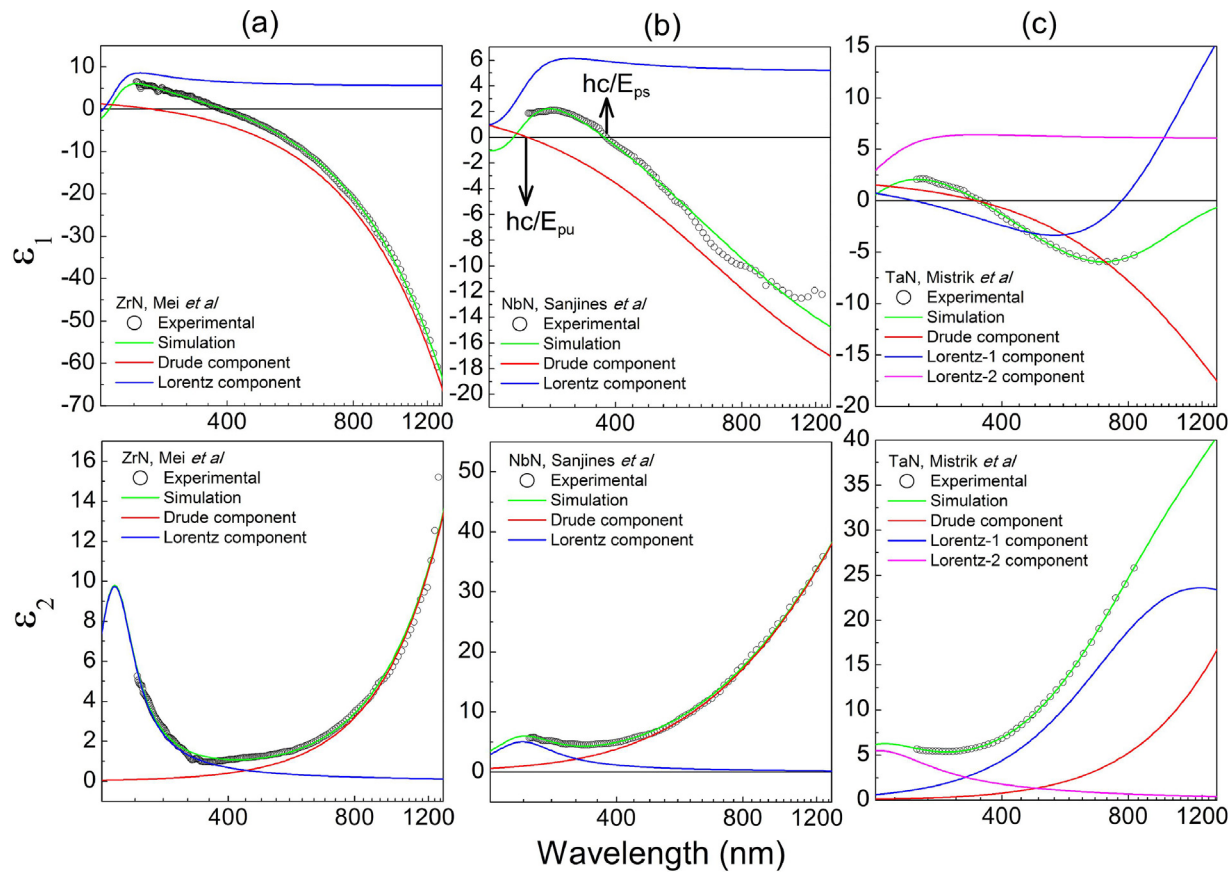


Fig. 19. The experimental (open circles) and the fitted (green lines) real (ϵ_1) and the imaginary (ϵ_2) parts of the dielectric function of representative opaque (a) ZrN from Refs. [303,295] (b) NbN from Refs. [390,295] and (c) TaN from Refs. [380] films. The individual contributions of the Drude term (red lines) and the two Lorentz oscillators (blue and magenta lines) are also shown. Similar raw and deconvoluted data for TiN can be found in Ref. [177]. (For interpretation of the references to colour in this figure legend, the reader is referred to the web version of this article.)

electrons (which is increasing with increasing number of metal's valence electrons) constitute the Fermi gas. A major exception is B1-WN; in particular, the PLD-grown B1-WN follows the computational trends for E_{pu} and Γ_D , while sputtered B1-WN exhibit lower E_{pu} due to the stoichiometry variations [432] originating from the generation of point defects, which stabilize the B1 structure [574]. The direct consequence of the observed variations of E_{pu} and Γ_D is the substantial increase of resistivity with increasing group number and the subsequent reduction of MFP of conduction electrons in agreement with the computational results of Fig. 16a and b.

As a partial conclusion, we observe that the less optically lossy nitrides are those of group IVb metals (TiN, ZrN, HfN). Among them, ZrN shows the smallest average value of Γ_D , which in combination with the minimized dielectric losses, as discussed previously, is emerging as the most promising refractory conductor. Therefore, ZrN nanostructures are foreseen to exhibit the best plasmonic performance. In addition, TiN and ZrN exhibit small and large work function, respectively, while they have similar melting points and E_{pu} , which are associated with conduction electron density (Fig. 26). Therefore, they can constitute a platform of tunable plasmonic conductors for hot electron applications. Regarding the nitrides of Vb metals, they exhibit higher conduction electron density and E_{pu} and E_{ps} compared to group IVb nitrides, and thus a plasmonic performance towards UV is predicted. They all exhibit E_{pu} , Γ_D and MFP values similar to each other in the B1 structure. Given the metastable character of B1-TaN in contrast to the ease of fabricating epitaxial B1-NbN, we can safely conclude that for UV plasmonic applications B1-NbN is the most promising candidate.

B1-VN received less attention and in this review only data from one sample are reported. These data indicate that B1-VN is not inferior to B1-NbN, while having the additional asset of exceptionally low work function as shown in Fig. 26. The combination of the potential plasmonic response in the UV with the low work function of B1-VN might be a strong incentive for the investigation of B1-VN in plasmonics and hot electron applications, however, its real potential for such applications can not be solidly evaluated for the time being due to the lack of data from other research groups that would confirm its reported optical behavior. Finally, B1-MoN and B1-WN are exceptionally and excessively lossy due to both their inherent characteristics as calculated by LAPW and presented in Figs. Fig. 13, 15, 16a and b, and their metastable character, which results in the incorporation of a high concentration of point defects to stabilize them. Consequently, they do not seem appropriate for applications, such as plasmonics, where high conductivity is required.

2.2.5. Experimental dielectric function spectra of ternary nitrides

As we have seen and discussed, there are certain spectral limitations on the use of binary TMN for various applications. In particular, λ_{ps} of binary TMN can be hardly extended beyond 600 nm, while the extension towards UV is hard due to the metastability and structural degradation of most nitrides of group Vb and Vlb metals. Alloying and forming ternary TMN, with TiN or ZrN as basis, has been proposed as viable solutions to these two limitations [184,439,441,453,471]. Thus, the conduction electron density, and consequently E_{ps} and λ_{ps} as well, can be quite accurately tuned by varying the effective number of valence

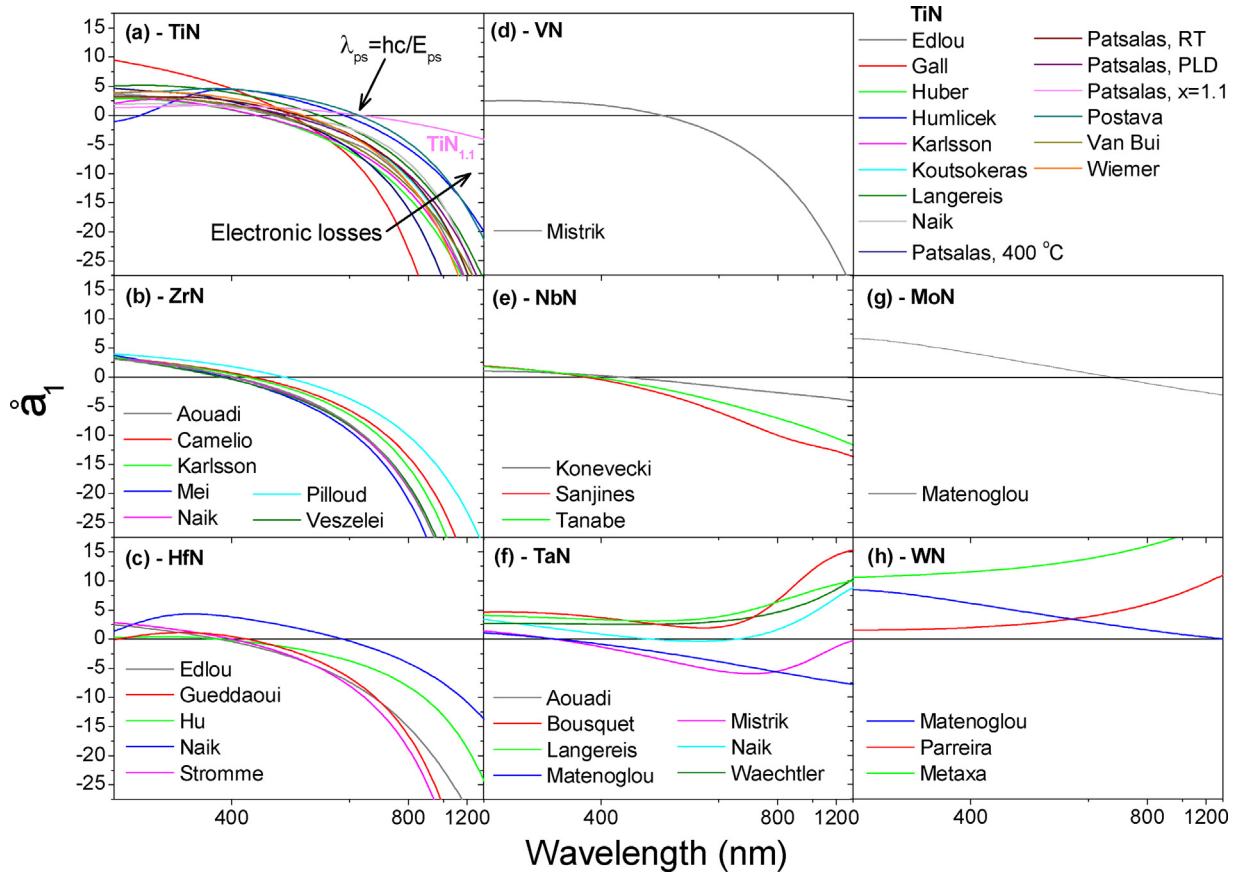


Fig. 20. Extrapolated ϵ_1 spectra in the 350–1300 nm wavelength of light using the best fit value parameters presented in Table 3 for (a) TiN, (b) ZrN, (c) HfN, (d) VN, (e) NbN, (f) TaN, (g) MoN, and (h) WN; the fits were performed on experimental spectra reported by various groups worldwide (References presented in detail in Table 3); note that the spectra for TaN by Aouadi and Waechtler coincide.

electrons of the constituent metals in $Ti_xMe_{1-x}N$ or $Zr_xMe_{1-x}N$ (where Me can be either a group IIb, IIIb, and IIIa element or a group Vb and VIb element):

$$N_{eff} = x \cdot V_1 + (1 - x) \cdot V_2, \quad (13)$$

where V_1 is four for Ti or Zr (d^2s^2 valence electrons) and V_2 is the number of electrons of the alloying elements, which is two for Mg, Ca, three for Sc, Y, La, and Al, five for Nb, and Ta, and six for Mo. The spectra of the real (ϵ_1) and imaginary (ϵ_2) parts of the dielectric functions of a wide variety of ternary nitrides, grown by various techniques, such as hybrid CVA (HCVA), DIBS, MS and PLD, and which were originally reported in Refs. [184,439,471], are presented in Figs. 27 and 28, respectively. The E_{pu} and Γ_D values resulted from the fits by Eq. (11), as well as the resistivity and MFP values determined using Eqs. (4) and (5) are summarized in Table 5. All the spectra of Figs. 27 and 28 are for polycrystalline samples, so their electron losses are expected to be affected accordingly. The fit results from $Ti_xLa_{1-x}N$ films are also summarized in Table 5, while the corresponding spectra are not included in Figs. 27 and 28 but can be found in Ref. [441,471]. $Ti_xLa_{1-x}N$ films are amorphous due to the large lattice mismatch of the constituents (TiN and LaN). All the presented spectra are characteristic of good conductors, with the major exception of $Ti_xMo_{1-x}N$. In the latter case of $Ti_xMo_{1-x}N$ the ϵ_1 for wavelenghts longer than λ_{ps} gets very small negative values, which are indicative of excessive electron loss. These films were not found to consist by the B1 phase, although they were grown with identical conditions with TiN. This can be attributed to the inherent metastable character of the B1-MoN and the intrinsic structural defects that are formed in B1-MoN [186,387]. Therefore, Ti atoms

into $Ti_xMo_{1-x}N$ are not as effective stabilizers of the B1 phase as in the case of B1- $Ti_xTa_{1-x}N$. Further work is required to clarify this issue.

The basic features of all spectra are the redshift of λ_{ps} (i.e. reduction of E_{ps}) when alloying TiN or ZrN with group II or group III elements, and the blueshift of λ_{ps} (i.e. increasing of E_{ps}) when alloying with group Vb elements, as a direct consequence of the variation of the effective number of valence electrons of the constituent metals according to Eq. (13). This is clearly illustrated in Fig. 23, where a correlation of E_{ps} with N_{eff} is presented. Indeed, in Fig. 23 the scattering of the experimental points for ternary nitrides is less than for their binary counterparts, suggesting that alloying the B1 phase may be a more effective and controlled way of tuning E_{ps} than varying the composition and microstructure of binary TMN. In particular, the optical performance, in terms of E_{ps} , of Ta-rich $Ti_xTa_{1-x}N$ and Mo-rich $Ti_xMo_{1-x}N$ is superior to their metastable binary counterparts, indicating that small amounts of Ti may stabilize the B1 structure (at least for the case of $Ti_xTa_{1-x}N$) and provide a viable candidate for violet and UV plasmonics. The correlation of the electron losses via Γ_D , and the operation range via λ_{ps} presented in Fig. 24, shows that the polycrystalline ternary nitrides exhibit similar electron losses with their binary counterparts, which are higher than those of the epitaxial or fully dense binary TMN. This observation suggests that there is no substantial alloying scattering in such ternary systems and that better tunable optical performance would be achieved, if such ternary nitrides were grown epitaxially. This provides a strong incentive to put more effort in the crystal growth technology of conductive ternary TMN. With the current view of Fig. 24, the electron losses

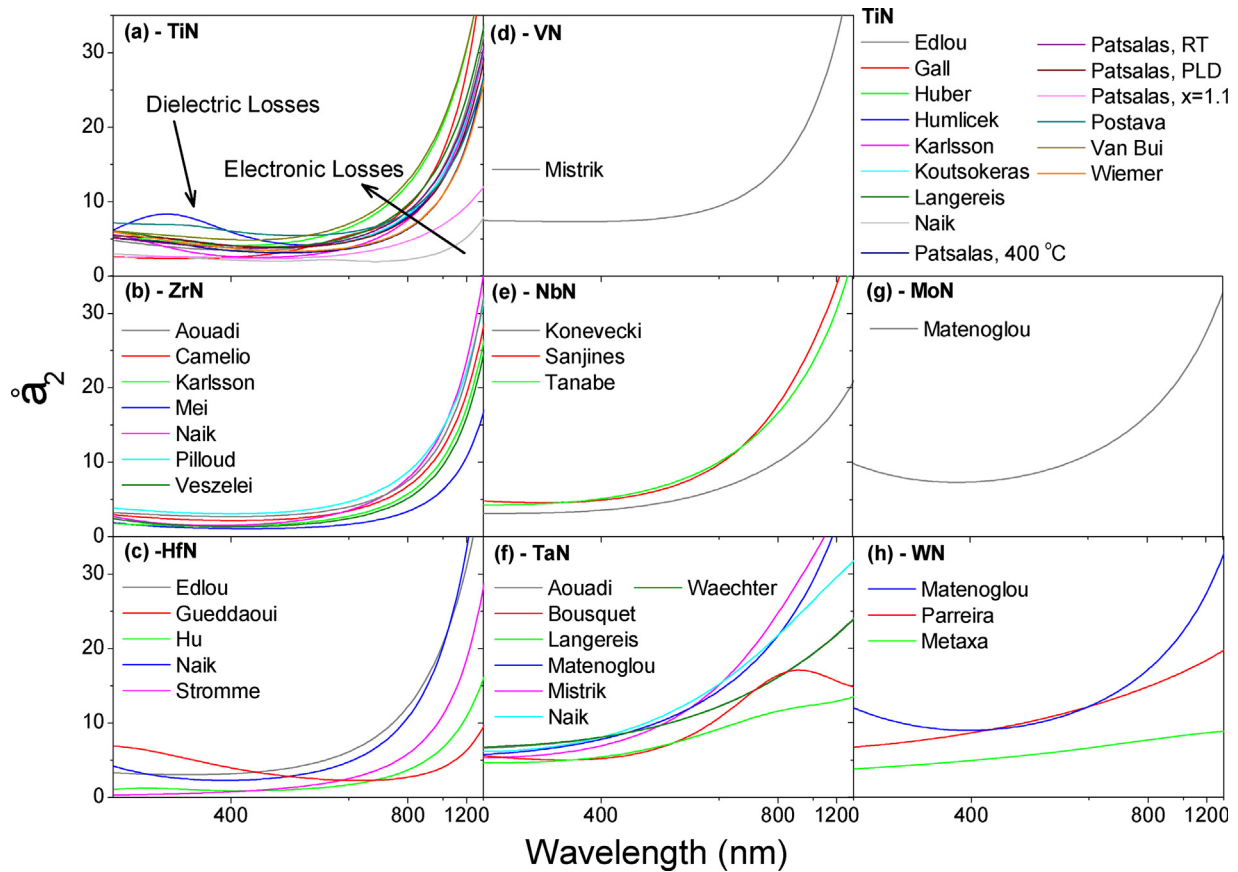


Fig. 21. Extrapolated ϵ_2 spectra in the 350–1300 nm wavelength of light using the best fit value parameters presented in Table 3 for (a) TiN, (b) ZrN, (c) HfN, (d) VN, (e) NbN, (f) TaN, (g) MoN, and (h) WN; the fits were performed on experimental spectra reported by various groups worldwide (References presented in detail in Table 3).

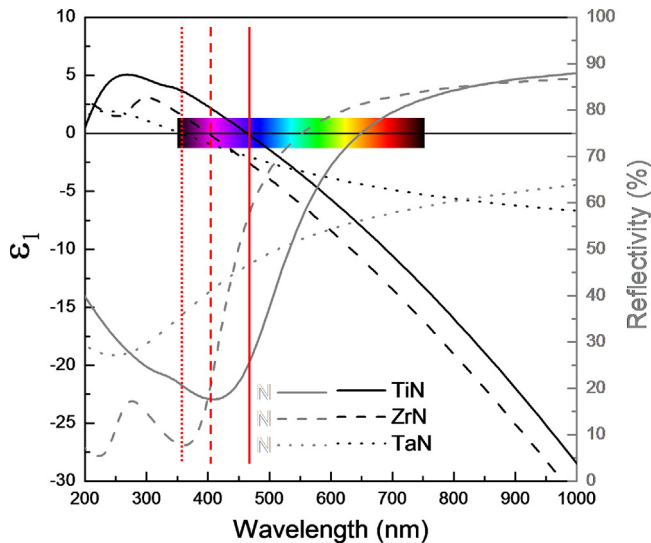


Fig. 22. Reflectivity (gray lines) and real part of the dielectric function (black lines) spectra for B1-TiN, B1-ZrN and B1-TaN; λ_{ps} lies into the visible range for TiN and ZrN and in the verge of visible for TaN, and defines the reflectivity edge. Vertical red lines indicate λ_{ps} for the three nitrides. (For interpretation of the references to colour in this figure legend, the reader is referred to the web version of this article.)

are minimized in the visible spectral range of λ_{ps} , while extensions of the operating range towards both UV and infrared come in expense of the electron losses. This has to be taken into account when designing optical devices based on ternary TMN.

A better evaluation of the optical performance of the various ternary nitrides can be done based on the correlations of E_{pu} , Γ_D , resistivity and MFP vs. the N_{eff} as presented in Fig. 29. E_{pu} (we remind that it is correlated with the conduction electron density) and Γ_D are rationally increasing with N_{eff} for all binary and ternary TMN in the B1 structure, in agreement with the computational results presented previously. TaN and $Ti_xMo_{1-x}N$ samples that do not consist exclusively of the B1 phase are distinguished by the dotted black line and they exhibit substantially lower E_{pu} and carrier density than the B1 samples. For N_{eff} between four and five, fully dense samples of low electron losses and resistivity can be developed in the $Ti_xTa_{1-x}N$ system. These samples are expected to exhibit plasmonic behavior at shorter wavelengths than TiN and ZrN. Note that the $Zr_xTa_{1-x}N$ exhibits smaller E_{pu} (carrier density) and higher electron losses and resistivity compared to $Ti_xTa_{1-x}N$ of similar N_{eff} . This observation indicates that, despite of ZrN being a better optical conductor than TiN in its own merit, as we have already discussed, it is a less effective alloying constituent than TiN. This is possibly due to the large size of the cubic cell of B1-ZrN that is mismatched with most of the rest of TMN thus resulting to finer grains when alloyed to form ZrN-based ternary TMN. It could also be due to the large atomic mass of Zr that usually results in a higher amount of intrinsic stress and structural defects than TiN grown with similar conditions, mostly for kinetic reasons [309]. It seems that for $N_{eff} > 5$ all TMN exhibit excessive electron losses and high resistivity values, which make their perspectives for applications in plasmonics quite questionable. However, the relevant available experimental points are rather few to provide a solid conclusion on this issue.

For N_{eff} below four, several alloying elements have been investigated. Among them, $Ti_xSc_{1-x}N$ emerges as the most

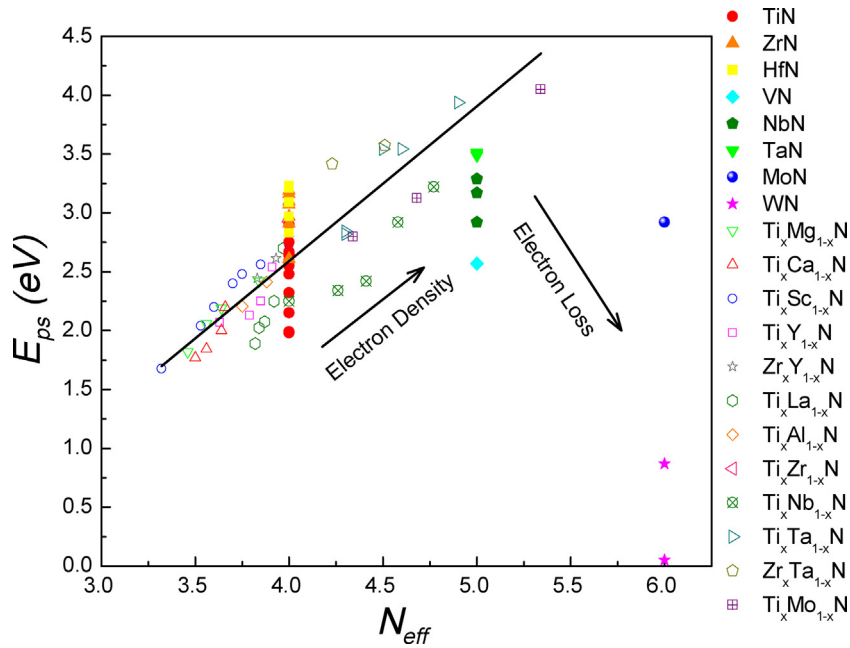


Fig. 23. The variation of E_{ps} with the effective number of valence electrons N_{eff} for binary (solid symbols) and ternary (open symbols) TMN.

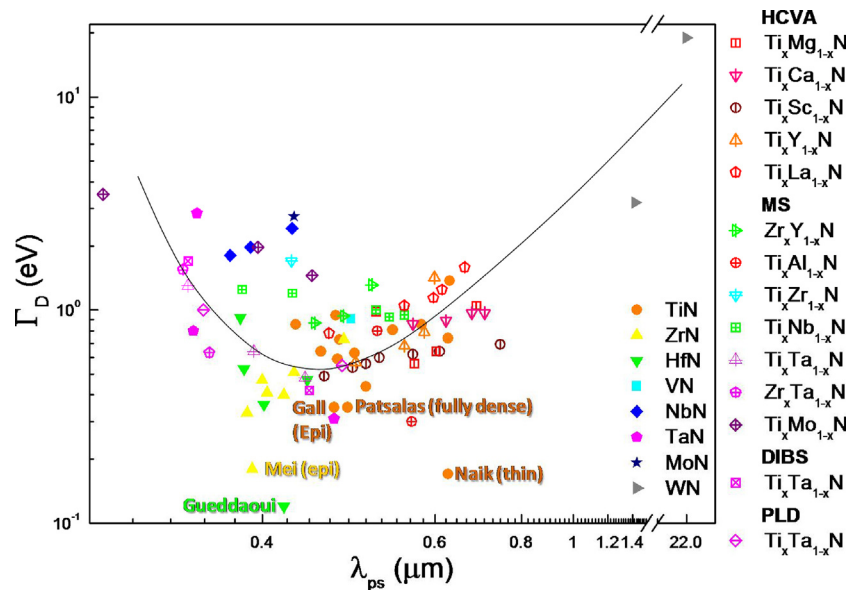


Fig. 24. Correlation of Γ_D , which is associated with the electron loss, with the wavelength λ_{ps} where $\epsilon_1 = 0$, which may indicate the operation range of plasmonic devices; the line is a guide to the eye and does not imply any physical interpretation. Solid and open symbols represent binary and ternary TMN, respectively.

promising system due to the overall lower electron losses and resistivity, and E_{pu} values that are compatible with fully dense films with very few structural defects [471]. This is due to a combination of reasons such as the good lattice match between TiN and ScN, their structural compatibility (both TiN and ScN are stable in the B1 structure), and the similar valence electron configuration (d^2s^2 for Ti, d^1s^2 for Sc) and bonding with nitrogen. The main drawback of the $Ti_xSc_{1-x}N$ system is the very limited abundance of Sc in Earth's crust, and the associated high cost of raw materials. An alternative and abundant candidate would be $Ti_xMg_{1-x}N$, which exhibits the second best performance in terms of E_{pu} , Γ_D , resistivity and MFP in this N_{eff} range. Although Mg is not soluble into TiN in the entire compositional range [471], there is a sufficient solubility range (mostly due to the similar atomic radii of

Ti and Mg) where B1- $Ti_xMg_{1-x}N$ with plasmonic performance in the near infrared can be grown [441].

The correlation of the conduction electron (carrier) density N with the cell size of the various ternary nitrides is very important for applications involving heteroepitaxial structures. Fig. 30 shows the variation of E_{pu}^2 and N (calculated from E_{pu} according to Eq. (1)) vs. the lattice constant of the various binary and ternary nitrides in the B1 cubic phase. Open points correspond to representative conductive nitrides grown by PLD in Ref. [184] and having $N_{eff} \geq 4$; note that the binary nitrides are included in these sets of ternary data for $x = 0$, i.e. are the extreme value points of each set. Magenta stars correspond to the $Ti_xAl_{1-x}N$ with $N_{eff} < 4$ reported in Ref. [453]. Finally solid symbols correspond to $Ti_xSc_{1-x}N$, $Ti_xY_{1-x}N$, $Ti_xMg_{1-x}N$, and $Ti_xCa_{1-x}N$ ($Ti_xLa_{1-x}N$ is excluded from this

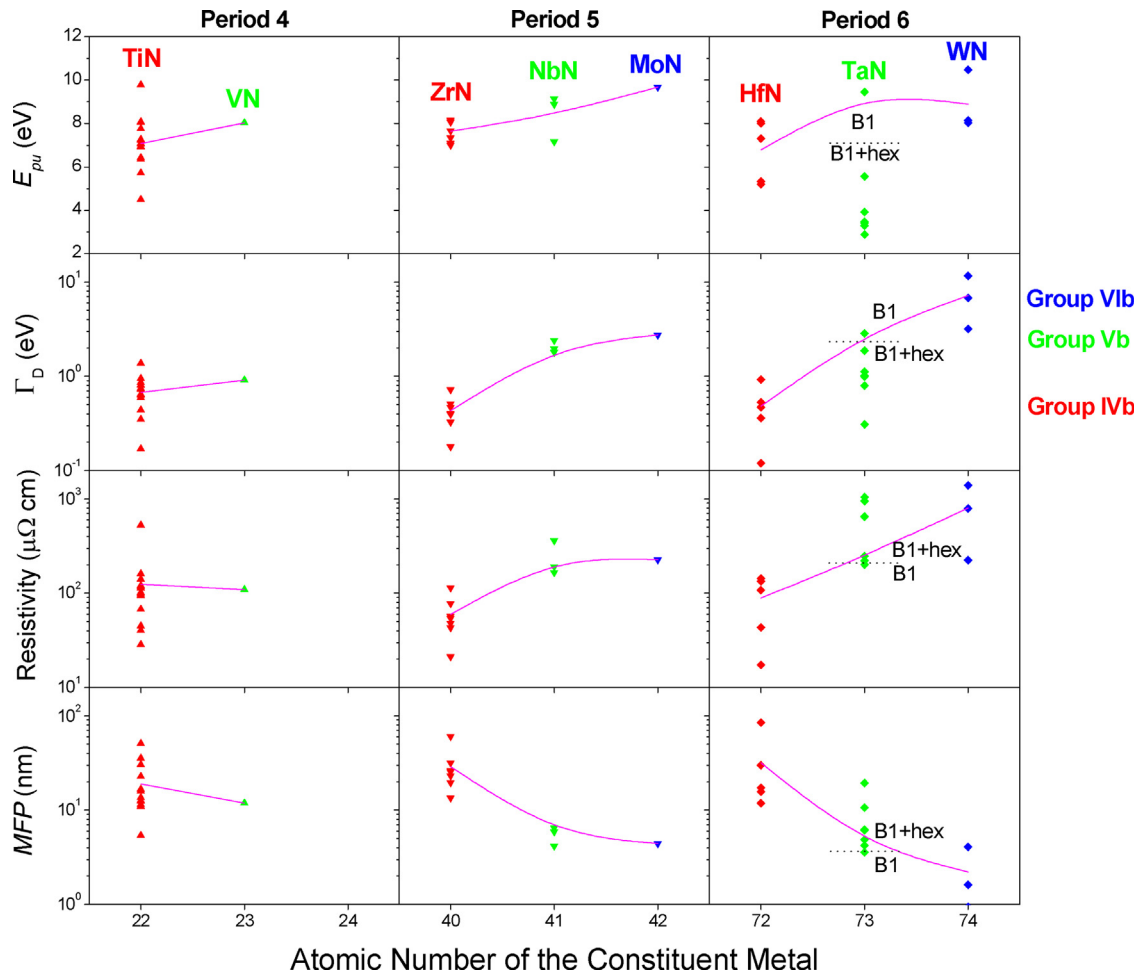


Fig. 25. The variations of E_{pu} and Γ_D , as determined by fitting the experimental spectra by Eq. (11), and as summarized in Table 4, and of the resistivity and the MFP, determined according to Eqs. (4) and (5), of binary nitrides vs. the atomic number of the constituent metal.

comparison because it is amorphous for the most cases) reported in Ref. [471] and having $N_{eff} < 4$, as well. ZrN exhibits the larger cubic cell size among all. The E_{pu}^2 values of each ternary nitride

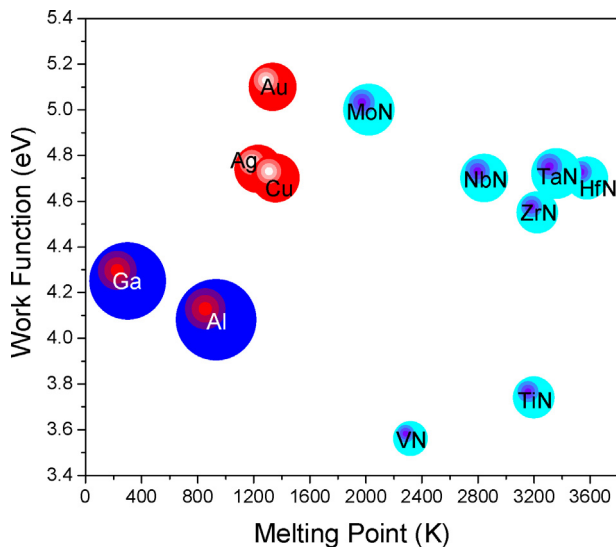


Fig. 26. The correlation of the WF of binary TMN with their melting point and $E_{pu}/$ carrier concentration (disk diameter) in comparison with noble metals (red disks) and group IIIa metals (blue disks). (For interpretation of the references to colour in this figure legend, the reader is referred to the web version of this article.)

system follow almost linear correlations with the lattice constant and the composition x of the films. All the ternary nitrides with Vb and IVb group elements exhibit higher E_{pu} values than the $Ti_xZr_{1-x}N$ system due to the additional valence electrons of the constituent metals and, thus, they cover the upper part of the phase space. The $Ti_xAl_{1-x}N$ system exhibits both smaller E_{pu} and lattice size values compared to $Ti_xZr_{1-x}N$. Using the experimental data for $Ti_xAl_{1-x}N$ and the calculated lattice size of B1-AlN [585] we can conclude that $Ti_xAl_{1-x}N$ can be grown fully dense, since the experimental points (magenta stars) coincide with the theoretical magenta line. On the other hand, the $Ti_xSc_{1-x}N$, $Ti_xY_{1-x}N$, $Ti_xMg_{1-x}N$, and $Ti_xCa_{1-x}N$ systems cover a lattice size range comparable with the $Ti_xZr_{1-x}N$ system, while they exhibit substantially lower E_{pu} values. Among them, the experimental values of the $Ti_xSc_{1-x}N$ system (black disks) are lying on the line (black line) that connects the TiN and ScN points, suggesting the formation of fully dense ternary compounds over the entire compositional range. On the contrary, the experimental E_{pu} values of $Ti_xY_{1-x}N$, $Ti_xMg_{1-x}N$, and $Ti_xCa_{1-x}N$ (solid up and down triangles, and diamonds, respectively) are inferior to the predicted values (red and green lines, respectively), defined by the calculated lattice sizes of B1-YN [492], B1-MgN [586] and B1-CaN [587], further supporting the formation of underdense ternary compounds. Especially $Ti_xMg_{1-x}N$ and $Ti_xCa_{1-x}N$, for high x -values, exhibit E_{pu}^2 values higher than TiN, indicating the existence of excess Mg and Ca atoms possibly in interstitial and not in substitutional positions.

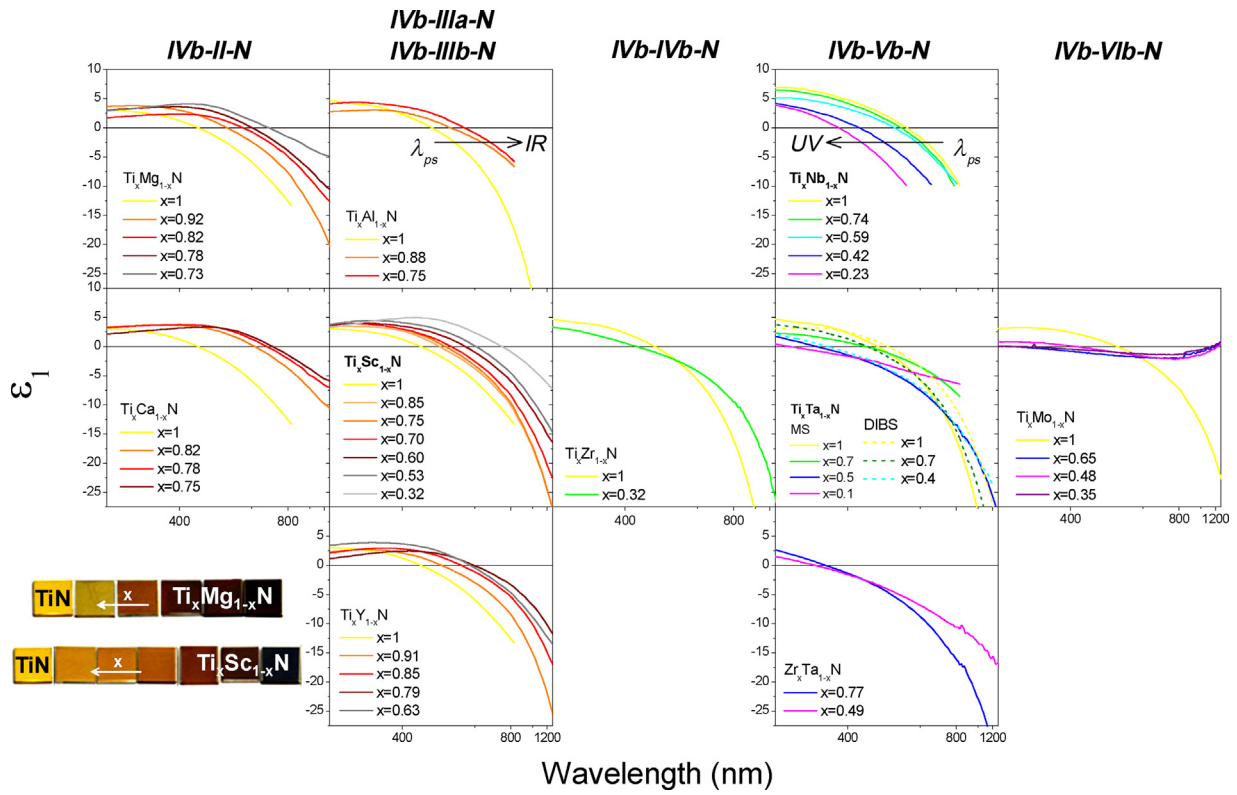


Fig. 27. Spectra of the real part of the dielectric function (real permittivity) of a variety of ternary nitrides based on TiN and ZrN. First column: TMN consisting of a group II element (Mg, Ca) and a group IVb element (Ti). Second column: TMN consisting of a group IIIa element (Al) or a group IIIb element (Sc, Y) and a group IVb element (Ti, Zr). Third column: TMN consisting of a two group IVb elements (Ti, Zr). Fourth column: TMN consisting of a group Vb element (Nb, Ta) and a group IVb element (Ti, Zr). Fifth column: TMN consisting of a group VIb element (Mo) and a group IVb element (Ti). In the low left corner the visual appearance of various ternary nitride samples. Data from Refs. [439,448,453,471].

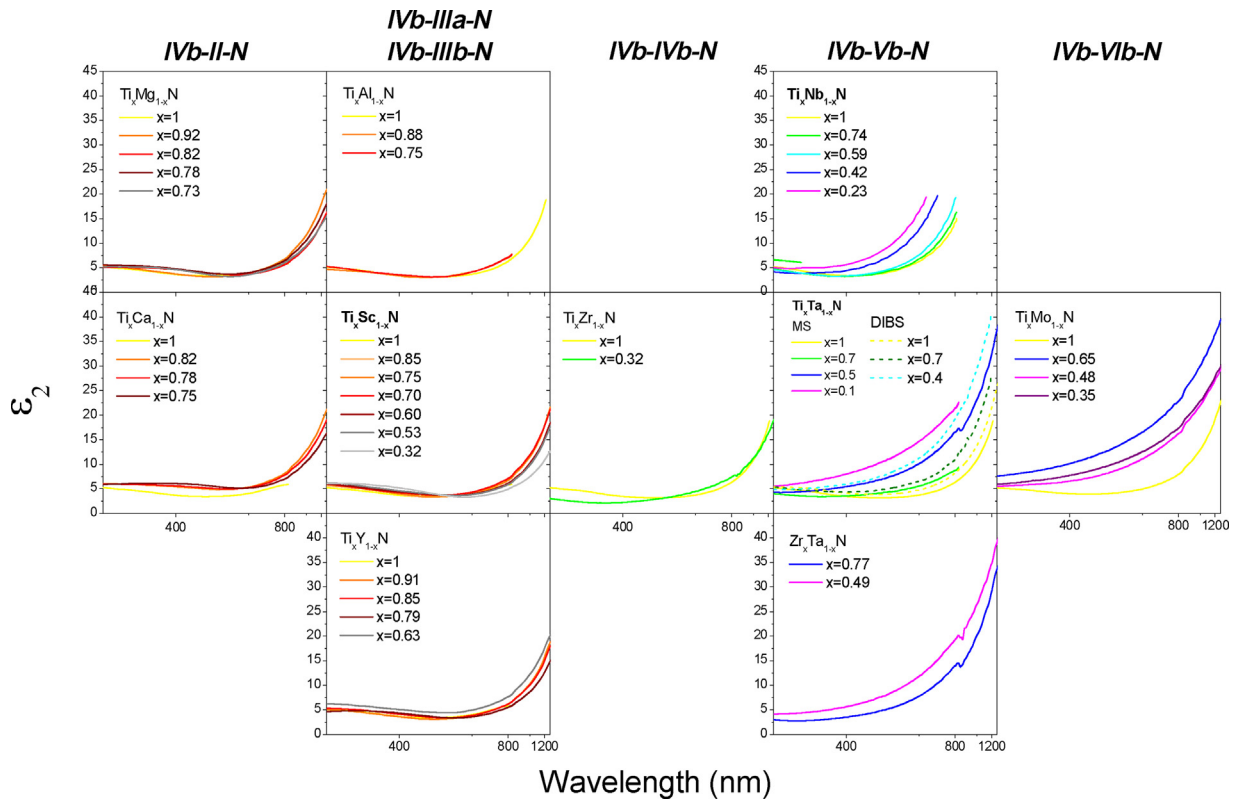


Fig. 28. Spectra of the imaginary part of the dielectric function (imaginary permittivity) of a variety of ternary nitrides based on TiN and ZrN. First column: TMN consisting of a group II element (Mg, Ca) and a group IVb element (Ti). Second column: TMN consisting of a group IIIa element (Al) or a group IIIb element (Sc, Y) and a group IVb element (Ti, Zr). Third column: TMN consisting of a two group IVb elements (Ti, Zr). Fourth column: TMN consisting of a group Vb element (Nb, Ta) and a group IVb element (Ti, Zr). Fifth column: TMN consisting of a group VIb element (Mo) and a group IVb element (Ti). Data from Refs. [439,448,453,471].

Table 5
Summary of the Drude parameters of ternary TMN used to reduce the conduction electron density of TiN and ZrN and redshift the plasmonic performance.

	Material	Ref.	First Author	Growth Technique	X	E_{pu} (eV)	G_D (eV)	MFP (nm)	Resistivity ($\mu\Omega\text{ cm}$)	E_{ps} (eV)
1	Ti _x Mg _{1-x} N	[471]	Kassavetis	Hybrid CVA	0.92	7.14	0.98	10.3	148	2.42
2					0.82	5.59	0.56	15.2	138	2.19
3					0.78	5.65	0.64	13.4	155	2.06
4					0.73	5.16	1.05	7.7	304	1.82
5	Ti _x Ca _{1-x} N	[471]	Kassavetis	Hybrid CVA	0.83	5.95	0.86	10.3	187	2.20
6					0.82	5.65	0.89	9.7	215	2.00
7					0.78	5.61	0.97	8.8	239	1.85
8					0.75	5.20	0.97	8.4	275	1.77
9	Ti _x Sc _{1-x} N	[471]	Kassavetis	Hybrid CVA	0.85	6.73	0.54	17.9	92	2.56
10					0.75	6.70	0.56	17.1	97	2.48
11					0.70	6.48	0.60	15.6	111	2.40
12					0.60	5.85	0.62	14.1	140	2.20
13					0.53	5.65	0.64	13.4	156	2.04
14					0.32	4.79	0.69	11.1	233	1.68
15	Ti _x Y _{1-x} N	[471]	Kassavetis	Hybrid CVA	0.91	6.13	0.57	16.1	116	2.54
16					0.85	5.70	0.68	12.6	163	2.25
17					0.79	5.17	0.79	10.3	227	2.13
18					0.63	4.53	1.42	5.2	535	2.07
19	Ti _x La _{1-x} N	[471]	Kassavetis	Hybrid CVA	0.97	7.32	0.78	13.11	11	2.70
20	(amorphous)				0.93	6.32	1.05	8.85	202	2.25
21					0.87	6.08	1.14	7.91	238	2.08
22					0.84	6.27	1.25	7.39	245	2.03
23	Zr _x Y _{1-x} N	[441]	Metaxa	dual-cathode MS	1.00	6.60	0.87	11.0	154	2.79
24					0.93	6.58	0.94	10.1	168	2.61
25					0.83	6.19	1.31	7.0	264	2.45
26	Ti _x Al _{1-x} N	[439]	Kassavetis	dual-cathode MS	0.88	6.3	0.82	11.6	1556	2.41
27					0.75	4.6	0.34	25.0	109	2.21
28	Ti _x Zr _{1-x} N	[439]	Kassavetis	dual-cathode MS	0.32	7.6	1.7	6.2	227	2.92
29	Ti _x Nb _{1-x} N	[448]	Vasu	MS with composite target	1.00	N/A	0.95	N/A	N/A	2.25
30					0.74	N/A	0.93	N/A	N/A	2.34
31					0.59	N/A	1.02	N/A	N/A	2.42
32					0.42	N/A	1.21	N/A	N/A	2.92
33	Ti _x Ta _{1-x} N	[248]	Matenoglou	DIBS	0.7	8.31	0.42	26.5	47	2.82
34					0.4	9.11	1.7	7.0	158	3.54
35	Ti _x Ta _{1-x} N	[439]	Kassavetis	dual-cathode MS	0.7	7.97	0.48	22.5	58	2.84
36					0.5	8.72	0.64	17.9	65	3.15
37					0.1	9.32	1.3	9.2	116	3.54
38	Ti _x Ta _{1-x} N	[248]	Matenoglou	PLD	0.95	8.48	1.05	11.3	107	3.45
39					0.28	6.93	0.55	17.9	88	2.62
40	Zr _x Ta _{1-x} N	[439]	Kassavetis	dual-cathode MS	0.77	0.63	6.8	15.4	105	3.42
41					0.49	1.55	7.5	6.7	213	3.57
42	Ti _x Mo _{1-x} N	This work		MS with composite target	0.83	5.55	1.45	5.86	363	2.80
43	(mixed phase)				0.66	3.87	1.97	3.39	1015	3.12
44					0.33	5.7	3.5	2.47	831	4.05

3. TMN nanostructures and plasmonic applications

3.1. Quality factors of plasmonic resonances

The dielectric function spectra (or complex permittivities), so far reviewed and studied in this work, are defining the plasmonic performance of the conductors. In principle, a conductor may sustain a plasmonic resonance, either an SPP at a planar interface or an LSPR in nanoparticles, at any given wavelength where ϵ_1 is negative; however, the quality of such resonance would be severely affected by the electron losses, which are mostly affected by ϵ_2 . As a result, the most important question is not whether a resonance can be sustained but which is the quality of such resonance. Based on fundamental considerations, certain quality factors for SPP and LSPR have been established using ϵ_1 , ϵ_2 [168,588]. In particular, for SPP at an interface between a planar TMN and a dielectric:

$$Q_{SPP} = \frac{\epsilon_{1,TMN} + \epsilon_{1,d}}{\epsilon_{1,TMN} \cdot \epsilon_{1,d}} \times \frac{\epsilon_{1,TMN}^2}{\epsilon_{2,TMN}}, \quad (14)$$

and for spherical nanoparticles of TMN in air, the Q_{LSPR} :

$$Q_{LSPR} = \frac{-\epsilon_1^{\square}, TMN}{\epsilon_{2,TMN}}, \quad (15)$$

where $\epsilon_{1,TMN}$ and $\epsilon_{2,TMN}$ are the real and imaginary parts of the dielectric function of the TMN, and the $\epsilon_{1,d}$ is the real part of the dielectric function of the adjacent dielectric ($\epsilon_{1,d} = 1$ for air).

As a case study, we calculated the Q_{SPP} for a thin TMN film adjacent to a thermal SiO₂ layer ($\epsilon_{1,d} = \epsilon_{1,SiO_2} = 1.9$) for all the binary nitrides listed in Table 3 excluding the exceptionally lossy B1-MoN and B1-WN, and for the most promising ternary nitrides according to the data of Fig. 29. SiO₂ is chosen as an important demonstrator, as it is the major dielectric of Si microelectronics and of fiber optic telecommunications. The variations of Q_{SPP} vs. the wavelength of the incoming light for binary and ternary nitrides are presented in Figs. 31 and 32, respectively. The vertical dotted lines in Fig. 31 separate the spectral range where $\epsilon_1 < 0$ (intraband region) and $\epsilon_1 > 0$ (interband region); the latter region has no physical importance and should be neglected. In Fig. 31 a strikingly difference of the Q_{SPP} values between group IVb and Vb binary

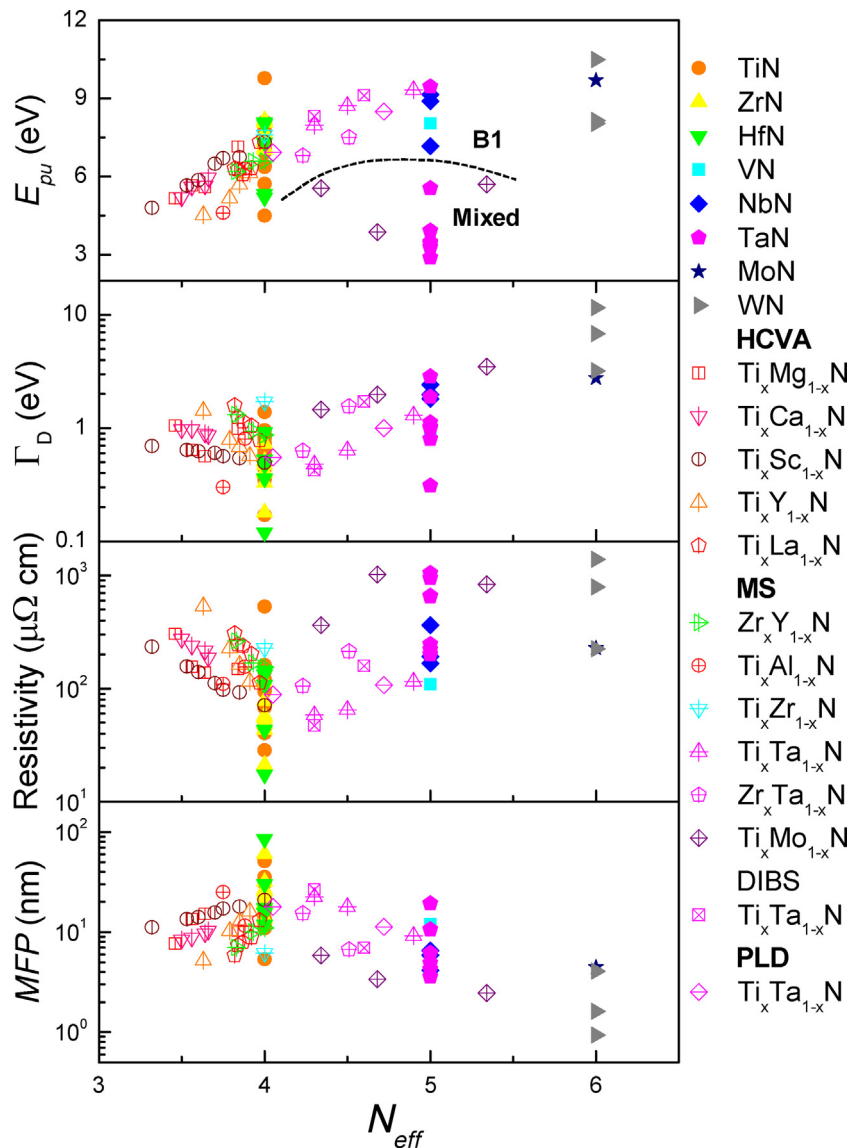


Fig. 29. E_{pu} , Γ_D , resistivity, and MFP vs. the effective number of valence electrons of the constituent metals (N_{eff}). Solid and open symbols represent binary and ternary TMN, respectively.

nitrides is observed unequivocally proving the superior character of group IVb nitrides (TiN, ZrN, HfN) as plasmonic materials. Among them, the maximum Q_{SPP} is observed for HfN, while the dielectric functions of more ZrN sample result in high Q_{SPP} values, therefore, suggesting ZrN being the best plasmonic TMN taking into account the statistical significance of the measurements, as well. It seems that TiN is the worse among the three, albeit being the most widely studied so far. In addition, optimal Q_{SPP} are observed for epitaxial and/or ultra-thin samples. Similar trends can be identified for Q_{LSPR} in Fig. 33, as well, albeit with less contrasting differences among the Q_{LSPR} values of various binary TMN, suggesting that for LSPR applications, the range of viable plasmonic TMN can be wider.

Regarding the ternary TMN, the observed Q_{SPP} (Fig. 32) and Q_{LSPR} (Fig. 34) are optimal for $Ti_xTa_{1-x}N$ and $Ti_xSc_{1-x}N$ compared to $Zr_xTa_{1-x}N$ and $Ti_xMg_{1-x}N$. The inferior Q_{SPP} and Q_{LSPR} for $Zr_xTa_{1-x}N$ compared to $Ti_xTa_{1-x}N$ confirms the previous discussion that although ZrN emerges as the most efficient plasmonic conductor on its own merit, it is a poor basis for alloying, possibly due to its long lattice cell size and the subsequent high lattice mismatch with the rest of TMN. However, this observation lacks statistical

significance, as it is based on very few samples, and its general validity should be into scrutiny. Regarding the comparison between $Ti_xSc_{1-x}N$ and $Ti_xMg_{1-x}N$, the superior performance of the former is attributed to the stability of the B1-ScN as alloying element and the electronic compatibility of Ti (d^2s^2 valence electrons) and Sc (d^1s^2 valence electrons). However, given the abundance of Mg, in contrast to the shortage of Sc, it is worth dedicating efforts for the improvement of its growth and plasmonic performance in order to implement it industrially.

Overall, the reported ternary TMN exhibit Q_{SPP} and Q_{LSPR} values comparable to polycrystalline and optically poorer binary group IVb TMN. Given that there is no systematic study of the optical properties and dielectric function spectra of epitaxial ternary TMN in the literature, their actual potential as plasmonic materials cannot be firmly evaluated given that the polycrystalline ternary TMN are usually of inferior crystalline quality, as presented in Section 2.2.4 and depicted in Fig. 5, and thus their inferior plasmonic performance can originate from the higher density of structural defects [384,471]. Therefore, a more systematic, experimental study of the optical properties of epitaxial ternary nitrides is of paramount importance in the field of alternative plasmonic materials.

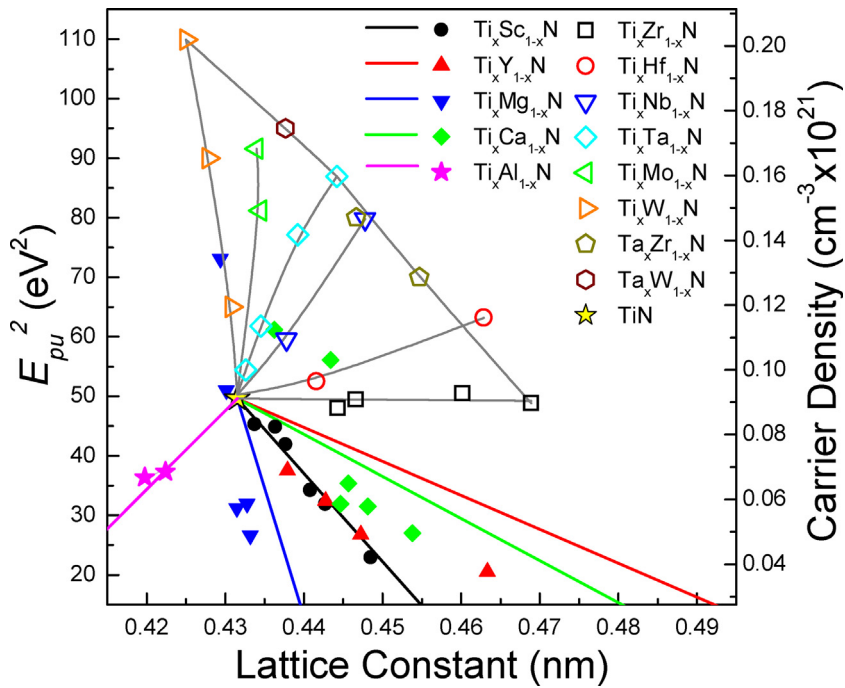


Fig. 30. The phase space of E_{pu}^2 , which is proportional to the carrier (conduction electron) density, vs. the nitride's lattice constant for the cubic B1 structure. Solid symbols represent the values of the systems with $N_{eff} < 4$ studied in Refs. [471] and [453], while open symbols are for $N_{eff} \geq 4$ from Ref. [184]. Grey lines are guides to the eye, while colored straight lines connect the values for TiN with the calculated values of the corresponding binary nitride (B1-AlN, B1-ScN, etc).

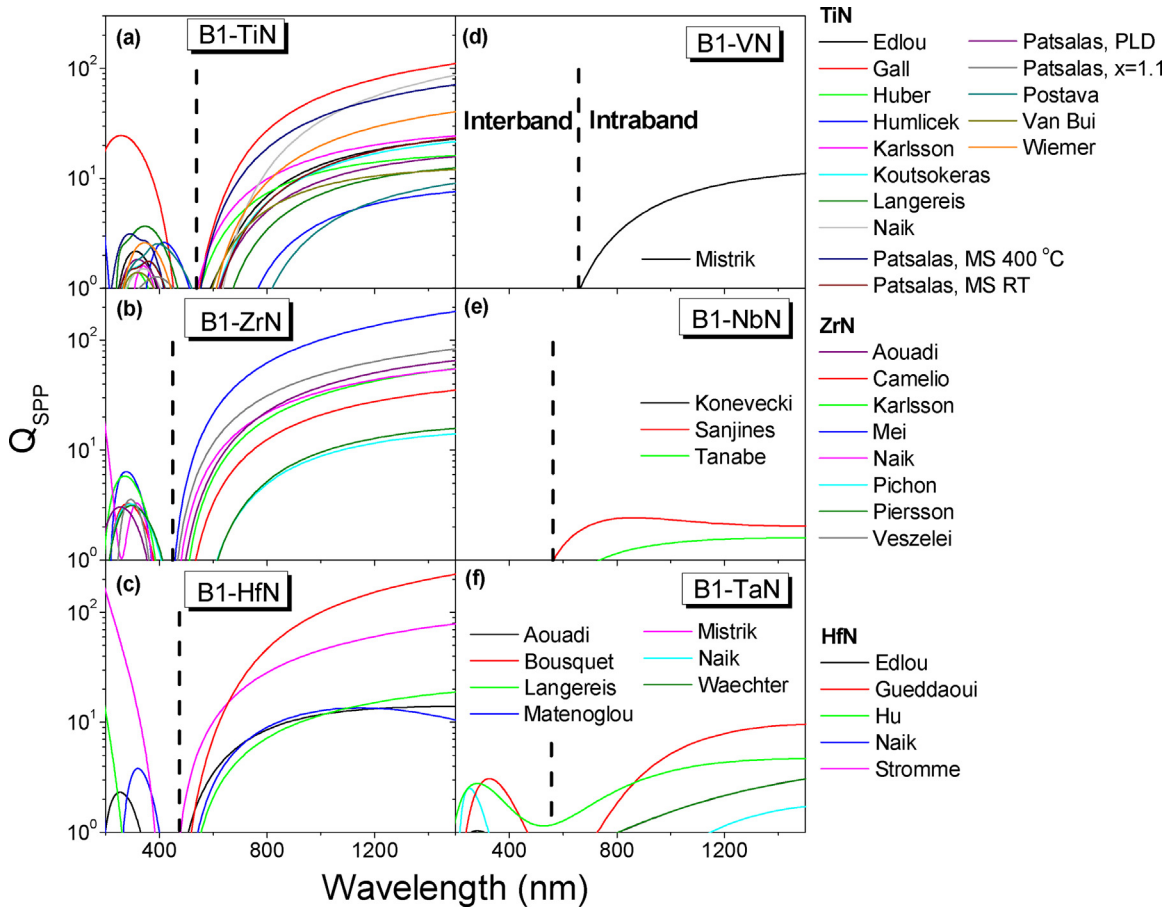


Fig. 31. Q_{SPP} at the interface of binary TMN/SiO₂ vs. the wavelength of incoming light calculated using Eq. (14).

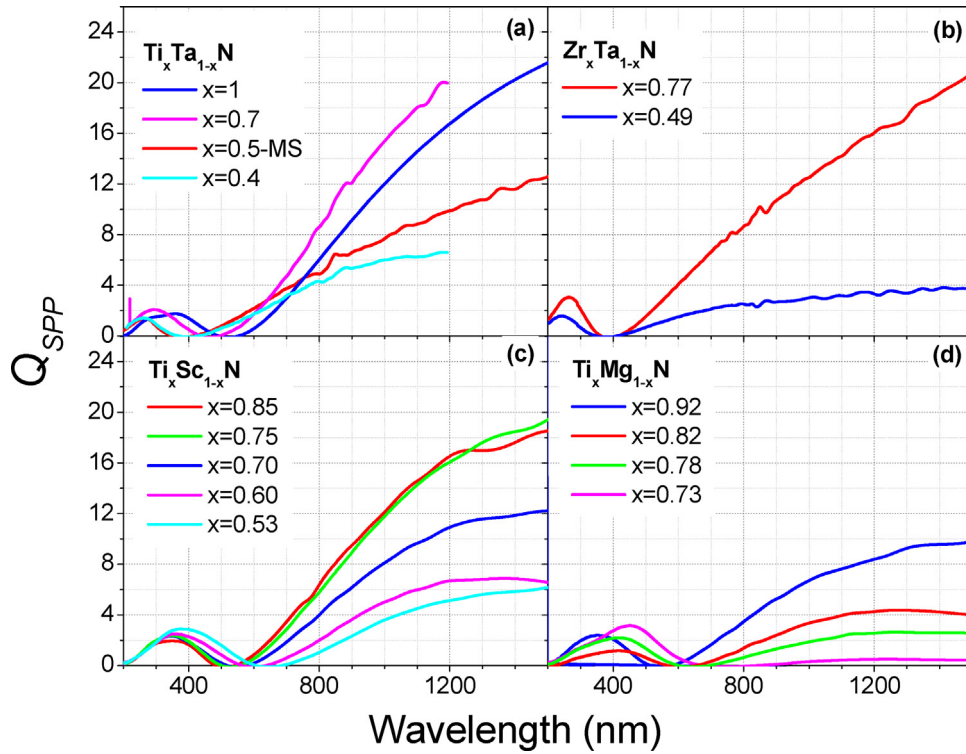


Fig. 32. Q_{SPP} at the interface of representative ternary TMN/SiO₂ vs. the wavelength of incoming light calculated using Eq. (14).

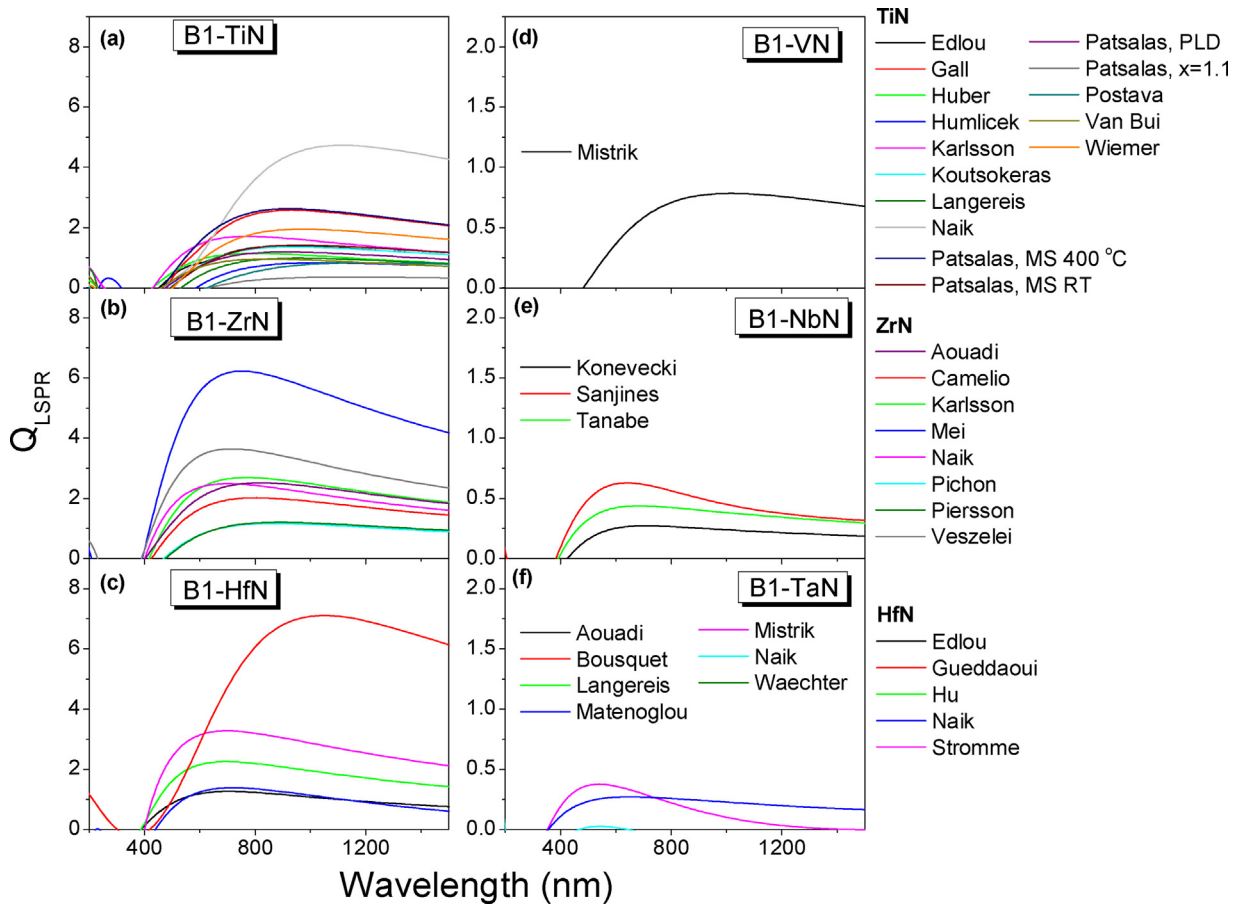


Fig. 33. Q_{LSPR} of binary TMN in air vs. the wavelength of incoming light calculated using Eq. (15).

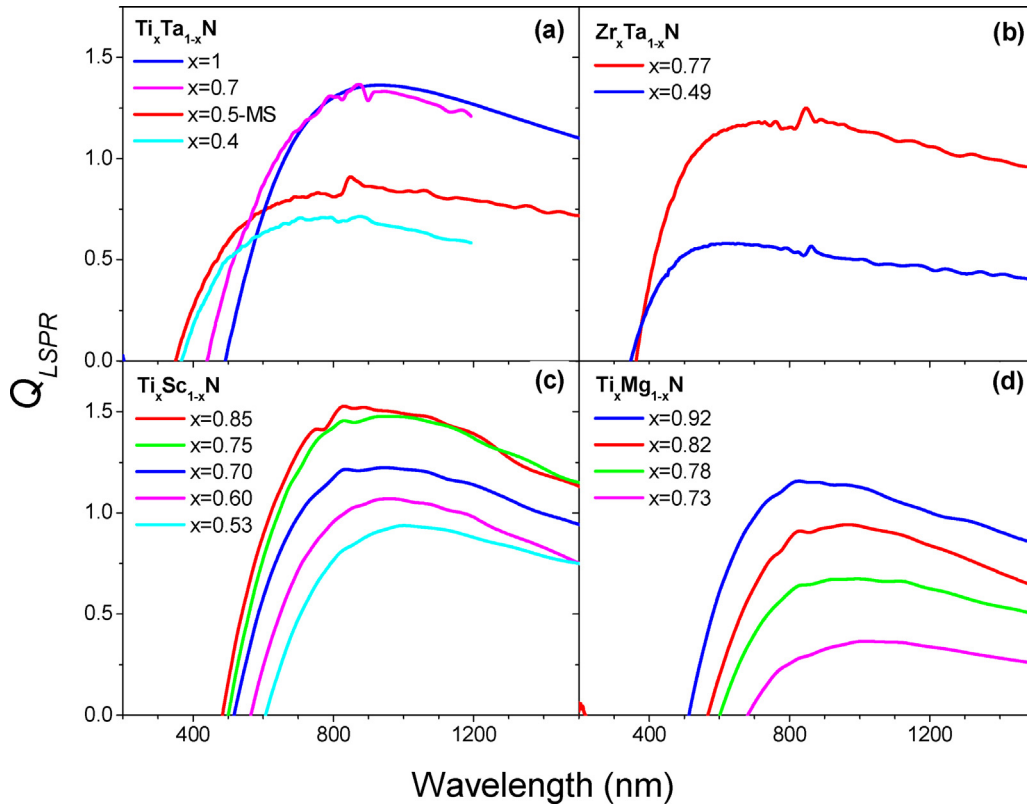


Fig. 34. Q_{LSPR} of representative ternary TMN in air vs. the wavelength of incoming light calculated using Eq. (15).

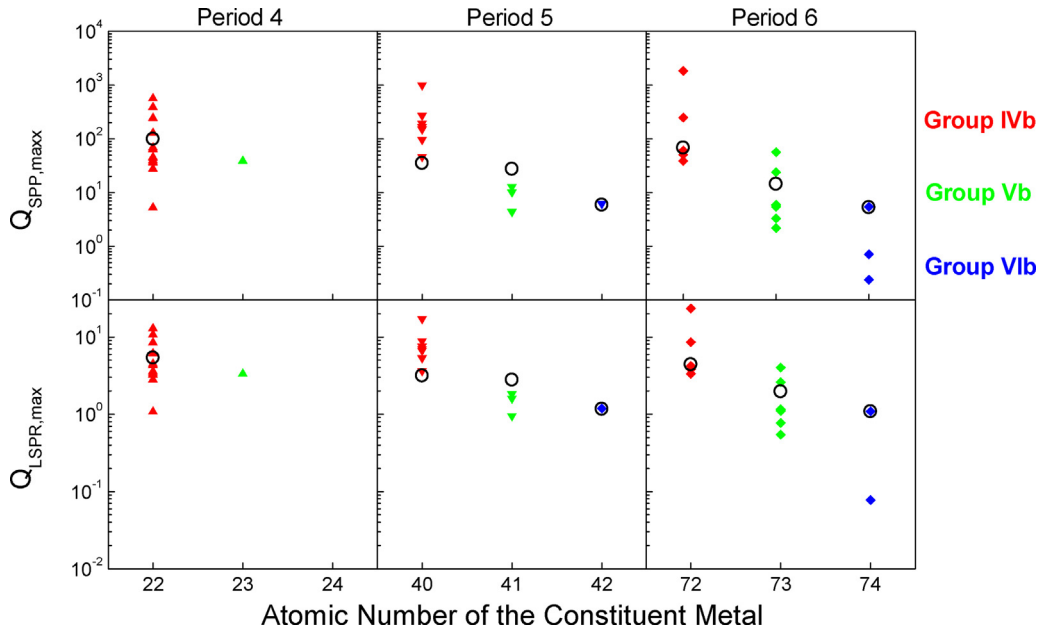


Fig. 35. The maximum quality factors $Q_{SPP,max}$ and $Q_{LSPR,max}$ calculated using Eqs. (16), (17), vs. the atomic number of the constituent metal of binary TMN. Open circles correspond to a set of binary TMN grown using identical PLD conditions in Ref. [184]. Note that $Q_{SPP,max}$ and $Q_{LSPR,max}$ are not manifested at the same wavelength for all TMN.

A more quantitative picture of the plasmonic performance of TMN can be drawn from the maximum values of the quality factors $Q_{SPP,max}$ and $Q_{LSPR,max}$ for SPP and LSPR, respectively [588]. Under quasistatic conditions, *i.e.* where the feature size of a given plasmonic system is far smaller than the wavelength of the incoming light, which should be actually the case for any TMN due to their short *MFP* values (see Fig. 29) as we will discuss in more detail below, and for the case of minimum electron loss, *i.e.* for

minimum ϵ_2 which occurs at the spectral vicinity of λ_{ps} as it is demonstrated in Figs. 19, 20 and 27, 28, $Q_{SPP,max}$ and $Q_{LSPR,max}$ can be expressed exclusively in terms of the E_{pu} and Γ_D parameters [588]:

$$Q_{SPP,max} = \frac{E_{pu}^2}{2\Gamma_D^2}, \quad (16)$$

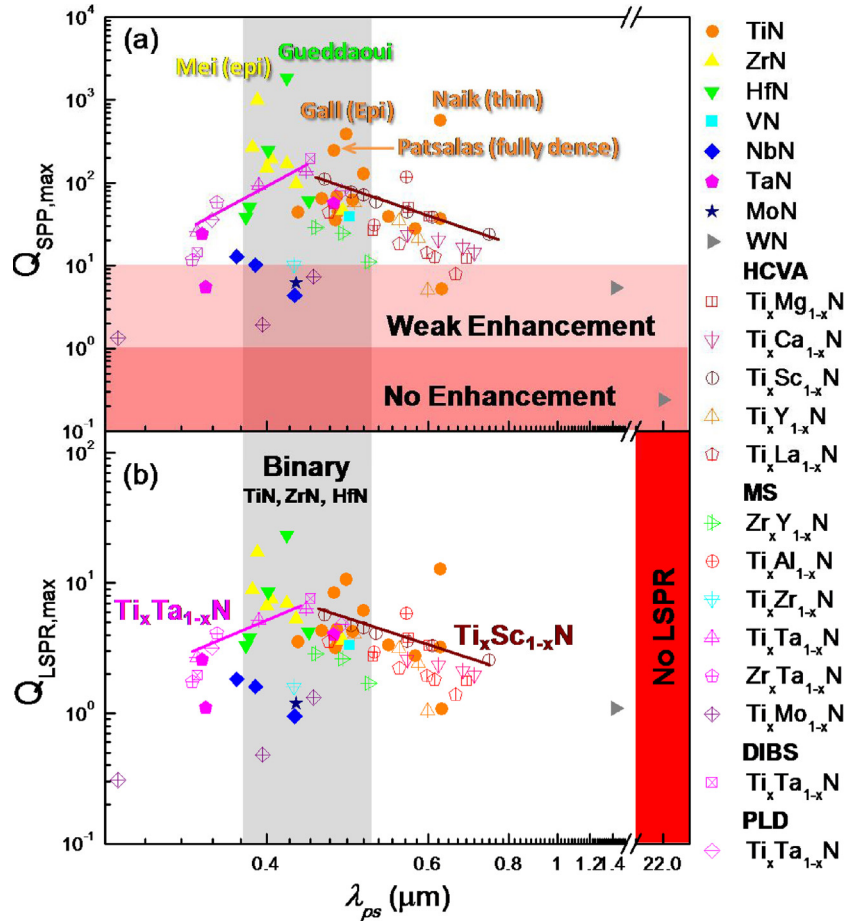


Fig. 36. The correlation of $Q_{SPP,max}$ and $Q_{LSPR,max}$ values vs. λ_{ps} for binary (solid points) and ternary (open points) TMN. Optimal values are observed for group IVb TMN (TiN, ZrN, HfN) in epitaxial, fully dense and/or ultrathin forms, which however operate in the narrow λ_{ps} window of 390–510 nm. Extending towards UV or infrared comes in expense of reducing $Q_{SPP,max}$ and $Q_{LSPR,max}$ values. The magenta and wine lines indicate the candidate TMN with the optimal $Q_{SPP,max}$ and $Q_{LSPR,max}$ values towards UV and infrared, which are $Ti_xTa_{1-x}N$ and $Ti_xSc_{1-x}N$, respectively.

$$Q_{LSPR,max} = \frac{(E_{pu}^2 - \Gamma_D^2)_{\omega_{sp}}}{3\sqrt{3}\Gamma_D^2 E_{pu}^2} \quad (17)$$

First we correlate the $Q_{SPP,max}$ and $Q_{LSPR,max}$ with the atomic number of the constituent metal of binary TMN (Fig. 35) in an effort to identify the intrinsic plasmonic potential of TMN due to their electronic structure. As there is substantial scattering of data for all TMN, we demonstrate with open circles the $Q_{SPP,max}$ and $Q_{LSPR,max}$ values of a set of binary TMN grown by PLD using identical conditions [184] in order to be directly comparable to each other.

The $Q_{SPP,max}$ and $Q_{LSPR,max}$ of group IVb TMN are superior to the rest of the considered nitrides and similar to each other. ZrN and HfN are quite more effective than TiN for SPP, while their differences for LSPR are less pronounced. With increasing group number (and consequently increasing density of conduction electrons, as well) $Q_{SPP,max}$ and $Q_{LSPR,max}$ are substantially, and very reasonably, reduced. Having said that, we should take into account that this is not the complete story, as the reduced quality of a plasmonic resonance may be accompanied by the benefit of a substantial spectral shift. So the most complete view can emerge by correlating $Q_{SPP,max}$ and $Q_{LSPR,max}$ values with the λ_{ps} , at whose spectral vicinity the plasmonic resonances are expected to occur; such a correlation for all the considered binary and ternary TMN of this work is presented in Fig. 36.

In Fig. 36, it is revealed that the optimal $Q_{SPP,max}$ and $Q_{LSPR,max}$ values are for group IVb TMN (TiN, ZrN, HfN) in epitaxial, fully dense and/or ultrathin forms, which however operate in the narrow

λ_{ps} window of 390–510 nm (grey shade in Fig. 36). ZrN and HfN combine stronger resonances at shorter wavelengths compared to TiN. The rest of the binary nitrides exhibit inferior $Q_{SPP,max}$ and $Q_{LSPR,max}$ values compared to both TiN–ZrN–HfN and Ti-based ternary nitrides operating at the same λ_{ps} . In particular, group VIb nitrides (MoN and WN) exhibit very poor $Q_{SPP,max}$ and $Q_{LSPR,max}$ values rendering them quite inappropriate for plasmonic applications, as they exhibit either no plasmonic enhancement at all ($Q < 1$) or very weak enhancement ($1 < Q < 10$). Especially the very lossy WN does not exhibit an LSPR at all ($Q_{LSPR,max}$ is not a real number).

There is also a general trend of reducing $Q_{SPP,max}$ and $Q_{LSPR,max}$ when extending λ_{ps} towards UV and infrared. For the extension towards infrared, the best performing candidate is $Ti_xSc_{1-x}N$, which is the most stable among the candidate ternary nitrides [439,441] and consequently is expected to have the less structural defects (be reminded that no binary nitride can extend its maximum resonance to infrared). This reduction comes mostly for physical reasons, *i.e.* the less conduction electrons result in weaker resonance. This is more prominent for $Q_{SPP,max}$, where E_{pu}^2 (which is proportional to the conduction electron density) is the numerator. However, some moderate improvement of the quality factors of $Ti_xSc_{1-x}N$ can be achieved by epitaxial growth that minimizes the structural defects and Γ_D [441].

There is a similar picture of reducing $Q_{SPP,max}$ and $Q_{LSPR,max}$ when extending λ_{ps} towards UV, albeit for all different reasons. Indeed, reducing λ_{ps} is accompanied by increasing N_{eff} , which result in intrinsic enhancement of Γ_D , for both binary and ternary TMN as it

is shown by the *ab initio* calculations presented in Figs. 15 and 18, respectively. Adding to that the inferior crystalline quality of group Vb nitrides compared to IVb nitrides [439] and the degrading crystallinity of ternary nitrides by enriching with a group Vb element [384], as presented in Fig. 5, explains this behavior. Therefore, the reducing $Q_{SPP,max}$ and $Q_{LSPR,max}$ in the UV range, either for NbN, TaN or $Ti_xTa_{1-x}N$ come due to increased Γ_D in contrast to the infrared range, where they are degrading due to reduced E_{pu} .

Any enhancement, either in the UV or infrared ranges, can be achieved by improving the crystalline quality of nitrides for plasmonics. In particular, the presented results clearly indicate that $Ti_xTa_{1-x}N$ performs better than NbN and TaN, suggesting that the addition of Ti into TaN stabilizes the B1 structure and reduce the structural defects affecting Γ_D . Further enhancement unequivocally calls for the epitaxial growth of such nitrides (VN, NbN, TaN, $Ti_xTa_{1-x}N$ and $Ti_xSc_{1-x}N$) at high temperature and on lattice-matched dielectric substrates. The study of the optical properties of such epitaxial TMN by an accurate and straightforward technique such as spectroscopic ellipsometry, which is still missing in the literature, will clarify their actual potential for realistic plasmonic applications. Finally, the variation of $Q_{LSPR,max}$ values among various TMN is less than $Q_{SPP,max}$ suggesting that for LSPR applications the selection of nitride might be less critical than for SPP applications, and other assets than quality factor such as spectral operation, work function, lattice size (for heteroepitaxy) and melting point may become prevalent.

The $Q_{SPP,max}$ and $Q_{LSPR,max}$ values of all the considered ternary nitrides are orders of magnitude inferior to the values reported for Ag and Au [588]; however, the reported $Q_{SPP,max}$ and $Q_{LSPR,max}$ values for Ag and Au [588] refer to highly crystalline metals with grain size larger than 300 nm [524], while most of the studied nitride samples consist of ultrafine grains less than 20 nm long [439,441]. Therefore, a fair comparison would be to the Ag and Au of the same grain size; in that case, the ternary nitrides are still inferior but their plasmonic performance is comparable in the same order of magnitude to Au and Ag [439]. We will come back later to this issue. Likewise, Al might be a more efficient plasmonic material in the UV [148] than $Ti_xTa_{1-x}N$, but this is accompanied by its tendency to oxidize fast [148] and its low melting point, two major drawbacks for realistic applications, especially when high photon fluxes are necessary [183]. Thus, $Ti_xTa_{1-x}N$ is emerging as a viable and stable candidate for UV plasmonics.

3.2. SPP performance at TMN/dielectric interfaces

The $Q_{SPP,max}$ and $Q_{LSPR,max}$ as expressed in Eqs. (16) and (17) and as displayed in Fig. 36 vs. λ_{ps} provide an indication of the intrinsic plasmonic properties of the conductor as it based on quantities associated with bulk plasmons into the corresponding conductors, but cannot describe entirely and accurately the SPP and LSPR phenomena as they neglect the contribution of the adjacent dielectric (especially for SPP that occurs at conductor dielectric interfaces when illuminated via the dielectric) and of the geometry of the device (e.g. size and shape of nanoparticles for LSPR). Therefore, a more realistic view of the potential of TMN for SPP applications can be extracted from the dispersion relation that correlates the frequency ω with the wave vector k_x in the direction of propagation of SPP, in such a configuration, i.e. along a conductor/dielectric interface. The general equation that defines the aforementioned relation is the following [1]:

$$k_x = \frac{\omega}{c} \sqrt{\frac{\tilde{\epsilon}_{TMN} \cdot \tilde{\epsilon}_d}{\tilde{\epsilon}_{TMN} + \tilde{\epsilon}_d}} \quad (18)$$

where $\tilde{\epsilon}_{TMN}$ and $\tilde{\epsilon}_d$ are the complex dielectric functions of the TMN and the dielectric, respectively. Given that the dielectric functions are inherently complex, Eq. (18) should be modified to:

$$k_x = \frac{\omega}{c} \text{Re} \left(\sqrt{\frac{\tilde{\epsilon}_{TMN} \cdot \tilde{\epsilon}_d}{\tilde{\epsilon}_{TMN} + \tilde{\epsilon}_d}} \right), \quad (19)$$

when optical attenuation in the conductor exists; this is very important for the conductive nitrides, due to their strong electron losses. A more convenient way of writing the dispersion relation in order to be more easily compared to the experiments is:

$$\hbar k_{xc} = \hbar \omega \cdot \text{Re} \left(\sqrt{\frac{\tilde{\epsilon}_{TMN} \cdot \tilde{\epsilon}_d}{\tilde{\epsilon}_{TMN} + \tilde{\epsilon}_d}} \right). \quad (20)$$

Fig. 37 presents the case study of calculated (via Eq. (20)) SPP dispersion relations at the interfaces between w-AlN and (a) TiN and the TiN-based ternaries that exhibit the optimal $Q_{SPP,max}$, and (b) group IVb TMN (TiN, ZrN, HfN). w-AlN was selected for this case study as a dielectric material with very wide range of transparency (see Fig. 38) and an almost constant refractive index and dielectric function in the entire range of plasmonic operation of TiN, ZrN, HfN, and TiN-based ternary TMN; in addition, w-AlN is a proven effective dielectric for SPP devices [589] and can be structurally compatible with TMN as w-AlN[0002]/TMN[111] can be grown pseudoepitaxially, similar to GaN[0002]/TMN[111], which is reported in Ref. [224] and shown in Fig. 2b.

The first significant observation is that in all cases the dispersion relations are characteristic of lossy metals and, therefore, involve finite extreme values of k_x [1] due to conduction electron (due to finite Γ_D values of all ternary nitrides) and dielectric (due to the existence of interband transitions) losses. The consequence of this observation is the existence of quasi-bound modes at which the slope of the dispersion curve is inverted and the existence of a cross-over energy at which the SPP dispersion curve crosses the photon line (black straight lines). The maximum $\hbar k_{xc,max}$ below the light line defines the resonance point, which occurs for incoming light with the corresponding photon energy (Y-axis in Fig. 37). It is evident from Fig. 37a that by varying the microstructure and/or stoichiometry of TiN, SPP resonances in the light range of 1.6–2.3 eV (775–539 nm) can be achieved (yellow region in Fig. 37a). In order to probe effectively resonances beyond this range to either directions, TiN should be alloyed either with TaN or ScN to form $Ti_xTa_{1-x}N$ and $Ti_xSc_{1-x}N$, respectively. Thus, SPP resonances up to 2.57 eV (482 nm), represented by the blue region in Fig. 37a, or down to 1.19 eV (1042 nm) represented by the grey region in Fig. 37a, can take place.

On the other hand, comparing TiN with ZrN and HfN (Fig. 37b) reveals that these three nitrides can sustain resonances in an overlapping range (yellow region in Fig. 37b); ZrN's resonances extend slightly towards blue (yellow region in Fig. 37b), but still not as far as $Ti_xTa_{1-x}N$'s. This similarity is a consequence of their similar E_{pu} values as we have shown in Fig. 29. Their major difference is the maximum $\hbar k_{xc,max}$ that is 5.5, 7.5 and 7 eV for TiN, HfN, and ZrN, respectively, and represented by light, intermediate and dark grey regions in Fig. 37b. This behavior is attributed to the gradually less dielectric losses of TiN, HfN, and ZrN as revealed by the comparison of their dielectric function spectra in Fig. 21. As a result, an SPP at the resonance point on a ZrN/w-AlN interface will have shorter wavelength than on a TiN/w-AlN interface making ZrN more appropriate for sub-wavelength optics. The less losses for ZrN compared to TiN also result in longer propagation lengths L_{SPP} , which may be given by [590]:

$$L_{SPP} = \lambda_{light} \cdot \frac{\epsilon_{1,TMN}^2}{2\pi \cdot \epsilon_{2,TMN}} \cdot \left(\sqrt{\frac{\epsilon_{1,TMN} + \epsilon_{1,d}}{\epsilon_{1,TMN} \cdot \epsilon_{1,d}}} \right)^3 \quad (21)$$

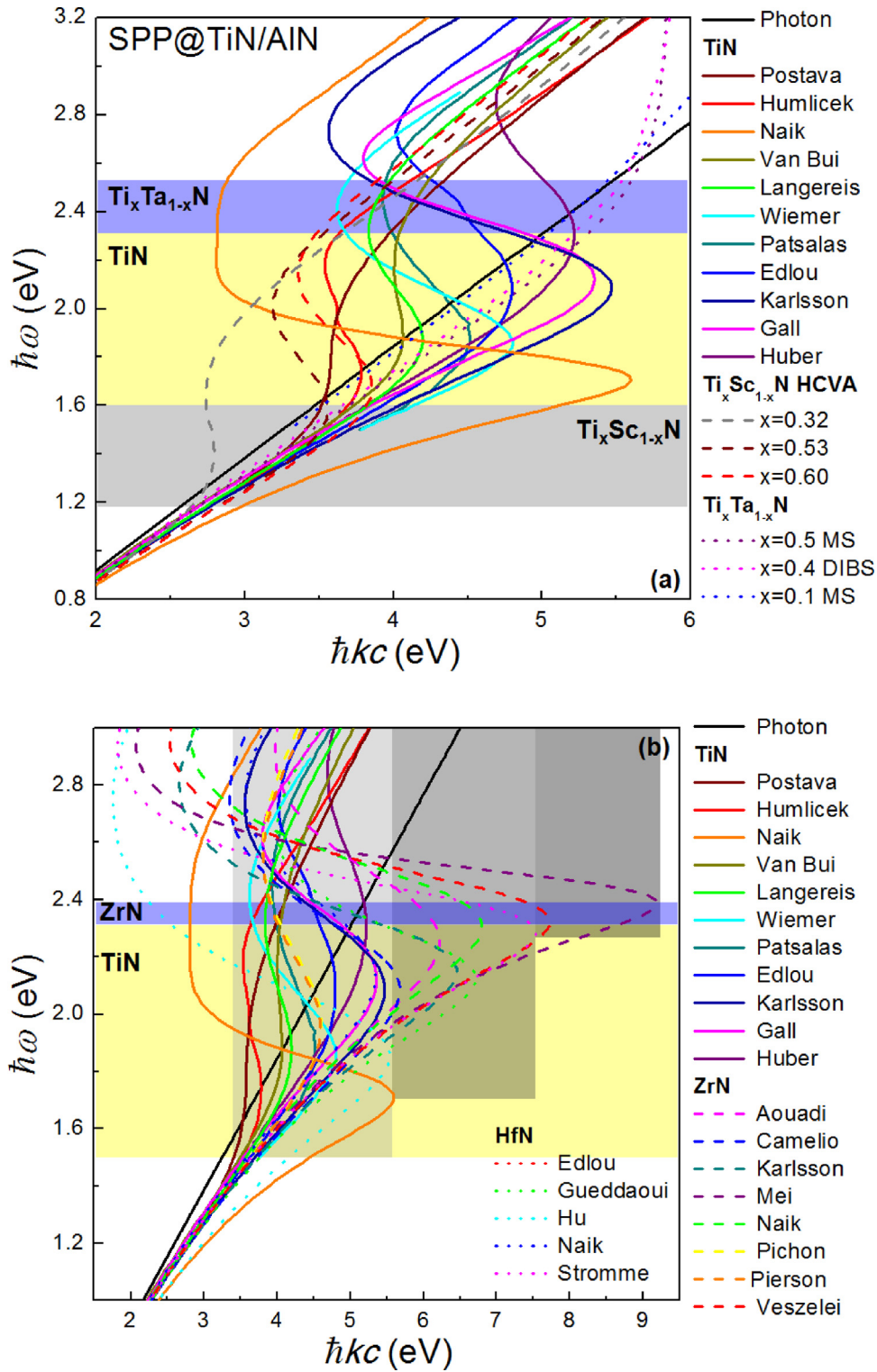


Fig. 37. SPP dispersion relations for (a) TiN and the TiN-based ternaries that exhibit the optimal $Q_{SPP,max}$, and (b) group IVb TMN (TiN, ZrN, HfN) in contact with a w-AlN dielectric.

For example, for the usual telecom wavelength of $\lambda_{light} = 1350$ nm, the propagation wavelength of SPP for TiN and ZrN is $2.5 \mu\text{m}$ and $6 \mu\text{m}$, respectively; both are exceptionally short and this should be taken into account in any device design.

Of special importance for a variety of applications, predominantly for telecommunications [441] and for biosensing [591], as well, are plasmonic devices operating in the near infrared range (700–1600 nm). This spectral range is overlapping and adjacent to

the wide range of transparency of most inorganic dielectrics and semiconductors spanning from 1100 to 5500 nm [592–595], as shown in Fig. 38 where the refractive index spectra of the most popular dielectrics and semiconductors reported in Ref. [592–597] are summarized. The combined 700–5500 nm near infrared range includes the well known biological window (where tissues, blood, and fat are transparent [591]) and the telecom window, which includes the 850, 1300/1550 nm bands used in fiber-optics and Si

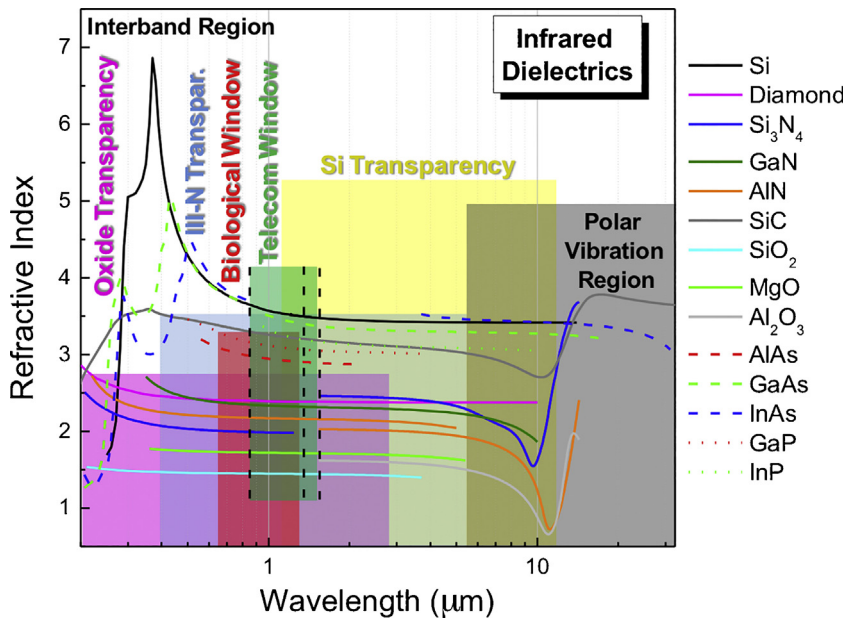


Fig. 38. Refractive index spectra of the most common inorganic dielectrics and semiconductors. Polar compounds are not transparent for wavelengths longer than 5500 nm due to polarity vibrations. A wide part of this range (1155–5500 nm and beyond) is covered by Si, for shorter wavelengths transparent dielectrics include nitrides (down to 200 nm for w-AlN) and oxides (MgO, quartz and sapphire being transparent below 200 nm). The biological and telecom windows are indicated by red and green shadows respectively. The most common telecom bands (850, 1300, 1550 nm) are also indicated by vertical dashed black lines. (For interpretation of the references to colour in this figure legend, the reader is referred to the web version of this article.)

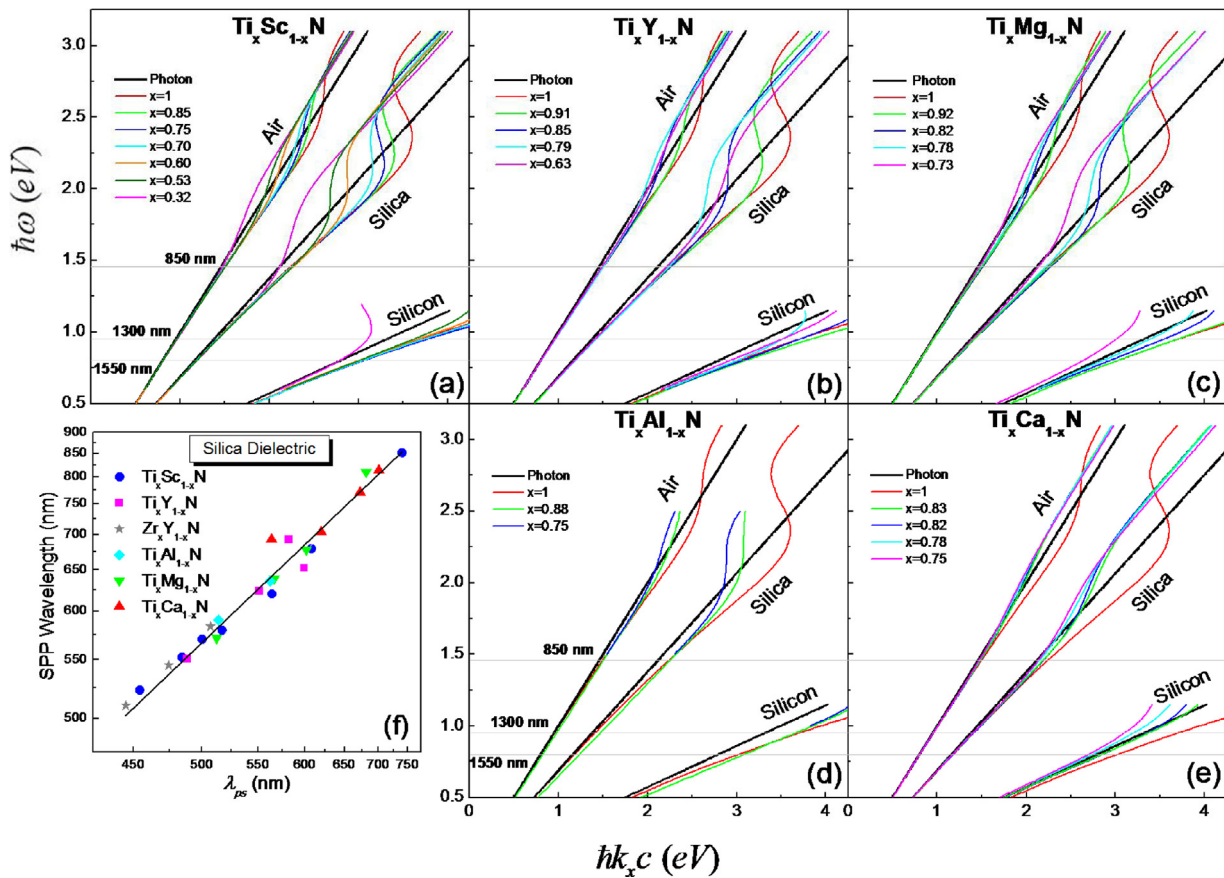


Fig. 39. SPP dispersion relations at the nitride/dielectric interfaces for air and the two most widely used dielectrics in telecom technologies, i.e. silica and silicon for: (a) $Ti_xSc_{1-x}N$, (b) $Ti_xY_{1-x}N$, (c) $Ti_xMg_{1-x}N$ (d) $Ti_xAl_{1-x}N$, and (e) $Ti_xCa_{1-x}N$; the black lines are the dispersion relations of the light into the dielectrics; horizontal grey lines indicate the three bands used for telecommunications with today’s technology. (f) The scaling of the free space wavelength of light at SPP, which corresponds to the maximum $\hbar k_x c_{max}$, with λ_{ps} .

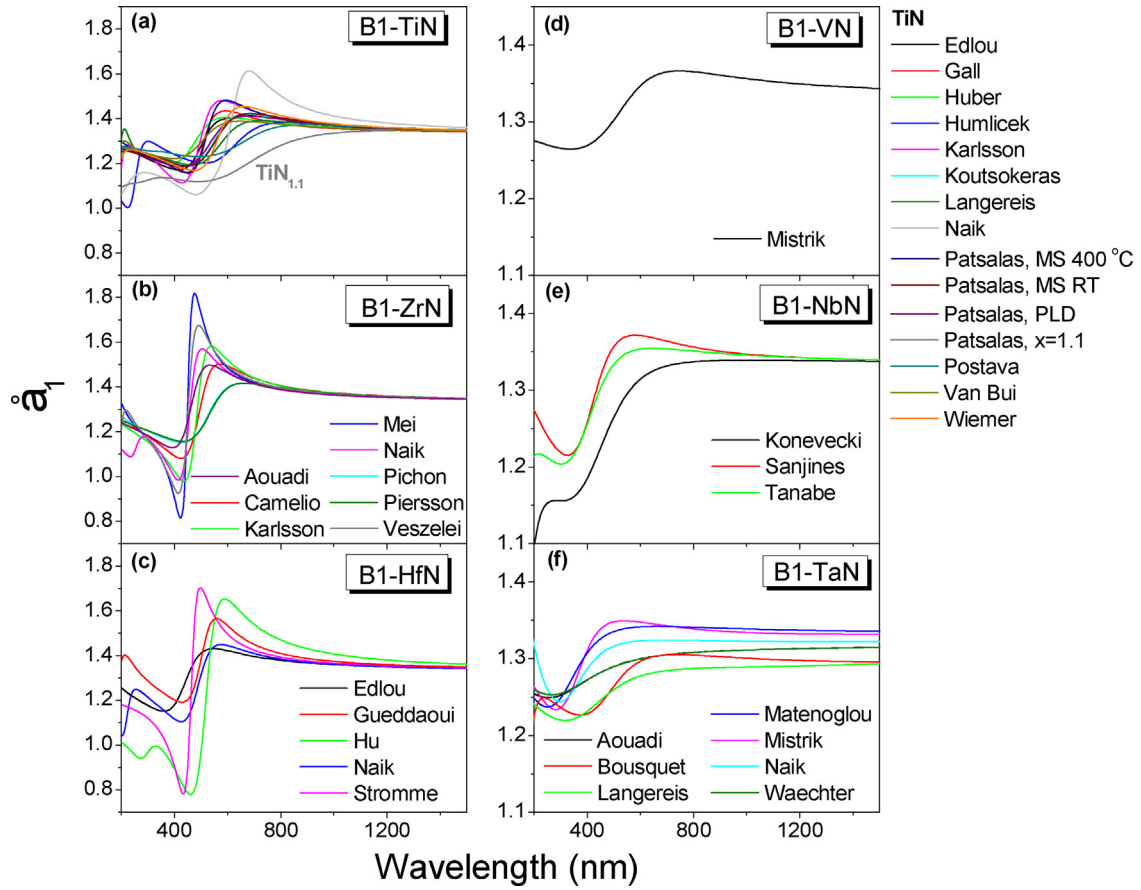


Fig. 40. Spectra of the real part of the dielectric function (ϵ_1) of spherical nanoparticles of various binary TMNs with filling ratio 10% vol in air calculated by MG-EMA.

telecoms, respectively [598]. Therefore, materials that can sustain plasmonic resonances in this range are technologically essential.

As a second case study we evaluate the SPP performance of ternary TMN with $N_{eff} < 4$ in contact with SiO_2 or Si, in order to investigate their suitability for telecom applications [441]. Fig. 39 presents the calculated (via Eq. (20)) SPP dispersion relations at the interfaces between air, silica or silicon and (a) $\text{Ti}_x\text{Sc}_{1-x}\text{N}$, (b) $\text{Ti}_x\text{Y}_{1-x}\text{N}$, (c) $\text{Ti}_x\text{Mg}_{1-x}\text{N}$, (d) $\text{Ti}_x\text{Al}_{1-x}\text{N}$, and (e) $\text{Ti}_x\text{Ca}_{1-x}\text{N}$, respectively. Note that the calculation for silicon was performed only for the transparent region, i.e. for photon energies in free space below the band gap of 1.112 eV (wavelength longer than 1115 nm), which lies exclusively in the infrared spectral range. All nitrides of this category behave like lossy conductors as their counterparts presented in Fig. 37. The photon energy that corresponds to the maximum $\hbar k_{xc,max}$, which defines the SPP point, is scaled to λ_{ps} for all the ternary nitrides in the infrared spectral range; this is clearly illustrated for the silica dielectric in Fig. 39f. However, these two quantities do not coincide and the wavelength of photons in free space that corresponds to $\hbar k_{xc,max}$ is longer than the wavelength λ_{ps} and fulfills the requirement for operation at 850 nm for silica fiber optics when $\text{Ti}_{0.32}\text{Sc}_{0.68}\text{N}$ is used, while $\text{Ti}_{0.73}\text{Mg}_{0.27}\text{N}$ and $\text{Ti}_{0.75}\text{Ca}_{0.25}\text{N}$ are also pretty close to fulfill this requirement possibly with a small further enrichment with Mg or Ca. Air can hardly sustain a SPP mode for all cases, while clear SPP is observed for silica albeit at shorter wavelengths than the 850 nm telecom band in most cases with the major exception of $\text{Ti}_x\text{Sc}_{1-x}\text{N}$.

The inability to meet the requirement of 850 nm wavelength is not a deficit of the experimental range reported in Ref. [441], but it is also due to physical limitations for various ternary conductive nitrides; for example further enrichment with Al or Y in order to extend the range of operation of $\text{Ti}_x\text{Al}_{1-x}\text{N}$ and $\text{Ti}_x\text{Y}_{1-x}\text{N}$ would

cause a phase transition from the B1 phase to pseudo-wurtzite [453] or further grain refinement due to the lattice mismatch between TiN and YN [471], respectively, while $\text{Ti}_x\text{Ca}_{1-x}\text{N}$ is characterized by inherent excessive electron loss [471]. The only family of conductive nitrides that can sustain a SPP for the silicon telecom bands (1300 nm and 1550 nm) is the Sc-rich $\text{Ti}_x\text{Sc}_{1-x}\text{N}$, while for the silica fiber band (850 nm) both $\text{Ti}_x\text{Sc}_{1-x}\text{N}$ and $\text{Ti}_x\text{Mg}_{1-x}\text{N}$ might be considered. The later is inferior in terms of the quality factor $Q_{SPP,max}$, as we have already discussed, but given the abundance of Mg, in contrast to the shortage of Sc, it is worth dedicating efforts for the improvement of its growth and plasmonic performance in order to implement it industrially.

3.3. LSPR performance of TMN nanoparticles

3.3.1. Far field properties

Having a massive volume of optical data for binary and ternary TMN may enable us to evaluate the expected LSPR performance of the hypothetical equivalent nanoparticles via the by Maxwell-Garnett Effective Medium Approximation (MG-EMA) [15]. Although MG-EMA is not as accurate as the exact Finite Difference Time Domain (FDTD) calculations and lacks the versatility of the later regarding the shape of nanoparticles or nanoantennas, it might provide a reasonable and effective preliminary comparison of the various binary and ternary nitrides. Otherwise, such a critical comparison would require an immense experimental effort in an unrealistic scale. Indeed, the far-field optical response of spherical TMN nanoparticle assemblies can be reasonably described by MG-EMA:

$$\frac{\tilde{\epsilon} - \tilde{\epsilon}_{TMN}}{\tilde{\epsilon} + 2\tilde{\epsilon}_{TMN}} = f_{TMN} \frac{\tilde{\epsilon}_{TMN} - \tilde{\epsilon}_d}{\tilde{\epsilon} + 2\tilde{\epsilon}_{TMN}}, \quad (22)$$

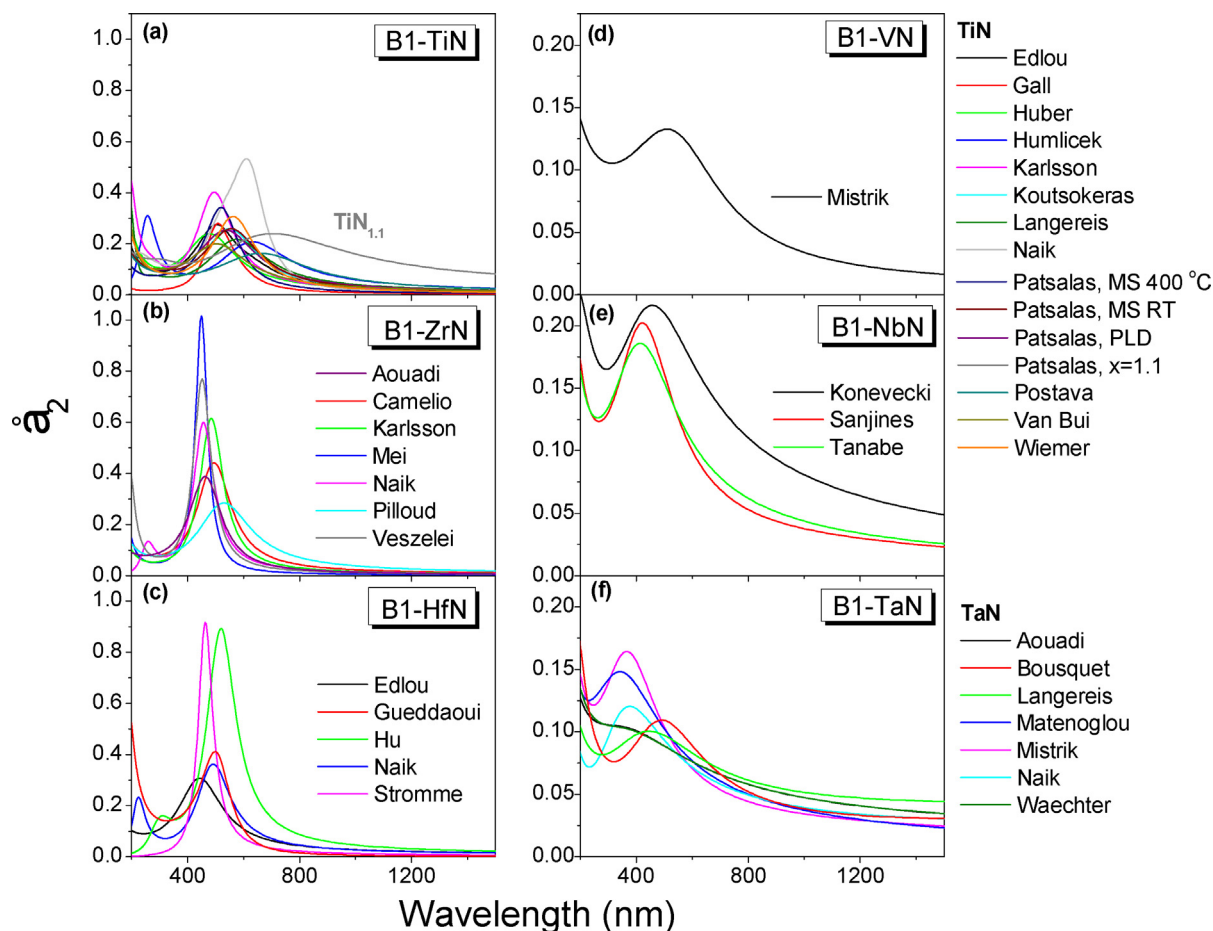


Fig. 41. Spectra of the real part of the dielectric function (ϵ_2) of spherical nanoparticles of various binary TMNs with filling ratio 10% vol in air calculated by MG-EMA.

which describes the effective complex dielectric function $\tilde{\epsilon}$ of a composite material consisting of a dielectric host (matrix) with complex dielectric function $\tilde{\epsilon}_d$ and isolated spherical inclusions of the secondary phase (TMN in our case) having complex dielectric function $\tilde{\epsilon}_{TMN}$ with a filling ratio f_{TMN} . The information of particle size is introduced via $\tilde{\epsilon}_{TMN}$ through the *MFP*, given that for small particles (up to 40 nm) these quantities are closely related [551].

As a case study we consider $\tilde{\epsilon}_d = 1$ assuming air as the host medium. The ϵ_1 and ϵ_2 spectra of binary TMN nanoparticle assemblies in air with filling ratio $f_{TMN} = 10\%$ vol calculated by MG-EMA are presented in Figs. 40 and 41, respectively. Note that MoN and WN are excluded from this comparison because of their poor $Q_{LSPR,max}$ values. The LSPR is spectrally located at the wavelength where the ϵ_2 of the nanoparticles gets the maximum value. Stronger and sharper resonances are observed for group IVb nitrides, and in particular for ZrN and HfN, which are also moderately blueshifted compared to the resonances for TiN; indeed, ZrN is emerging as the most efficient TMN for LSPR applications. Among group Vb nitrides, NbN exhibits by far the stronger and sharper resonances, which are comparable to medium-quality TiN, albeit substantially blueshifted.

The spectral position of the LSPR of TMN nanoparticles is scaled with the λ_{ps} of the opaque, continuous TMN films, as presented in Fig. 42. There is remarkable low scattering of the points with very few samples not following the linear trend. The solid line is a linear fit to the data, while the dashed line stands for $\lambda_{LSPR} = \lambda_{ps}$. The two lines are parallel and λ_{LSPR} is longer than λ_{ps} by 40 nm. This firm and quantitative scaling may provide a design tool for plasmonic devices based on TMN, especially for top-down fabrication, such as nanoimprint lithography combined with reactive ion etching of

continuous TMN films (whose λ_{ps} can be known before patterning) [599].

The asset of the refractory character and thermal stability of TMN comes with the liability of the growth of fine grains. Thus, the range of spectral tunability via tailoring of size of TMN nanostructures, which is common practice for Au and Ag nanostructures nanoantennas [600], is very limited. Indeed, in most cases of TMN the *MFP* is less than 40 nm and in exceptional cases of epitaxial nitrides may be as long as 100 nm (Fig. 29). Producing nanoantennas longer than the *MFP* of the nitride would not perform adequately and would not result in spectral plasmonic tunability. This drawback was recently addressed by introducing ternary TMN as tunable plasmonic materials [439].

MG-EMA calculations of the optical response of representative hypothetical nanoparticles of ternary nitrides in air with a filling ratio 10% vol are presented in Fig. 43. In particular, we present the ϵ_1 , ϵ_2 spectra of polycrystalline nanoparticles modelled by DIBS-grown $Ti_xTa_{1-x}N$ (Fig. 43a,b), and MS-grown $Ti_xTa_{1-x}N$ and $Ti_xAl_{1-x}N$ (Fig. 43c,d), and single-crystal nanoparticles modelled by epitaxial $Ti_xSc_{1-x}N$ (Fig. 43e,f) using the reference dielectric function spectra of opaque continuous $Ti_xTa_{1-x}N$ and $Ti_xAl_{1-x}N$ films presented in Fig. 27 and 28. For the later case (single-crystal $Ti_xSc_{1-x}N$) the reference dielectric function spectra were extracted by analyzing the optical reflectivity spectra presented in the inset of Fig. 43e and retrieved and reproduced from Ref. [469].

The λ_{LSPR} of all ternary TMN (not only those presented in Fig. 43) follows the scaling relation of their binary counterparts with λ_{ps} and extend the operational range towards UV (open magenta symbols standing for various types of $Ti_xTa_{1-x}N$) and towards infrared (open wine circles and open red squares standing for $Ti_xSc_{1-x}N$).

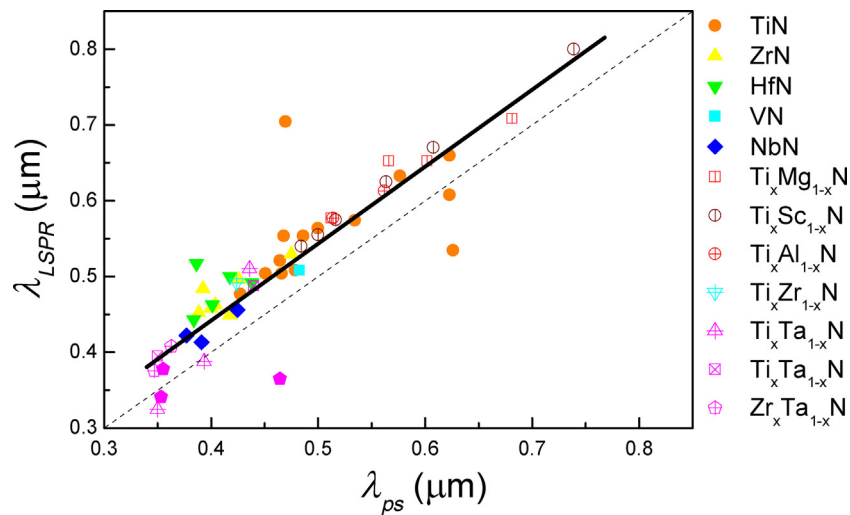


Fig. 42. Scaling of the wavelength of incoming light where LSPR occurs (λ_{LSPR}) with the λ_{ps} of the corresponding continuous nitride. The solid line is a linear fit to the data, while the dashed line stands for $\lambda_{LSPR} = \lambda_{ps}$.

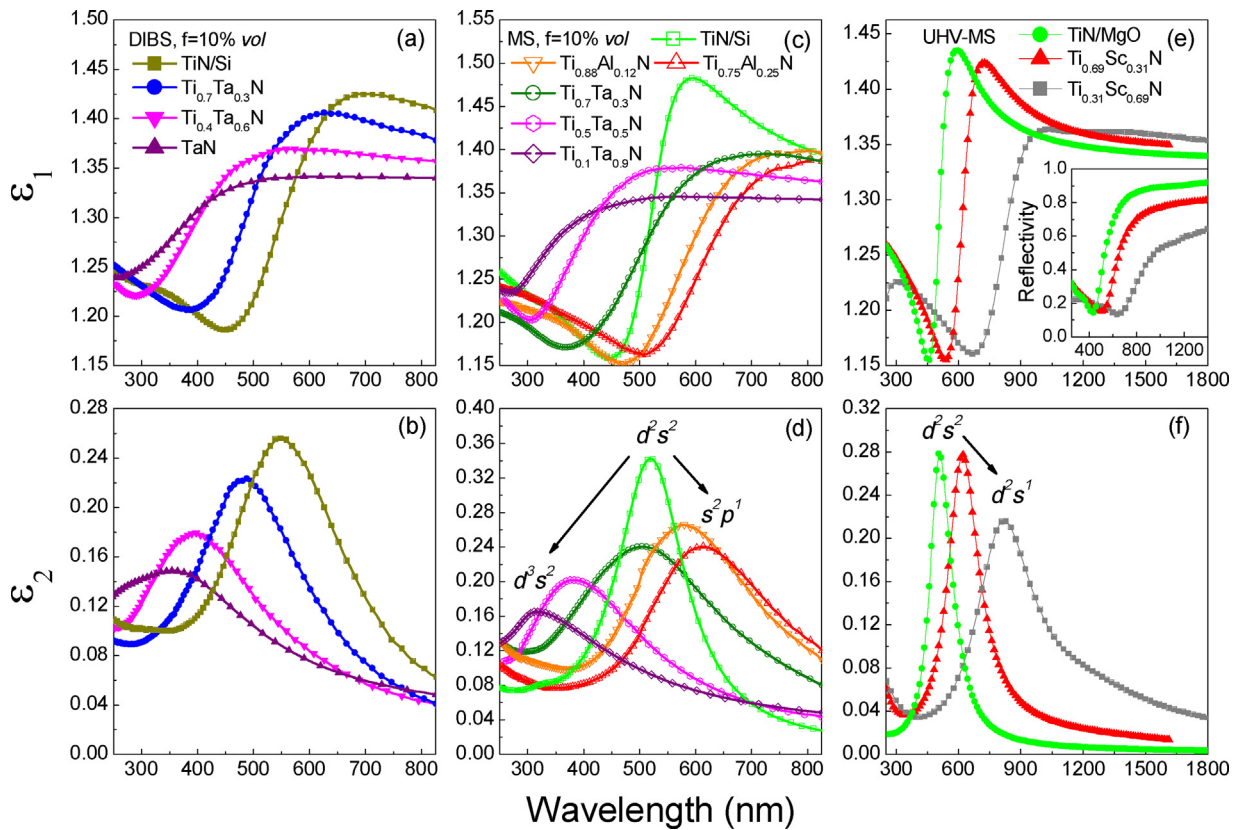


Fig. 43. ϵ_1 , ϵ_2 spectra of hypothetical polycrystalline nanoparticles determined by MG-EMA ($f_{TMN} = 10\%$ vol) using the reference dielectric functions of DIBS-grown $Ti_xTa_{1-x}N$ (a,b), MS-grown $Ti_xTa_{1-x}N$ and $Ti_xAl_{1-x}N$ (c,d), and of hypothetical single-crystal nanoparticles using the reference dielectric functions of epitaxial $Ti_xSc_{1-x}N$ (e,f). Inset shows the raw optical data for $Ti_xSc_{1-x}N$, as retrieved from Ref. [469], and the corresponding fit.

xN and $Ti_xMg_{1-x}N$, respectively). Given that λ_{ps} and E_{ps} are strongly correlated with the effective number N_{eff} of valence electrons of the constituent metals (Fig. 23), the importance of N_{eff} to the LSPR spectral location is indirectly revealed. Thus, when TiN is alloyed with TaN, which has substantially higher conduction electron density, to form $Ti_xTa_{1-x}N$ the LSPR wavelength is gradually blueshifted with increasing Ta content. On the contrary, when Al or Sc is incorporated into TiN to form $Ti_xAl_{1-x}N$ or $Ti_xSc_{1-x}N$ the conduction electron density is reduced and, consequently, the LSPR is redshifted. $Ti_xSc_{1-x}N$ exhibit sharper LSPR and spans deeper into

infrared than $Ti_xAl_{1-x}N$ due to the structural, electronic and chemical compatibility with TiN as we have already discussed. An additional asset of ternary TMN nanostructures, especially $Ti_xSc_{1-x}N$, which operates in the infrared range, is that can be spectrally tunable while retaining miniature size of a few tens of nm in contrast to noble metal nanoantennas [600] or nanoparticles [132], which require a feature size an order of magnitude larger, i.e. a few hundreds of nm, in order to exhibit resonances in the infrared. Therefore, $Ti_xSc_{1-x}N$ might be more efficient for miniature infrared plasmonic devices, thus turning the liability of fine grains into an asset.

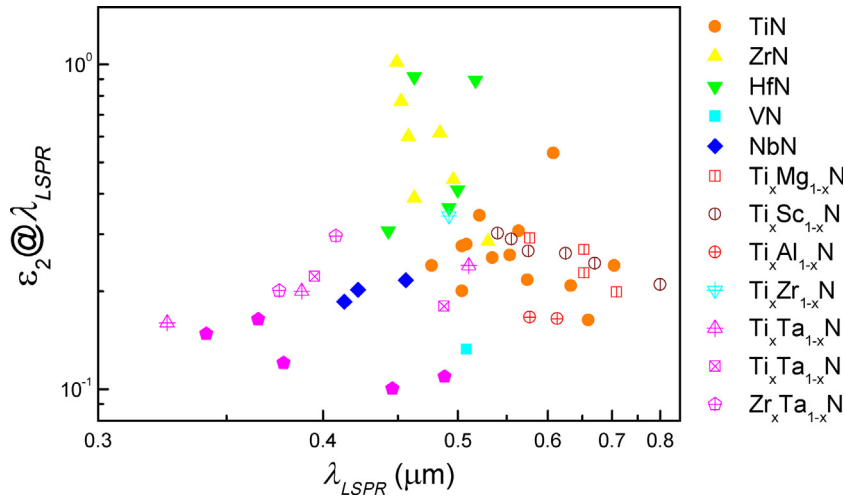


Fig. 44. The spectral position of the maximum strength of LSPR expressed as the value of ϵ_2 at the LSPR wavelength.

The strength of LSPR may be expressed by the actual ϵ_2 value at the resonance wavelength λ_{LSPR} (see Fig. 44). Maximum strength is achieved for ZrN and HfN among all the considered TMN, however, only in the narrow spectral window 450–510 nm. For longer wavelengths (510–560 nm) TiN provides the stronger resonance, albeit far weaker than those of ZrN and HfN; for further longer wavelengths (>560 nm) firstly $Ti_xSc_{1-x}N$ and secondarily $Ti_xMg_{1-x}N$ are the most efficient conductors for LSPR. On the opposite side, for wavelengths shorter than 450 nm, $Ti_xTa_{1-x}N$ is the best candidate, NbN exhibits intermediate performance (which is anticipated to improve, if NbN is grown epitaxially), and TaN's performance is very poor. As a partial conclusion, if the priority of a certain plasmonic device is the strength and sharpness of LSPR, then ZrN is the undisputed best choice. Else, if spectral selectivity was of importance, a range of TMN that include $Ti_xTa_{1-x}N$, ZrN, TiN, and $Ti_xSc_{1-x}N$ would be considered.

Another open question is whether stronger and/or sharper resonances can be achieved by single-crystalline TMN nanoparticles compared to the polycrystalline nanoparticles mostly considered so far. In order to clarify this point we considered the dielectric functions of hypothetical $Ti_xSc_{1-x}N$ nanoparticles of varying x calculated by MG-EMA using the reference dielectric functions of polycrystalline and epitaxial $Ti_xSc_{1-x}N$ films respectively [441]. From Fig. 45, it is evident that the polycrystalline $Ti_xSc_{1-x}N$ quite wider and a bit weaker resonances than the epitaxial $Ti_xSc_{1-x}N$. By comparing polycrystalline and epitaxial $Ti_xSc_{1-x}N$ samples with almost the same x values, we conclude that the use of epitaxial quality single-crystal nanoparticles exhibit sharper resonances, which are slightly redshifted with respect to those of the corresponding polycrystalline nanoparticles. This can be quantified by the Q -factor of the resonance [601]:

$$Q\text{-factor} = \lambda_{LSPR} / \Delta\lambda, \quad (23)$$

which should not be confused with Q_{LSPR} in Eq. (15); $\Delta\lambda$ is the bandwidth (full width at half maximum) of the resonance. The inset in Fig. 45 shows the variation of Q -factor of $Ti_xSc_{1-x}N$ nanoparticles, polycrystalline or of epitaxial quality, with the wavelength of LSPR. The epitaxial quality nanoparticles exhibit substantially higher Q -factor for all cases; however, Q -factor is reducing towards infrared even for the epitaxial quality nanoparticles due to reducing conduction electron density.

After this long story on the importance of TMN nanoparticles as plasmonic materials, we should provide a direct comparison with noble metals as a final assessment. A fair comparison would be among nanoparticles of the same size (radius) r . For ZrN and TiN we

accept the assumption $2r = MFP$ and we use for MG-EMA dielectric functions that correspond to samples with $MFP \sim 40$ nm. For Au and Ag, the appropriate dielectric functions of nanoparticles should include the surface scattering contribution in the free electron relaxation time τ and Γ_D parameter [139]:

$$\frac{1}{\tau_{NP}} = \frac{1}{\tau_{bulk}} + \frac{v_F}{r} \Rightarrow \Gamma_{NP}^{Hz} = \Gamma_{bulk}^{Hz} + \frac{v_F}{r}, \quad (24)$$

where τ_{NP} and τ_{bulk} are the electron relaxation times, and Γ_{NP}^{Hz} and Γ_{bulk}^{Hz} are the Drude broadenings (expressed in Hz and not in eV as in the rest of this work) of the nanoparticles and the corresponding bulk metal, respectively, and r is the particle radius (20 nm in our study to result in particle size of 40 nm) and v_F is the Fermi velocity. The results of the MG-EMA calculations of the imaginary part ϵ_2 of the effective dielectric function of assemblies of nanoparticles of Au, Ag, TiN, and ZrN in air with 10% vol filling ratio are presented in Fig. 46. Au and TiN exhibit LSPR at very similar wavelengths, and the strengths of their resonances are comparable. Au's LSPR exhibits sharper LSPR (higher Q -factor) but higher dielectric losses at short wavelengths, as well, than TiN making TiN's LSPR more clear and well-shaped. ZrN exhibits stronger but wider LSPR than Au that makes it a very appealing candidate for a variety of plasmonic applications. Of course, none of them can compete Ag exclusively in terms of plasmonic performance. In conclusion ZrN and TiN exhibit broader LSPR than Au and Ag, as a result of their high electronic losses, but the strength of their LSPR is superior to Au. Taking into account all the rest of their assets (CMOS-compatibility, thermal stability, mechanical rigidity, etc), they definitely deserve to be implemented in various plasmonic devices.

3.3.2. Near field properties

The near field properties of representative binary and ternary TMN and the plasmonic enhancement provided by the TMN were studied using FDTD simulations (in which Maxwell equations are solved explicitly [602]) and presented in Fig. 48. For FDTD we used as input the experimental dielectric functions presented in Ref. [439]. We simulate an array of nanoparticles (40 nm diameter) suspended in air under plane wave illumination, for a wide range of volume filling ratios from $\sim 5\%$ up to $\sim 45\%$. We extract the maximum intensity enhancement, which occurs at the nanoparticle surface (see inset of Fig. 48), for each plasmonic TMN and volume filling ratio. We observe that all TMN exhibit very similar plasmonic enhancements, irrespective to the volume filling ratio, and even more, this plasmonic response is somehow inferior, yet in the same order of magnitude, to the field enhancement of Au. It is

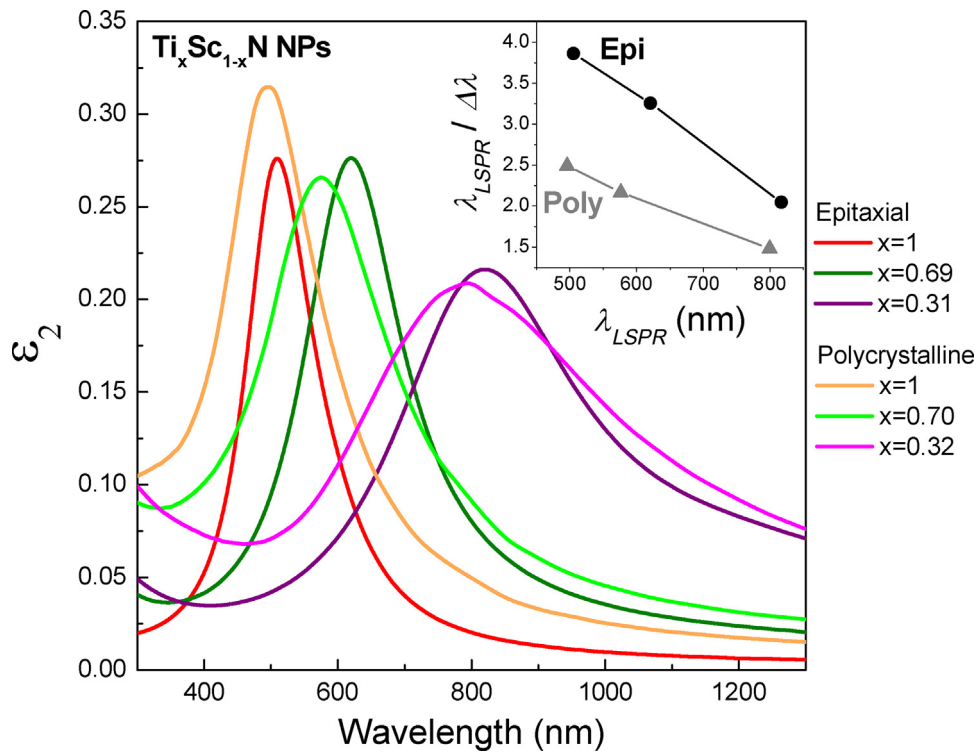


Fig. 45. MG-EMA calculations of the ϵ_2 spectra of hypothetical polycrystalline and single-crystalline (epitaxial-quality) $\text{Ti}_x\text{Sc}_{1-x}\text{N}$ nanoparticles in air showing clear LSPR; the inset shows the Q -factor of the resonance, which is superior for epitaxial quality nanoparticles, and it is reducing as the resonance shifts towards infrared.

worth noting that the maximum field enhancement is almost constant for all TMN for the entire visible (400–700 nm) and UVA (315–400 nm). We thus conclude that TMNs offer an excellent platform for tunable plasmonic responses, with their near field effects being competitive, given their additional assets (mechanical and thermal stability, refractory character, varying work function), to the ones obtained by standard plasmonic metals such as Au, and with exceptional spectral tunability (Fig. 47).

3.3.3. Photothermal properties

High temperatures are developed inside plasmonic nanoparticles when they are irradiated by strong beams at their LSPR frequency, for example in applications in immunoassays [603], chemical and biological sensing [25,109,604–607] and surface enhanced spectroscopies [108,123,132,608–612]. Typically this is something to be avoided as it could result into nanoparticle reshaping [77,613–615] and thus into the destruction of the plasmonic template. The use of TMN nanoparticles, however, can uplift this limitation and open up a new window of opportunity into high-temperature plasmonic operation, involving simultaneous hot-electron and hot-lattice excitations. In this work we attempt a comprehensive theoretical evaluation of the TMN plasmonic response within a wide range of operating temperatures (300–3200 K) and compare it with the corresponding response of noble metals. Specifically, the bulk melting points of ZrN, TiN and TaN are a little over 3200 K [616] while the corresponding values for Ag and Au are 1236 K and 1338 K respectively and even lower for small nanoparticles (<40 nm diameter) [617,618].

We simulate a semi-infinite array of hemispherical nanoparticles on a Si substrate (including 2 nm of native SiO_2), a structure typically used in surface enhanced spectroscopy applications [132]. We note that this is not the structure with maximal plasmonic enhancement but rather a standard model that makes our high-temperature study simpler. In our calculations we consider two TMN nanoparticles (TiN and ZrN) and two noble metals

(Au and Ag) with a nanoparticle diameter of 40 nm arranged in a 44 nm square lattice (surface coverage 65%) within the 300–3200 K temperature range. We calculate the intensity enhancement in the middle of the gap between the nanoparticles under plane wave illumination in the spectral range of 0.3–3 μm . To do so we use the finite-difference time-domain (FDTD) method in which Maxwell's equations including the material polarization are solved on a computational grid [139,602,619]. Material dielectric functions are inserted through a Drude-Lorentz polarizability model. The model's parameters are

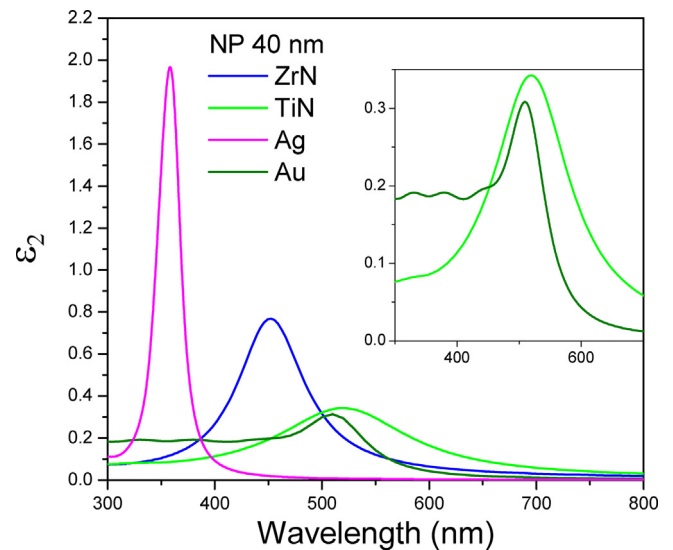


Fig. 46. Spectra of the imaginary part of the dielectric function of 40 nm nanoparticles of Au, Ag, TiN, and ZrN in air with filling ratio 10% vol calculated by MG-EMA. The inset is a magnification of the spectra at the vicinity of the LSPR of Au and TiN.

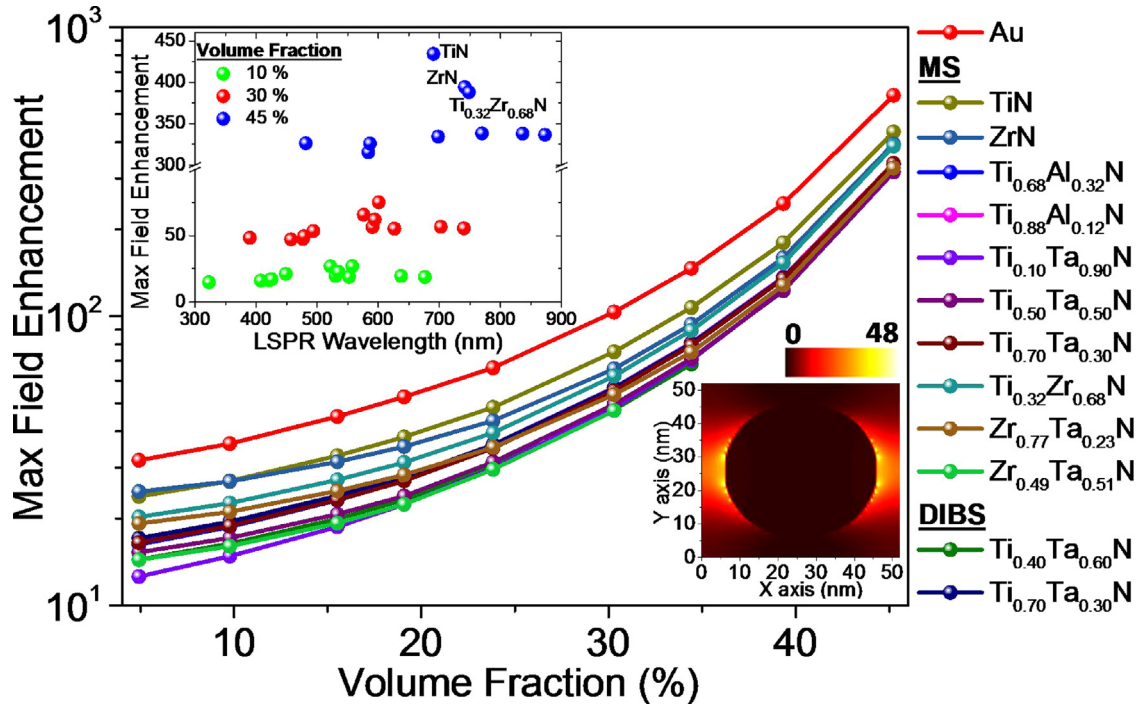


Fig. 47. Maximum field intensity enhancement (at the nanoparticle surface) as a function of volume filling ratio, and of the LSPR wavelength (in the upper inset) for 40 nm TMN spherical nanoparticles (half-filled squares, triangles and circles correspond to filling ratios of 10%, 30% and 45%, respectively). The enhancement for a 40 nm Au nanoparticle is also shown for comparison. The lower inset depicts the resonant intensity enhancement of a TiN nanoparticle at volume ratio 25%. Reproduced from Ref. [439].

fitted to the experimentally measured dielectric functions (TiN and ZrN from this work and also [439], Au [524] and Ag [522]). In order to get the appropriate dielectric constant for the nanoparticles, we need to include the surface scattering contribution in the free electron relaxation time [139] according to Eq. (24).

The goal of our study is to model the optical properties of the TMN and noble metal nanoparticles over a wide temperature range. The dominant effect of temperature is on the free electron relaxation time through the temperature dependence of the phonon population and of the crystal vacancies and imperfections [620,621]. Other, more minor effects such electron–electron scattering and small modifications of electron concentration due to nanoparticle volume expansion (which can cause a small redshift in the LSPR frequency) [620] or changes in the Fermi velocity ($k_B T \ll \frac{mv_F^2}{2}$ even close to melting [621]) are ignored for simplicity. We use a semi-empirical model for creating a temperature-dependent Drude-Lorentz model [622], via the electron relaxation time τ , similarly to what has been used in previous theoretical works [622,623]:

$$\frac{1}{\tau'(T)} = \frac{1}{\tau} \left(\frac{T}{T_0} \right)^a + \frac{v_F}{r}, \quad (25)$$

where $T_0 = 300$ K and T is the operating temperature. The parameter a should be fitted from thermal emissivity data [622,623]. Due to the lack of such experimental data for TMN and noble metals, however, we follow a simpler approach in which we assume that the temperature dependence of the optical (AC) relaxation time is similar to that of the static (DC) case. In the latter case the relaxation time is given by the Drude model $\tau_{DC}^{-1}(T) \propto \rho(T)$ [624], thus the optical relaxation time is simply:

$$\frac{1}{\tau'(T)} = \frac{1}{\tau} \cdot \frac{\rho(T)}{\rho(T_0)} + \frac{v_F}{r}, \quad (26)$$

We use $h\tau^{-1} = 0.068$ and 0.071 eV for Au and Ag respectively at 300 K and literature data for $\rho(T)$ [625] and adjust the exponent a

in Eq. (25). This empirical $\tau(T)$ is excellently fitted by the same $a=1.14$ for the both metals, as shown in Fig. 48. This value is also in excellent agreement with literature values of the linear temperature coefficient of resistivity (TCR) $a' = a/T_0$ [625], as found after linearly expanding Eq. (25) $(T/T_0)\alpha \rightarrow (1 + \alpha'\Delta T)$, with $\alpha' = \alpha/T_0$ and $\Delta T = T - T_0$.

High temperature TMN electrical resistivity has not been studied in the literature. The available data to our knowledge for TiN [303,469,626,627] are found in the 10–400 K temperature range and in 10–300 K for ZrN [303,311]. The electrical resistivity

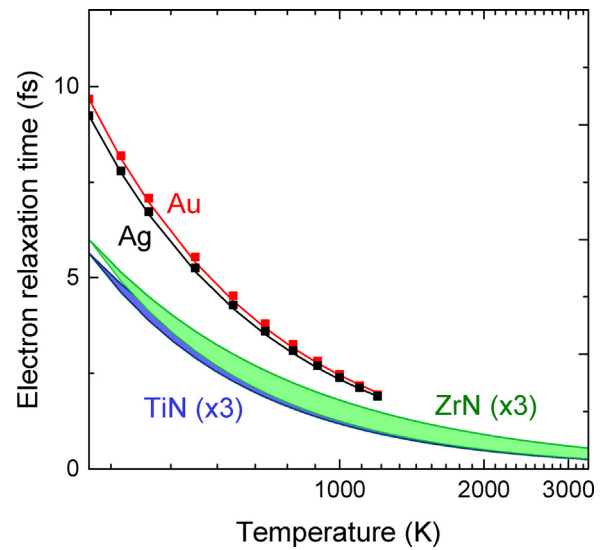


Fig. 48. The temperature dependence of the free electron relaxation time for Au, Ag, TiN and ZrN. For the noble metals, symbols are experimental data and lines are fits to Eq. (25). For the nitrides, we use the experimental values at 300 K and assume a range 1–1.3 of the exponent a in Eq. (25) (nitride values have been multiplied by 3 to fit in the same scale with the noble metals).

strongly depends on the TMN crystallinity, which in turn is related to the growth protocol. Specifically, the room temperature electrical resistivity of TiN is found to vary between 13 and 200 $\mu\Omega\text{cm}$ for single crystal and polycrystalline films, while for ZrN the corresponding variation is between 12 and 2000 $\mu\Omega\text{cm}$ [303]. We use the linear TCR at 300 K to get $a = aT_0$ for TiN and ZrN. For polycrystalline films we get $a \approx 1$ [626] for both metals, while for single crystal films $a = 1.2$ is more appropriate [469] (a smaller coefficient points to a smaller effect of scattering from phonons compared to scattering from structural defects such as grain boundaries). In order to cover all ranges and possibilities, we consider the range $a = 1-1.3$. Using $\hbar\tau^{-1} = 0.35$ and 0.33 eV for TiN and ZrN at 300 K (as obtained from the Drude-Lorentz fit of the ellipsometric data), we plot the corresponding $\tau(T)$ in Fig. 48.

We extract from the FDTD solutions the electromagnetic fields at every point in the structure in time domain and by Fourier transforms we get the corresponding quantities in frequency domain [628]. The spectrally resolved intensity enhancement is calculated in the midgap position between the nanoparticles and is defined as $|E(\omega)|^2/|E_0(\omega)|^2$ where E is the electric field at the specific point and E_0 is the incident electric field. This is shown in Fig. 49 for TiN nanoparticles at different temperatures. The top inset depicts the simulated structure while the bottom inset shows the intensity enhancement at the LSPR frequency at 300 K. For increasing temperature we observe a small redshift and a significant broadening that eventually flattens out the LSPR response. A similar response is found also for the nanoparticle absorption.

We attempt now a side-by-side comparison of the two nitrides with the two noble metals in a realistic high-power high-temperature operation. To do so we adopt the thermal transient heating calculations of Ag nanoparticles on Si under pulsed laser illumination that were conducted in a recent study for the same exactly system [615]. Specifically, it was found that under a Nd:YAG pulse at 532 nm with fluence $f=1$ mJ/cm^2 (FWHM = 6 ns, peak power $P_{\text{peak}} = 0.162$ MW/cm^2) the nanoparticle structure was heated up to a peak $\Delta T = 1.75$ K. The pulse profile is shown in the

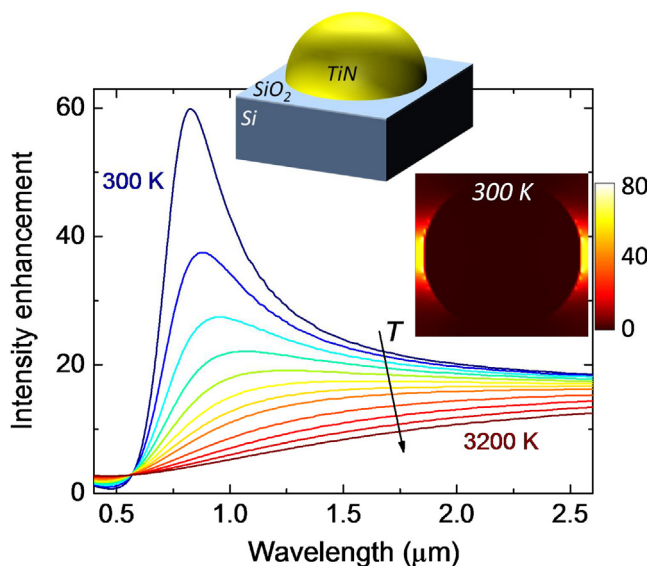


Fig. 49. a) Simulated spectral intensity enhancement for TiN nanoparticles on Si assuming $a = 1$. The top inset shows a schematic of the simulation system: 40 nm TiN hemispherical nanoparticles on top of a Si substrate, including a 2 nm native oxide. The Si substrate is for simplicity assumed to have a dielectric constant of 11.9, while the nanoparticles are arranged at a 44 nm period leaving 4 nm gaps in between them. The bottom inset shows the intensity distribution at the LSPR frequency for 300 K.

inset of Fig. 50b. We assume a linear dependence $P_{\text{peak}}A(T) = \Gamma\Delta T$, where Γ is the thermal conductance between the nanoparticles and the Si substrate and $A(T)$ the calculated nanoparticle absorption ratio at temperature T . In [615] the absorption for the 40 nm Ag nanoparticles was calculated $A(300\text{ K})=0.14$, from which we find $\Gamma = 130$ $\text{MW}/\text{m}^2\text{K}$. For simplicity we use this value for all materials hereafter. We can thus associate any given ΔT to a P_{peak} and thus to an incident peak electric field $|E_0|_{\text{peak}} = (2z_0P_{\text{peak}})^{1/2}$, where $z_0 = 377$ Ω is the impedance of the free space. Furthermore, from the calculated intensity enhancement $F(T)$ we get for the enhanced peak near-field $|E|_{\text{peak}} = |E_0|_{\text{peak}}[F(T)]^{1/2} = [2z_0\Gamma F(T)\Delta T/A(T)]^{1/2}$.

The peak near field and the corresponding ΔT are plotted as a function of laser fluence in Fig. 50 for all four considered materials, each for the corresponding wavelength at which the LSPR appears at 300 K. We find that the E-field rises very quickly for the noble metals, but it is still comparable to that of the nitrides. We plot the response up to the corresponding melting point and as expected, the nitride nanoparticle response extends for up to much higher laser fluence, eventually providing for equally strong electric fields as that of the noble metals. What is most interesting in these results, we believe, is the possibility of finely tuning the nanoparticle temperature up to very high values making it an important parameter of the plasmonic response. For example, being able to access temperatures up to 3000 K, where $k_B T = 0.26$ eV, brings the nanoparticle thermal bath into the energy range of most molecule vibrational modes and thus potentially

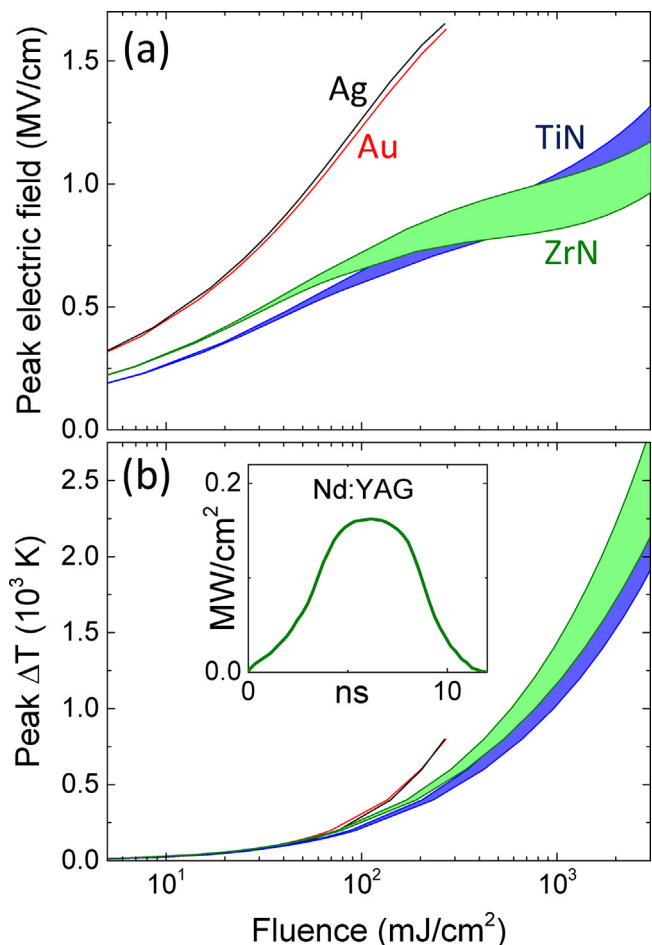


Fig. 50. The enhanced plasmonic near field for Au, Ag, TiN and ZrN nanoparticles on Si as a function of the laser fluence. The range for the nitrides corresponds to the exponent in Eq. (25) taking values between 1 and 1.3. The inset shows the Nd:YAG laser pulse profile (FWHM = 6 ns) assumed in the simulations.

makes it an important parameter in any SERS or surface-enhanced infrared absorption process.

4. Conclusions and outlook

The *ab initio* calculations reveal a qualitative common understanding for the optical properties of binary and ternary transition nitrides. The electronic conductivity of all these nitrides comes from the excess metal-*d* electrons that do not participate to the Metal-*N* bonding, which is the origin of the *N-p* → Metal-*d* interband transitions and of the accompanying dielectric losses. Quantitative variations do exist among the various nitrides, with the major trends being the increase of conduction electron density and the substantial blueshift of the interband transitions with increasing the number of valence electrons of the constituent metal. However, relying exclusively to *ab initio* calculations, which assume an ideal, defect-free nitride crystal in the B1 cubic structure, might be misleading. This is because of the metastable nature of some B1 nitrides (e.g. B1-TaN) and the intrinsic point defects, which are necessary to stabilize the B1 structure (e.g. B1-MoN and B1-WN). Even for the cases where the B1 structure is stable (such as B1-TiN, B1-ZrN and B1-NbN) kinetic and thermodynamic factors can severely affect the crystal growth process altering, or even opposing, the predictions of the *ab initio* calculations regarding the optical and plasmonic properties of these nitrides.

The critical comparison of the experimental optical spectra undisputedly reveals that the less optically lossy nitrides are those of group IVb metals (TiN, ZrN, HfN). Among them, ZrN shows the longest average value electron relaxation time, combined with the minimized dielectric losses, and it is emerging as the most promising refractory conductor for plasmonics. In addition, TiN and ZrN exhibit small and large work function, respectively, while they have similar melting points and conduction electron densities. Therefore, they and their alloys can constitute a platform of plasmonic conductors of tunable work function for hot electron applications. TiN by itself (*i.e.* without alloying) can be quite tunable, while ZrN is less tunable but it can be superior in its short range of operation by providing shorter SPP wavelengths due to the less dielectric losses. The LSPR performance of TiN is as strong as that of gold albeit with broader resonances, and manifests at exactly the same spectral range with gold. ZrN exhibits LSPR that is spectrally in between of gold and silver, and the strength of the resonance is intermediate between gold and silver as well. HfN exhibits intermediate optical performance and cell size, and given its scarcity and high cost seems to be less appealing for plasmonic applications.

Regarding the nitrides of Vb metals, they exhibit higher conduction electron density compared to group IVb nitrides, and thus a plasmonic performance towards UV is predicted. Given the metastable character of B1-TaN in contrast to the ease of fabricating epitaxial B1-NbN, we can safely conclude that for UV plasmonic applications B1-NbN is the most promising candidate. B1-VN received less attention and in this review only data from one sample are reported. These data indicate that B1-VN is not inferior to B1-NbN, while having the additional asset of exceptionally low work function. The combination of the potential plasmonic response in the UV with the low work function of B1-VN might be a strong incentive for the investigation of B1-VN in plasmonics and hot electron applications; however, its real potential for such applications cannot be solidly evaluated for the time being due to the lack of data. B1-TaN has quite acceptable optical and plasmonic response, but its growth without a high concentration of structural defects or the existence of a secondary phase is quite rare.

Finally, B1-MoN and B1-WN are exceptionally and excessively lossy due to both their inherent characteristics, and their metastable character, which results in the incorporation of a high concentration of point defects to stabilize them. Consequently,

they do not seem appropriate for applications, such as plasmonics, where high conductivity is required.

All conductive transition metal nitrides exhibit very short intrinsic conduction electron mean free paths; consequently, their spectral tunability by varying the size and/or the shape of nanostructures is quite limited. This limitation can be overcome by the introduction of ternary conductive nitrides of varying conduction electron density. TiN-based alloyed ternary nitrides were found to outperform the ZrN-based ternaries, despite of the superior character of pure ZrN on its own merit. This is attributed to the very large mismatch of ZrN compared to the rest of the transition metal nitrides, which may cause the formation of extended structural defects that reduce the conductivity, as well as to the kinetically-hindered growth of Zr-containing nitride crystals. By evaluating and comparing an immense range of ternary combinations, we conclude that the most promising candidates based both on technical merit and on the abundance of the constituent elements, are $Ti_xTa_{1-x}N$, $Ti_xZr_{1-x}N$, $Ti_xSc_{1-x}N$, $Ti_xAl_{1-x}N$, and $Ti_xMg_{1-x}N$ in the B1 rocksalt structure. They share the important plasmonic features with their binary counterparts, while having the additional asset of the exceptional spectral tunability in the entire visible (400–700 nm) Near Infrared (NIR, 700–1350 nm) and UVA (315–400 nm) spectral ranges depending on their net valence electrons per unit cell; thus, $Ti_xTa_{1-x}N$ is recommended for plasmonic devices in blue, violet and UV, $Ti_xAl_{1-x}N$ for deep red, and $Ti_xSc_{1-x}N$ and $Ti_xMg_{1-x}N$ for NIR. Especially, Ta -rich $Ti_xTa_{1-x}N$ outperforms the binary B1-TaN (and even the binary B1-NbN with the current state-of-the-art, however, the comparison to B1-NbN cannot be conclusive due to the lack of optical spectra of epitaxial B1-NbN) for plasmonics; it seems that the incorporation of a small Ti content into TaN stabilizes the cubic B1 structure with beneficial results to the optical and plasmonic performance.

We have shown that nanoparticles of such ternary nitrides can exhibit maximum field enhancement factors inferior but comparable with gold in the aforementioned broadband range (315–1350 nm). These nitrides exhibit substantial electronic losses mostly due to fine crystalline grains that deteriorate the plasmonic field enhancement unequivocally calling for the improvement of the current crystal growth technology for these materials.

Finally, the transition metal nitrides are remarkably stable up to very high temperatures, due to their refractory character, and thus can endure the interactions with strong electric fields, such as in lasers. This opens new possibilities such as finely tuning the nanoparticle temperature up to very high values making it an important parameter of the plasmonic response, e.g. by inducing to the nitride nanoparticles a thermal bath into the energy range of most molecule vibrational modes affecting the SERS or surface-enhanced infrared absorption processes.

Acknowledgements

P.P. would like to acknowledge Prof. S. Logothetidis of Aristotle University for his guidance at the initial steps of the nitride research, Dr G.M. Matenoglou (now at Texas A&M University at Qatar) and Dr L.E. Koutsokeras (now at Cyprus University of Technology) for their massive experimental work on the growth of conductive nitrides, and Prof. J.-F. Pierson of University of Lorraine – France, and Prof. D. Gall of Rensselaer Polytechnic Institute – USA for their collaboration in studying ternary nitrides.

References

- [1] S.A. Maier, *Plasmonics: Fundamentals and Applications*, Springer, US, 2010.
- [2] S. Enoch, N. Bonod, *Plasmonics: From Basics to Advanced Topics*, Springer, Berlin, Heidelberg, 2012.
- [3] H. Wei, H. Xu, *Mater. Today* 17 (2014) 372–380.

- [4] C.W. Hsu, B. Zhen, W. Qiu, O. Shapira, B.G. DeLacy, J.D. Joannopoulos, M. Soljačić, *Nat. Commun.* 5 (2014) 3152.
- [5] P. Berini, I. De Leon, *Nat. Photonics* 6 (2012) 16–24.
- [6] S. Lal, S. Link, N.J. Halas, *Nat. Photonics* 1 (2007) 641–648.
- [7] W.L. Barnes, A. Dereux, T.W. Ebbesen, *Nature* 424 (2003) 824–830.
- [8] J. Lin, J.P.B. Mueller, Q. Wang, G.H. Yuan, N. Antoniou, X.C. Yuan, F. Capasso, *Science* 340 (2013) 331–334.
- [9] A. Polman, *Science* 322 (2008) 868–869.
- [10] E. Ozbay, *Science* 311 (2006) 189–193.
- [11] M.L. Brongersma, V.M. Shalaev, *Science* 328 (2010) 440.
- [12] J.A. Fan, C.H. Wu, K. Bao, J.M. Bao, R. Bardhan, N.J. Halas, V.N. Manoharan, P. Nordlander, G. Shvets, F. Capasso, *Science* 328 (2010) 1135–1138.
- [13] N.J. Halas, *Nano Lett.* 10 (2010) 3816–3822.
- [14] R.P. Van Duyne, *Science* 306 (2004) 985–986.
- [15] J.C. Maxwell Garnett, *Phil. Trans. R. Soc. A* 203 (1904) 385.
- [16] G. Mie, *Ann. Phys.* 330 (1908) 377–445.
- [17] J.A. Dionne, K. Diest, L.A. Sweatlock, H.A. Atwater, *Nano Lett.* 9 (2009) 897–902.
- [18] J.D. Lin, H. Li, H. Zhang, W. Chen, *Appl. Phys. Lett.* 102 (2013) 203109.
- [19] N. Guo, W.D. Hu, X.S. Chen, L. Wang, W. Lu, *Opt. Express* 21 (2013) 1606–1614.
- [20] L. Wang, W.D. Hu, J. Wang, X.D. Wang, S.W. Wang, X.S. Chen, W. Lu, *Appl. Phys. Lett.* 100 (2012) 123501.
- [21] T. Isoniemi, A. Johansson, T.K. Hakala, M. Rinkio, P. Torma, J.J. Toppari, H. Kunttu, *Appl. Phys. Lett.* 99 (2011) 031105.
- [22] R.W. Heeres, L.P. Kouwenhoven, V. Zwiller, *Nat. Nanotechnol.* 8 (2013) 719–722.
- [23] J.M. Luther, J.L. Blackburn, *Nat. Photonics* 7 (2013) 675–677.
- [24] M.T. Sheldon, J. van de Groep, A.M. Brown, A. Polman, H.A. Atwater, *Science* 346 (2014) 828–831.
- [25] J.N. Anker, W.P. Hall, O. Lyandres, N.C. Shah, J. Zhao, R.P. Van Duyne, *Nat. Mater.* 7 (2008) 442–453.
- [26] H. Im, H.L. Shao, Y.I. Park, V.M. Peterson, C.M. Castro, R. Weissleder, H. Lee, *Nat. Biotechnol.* 32 (2014), 490–U219.
- [27] B. Zhang, R.B. Kumar, H.J. Dai, B.J. Feldman, *Nat. Med.* 20 (2014) 948–953.
- [28] W.E. Doering, S. Nie, *J. Phys. Chem. B* 106 (2002) 311–317.
- [29] R. Zhang, Y. Zhang, Z.C. Dong, S. Jiang, C. Zhang, L.G. Chen, L. Zhang, Y. Liao, J. Aizpurua, Y. Luo, J.L. Yang, J.G. Hou, *Nature* 498 (2013) 82–86.
- [30] V.G. Kravets, F. Schedin, R. Jalil, L. Britnell, R.V. Gorbachev, D. Ansell, B. Thackray, K.S. Novoselov, A.K. Geim, A.V. Kabashin, A.N. Grigorenko, *Nat. Mater.* 12 (2013) 304–309.
- [31] F. De Angelis, G. Das, P. Candeloro, M. Patrini, M. Galli, A. Bek, M. Lazzarino, I. Maksymov, C. Liberale, L.C. Andreani, E. Di Fabrizio, *Nat. Nanotechnol.* 5 (2010) 67–72.
- [32] A.V. Kabashin, P. Evans, S. Pastkovsky, W. Hendren, G.A. Wurtz, R. Atkinson, R. Pollard, V.A. Podolskiy, A.V. Zayats, *Nat. Mater.* 8 (2009) 867–871.
- [33] T.H. Taminiou, F.D. Stefani, F.B. Segerink, N.F. Van Hulst, *Nat. Photonics* 2 (2008) 234–237.
- [34] C. Sonnichsen, B.M. Reinhard, J. Liphardt, A.P. Alivisatos, *Nat. Biotechnol.* 23 (2005) 741–745.
- [35] D.Y. Qi, L.J. Lu, L.Z. Wang, J.L. Zhang, *J. Am. Chem. Soc.* 136 (2014) 9886–9889.
- [36] L. Weng, H. Zhang, A.O. Govorov, M. Ouyang, *Nat. Commun.* 5 (2014) 4792.
- [37] S. Mubeen, J. Lee, N. Singh, S. Kramer, G.D. Stucky, M. Moskovits, *Nat. Nanotechnol.* 8 (2013) 247–251.
- [38] S. Linic, P. Christopher, D.B. Ingram, *Nat. Mater.* 10 (2011) 911–921.
- [39] T.J. Antosiewicz, S.P. Apell, *RSC Adv.* 5 (2015) 6378–6384.
- [40] J.S. DuChene, B.C. Sweeny, A.C. Johnston-Peck, D. Su, E.A. Stach, W.D. Wei, *Angew. Chem. Int. Ed.* 53 (2014) 7887–7891.
- [41] K. Qian, B.C. Sweeny, A.C. Johnston-Peck, W.X. Niu, J.O. Graham, J.S. DuChene, J.J. Qiu, Y.C. Wang, M.H. Engelhard, D. Su, E.A. Stach, W.D. Wei, *J. Am. Chem. Soc.* 136 (2014) 9842–9845.
- [42] G. Manna, R. Bose, N. Pradhan, *Angew. Chem. Int. Ed.* 53 (2014) 6743–6746.
- [43] Z. Wang, C.Y. Yang, T.Q. Lin, H. Yin, P. Chen, D.Y. Wan, F.F. Xu, F.Q. Huang, J.H. Lin, X.M. Xie, M.H. Jiang, *Adv. Funct. Mater.* 23 (2013) 5444–5450.
- [44] S.K. Cushing, J. Li, F. Meng, T.R. Senty, S. Suri, M. Zhi, M. Li, A.D. Bristow, N. Wu, *J. Am. Chem. Soc.* 134 (2012) 15033–15041.
- [45] E.M. Larsson, C. Langhammer, I. Zoric, B. Kasemo, *Science* 326 (2009) 1091–1094.
- [46] H.A. Atwater, A. Polman, *Nat. Mater.* 9 (2010) 205–213.
- [47] A. Aubry, D.Y. Lei, A.I. Fernandez-Dominguez, Y. Sonnefraud, S.A. Maier, J.B. Pendry, *Nano Lett.* 10 (2010) 2574–2579.
- [48] F. Pelayo Garcia de Arquer, A. Mihi, G. Konstantatos, *Nanoscale* 7 (2015) 2281–2288.
- [49] S.J. Kim, I. Thomann, J. Park, J.-H. Kang, A.P. Vasudev, M.L. Brongersma, *Nano Lett.* 14 (2014) 1446–1452.
- [50] H.I. Park, S. Lee, J.M. Lee, S.A. Nam, T. Jeon, S.W. Han, S.O. Kim, *ACS Nano* 8 (2014) 10305–10312.
- [51] H. Zoubos, L.E. Koutsokeras, D.F. Anagnostopoulos, E. Lidorikis, S.A. Kalogirou, A.R. Wildes, P.C. Kelires, P. Patsalas, *Sol. Energy Mater. Sol. Cells* 117 (2013) 350–356.
- [52] Q.Q. Gan, F.J. Bartoli, Z.H. Kafafi, *Adv. Mater.* 25 (2013) 2385–2396.
- [53] X.N. Dang, J.F. Qi, M.T. Klug, P.Y. Chen, D.S. Yun, N.X. Fang, P.T. Hammond, A.M. Belcher, *Nano Lett.* 13 (2013) 637–642.
- [54] C.S. Kao, F.C. Chen, C.W. Liao, M.H. Huang, C.S. Hsu, *Appl. Phys. Lett.* 101 (2012).
- [55] P. Reineck, G.P. Lee, D. Brick, M. Karg, P. Mulvaney, U. Bach, *Adv. Mater.* 24 (2012) 4750–4755.
- [56] N. Kalfagiannis, P.G. Karagiannidis, C. Pitsalidis, N.T. Panagiotopoulos, C. Gravalidis, S. Kassavetis, P. Patsalas, S. Logothetidis, *Sol. Energy Mater. Sol. Cells* 104 (2012) 165–174.
- [57] L. Hong, Rusli, X.C. Wang, H.Y. Zheng, L.N. He, X.Y. Xu, H. Wang, H.Y. Yu, *J. Appl. Phys.* 112 (2012) 054326.
- [58] T.P. White, K.R. Catchpole, *Appl. Phys. Lett.* 101 (2012) 073905.
- [59] M.G. Deceglie, V.E. Ferry, A.P. Alivisatos, H.A. Atwater, *Nano Lett.* 12 (2012) 2894–2900.
- [60] V.E. Ferry, A. Polman, H.A. Atwater, *ACS Nano* 5 (2011) 10055–10064.
- [61] N.J. Hogan, A.S. Urban, C. Ayala-Orozco, A. Pimpinelli, P. Nordlander, N.J. Halas, *Nano Lett.* 14 (2014) 4640–4645.
- [62] R.A. Pala, J.S.Q. Liu, E.S. Barnard, D. Askarov, E.C. Garnett, S.H. Fan, M.L. Brongersma, *Nat. Commun.* 4 (2013) 2095.
- [63] B. Paci, G.D. Spyropoulos, A. Generosi, D. Bailo, V.R. Albertini, E. Stratakis, E. Kymakis, *Adv. Funct. Mater.* 21 (2011) 3573–3582.
- [64] E. Stratakis, E. Kymakis, *Mater. Today* 16 (2013) 133–146.
- [65] A. Sobhani, M.W. Knight, Y.M. Wang, B. Zheng, N.S. King, L.V. Brown, Z.Y. Fang, P. Nordlander, N.J. Halas, *Nat. Commun.* 4 (2013) 1643.
- [66] G. Konstantatos, E.H. Sargent, *Nat. Nanotechnol.* 5 (2010) 391–400.
- [67] A. Pescaglino, A. Martin, D. Cammi, G. Juska, C. Ronning, E. Pelucchi, D. Iacopino, *Nano Lett.* 14 (2014) 6202–6209.
- [68] J.D. Hwang, F.H. Wang, C.Y. Kung, M.J. Lai, M.C. Chan, *J. Appl. Phys.* 115 (2014) 173110.
- [69] S.S. Mousavi, A. Stohr, P. Berini, *Appl. Phys. Lett.* 104 (2014).
- [70] H. Chalabi, D. Schoen, M.L. Brongersma, *Nano Lett.* 14 (2014) 1374–1380.
- [71] S.B. Wang, R.S. Chen, S.J. Chang, H.C. Han, M.S. Hu, K.H. Chen, L.C. Chen, *Nanoscale* 6 (2014) 1264–1270.
- [72] P. Senanayake, C.H. Hung, A. Farrell, D.A. Ramirez, J. Shapiro, C.K. Li, Y.R. Wu, M.M. Hayat, D.L. Huffaker, *Nano Lett.* 12 (2012) 6448–6452.
- [73] P. Senanayake, C.-H. Hung, J. Shapiro, A. Lin, B. Liang, B.S. Williams, D.L. Huffaker, *Nano Lett.* 11 (2011) 5279–5283.
- [74] A. Akbari, P. Berini, *Appl. Phys. Lett.* 95 (2009) 021104.
- [75] Y. Montelongo, J.O. Tenorio-Pearl, C. Williams, S. Zhang, W.I. Milne, T.D. Wilkinson, *Proc. Natl. Acad. Sci. U. S. A.* 111 (2014) 12679–12683.
- [76] J. Olson, A. Manjavacas, L.F. Liu, W.S. Chang, B. Foerster, N.S. King, M.W. Knight, P. Nordlander, N.J. Halas, S. Link, *Proc. Natl. Acad. Sci. U. S. A.* 111 (2014) 14348–14353.
- [77] A. Siozios, D.C. Koutsogeorgis, E. Lidorikis, G.P. Dimitrakopoulos, T. Kehagias, H. Zoubos, P. Komninou, W.M. Cranton, C. Kosmidis, P. Patsalas, *Nano Lett.* 12 (2012) 259–263.
- [78] P. Zijlstra, J.W.M. Chon, M. Gu, *Nature* 459 (2009) 410–413.
- [79] D.H. Wan, H.L. Chen, S.C. Tseng, L.A. Wang, Y.P. Chen, *ACS Nano* 4 (2010) 165–173.
- [80] A. Royon, K. Bourhis, M. Bellec, G. Papon, B. Bousquet, Y. Deshayes, T. Cardinal, L. Canioni, *Adv. Mater.* 22 (2010) 5282–5286.
- [81] W.T. Chen, P.C. Wu, C.J. Chen, C.J. Weng, H.C. Lee, T.J. Yen, C.H. Kuan, M. Mansuripur, D.P. Tsai, *Appl. Phys. Lett.* 98 (2011) 171106.
- [82] K. Kumar, H.G. Duan, R.S. Hegde, S.C.W. Koh, J.N. Wei, J.K.W. Yang, *Nat. Nanotechnol.* 7 (2012) 557–561.
- [83] A.B. Taylor, J. Kim, J.W.M. Chon, *Opt. Express* 20 (2012) 5069–5081.
- [84] J.R. Sanchez-Valencia, J. Toudert, A. Borras, A. Barranco, R. Lahoz, G.F. de la Fuente, F. Frutos, A.R. Gonzalez-Elipide, *Adv. Mater.* 23 (2011) 848–853.
- [85] KuipersL SandtkeM, *Nat. Photonics* 1 (2007) 573–576.
- [86] H. Moayyed, I.T. Leite, L. Coelho, J.L. Santos, D. Viegas, *Plasmonics* 10 (2015) 979–987.
- [87] S.P. Burgos, H.W. Lee, E. Feigenbaum, R.M. Briggs, H.A. Atwater, *Nano Lett.* 14 (2014) 3284–3292.
- [88] W. Shin, W.S. Cai, P.B. Catrysse, G. Veronis, M.L. Brongersma, S.H. Fan, *Nano Lett.* 13 (2013) 4753–4758.
- [89] A. Apuzzo, M. Fevrier, R. Salas-Montiel, A. Bruyant, A. Chelnokov, G. Lerondel, B. Dagens, S. Blaize, *Nano Lett.* 13 (2013) 1000–1006.
- [90] P.K. Jha, X.B. Yin, X. Zhang, *Appl. Phys. Lett.* 102 (2013) 091111.
- [91] X.E. Li, T. Jiang, L.F. Shen, X.H. Deng, *Appl. Phys. Lett.* 102 (2013) 031606.
- [92] R.M. Briggs, J. Grandidier, S.P. Burgos, E. Feigenbaum, H.A. Atwater, *Nano Lett.* 10 (2010) 4851–4857.
- [93] T. Holmgaard, S.I. Bozhevolnyi, L. Markey, A. Dereux, A.V. Krasavin, P. Bolger, A.V. Zayats, *Phys. Rev. B* 78 (2008) 165431.
- [94] T. Nikolajsen, K. Leosson, S.I. Bozhevolnyi, *Appl. Phys. Lett.* 85 (2004) 5833–5835.
- [95] D.R. Smith, J.B. Pendry, M.C.K. Wiltshire, *Science* 305 (2004) 788–792.
- [96] J.B. Pendry, L. Martin-Moreno, F.J. Garcia-Vidal, *Science* 305 (2004) 847–848.
- [97] C.R. Williams, S.R. Andrews, S.A. Maier, A.I. Fernandez-Dominguez, L. Martin Moreno, F.J. Garcia-Vidal, *Nat. Photonics* 2 (2008) 175–179.
- [98] A. Boltasseva, *MRS Bull.* 39 (2014) 461–468.
- [99] A. Boltasseva, V.M. Shalaev, *Metamaterials* 2 (2008) 1–17.
- [100] K.C.Y. Huang, M.-K. Seo, T. Sarmiento, Y. Huo, J.S. Harris, M.L. Brongersma, *Nat. Photonics* 8 (2014) 244–249.
- [101] D.K. Gramotnev, S.I. Bozhevolnyi, *Nat. Photonics* 8 (2014) 14–23.
- [102] D.K. Gramotnev, S.I. Bozhevolnyi, *Nat. Photonics* 4 (2010) 83–91.
- [103] S.A. Maier, P.G. Kik, H.A. Atwater, S. Meltzer, E. Harel, B.E. Koel, A.A.G. Requicha, *Nat. Mater.* 2 (2003) 229–232.
- [104] T.V. Shahbazyan, M.I. Stockman, *Plasmonics: Theory and Applications*, Springer, Netherlands, 2014.
- [105] T.P.H. Sidiropoulos, R. Roder, S. Geburt, O. Hess, S.A. Maier, C. Ronning, R.F. Oulton, *Nat. Phys.* 10 (2014) 870–876.
- [106] V.V. Temnov, *Nat. Photonics* 6 (2012) 728–736.
- [107] K.F. MacDonald, Z.L. Samson, M.I. Stockman, N.I. Zheludev, *Nat. Photonics* 3 (2009) 55–58.
- [108] E. Lidorikis, *J. Quant. Spectrosc. Radiat. Transfer* 113 (2012) 2573–2584.
- [109] K. Marchuk, K.A. Willets, *Chem. Phys.* 445 (2014) 95–104.
- [110] C. Clavero, *Nat. Photonics* 8 (2014) 95–103.
- [111] A. Giugni, B. Torre, A. Toma, M. Francardi, M. Malerba, A. Alabastri, R. Proietti Zaccaria, M.I. Stockman, E. Di Fabrizio, *Nat. Photonics* 8 (2013) 845–852.

- [112] H. Chalabi, M.L. Brongersma, *Nat. Nanotechnol.* 8 (2013) 229–230.
- [113] A. Manjavacas, J.G. Liu, V. Kulkarni, P. Nordlander, *ACS Nano* 8 (2014) 7630–7638.
- [114] J. Kupersztich, P. Monchicourt, M. Raynaud, *Phys. Rev. Lett.* 86 (2001) 5180–5183.
- [115] D.L. Mills, M. Weber, *Phys. Rev. B* 26 (1982) 1075–1078.
- [116] C. Ciraci, R.T. Hill, J.J. Mock, Y. Urzhumov, A.I. Fernández-Domínguez, S.A. Maier, J.B. Pendry, A. Chilkoti, D.R. Smith, *Science* 337 (2012) 1072.
- [117] A.L. Falk, F.H.L. Koppens, C.L. Yu, K. Kang, N. de Leon Snapp, A.V. Akimov, M.–H. Jo, M.D. Lukin, H. Park, *Nat. Phys.* 5 (2009) 475–479.
- [118] S. Kawata, Y. Inoué, P. Verma, *Nat. Photonics* 3 (2009) 388–394.
- [119] N. Lagos, M.M. Sigalas, E. Lidorikis, *Appl. Phys. Lett.* 99 (2011) 063304.
- [120] G. McNay, D. Eustace, W.E. Smith, K. Faulds, D. Graham, *Appl. Spectrosc.* 65 (2011) 825–837.
- [121] G.A. Baker, D.S. Moore, *Anal. Bioanal. Chem.* 382 (2005) 1751–1770.
- [122] N.J. Halas, S. Lal, W.–S. Chang, S. Link, P. Nordlander, *Chem. Rev.* 111 (2011) 3913–3961.
- [123] K. Katrin, K. Harald, I. Irving, R.D. Ramachandra, S.F. Michael, J. Phys.: *Condens. Matter* 14 (2002) R597.
- [124] M.R. Jones, K.D. Osberg, R.J. Macfarlane, M.R. Langille, C.A. Mirkin, *Chem. Rev.* 111 (2011) 3736–3827.
- [125] J.P. Camden, J.A. Dieringer, Y.M. Wang, D.J. Masiello, L.D. Marks, G.C. Schatz, R.P. Van Duyne, *J. Am. Chem. Soc.* 130 (2008) 12616–12617.
- [126] X. Zhang, M.A. Young, O. Lyandres, R.P. Van Duyne, *J. Am. Chem. Soc.* 127 (2005) 4484–4489.
- [127] R.A. Alvarez-Puebla, J.P. Bravo-Vasquez, B. Cui, T. Veres, H. Fenniri, *Chem. Med. Chem.* 2 (2007) 1165–1167.
- [128] I. Izquierdo-Lorenzo, J.V. García-Ramos, S. Sanchez-Cortes, *J. Raman Spectrosc.* 44 (2013) 1422–1427.
- [129] F. Schertz, M. Schmelzeisen, M. Kreiter, H.–J. Elmers, G. Schönhense, *Phys. Rev. Lett.* 108 (2012) 237602.
- [130] R.C. Word, J.P.S. Fitzgerald, R. Könenkamp, *Surf. Sci.* 607 (2013) 148–152.
- [131] J.C. Love, L.A. Estroff, J.K. Kriebel, R.G. Nuzzo, G.M. Whitesides, *Chem. Rev.* 105 (2005) 1103–1170.
- [132] N.T. Panagiotopoulos, N. Kalfagiannis, K.C. Vasilopoulos, N. Pliatsikas, S. Kassavetis, G. Vourlias, M.A. Karakassides, P. Patsalas, *Nanotechnology* 26 (2015) 205603.
- [133] A.P. Chernyshev, *Mater. Lett.* 63 (2009) 1525–1527.
- [134] H.A. Alarifí, M. Atiş, C. Özdoğan, A. Hu, M. Yavuz, Y. Zhou, *J. Phys. Chem. C* 117 (2013) 12289–12298.
- [135] A. Boltasseva, H.A. Atwater, *Science* 331 (2011) 290–291.
- [136] C.M. Soukoulis, T. Koschny, P. Tassin, N.–H. Shen, B. Dastmalchi, What is a good conductor for metamaterials or plasmonics, *Nanophotonics*, vol. 4, 2015, p. 69.
- [137] P. Tassin, T. Koschny, M. Kafesaki, C.M. Soukoulis, *Nat. Photonics* 6 (2012) 259–264.
- [138] D.R. Lide, *CRC Handbook of Chemistry and Physics*, 85th ed., Taylor & Francis, 2004.
- [139] E. Lidorikis, S. Egusa, J.D. Joannopoulos, *J. Appl. Phys.* 101 (2007) 054304.
- [140] V.G. Kravets, R. Jalil, V.J. Kim, D. Ansell, D.E. Aznakeyeva, B. Thackray, L. Britnell, B.D. Belle, F. Withers, I.P. Radko, Z. Han, S.I. Bozhevolnyi, K.S. Novoselov, A.K. Geim, A.N. Grigorenko, *Sci. Rep.* 4 (2014) 5517.
- [141] Q.–C. Sun, Y. Ding, S.M. Goodman, H.H. Funke, P. Nagpal, *Nanoscale* 6 (2014) 12450–12457.
- [142] K.M. McPeak, S.V. Jayanti, S.J.P. Kress, S. Meyer, S. Iotti, A. Rossinelli, D.J. Norris, *ACS Photonics* 2 (2015) 326–333.
- [143] G.H. Chan, J. Zhao, E.M. Hicks, G.C. Schatz, R.P. Van Duyne, *Nano Lett.* 7 (2007) 1947–1952.
- [144] E. Sacht, C.T. Shelton, J.S. Harris, B.E. Gaddy, D.L. Irving, S. Curtarolo, B.F. Donovan, P.E. Hopkins, P.A. Sharma, A.L. Sharma, J. Ihlefeld, S. Franzen, J.–P. Maria, *Nat. Mater.* 14 (2015) 414–420.
- [145] J. Chen, M. Badioli, P. Alonso-Gonzalez, S. Thongrattanasiri, F. Huth, J. Osmond, M. Spasenovic, A. Centeno, A. Pesquera, P. Godignon, A. Zurutuza Elorza, N. Camara, F.J.G. de Abajo, R. Hillenbrand, F.H.L. Koppens, *Nature* 487 (2012) 77–81.
- [146] L. Ju, B. Geng, J. Horng, C. Girit, M. Martin, Z. Hao, H.A. Bechtel, X. Liang, A. Zettl, Y.R. Shen, F. Wang, *Nat. Nanotechnol.* 6 (2011) 630–634.
- [147] M.M.Y.A. Alsaif, K. Latham, M.R. Field, D.D. Yao, N.V. Medehkar, G.A. Beane, R.B. Kaner, S.P. Russo, J.Z. Ou, K. Kalantar-zadeh, *Adv. Mater.* 26 (2014) 3931–3937.
- [148] M.W. Knight, N.S. King, L. Liu, H.O. Everitt, P. Nordlander, N.J. Halas, *ACS Nano* 8 (2014) 834–840.
- [149] J.B. Pendry, A.J. Holden, W.J. Stewart, I. Youngs, *Phys. Rev. Lett.* 76 (1996) 4773–4776.
- [150] F. Bisio, R. Proietti Zaccaria, R. Moroni, G. Maidecchi, A. Alabastri, G. Gonella, A. Giglia, L. Andolfi, S. Nannarone, L. Mattera, M. Canepa, *ACS Nano* 8 (2014) 9239–9247.
- [151] M. Castro-Lopez, D. Brinks, R. Sapienza, N.F. van Hulst, *Nano Lett.* 11 (2011) 4674–4678.
- [152] G. Davy, K.G. Stephen, *J. Phys. D: Appl. Phys.* 48 (2015) 184001.
- [153] M.W. Knight, L. Liu, Y. Wang, L. Brown, S. Mukherjee, N.S. King, H.O. Everitt, P. Nordlander, N.J. Halas, *Nano Lett.* 12 (2012) 6000–6004.
- [154] M.B. Ross, G.C. Schatz, *J. Phys. Chem. C* 118 (2014) 12506–12514.
- [155] M.W. Knight, T. Coenen, Y. Yang, B.J.M. Brenny, M. Losurdo, A.S. Brown, H.O. Everitt, A. Polman, *ACS Nano* 9 (2015) 2049–2060.
- [156] C. Yi, T.–H. Kim, W. Jiao, Y. Yang, A. Lazarides, K. Hingerl, G. Bruno, A. Brown, M. Losurdo, *Small* 8 (2012) 2721–2730.
- [157] P.C. Wu, M. Losurdo, T.–H. Kim, S. Choi, G. Bruno, A.S. Brown, *J. Vac. Sci. Technol. B* 25 (2007) 1019–1023.
- [158] C. Zhu, J. Li, Y. Yang, J. Huang, Y. Lu, R. Tan, N. Dai, W. Song, *Phys. Status Solidi A* 212 (2015) 1713–1718.
- [159] A.K. Pradhan, R.M. Mundle, K. Santiago, J.R. Skuza, B. Xiao, K.D. Song, M. Bahoura, R. Cheaito, P.E. Hopkins, *Sci. Rep.* 4 (2014) 6415.
- [160] C.T. Riley, T.A. Kieu, J.S.T. Smalley, S.H.A. Pan, S.J. Kim, K.W. Post, A. Kargar, D.N. Basov, X. Pan, Y. Fainman, D. Wang, D.J. Sirbully, *Phys. Status Solidi – Rapid Res. Lett.* 8 (2014) 948–952.
- [161] H. Kim, M. Osofsky, S.M. Prokes, O.J. Glembocki, A. Piqué, *Appl. Phys. Lett.* 102 (2013) 171103.
- [162] S.Q. Li, P. Guo, L. Zhang, W. Zhou, T.W. Odom, T. Seideman, J.B. Ketterson, R.P.H. Chang, *ACS Nano* 5 (2011) 9161–9170.
- [163] D. Traviss, R. Bruck, B. Mills, M. Abb, O.L. Muskens, *Appl. Phys. Lett.* 102 (2013) 121112.
- [164] S. Franzen, C. Rhodes, M. Cerruti, R.W. Gerber, M. Losego, J.–P. Maria, D.E. Aspnes, *Opt. Lett.* 34 (2009) 2867–2869.
- [165] G.V. Naik, J. Liu, A.V. Kildishev, V.M. Shalaev, A. Boltasseva, *Proc. Natl. Acad. Sci.* 109 (2012) 8834–8838.
- [166] J. Kim, Y. Zhao, A. Dutta, S.M. Choudhury, A. Kildishev, A. Alu, A. Boltasseva, Nanostructured transparent conducting oxide films for polarization control with plasmonic metasurfaces, in: *CLEO: 2014, Optical Society of America, San Jose, California, 2014*, p. FF2C.2.
- [167] J. Kim, G.V. Naik, A.V. Gavrilenko, K. Dondapati, V.I. Gavrilenko, S.M. Prokes, O.J. Glembocki, V.M. Shalaev, A. Boltasseva, *Phys. Rev. X* 3 (2013) 041037.
- [168] P.R. West, S. Ishii, G.V. Naik, N.K. Emani, V.M. Shalaev, A. Boltasseva, *Laser Photonics Rev.* 4 (2010) 795–808.
- [169] G.V. Naik, V.M. Shalaev, A. Boltasseva, *Adv. Mater.* 25 (2013) 3264–3294.
- [170] G.V. Naik, J.L. Schroeder, X. Ni, A.V. Kildishev, T.D. Sands, A. Boltasseva, *Opt. Mater. Express* 2 (2012) 478–489.
- [171] U. Guler, V.M. Shalaev, A. Boltasseva, *Mater. Today* 18 (2015) 227–237.
- [172] G.V. Naik, B. Saha, J. Liu, S.M. Saber, E.A. Stach, J.M.K. Irudayaraj, T.D. Sands, V.M. Shalaev, A. Boltasseva, *Proc. Natl. Acad. Sci.* 111 (2014) 7546–7551.
- [173] W. Li, U. Guler, N. Kinsey, G.V. Naik, A. Boltasseva, J. Guan, V.M. Shalaev, A.V. Kildishev, *Adv. Mater.* 26 (2014) 7959–7965.
- [174] G.V. Naik, J. Kim, A. Boltasseva, *Opt. Mater. Express* 1 (2011) 1090–1099.
- [175] A.E. Khalifa, M.A. Swillam, *J. Nanophotonics* 8 (2014) 084098.
- [176] P. Patsalas, S. Logothetidis, *J. Appl. Phys.* 90 (2001) 4725–4734.
- [177] P. Patsalas, N. Kalfagiannis, S. Kassavetis, *Materials* 8 (2015) 3128–3154.
- [178] M.B. Cortie, J. Giddings, A. Dowd, *Nanotechnology* 21 (2010) 115201.
- [179] A. Reinholdt, R. Pecena, A. Pinchuk, S. Runte, A.L. Stepanov, T.E. Weirich, U. Kreibitz, *Eur. Phys. J. D* 31 (2004) 69–76.
- [180] D. Steinmüller-Nethl, R. Kovacs, E. Gornik, P. Rödhammer, *Thin Solid Films* 237 (1994) 277–281.
- [181] S. Murai, K. Fujita, Y. Daido, R. Yasuhara, R. Kamakura, K. Tanaka, *Opt. Express* 24 (2016) 1143–1153.
- [182] U. Guler, J.C. Ndukaife, G.V. Naik, A.G.A. Nnanna, A.V. Kildishev, V.M. Shalaev, A. Boltasseva, *Nano Lett.* 13 (2013) 6078–6083.
- [183] L. Gui, S. Bagheri, N. Strohhfeldt, M. Hentschel, C.M. Zgrabik, B. Metzger, H. Linnenbank, E.L. Hu, H. Giessen, *Nano Lett.* 16 (2016) 5708–5713.
- [184] G.M. Matenoglou, L.E. Koutsokeras, P. Patsalas, *Appl. Phys. Lett.* 94 (2009) 152108.
- [185] D. Gall, C.S. Shin, R.T. Haasch, I. Petrov, J.E. Greene, *J. Appl. Phys.* 91 (2002) 5882–5886.
- [186] F.F. Klimashin, N. Koutná, H. Euchner, D. Holec, P.H. Mayrhofer, *J. Appl. Phys.* 120 (2016) 185301.
- [187] B.D. Ozsdolay, C.P. Mulligan, M. Guerette, L. Huang, D. Gall, *Thin Solid Films* 590 (2015) 276–283.
- [188] J.M. Molarius, A.S. Korhonen, E. Harju, R. Lappalainen, *Surf. Coat. Technol.* 33 (1987) 117–132.
- [189] L. Hiltunen, M. Leskelä, M. Mäkelä, L. Niinistö, E. Nykänen, P. Soininen, *Thin Solid Films* 166 (1988) 149–154.
- [190] A.J. Perry, J. Schoenes, *Vacuum* 36 (1986) 149–155.
- [191] R. Fix, R.G. Gordon, D.M. Hoffman, *Chem. Mater.* 5 (1993) 614–619.
- [192] R.A. Andrievskii, I.A. Anisimov, V.P. Makarov, V.P. Popova, *Thin Solid Films* 261 (1995) 83–86.
- [193] F. Esaka, K. Furuya, *J. Vac. Sci. Technol. A: Vac. Surf. Films* 15 (1997) 2521–2528.
- [194] L. Soriano, M. Abbate, H. Pen, P. Prieto, J.M. Sanz, *Solid State Commun.* 102 (1997) 291–296.
- [195] C. Mitterer, P.H. Mayrhofer, W. Waldhauser, E. Kelesoglu, P. Losbichler, *Surf. Coat. Technol.* 108–109 (1998) 230–235.
- [196] E. Budke, J. Kreppele-Hesse, H. Maidhof, H. Schüssler, *Surf. Coat. Technol.* 112 (1999) 108–113.
- [197] F. Lévy, P. Hones, P.E. Schmid, R. Sanjinés, M. Diserens, C. Wiemer, *Surf. Coat. Technol.* 120–121 (1999) 284–290.
- [198] L. Hultman, *Vacuum* 57 (2000) 1–30.
- [199] S. Niyomsoan, W. Grant, D.L. Olson, B. Mishra, *Thin Solid Films* 415 (2002) 187–194.
- [200] L.E. Koutsokeras, G.M. Matenoglou, P. Patsalas, *Thin Solid Films* 528 (2013) 49–52.
- [201] M. Östling, S. Nygren, C.S. Pettersson, H. Norström, R. Buchta, H.O. Blom, S. Berg, *Thin Solid Films* 145 (1986) 81–88.
- [202] M.H. Tsai, S.C. Sun, C.E. Tsai, S.H. Chuang, H.T. Chiu, *J. Appl. Phys.* 79 (1996) 6932–6938.
- [203] K.–H. Min, K.–C. Chun, K.–B. Kim, *J. Vac. Sci. Technol. B* 14 (1996) 3263–3269.
- [204] G.S. Chen, S.C. Huang, S.T. Chen, T.J. Yang, P.Y. Lee, J.H. Jou, T.C. Lin, *Appl. Phys. Lett.* 76 (2000) 2895–2897.
- [205] Y. Zeng, S.W. Russell, A.J. McKerrrow, L. Chen, T.L. Alford, *J. Vac. Sci. Technol. B* 18 (2000) 221–230.

- [206] S. Masaru, B.T. Mayumi, H. Yuichirou, A. Eiji, N. Atsushi, *Jpn. J. Appl. Phys.* 50 (2011) 05EA07.
- [207] K.E. Elers, V. Saanila, P.J. Soiminen, W.M. Li, J.T. Kostamo, S. Haukka, J. Juhanaja, W.F.A. Besling, *Chem. Vap. Deposition* 8 (2002) 149–153.
- [208] S.M. Aouadi, P.K. Shreeman, M. Williams, *J. Appl. Phys.* 96 (2004) 3949–3955.
- [209] J.P. Manaud, A. Poulon, S. Gomez, Y.L. Petitcorps, *Surf. Coat. Technol.* 202 (2007) 222–231.
- [210] H.-H. Hsu, C.-H. Cheng, Y.-L. Lin, S.-H. Chiou, C.-H. Huang, C.-P. Cheng, *Appl. Phys. Lett.* 103 (2013) 053902.
- [211] Y. Haruo, *Jpn. J. Appl. Phys.* 23 (1984) L895.
- [212] K.M. Yu, J.M. Jaklevic, E.E. Haller, S.K. Cheung, P.S. Kwok, *J. Appl. Phys.* 64 (1988) 1284–1291.
- [213] C.A. Dimitriadis, J.I. Lee, P. Patsalas, S. Logothetidis, D.H. Tassis, J. Brini, G. Kamarinos, *J. Appl. Phys.* 85 (1999) 4238–4242.
- [214] N. Kobayashi, H. Tanoue, G. Linker, *Nucl. Instrum. Methods Phys. Res., Sect. B* 33 (1988) 795–798.
- [215] H. Knau, A. Welti, A. Mielke, S. Senz, H.E. Stier, *Phys. C: Supercond.* 182 (1991) 39–46.
- [216] Z. Wang, A. Kawakami, Y. Uzawa, B. Komiyama, *J. Appl. Phys.* 79 (1996) 7837–7842.
- [217] R. Romestain, B. Delaet, P. Renaud-Goud, I. Wang, C. Jorel, J.C. Villegier, J.P. Poizat, *New J. Phys.* 6 (2004) 129.
- [218] J. Wu, B. Jin, Y. Xue, C. Zhang, H. Dai, L. Zhang, C. Cao, L. Kang, W. Xu, J. Chen, P. Wu, *Opt. Express* 19 (2011) 12021–12026.
- [219] S. Chaudhuri, I.J. Maasilta, *Appl. Phys. Lett.* 104 (2014) 122601.
- [220] M.H. Oliver, J.L. Schroeder, D.A. Ewoldt, I.H. Wildeson, V. Rawat, R. Colby, P.R. Cantwell, E.A. Stach, T.D. Sands, *Appl. Phys. Lett.* 93 (2008) 023109.
- [221] H. Goto, S.W. Lee, H.J. Lee, H.-J. Lee, J.S. Ha, M.W. Cho, T. Yao, *Phys. Status Solidi (c)* 5 (2008) 1659–1661.
- [222] K. Okamoto, S. Inoue, T. Nakano, J. Ohta, H. Fujioka, *J. Cryst. Growth* 311 (2009) 1311–1315.
- [223] Y. Gotoh, Y. Kashiwagi, M. Nagao, T. Kondo, H. Tsuji, J. Ishikawa, *J. Vac. Sci. Technol. B* 19 (2001) 1373–1376.
- [224] S. Gautier, Ph. Kominou, P. Patsalas, Th. Karakostas, S. Logothetidis, C.A. Dimitriadis, G. Nouet, *Semicond. Sci. Technol.* 18 (2003) 594.
- [225] A. Katz, S.J. Pearton, S. Nakahara, F.A. Baiocchi, E. Lane, J. Kovalchick, *J. Appl. Phys.* 73 (1993) 5208–5212.
- [226] P. Patsalas, C. Charitidis, S. Logothetidis, C.A. Dimitriadis, O. Valassiades, *J. Appl. Phys.* 86 (1999) 5296–5298.
- [227] Q. Sun, Z.-W. Fu, *Electrochim. Acta* 54 (2008) 403–409.
- [228] S.M. Kang, S.G. Yoon, S.J. Suh, D.H. Yoon, *Thin Solid Films* 516 (2008) 3568–3571.
- [229] S. Schleussner, T. Kubart, T. Törndahl, M. Edoff, *Thin Solid Films* 517 (2009) 5548–5552.
- [230] A. Malmros, K. Andersson, N. Rorsman, *Thin Solid Films* 520 (2012) 2162–2165.
- [231] R. Lucio-Porto, S. Bouhtiyaa, J.F. Pierson, A. Morel, F. Capon, P. Boulet, T. Brousse, *Electrochim. Acta* 141 (2014) 203–211.
- [232] E.K. Evangelou, N. Konofaos, X.A. Aslanoglou, C.A. Dimitriadis, P. Patsalas, S. Logothetidis, M. Kokkoris, E. Kossionides, R. Vlastou, R. Groetschel, *J. Appl. Phys.* 88 (2000) 7192–7196.
- [233] C.S. Kang, H.-J. Cho, Y.H. Kim, R. Choi, K. Onishi, A. Shahriar, J.C. Lee, *J. Vac. Sci. Technol. B* 21 (2003) 2026–2028.
- [234] H. Chih-Feng, T. Bing-Yue, L. Chih-Hsun, *Jpn. J. Appl. Phys.* 47 (2008) 872.
- [235] S. Chatterjee, Y. Kuo, J. Lu, *Microelectron. Eng.* 85 (2008) 202–209.
- [236] S. Lenci, B.D. Jaeger, L. Carbonell, J. Hu, G. Mannaert, D. Wellekens, S. You, B. Bakeroot, S. Decoutere, *IEEE Electron Device Lett.* 34 (2013) 1035–1037.
- [237] V.E. Babicheva, N. Kinsey, G.V. Naik, M. Ferrera, A.V. Lavrinenko, V.M. Shalaev, A. Boltasseva, *Opt. Express* 21 (2013) 27326–27337.
- [238] C. Wiemer, F. Lévy, F. Bussy, *Surf. Coat. Technol.* 68 (1994) 181–187.
- [239] C. Wiemer, R. Sanjinés, F. Lévy, *Surf. Coat. Technol.* 86 (1996) 372–376.
- [240] D. Gall, I. Petrov, J.E. Greene, *J. Appl. Phys.* 89 (2000) 401–409.
- [241] S.M. Aouadi, K.C. Wong, K.A.R. Mitchell, F. Namavar, E. Tobin, D.M. Mihut, S.L. Rohde, *Appl. Surf. Sci.* 229 (2004) 387–394.
- [242] S.M. Aouadi, P. Filip, M. Debessai, *Surf. Coat. Technol.* 187 (2004) 177–184.
- [243] M. Debessai, P. Filip, S.M. Aouadi, *Appl. Surf. Sci.* 236 (2004) 63–70.
- [244] S.M. Aouadi, A. Bohnhoff, T. Amriou, M. Williams, J.N. Hilfiker, N. Singh, J.A. Woollam, *J. Phys.: Condens. Matter* 18 (2006) S1691.
- [245] S.M. Aouadi, T. Maeruf, R.D. Twesten, D.M. Mihut, S.L. Rohde, *Surf. Coat. Technol.* 200 (2006) 3411–3417.
- [246] L.E. Koutsokeras, G. Abadias, Ch.E. Lekka, G.M. Matenoglou, D.F. Anagnostopoulos, G.A. Evangelakis, P. Patsalas, *Appl. Phys. Lett.* 93 (2008) 011904.
- [247] G. Hyett, M.A. Green, I.P. Parkin, *Chem. Vap. Deposition* 14 (2008) 309–312.
- [248] G.M. Matenoglou, C.E. Lekka, L.E. Koutsokeras, G. Karras, C. Kosmidis, G.A. Evangelakis, P. Patsalas, *J. Appl. Phys.* 105 (2009) 103714.
- [249] G.M. Matenoglou, L.E. Koutsokeras, C.E. Lekka, G. Abadias, C. Kosmidis, G.A. Evangelakis, P. Patsalas, *Surf. Coat. Technol.* 204 (2009) 911–914.
- [250] P. Patsalas, G. Abadias, G.M. Matenoglou, L.E. Koutsokeras, C.E. Lekka, *Surf. Coat. Technol.* 205 (2010) 1324–1330.
- [251] L.E. Koutsokeras, N. Hastas, S. Kassavetis, O. Valassiades, C. Charitidis, S. Logothetidis, P. Patsalas, *Surf. Coat. Technol.* 204 (2010) 2038–2041.
- [252] P. Djemia, M. Benhamida, K. Bouamama, L. Belliard, D. Faurie, G. Abadias, *Surf. Coat. Technol.* 215 (2013) 199–208.
- [253] G. Zhao, C. Zhao, L. Wu, G. Duan, J. Wang, G. Han, *J. Alloys Compd.* 569 (2013) 1–5.
- [254] H. Reddy, U. Guler, Z. Kudyshev, A.V. Kildishev, V.M. Shalaev, A. Boltasseva, *ACS Photonics* (2017).
- [255] O. Neumann, A.S. Urban, J. Day, S. Lal, P. Nordlander, N.J. Halas, *ACS Nano* 7 (2013) 42–49.
- [256] B. Rauschenbach, *J. Mater. Sci.* 21 (1986) 395–404.
- [257] I.A. Khan, M. Hassan, R. Ahmad, A. Qayyum, G. Murtaza, M. Zakoullah, R.S. Rawat, *Thin Solid Films* 516 (2008) 8255–8263.
- [258] M. Chhowalla, H.E. Unalan, *Nat. Mater.* 4 (2005) 317–322.
- [259] S.W. Ming Xu, Gang Yin, Jing Li, Yuxiang Zheng, Liangyao Chen, Yu Jia, *Appl. Phys. Lett.* 89 (2006) 151908.
- [260] P.J. Clarke, *J. Vac. Sci. Technol.* 14 (1977) 141–142.
- [261] L. Hultman, S.A. Barnett, J.E. Sundgren, J.E. Greene, *J. Cryst. Growth* 92 (1988) 639–656.
- [262] J. Musil, S. Kadlec, V. Valvoda, R. Kužel, R. Černý, *Surf. Coat. Technol.* 43 (1990) 259–269.
- [263] W.D. Sproul, P.J. Rudnik, M.E. Graham, S.L. Rohde, *Surf. Coat. Technol.* 43 (1990) 270–278.
- [264] P. Patsalas, C. Charitidis, S. Logothetidis, *Surf. Coat. Technol.* 125 (2000) 335–340.
- [265] N. Martin, R. Sanjinés, J. Takadoum, F. Lévy, *Surf. Coat. Technol.* 142–144 (2001) 615–620.
- [266] P.H. Mayrhofer, F. Kunc, J. Musil, C. Mitterer, *Thin Solid Films* 415 (2002) 151–159.
- [267] G. Abadias, P. Guerin, *Appl. Phys. Lett.* 93 (2008) 111908.
- [268] S. Mahieu, D. Depla, *J. Phys. D: Appl. Phys.* 42 (2009) 053002.
- [269] A. Bendavid, P.J. Martin, X. Wang, M. Wittling, T.J. Kinder, *J. Vac. Sci. Technol. A* 13 (1995) 1658–1664.
- [270] B.K. Tay, X. Shi, H.S. Yang, H.S. Tan, D. Chua, S.Y. Teo, *Surf. Coat. Technol.* 111 (1999) 229–233.
- [271] Y.H. Cheng, B.K. Tay, S.P. Lau, H. Kupfer, F. Richter, *J. Appl. Phys.* 92 (2002) 1845–1849.
- [272] S. Vepřek, *Surf. Coat. Technol.* 43 (1990) 154–166.
- [273] H. Hamamura, H. Komiyama, Y. Shimogaki, *Jpn. J. Appl. Phys.* 40 (2001) 1517.
- [274] H. Wang, A. Tiwari, A. Kvit, X. Zhang, J. Narayan, *Appl. Phys. Lett.* 80 (2002) 2323–2325.
- [275] W. Ensinger, B. Rauschenbach, *Nucl. Instrum. Methods Phys. Res. B* 80 (1993) 1409–1414.
- [276] G. Abadias, Y.Y. Tse, P. Guérin, V. Pelosin, *J. Appl. Phys.* 99 (2006) 113519.
- [277] J. Paulitsch, M. Schenkel, T. Zufraß, P.H. Mayrhofer, W.D. Münz, *Thin Solid Films* 518 (2010) 5558–5564.
- [278] G. Håkansson, L. Hultman, J.E. Sundgren, J.E. Greene, W.D. Münz, *Surf. Coat. Technol.* 48 (1991) 51–67.
- [279] B.W. Karr, I. Petrov, D.G. Cahill, J.E. Greene, *Appl. Phys. Lett.* 70 (1997) 1703–1705.
- [280] T.Q. Li, S. Noda, H. Komiyama, T. Yamamoto, Y. Ikuhara, *J. Vac. Sci. Technol. A* 21 (2003) 1717–1723.
- [281] D. Gall, S. Kodambaka, M.A. Wall, I. Petrov, J.E. Greene, *J. Appl. Phys.* 93 (2003) 9086–9094.
- [282] P. Patsalas, C. Gravalidis, S. Logothetidis, *J. Appl. Phys.* 96 (2004) 6234–6246.
- [283] L. Hultman, U. Helmersson, S.A. Barnett, J.E. Sundgren, J.E. Greene, *J. Appl. Phys.* 61 (1987) 552–555.
- [284] T. Lee, H. Seo, H. Hwang, B. Howe, S. Kodambaka, J.E. Greene, I. Petrov, *Thin Solid Films* 518 (2010) 5169–5172.
- [285] B. Karlsson, R.P. Shimshock, B.O. Seraphin, J.C. Haygarth, *Phys. Scr.* 25 (1982) 775.
- [286] S.M. Edlou, J.C. Simons, G.A. Al-Jumaily, N.A. Raouf, Optical and electrical properties of reactively sputtered TiN, ZrN, and HfN thin films, *Proc SPIE*, vol. 2262, 1994, pp. 96–106.
- [287] A.J. Perry, M. Georgson, W.D. Sproul, *Thin Solid Films* 157 (1988) 255–265.
- [288] V. Braic, M. Braic, G. Pavelescu, D. Melinte, D. Necsoiu, Influence of deposition parameters on optical properties of titanium nitride thin films, *Proc SPIE*, vol. 2461, 1995, pp. 597–599.
- [289] A. Bendavid, P.J. Martin, R.P. Netterfield, T.J. Kinder, *Surf. Interface Anal.* 24 (1996) 627–633.
- [290] D.R. McKenzie, W.D. McFall, H.H. Nguyen, Y. Yin, *Surf. Sci.* 357 (1996) 954–960.
- [291] J. Humlíček, A. Nebojsa, J. Hora, M. Stráský, J. Spousta, T. Šikola, *Thin Solid Films* 332 (1998) 25–29.
- [292] P. Huber, D. Manova, S. Mändl, B. Rauschenbach, *Surf. Coat. Technol.* 142–144 (2001) 418–423.
- [293] K. Postava, M. Aoyama, T. Yamaguchi, *Appl. Surf. Sci.* 175–176 (2001) 270–275.
- [294] E. Langereis, S.B.S. Heil, H.C.M. Knoop, W. Keuning, M.C.M.v.d. Sanden, W.M.M. Kessels, *J. Phys. D: Appl. Phys.* 42 (2009) 073001.
- [295] H. Van Bui, A.Y. Kovalgin, R.A.M. Wolters, *Appl. Surf. Sci.* 269 (2013) 45–49.
- [296] Z. YaBin, I. Masahiro, M. Yoshihiro, T. Atsushi, F. Tomoteru, K. Masashi, *Jpn. J. Appl. Phys.* 46 (2007) L1000.
- [297] H.-M. Tung, J.-H. Huang, D.-G. Tsai, C.-F. Ai, G.-P. Yu, *Mater. Sci. Eng. A* 500 (2009) 104–108.
- [298] M. Veszelei, K.E. Andersson, A. Roos, C.-G. Ribbing, Optical constants of sputtered ZrN films for heat mirror applications, *Proc SPIE*, vol. 2017, 1993, pp. 25–34.
- [299] M.A. Signore, D. Valerini, L. Tapfer, G. Caretto, A. Rizzo, *J. Vac. Sci. Technol. A* 29 (2011) 061507.
- [300] M. Del Re, R. Gouttebaron, J.P. Dauchot, P. Leclère, G. Terwagne, M. Heqç, *Surf. Coat. Technol.* 174–175 (2003) 240–245.
- [301] W.-J. Chou, G.-P. Yu, J.-H. Huang, *Thin Solid Films* 405 (2002) 162–169.
- [302] D. Wu, Z. Zhang, D. Fu, W. Fan, H. Guo, *Appl. Phys. A* 64 (1997) 593–595.
- [303] A.B. Mei, A. Rockett, L. Hultman, I. Petrov, J.E. Greene, *J. Appl. Phys.* 114 (2013) 193708.
- [304] D.F. Arias, Y.C. Arango, A. Devia, *Appl. Surf. Sci.* 253 (2006) 1683–1690.
- [305] J. Musil, I. Štěpánek, M. Kolego, O. Bláhová, J. Vyskočil, J. Kasl, *Mater. Sci. Eng. A* 163 (1993) 211–214.
- [306] P.C. Johnson, H. Randhawa, *Surf. Coat. Technol.* 33 (1987) 53–62.

- [307] C. Seungchan, L. Keunwoo, S. Pungkeun, J. Hyeongtag, K. Yangdo, *Jpn. J. Appl. Phys.* 46 (2007) 4085.
- [308] M.M. Larijani, M. Kiani, E. Jafari-Khamse, V. Fathollahi, *Appl. Phys. A* 117 (2014) 1179–1183.
- [309] G. Abadias, L.E. Koutsokeras, P. Guerin, P. Patsalas, *Thin Solid Films* 518 (2009) 1532–1537.
- [310] L.E. Koutsokeras, G. Abadias, *J. Appl. Phys.* 111 (2012) 093509.
- [311] A.B. Mei, B.M. Howe, C. Zhang, M. Sardela, J.N. Eckstein, L. Hultman, A. Rockett, I. Petrov, J.E. Greene, *J. Vac. Sci. Technol. A* 31 (2013) 061516.
- [312] S.A. Barnett, L. Hultman, J.E. Sundgren, F. Ronin, S. Rohde, *Appl. Phys. Lett.* 53 (1988) 400–402.
- [313] F.T.J. Smith, *J. Appl. Phys.* 41 (1970) 4227–4231.
- [314] L. Yuan, G. Fang, C. Li, M. Wang, N. Liu, L. Ai, Y. Cheng, H. Gao, X. Zhao, *Appl. Surf. Sci.* 253 (2007) 8538–8542.
- [315] R. Nowak, S. Maruno, *Mater. Sci. Eng. A* 202 (1995) 226–237.
- [316] B.O. Johansson, J.E. Sundgren, U. Helmersson, M.K. Hibbs, *Appl. Phys. Lett.* 44 (1984) 670–672.
- [317] W.D. Sproul, *Thin Solid Films* 118 (1984) 279–284.
- [318] E.-J.K. Kim, D.-H. Kim, *Electrochem. Solid State Lett.* 8 (2006) 2721–2730.
- [319] Y. Kim, A. Baunemann, H. Parala, A. Devi, R.A. Fischer, *Chem. Vap. Deposition* 11 (2005) 294–297.
- [320] K. Volz, M. Kiuchi, W. Ensinger, *Surf. Coat. Technol.* 120–121 (1999) 353–357.
- [321] A. Parkhomovskiy, B.E. Ishaug, A.M. Dabiran, P.I. Cohen, *J. Vac. Sci. Technol. A* 17 (1999) 2162–2165.
- [322] H.S. Seo, T.Y. Lee, I. Petrov, J.E. Greene, D. Gall, *J. Appl. Phys.* 97 (2005) 083521.
- [323] H.S. Seo, T.Y. Lee, J.G. Wen, I. Petrov, J.E. Greene, D. Gall, *J. Appl. Phys.* 96 (2004) 878–884.
- [324] D. Pilloud, A.S. Dehlinger, J.F. Pierson, A. Roman, L. Pichon, *Surf. Coat. Technol.* 174–175 (2003) 338–344.
- [325] M. Veszelei, K. Andersson, C.G. Ribbing, K. Järrendahl, H. Arwin, *Appl. Opt.* 33 (1994) 1993–2001.
- [326] S. Camelio, T. Girardeau, L. Pichon, A. Straboni, C. Fayoux, G. Ph., *J. Opt. A* 2 (2000) 442.
- [327] M. Strømme, R. Karmhag, C.G. Ribbing, *Opt. Mater.* 4 (1995) 629–639.
- [328] H. Gueddaoui, S. Maabed, G. Schmerber, M. Guemaz, J.C. Parlebas, *Eur. Phys. J. B* 60 (2007) 305–312.
- [329] L.L. Farrell, R.J. Reeves, A.R.H. Preston, B.M. Ludbrook, J.E. Downes, B.J. Ruck, S.M. Durbin, *Appl. Phys. Lett.* 96 (2010) 071914.
- [330] S.M. Aouadi, D.P. Singh, D.S. Stone, K. Polychronopoulou, F. Nahif, C. Rebbholz, C. Muratore, A.A. Voevodin, *Acta Mater.* 58 (2010) 5326–5331.
- [331] K. Sarakinos, J. Alami, D. Severin, P.M. Karimi, M. Wuttig, *Thin Solid Films* 516 (2008) 4568–4573.
- [332] A.B. Mei, R.B. Wilson, D. Li, D.G. Cahill, A. Rockett, J. Birch, L. Hultman, J.E. Greene, I. Petrov, *J. Appl. Phys.* 115 (2014) 214908.
- [333] P. Lazar, B. Rashkova, J. Redinger, R. Podloucky, C. Mitterer, C. Scheu, G. Dehm, *Thin Solid Films* 517 (2008) 1177–1181.
- [334] J.J. Olaya, S.E. Rodil, S. Muhl, *Thin Solid Films* 516 (2008) 8319–8326.
- [335] K. Radhakrishnan, N. Geok Ing, R. Gopalakrishnan, *Mater. Sci. Eng. B* 57 (1999) 224–227.
- [336] X. Sun, E. Kolawa, J.-S. Chen, J.S. Reid, M.-A. Nicolet, *Thin Solid Films* 356 (1993) 347–351.
- [337] C.S. Shin, Y.W. Kim, D. Gall, J.E. Greene, I. Petrov, *Thin Solid Films* 402 (2002) 172–182.
- [338] T. Riekkinen, J. Molarius, T. Laurila, A. Nurmela, I. Suni, J.K. Kivilahti, *Microelectron. Eng.* 64 (2002) 289–297.
- [339] G.R. Lee, J.J. Lee, C.S. Shin, I. Petrov, J.E. Greene, *Thin Solid Films* 475 (2005) 45–48.
- [340] S. Noda, K. Tepsanongsuk, Y. Tsuji, Y. Kajikawa, Y. Ogawa, H. Komiyama, *J. Vac. Sci. Technol. A* 22 (2004) 332–338.
- [341] A. Bendavid, P.J. Martin, T.J. Kinder, E.W. Preston, *Surf. Coat. Technol.* 163–164 (2003) 347–352.
- [342] V.N. Zhitomirsky, I. Grimberg, L. Rapoport, N.A. Travitzky, R.L. Boxman, S. Goldsmith, A. Raihel, I. Lapsker, B.Z. Weiss, *Thin Solid Films* 326 (1998) 134–142.
- [343] K.S. Havey, J.S. Zabinski, S.D. Walck, *Thin Solid Films* 303 (1997) 238–245.
- [344] L. Li, E. Niu, G. Lv, X. Zhang, H. Chen, S. Fan, C. Liu, S.-Z. Yang, *Appl. Surf. Sci.* 253 (2007) 6811–6816.
- [345] C.M. Ghimbeu, F. Sima, R.V. Ostaci, G. Socol, I.N. Mihailescu, C. Vix-Guterl, *Surf. Coat. Technol.* 211 (2012) 158–162.
- [346] A.H. Farha, A.O. Er, Y. Ufuktepe, G. Myneni, H.E. Elsayed-Ali, *Surf. Coat. Technol.* 206 (2011) 1168–1174.
- [347] S. Chaudhuri, I.J. Maasilta, L. Chandernagor, M. Ging, M. Lahtinen, *J. Vac. Sci. Technol. A* 31 (2013) 061502.
- [348] G. Rampelberg, K. Devloo-Casier, D. Deduysche, M. Schaeckers, N. Blasco, C. Detavernier, *Appl. Phys. Lett.* 102 (2013) 111910.
- [349] B.T. Mayumi, S. Masaru, S. Hiroshi, M. Hideaki, I. Shun, A. Eiji, N. Atsushi, *Jpn. J. Appl. Phys.* 50 (2011) 05EA06.
- [350] M. Ritala, T. Asikainen, M. Leskelä, J. Jokinen, R. Lappalainen, M. Utriainen, L. Niinistö, E. Ristolainen, *Appl. Surf. Sci.* 120 (1997) 199–212.
- [351] R. Sreenivasan, T. Sugawara, K.C. Saraswat, P.C. McIntyre, *Appl. Phys. Lett.* 90 (2007) 102101.
- [352] H. Kim, A.J. Kellock, S.M. Rosnagel, *J. Appl. Phys.* 92 (2002) 7080–7085.
- [353] T. Chen, C. Xu, T.H. Baum, G.T. Stauff, J.F. Roeder, A.G. DiPasquale, A.L. Rheingold, *Chem. Mater.* 22 (2010) 27–35.
- [354] C.H. Ma, J.H. Huang, H. Chen, *Surf. Coat. Technol.* 133–134 (2000) 289–294.
- [355] M.L. Klingenberg, J.D. Demaree, *Surf. Coat. Technol.* 146–147 (2001) 243–249.
- [356] W. Ensinger, M. Kiuchi, M. Satou, *J. Appl. Phys.* 77 (1995) 6630–6635.
- [357] L. Hultman, M. Shinn, P.B. Mirkarimi, S.A. Barnett, *J. Cryst. Growth* 135 (1994) 309–317.
- [358] K. Kutschev, B. Rashkova, J. Shen, D. Edwards, C. Mitterer, G. Dehm, *Thin Solid Films* 516 (2007) 369–373.
- [359] A.B. Mei, M. Tuteja, D.G. Sangiovanni, R.T. Haasch, A. Rockett, L. Hultman, I. Petrov, J.E. Greene, *J. Mater. Chem. C* 4 (2016) 7924–7938.
- [360] K. Zhang, K. Balasubramanian, B.D. Ozsdolay, C.P. Mulligan, S.V. Khare, W.T. Zheng, D. Gall, *Surf. Coat. Technol.* 288 (2016) 105–114.
- [361] D.A. Papaconstantopoulos, W.E. Pickett, B.M. Klein, L.L. Boyer, *Phys. Rev. B* 31 (1985) 752–761.
- [362] A. Nigro, G. Nobile, M.G. Rubino, R. Vaglio, *Phys. Rev. B* 37 (1988) 3970–3972.
- [363] D.D. Bacon, A.T. English, S. Nakahara, F.G. Peters, H. Schreiber, W.R. Sinclair, R.B.V. Dover, *J. Appl. Phys.* 54 (1983) 6509–6516.
- [364] Z. Caihong, J. Biaobing, H. Jianguang, K. Iwao, M. Hironaru, J. Xiaoqing, L. Lanju, K. Lin, C. Jian, W. Peiheng, T. Masayoshi, *New J. Phys.* 15 (2013) 055017.
- [365] Z. Mario, F. Ludwig, D. Julia, L. Sven, A. Solveig, T. Julia, M. Hans-Georg, *Supercond. Sci. Technol.* 26 (2013) 025008.
- [366] S. Thakoor, J.L. Lamb, A.P. Thakoor, S.K. Khanna, *J. Appl. Phys.* 58 (1985) 4643–4648.
- [367] D.W. Deis, J.R. Gavalier, J.K. Hulm, C.K. Jones, *J. Appl. Phys.* 40 (1969) 2153–2156.
- [368] Y. Saito, T. Anayama, K. Yasohama, K. Yasukouchi, Y. Onodera, *Appl. Phys. Lett.* 14 (1969) 285–286.
- [369] J.C. Caicedo, G. Zambrano, W. Aperador, L. Escobar-Alarcon, E. Camps, *Appl. Surf. Sci.* 258 (2011) 312–320.
- [370] H. Kindlund, D.G. Sangiovanni, J. Lu, J. Jensen, V. Chirita, I. Petrov, J.E. Greene, L. Hultman, *J. Vac. Sci. Technol. A* 32 (2014) 030603.
- [371] B.A. Latella, B.K. Gan, K.E. Davies, D.R. McKenzie, D.G. McCulloch, *Surf. Coat. Technol.* 200 (2006) 3605–3611.
- [372] G. Ramirez, S.E. Rodil, H. Arzate, S. Muhl, J.J. Olaya, *Appl. Surf. Sci.* 257 (2011) 2555–2559.
- [373] M. Benkahoul, E. Martinez, A. Karimi, R. Sanjinés, F. Lévy, *Surf. Coat. Technol.* 180–181 (2004) 178–183.
- [374] M. Fenker, M. Balzer, R.V. Büchi, H.A. Jehn, H. Kappl, J.J. Lee, *Surf. Coat. Technol.* 163–164 (2003) 169–175.
- [375] G.R. Lee, H. Kim, H.S. Choi, J.J. Lee, *Surf. Coat. Technol.* 201 (2007) 5207–5210.
- [376] G. Abadias, L.E. Koutsokeras, S.N. Dub, G.N. Tolmachova, A. Debelle, T. Sauvage, P. Villechaise, *J. Vac. Sci. Technol. A* 28 (2010) 541–551.
- [377] E. Bozorg-Grayeli, Z. Li, M. Asheghi, G. Delgado, A. Pokrovsky, M. Panzer, D. Wack, K.E. Goodson, *Appl. Phys. Lett.* 99 (2011) 261906.
- [378] H.B. Nie, S.Y. Xu, S.J. Wang, L.P. You, Z. Yang, C.K. Ong, J. Li, T.Y.F. Liew, *Appl. Phys. A – Mater. Sci. Process.* 73 (2001) 229–236.
- [379] C.-C. Chang, J.S. Jeng, J.S. Chen, *Thin Solid Films* 413 (2002) 46–51.
- [380] J. Mistrik, K. Takahashi, R. Antos, M. Aoyama, T. Yamaguchi, Y. Anma, Y. Fukuda, M.B. Takeyama, A. Noya, Z.T. Jiang, S.M. Thurgate, G.V. Riessen, *Thin Solid Films* 455–456 (2004) 473–477.
- [381] G.M. Matenoglou, L.E. Koutsokeras, C.E. Lekka, G. Abadias, S. Camelio, G.A. Evangelakis, C. Kosmidis, P. Patsalas, *J. Appl. Phys.* 104 (2008) 124907.
- [382] E. Langereis, H.C.M. Knoops, A.J.M. Mackus, F. Roozeboom, M.C.M.v.d. Sanden, W.M.M. Sanden, W.M.M. Kessels, *J. Appl. Phys.* 102 (2007) 083517.
- [383] Y.Y. Wu, M. Eizenberg, *Mater. Chem. Phys.* 101 (2007) 269–275.
- [384] L.E. Koutsokeras, G. Abadias, P. Patsalas, *J. Appl. Phys.* 110 (2011) 043535.
- [385] C.S. Shin, D. Gall, Y.W. Kim, P. Desjardins, I. Petrov, J.E. Greene, M. Odén, L. Hultman, *J. Appl. Phys.* 90 (2001) 2879–2885.
- [386] C.S. Shin, D. Gall, P. Desjardins, A. Vailionis, H. Kim, I. Petrov, J.E. Greene, M. Odén, *Appl. Phys. Lett.* 75 (1999) 3808–3810.
- [387] K. Nikola, H. David, S. Ondřej, F.K. Fedor, H.M. Paul, *J. Phys. D: Appl. Phys.* 49 (2016) 375303.
- [388] A. Glaser, S. Surnev, M.G. Ramsey, P. Lazar, J. Redinger, R. Podloucky, F.P. Netzer, *Surf. Sci.* 601 (2007) 4817–4823.
- [389] K. Tanabe, H. Asano, Y. Katoh, O. Michikami, *J. Appl. Phys.* 63 (1988) 1733–1739.
- [390] R. Sanjinés, M. Benkahoul, C.S. Sandu, P.E. Schmid, F. Lévy, *Thin Solid Films* 494 (2006) 190–195.
- [391] M.W. Koneveckí, K.L. Westra, B.T. Sullivan, K.E. Kornelson, M.J. Brett, *Thin Solid Films* 232 (1993) 228–231.
- [392] D. Gall, C.-S. Shin, T. Spila, M. Odén, M.J.H. Senna, J.E. Greene, I. Petrov, *J. Appl. Phys.* 91 (2002) 3589–3597.
- [393] J.J. Olaya, S.E. Rodil, S. Muhl, E. Sánchez, *Thin Solid Films* 474 (2005) 119–126.
- [394] S. Logothetidis, N. Kalfagiannis, K. Sarakinos, P. Patsalas, *Surf. Coat. Technol.* 200 (2006) 6176–6180.
- [395] T. Hurkmans, D.B. Lewis, J.S. Brooks, W.D. Münz, *Surf. Coat. Technol.* 86 (1996) 192–199.
- [396] A.P. Ehiasarian, W.D. Münz, L. Hultman, U. Helmersson, I. Petrov, *Surf. Coat. Technol.* 163–164 (2003) 267–272.
- [397] J. Alami, K. Sarakinos, F. Uslu, M. Wuttig, *J. Phys. D: Appl. Phys.* 42 (2009) 015304.
- [398] Y.H. Liu, K. Wang, W. Lin, A. Chinchore, M. Shi, J. Pak, A.R. Smith, C. Constantin, *Thin Solid Films* 520 (2011) 90–94.
- [399] F. Schuster, F. Maury, J.F. Nowak, C. Bernard, *Surf. Coat. Technol.* 46 (1991) 275–288.
- [400] L. Cunha, M. Andritschky, K. Pischow, Z. Wang, *Thin Solid Films* 355–356 (1999) 465–471.
- [401] P. Hones, R. Sanjines, F. Levy, *Surf. Coat. Technol.* 94 (1997) 398–402.
- [402] A. Barata, L. Cunha, C. Moura, *Thin Solid Films* 398–399 (2001) 501–506.
- [403] P.H. Mayrhofer, G. Tischer, C. Mitterer, *Surf. Coat. Technol.* 142–144 (2001) 78–84.
- [404] G. Bertrand, H. Mahdjoub, C. Meunier, *Surf. Coat. Technol.* 126 (2000) 199–209.
- [405] X.-M. He, N. Baker, B.A. Kehler, K.C. Walter, M. Nastasi, Y. Nakamura, *J. Vac. Sci. Technol. A* 18 (2000) 30–36.

- [406] C. Gautier, H. Moussaoui, F. Elstner, J. Machet, *Surf. Coat. Technol.* 86 (1996) 254–262.
- [407] A. Leyland, M. Bin-Sudin, A.S. James, M.R. Kalantary, P.B. Wells, A. Matthews, J. Housden, B. Garside, *Surf. Coat. Technol.* 60 (1993) 474–479.
- [408] X.F. Duan, W.B. Mi, Z.B. Guo, H.L. Bai, *J. Appl. Phys.* 113 (2013) 023701.
- [409] A. Filippetti, W.E. Pickett, B.M. Klein, *Phys. Rev. B* 59 (1999) 7043–7050.
- [410] D. Gall, C.-S. Shin, R.T. Haasch, I. Petrov, J.E. Greene, *J. Appl. Phys.* 91 (2002) 5882–5886.
- [411] S.M. Aouadi, T.Z. Gorishnyy, D.M. Schultze, S.L. Rohde, *Surf. Coat. Technol.* 153 (2002) 1–9.
- [412] S. Logothetidis, P. Patsalas, K. Sarakinos, C. Charitidis, C. Metaxa, *Surf. Coat. Technol.* 180–181 (2004) 637–641.
- [413] J. Kim, D.M. Brown, W. Katz, *J. Electrochem. Soc.* 130 (1983) 1196.
- [414] C. Sarioglu, U. Demirler, M.K. Kazmanli, M. Urgen, *Surf. Coat. Technol.* 190 (2005) 238–243.
- [415] R. Sanjinés, P. Hones, F. Lévy, *Thin Solid Films* 332 (1998) 225–229.
- [416] Y. Zhang, N. Haberkorn, F. Ronning, H. Wang, N.A. Mara, M. Zhuo, L. Chen, J.H. Lee, K.J. Blackmore, E. Bauer, A.K. Burrell, T.M. McCleskey, M.E. Hawley, R.K. Schulze, L. Civalte, T. Tajima, Q. Jia, *J. Am. Chem. Soc.* 133 (2011) 20735–20737.
- [417] K. Inumaru, K. Baba, S. Yamanaka, *Phys. Rev. B* 73 (2006) 052504.
- [418] G. Linker, R. Smithey, O. Meyer, *J. Phys. F: Met. Phys.* 14 (1984) L115.
- [419] M. Maoujoud, L. Binst, P. Delcambe, M. Offergeld-Jardinier, F. Bouillon, *Surf. Coat. Technol.* 52 (1992) 179–185.
- [420] A.J. Perry, A.W. Baouchi, J.H. Petersen, S.D. Pozder, *Surf. Coat. Technol.* 54 (1992) 261–265.
- [421] W. Enginger, M. Kiuchi, *Surf. Coat. Technol.* 84 (1996) 425–428.
- [422] V. Miiikkulainen, M. Suvanto, T.A. Pakkanen, S. Siitonen, P. Karvinen, M. Kuittinen, H. Kisonen, *Surf. Coat. Technol.* 202 (2008) 5103–5109.
- [423] S.L. Roberson, D. Finello, R.F. Davis, *Surf. Coat. Technol.* 102 (1998) 256–259.
- [424] D.K. Nandi, U.K. Sen, D. Choudhury, S. Mitra, S.K. Sarkar, *ACS Appl. Mater. Interfaces* 6 (2014) 6606–6615.
- [425] M. Uekubo, T. Oku, K. Nii, M. Murakami, K. Takahiro, S. Yamaguchi, T. Nakano, T. Ohta, *Thin Solid Films* 286 (1996) 170–175.
- [426] M. Wen, Q.N. Meng, W.X. Yu, W.T. Zheng, S.X. Mao, M.J. Hua, *Surf. Coat. Technol.* 205 (2010) 1953–1961.
- [427] P.-C. Jiang, J.S. Chen, Y.K. Lin, *J. Vac. Sci. Technol. A* 21 (2003) 616–622.
- [428] N.B. Srinivasan, T.B. Thiede, T. de los Arcos, D. Rogalla, H.-W. Becker, A. Devi, R.A. Fischer, *Phys. Status Solidi A* 211 (2014) 260–266.
- [429] J.S. Becker, S. Suh, S. Wang, R.G. Gordon, *Chem. Mater.* 15 (2003) 2969–2976.
- [430] J.S. Becker, R.G. Gordon, *Appl. Phys. Lett.* 82 (2003) 2239–2241.
- [431] N.M.G. Parreira, T. Polcar, N. Martin, O. Banakh, A. Cavaleiro, *Plasma Process. Polym.* 4 (2007) S69–S75.
- [432] C. Metaxa, B.D. Ozsdolay, T. Zorba, K. Paraskevopoulos, D. Gall, P. Patsalas, *J. Vac. Sci. Technol. A* 35 (2017) 031501.
- [433] N. Koutná, D. Holec, O. Svoboda, F.F. Klimashin, P.H. Mayrhofer, *J. Phys. D* 49 (2016) 375303.
- [434] L.E. Koutsokeras, G. Abadias, G. Lekka, E. Ch, G.M. Matenoglou, D.F. Anagnostopoulos, G.A. Evangelakis, P. Patsalas, *Appl. Phys. Lett.* 93 (2008) 011904.
- [435] M. Prodyut, T. Christos, *Nanotechnology* 19 (2008) 205202.
- [436] S. Komiyama, Y. Sutou, J. Koike, *Metall. Mater. Trans. A* 42 (2011) 3310–3315.
- [437] J.H. Moser, F. Tian, O. Haller, D.B. Bergstrom, I. Petrov, J.E. Greene, C. Wiemer, *Thin Solid Films* 253 (1994) 445–450.
- [438] F. Tian, J. D'Arcy-Gall, T.Y. Lee, M. Sardela, D. Gall, I. Petrov, J.E. Greene, *J. Vac. Sci. Technol. A* 21 (2002) 140–146.
- [439] S. Kassavetis, D.V. Bellas, G. Abadias, E. Lidorikis, P. Patsalas, *Appl. Phys. Lett.* 108 (2016) 263110.
- [440] H. Klostermann, F. Fietzke, R. Labitzke, T. Modes, O. Zywitzki, *Surf. Coat. Technol.* 204 (2009) 1076–1080.
- [441] C. Metaxa, S. Kassavetis, J.F. Pierson, D. Gall, P. Patsalas, *ACS Appl. Mater. Interfaces* 9 (2017) 10825–10834.
- [442] G. Abadias, L.E. Koutsokeras, A. Sizios, P. Patsalas, *Thin Solid Films* 538 (2013) 56–70.
- [443] B.T. Mayumi, S. Masaru, A. Eiji, N. Atsushi, *Jpn. J. Appl. Phys.* 53 (2014) 02BC04.
- [444] F. Tian, J. D'Arcy-Gall, T.-Y. Lee, M. Sardela, D. Gall, I. Petrov, J.E. Greene, *J. Vac. Sci. Technol. A* 21 (2003) 140–146.
- [445] L. Cheng-Shih, C. Edward-Yi, C. Li, F. Chao-Yi, H. Yao-Lin, H. Jian-Sheng, *Jpn. J. Appl. Phys.* 42 (2003) 4193.
- [446] S. Miki, T. Yamashita, H. Terai, Z. Wang, *Opt. Express* 21 (2013) 10208–10214.
- [447] C. Schuck, W.H.P. Pernice, H.X. Tang, *Sci. Rep.* 3 (2013) 1893.
- [448] K. Vasu, G.M. Gopikrishnan, M. Ghanashyam Krishna, K.A. Padmanabhan, *Appl. Phys. A* 108 (2012) 993–1000.
- [449] O. Ambacher, *J. Phys. D: Appl. Phys.* 31 (1998) 2653.
- [450] W.M. Yim, E.J. Stofko, P.J. Zanzucchi, J.I. Pankove, M. Ettenberg, S.L. Gilbert, *J. Appl. Phys.* 44 (1973) 292–296.
- [451] J. Li, K.B. Nam, M.L. Nakarmi, J.Y. Lin, H.X. Jiang, P. Carrier, S.-H. Wei, *Appl. Phys. Lett.* 83 (2003) 5163–5165.
- [452] H. Yamashita, K. Fukui, S. Misawa, S. Yoshida, *J. Appl. Phys.* 50 (1979) 896–898.
- [453] S. Kassavetis, G. Abadias, G. Vourlias, G. Bantsis, S. Logothetidis, P. Patsalas, *Surf. Coat. Technol.* 295 (2016) 125–129.
- [454] N. Pliatsikas, A. Sizios, S. Kassavetis, G. Vourlias, P. Patsalas, *Surf. Coat. Technol.* 257 (2014) 63–69.
- [455] J.Y. Rauch, C. Rousselot, N. Martin, *Surf. Coat. Technol.* 157 (2002) 138–143.
- [456] S.B. Sant, K.S. Gill, *Surf. Coat. Technol.* 68 (1994) 152–156.
- [457] K. Valleti, D. Murali Krishna, S.V. Joshi, *Sol. Energy Mater. Sol. Cells* 121 (2014) 14–21.
- [458] R. Rachbauer, J.J. Gengler, A.A. Voevodin, K. Resch, P.H. Mayrhofer, *Acta Mater.* 60 (2012) 2091–2096.
- [459] S. Zhao, D. Zhu, C.-G. Ribbing, Colour control and selectivity in TiAlN solar-thermal absorbers, *Proc. of SPIE*, vol. 8168, 2011, pp. 81680G–81689.
- [460] H.C. Barshilia, N. Selvakumar, K.S. Rajam, A. Biswas, *Sol. Energy Mater. Sol. Cells* 92 (2008) 1425–1433.
- [461] Z. Ren, G.A.R. Jian, R.S. Williams, C.H. Booth, D.K. Shuh, *J. Appl. Phys.* 83 (1998) 7613–7617.
- [462] J. Neidhardt, Z. Czigany, B. Sartory, R. Tessadri, M. O'Sullivan, C. Mitterer, *Acta Mater.* 54 (2006) 4193–4200.
- [463] P.H. Mayrhofer, M. Stoiber, C. Mitterer, *Scr. Mater.* 53 (2005) 241–245.
- [464] S. Veprek, A. Niederhofer, K. Moto, T. Bolom, H.-D. Männling, P. Nesladek, G. Dollinger, A. Bergmaier, *Surf. Coat. Technol.* 133–134 (2000) 152–159.
- [465] T.D. Moustakas, T. Lei, R.J. Molnar, *Physica B* 185 (1993) 14.
- [466] M. Junaid, C.-L. Hsiao, J. Palisaitis, J. Jensen, P.O.A. Persson, L. Hultman, *J. Birch, Appl. Phys. Lett.* 98 (2011) 141915.
- [467] H.C.M. Knoop, L. Baggetto, E. Langerer, M.C.M. van de Sanden, J.H. Klootwijk, F. Roozeboom, R.A.H. Niessen, P.H.L. Notten, W.M.M. Kessels, *J. Electrochem. Soc.* 155 (2008) G287–G294.
- [468] O.H. Kim, D. Kim, T. Anderson, *J. Vac. Sci. Technol. A* 27 (2009) 923–928.
- [469] D. Gall, I. Petrov, J.E. Greene, *J. Appl. Phys.* 89 (2000) 401–409.
- [470] D. Gall, M. Stoehr, J.E. Greene, *Phys. Rev. B* 64 (2001) 174302.
- [471] S. Kassavetis, A. Hodroj, C. Metaxa, S. Logothetidis, J.F. Pierson, P. Patsalas, *J. Appl. Phys.* 120 (2016) 225106.
- [472] A. Hodroj, J.F. Pierson, *Appl. Surf. Sci.* 257 (2011) 8525–8528.
- [473] H. Shimizu, M. Shirai, N. Suzuki, *Physica B* 237 (1997) 546–547.
- [474] S.W. King, R.J. Nemanich, R.F. Davis, *Appl. Phys. Lett.* 105 (2014) 081606.
- [475] J.M. Gregoire, S.D. Kirby, G.E. Scopelianos, F.H. Lee, R.B.v. Dover, *J. Appl. Phys.* 104 (2008) 074913.
- [476] M.A. Moram, S.V. Novikov, A.J. Kent, C. Nörenberg, C.T. Foxon, C.J. Humphreys, *J. Cryst. Growth* 310 (2008) 2746–2750.
- [477] S. Mahieu, P. Ghekie, D. Depla, R. De Gryse, *Thin Solid Films* 515 (2006) 1229.
- [478] J.A. Thornton, *J. Vac. Sci. Technol. A* 4 (1986) 3059–3065.
- [479] A. Anders, *Thin Solid Films* 518 (2010) 4087–4090.
- [480] T.Q. Li, S. Noda, Y. Tsuji, T. Ohsawa, H. Komiyama, *J. Vac. Sci. Technol. A* 20 (2002) 583–588.
- [481] I. Petrov, P.B. Barna, L. Hultman, J.E. Greene, *J. Vac. Sci. Technol. A* 21 (2003) S117–S128.
- [482] S. Mahieu, D. Depla, R. De Gryse, *J. Phys.: Conf. Ser.* 100 (2008) 082003.
- [483] Y. Ren, X. Liu, X. Tan, E. Westkämper, *Comput. Mater. Sci.* 77 (2013) 102–107.
- [484] G. Abadias, W.P. Leroy, S. Mahieu, D. Depla, *J. Phys. D: Appl. Phys.* 46 (2013) 055301.
- [485] M. Marlo, V. Milman, *Phys. Rev. B* 62 (2000) 2899–2907.
- [486] A. Zaoui, S. Kacimi, A. Boukortt, B. Bouhaf, *Physica B* 405 (2010) 153–157.
- [487] D. Magnfält, A. Fillon, R.D. Boyd, U. Helmersson, K. Sarakinos, G. Abadias, *J. Appl. Phys.* 119 (2016) 055305.
- [488] E. Zhao, J. Wang, J. Meng, Z. Wu, *Comput. Mater. Sci.* 47 (2010) 1064–1071.
- [489] E. Chason, M. Karlson, J.J. Colin, D. Magnfält, K. Sarakinos, G. Abadias, *J. Appl. Phys.* 119 (2016) 145307.
- [490] J. Kim, S.-H. Jhi, K.R. Lee, *J. Appl. Phys.* 110 (2011) 083501.
- [491] R. Daniel, E. Jäger, J. Todt, B. Sartory, C. Mitterer, J. Keckes, *J. Appl. Phys.* 115 (2014) 203507.
- [492] C. Stampfl, W. Mannstadt, R. Asahi, A.J. Freeman, *Phys. Rev. B* 63 (2001) 155106.
- [493] I. Petrov, L. Hultman, J.-E. Sundgren, J.E. Greene, *J. Vac. Sci. Technol. A* 10 (1992) 265.
- [494] G. Abadias, *Surf. Coat. Technol.* 202 (2008) 2223–2235.
- [495] A.P. Ehiassarian, A. Vetushka, Y.A. Gonzalvo, G. Sfrn, L. Székely, P.B. Barna, *J. Appl. Phys.* 109 (2011) 104314.
- [496] J.-D. Kamminga, T.H.de Keijer, R. Delhez, E.J. Mittemeijer, *J. Appl. Phys.* 88 (2000) 6332.
- [497] G. Abadias, V.I. Ivashchenko, L. Belliard, P. Djemia, *Acta Mater.* 60 (2012) 5601–5614.
- [498] G. Abadias, M.B. Kanoun, S. Goumri-Said, L.E. Koutsokeras, S.N. Dub, Ph. Djemia, *Phys. Rev. B* 90 (2014) 144107.
- [499] M. Beckers, N. Schell, R.M.S. Martins, A. Mücklich, W. Möller, *J. Appl. Phys.* 98 (2005) 044901.
- [500] M. Beckers, N. Schell, R.M.S. Martins, A. Mücklich, W. Möller, *J. Vac. Sci. Technol. A* 23 (2005) 1384.
- [501] J.L.G. Greczynski, J. Jensen, S. Bolz, W. Kölker, Ch. Schiffers, O. Lemmer, J.E. Greene, L. Hultman, *Surf. Coat. Technol.* 257 (2014) 15–25.
- [502] N.J. Halas, M.L. Brongersma, P. Nordlander, *Nat. Nanotechnol.* 10 (2015) 25–34.
- [503] S. Ishii, S.L. Shinde, W. Jevasuwan, N. Fukata, T. Nagao, *ACS Photonics* (2016) 1552–1557.
- [504] H. Ferguson, U. Guler, N. Kinsey, V.M. Shalae, T.B. Norris, A. Boltasseva, Hot electron relaxation in thin titanium nitride films, *Conference on Lasers and Electro-Optics OSA Technical Digest* (2016), Opt. Soc. of America (Ed.).
- [505] S.M. Sze, *Physics of Semiconductor Devices*, J. Wiley & Sons, New York, 1981.
- [506] Y. Gotoh, H. Tsuji, J. Ishikawa, *J. Vac. Sci. Technol. B* 21 (2003) 1607–1611.
- [507] P.-C. Jiang, Y.-S. Lai, J.S. Chen, *Appl. Phys. Lett.* 89 (2006) 122107.
- [508] R. France, T. Xu, P. Chen, R. Chandrasekaran, T.D. Moustakas, *Appl. Phys. Lett.* 90 (2007) 062115.
- [509] D.C. Hoffman, D.M. Lee, V. Pershina, *Transactinides and the Future Elements*, In: *The Chemistry of the Actinide and Transactinide Elements*, Springer Science + - Business Media, The Netherlands, 2006.
- [510] P.E. Frieberthshauer, J.W. McCamont, *J. Vac. Sci. Technol. A* 6 (1969) 184–187.
- [511] I.C. McCollm, *Ceramic Science for Materials Technologists*, Kluwer Publishers, Boston, 1983.

- [512] L.B. Pankratz, J.M. Stuve, N.A. Gokcen, Thermodynamic Data for Mineral Technology, Bulletin 677, Bureau of Mines, U.S., 1984.
- [513] T. Akashi, IEEE Trans. Sens. Micromach. 125 (2005) 182–188.
- [514] E.C. Gemelli, N.H.A. Camargo, Revista Matéria 12 (2007) 525–531.
- [515] J.E. Nestell Jr., Optical Properties and Structure of Vanadium, Niobium, Tantalum, Chromium, Molybdenum, and Tungsten Films, Dartmouth College, Hanover, 1979, Thesis.
- [516] A.B. Mei, O. Hellman, N. Wireklint, C.M. Schlepütz, D.G. Sangiovanni, B. Alling, A. Rockett, L. Hultman, I. Petrov, J.E. Greene, Phys. Rev. B 91 (2015) 054101.
- [517] T. Yamashita, K. Hamasaki, T. Komata, Adv. Cryog. Eng. Mater. 32 (1986) 617–626.
- [518] N. Engheta, Phys. World 23 (2010) 31.
- [519] Z. Jacob, L.V. Alekseyev, E.E. Narimanov, Opt. Express 14 (2006) 8247–8256.
- [520] P.B. Johnson, R.W. Christy, Phys. Rev. B 9 (1974) 5056–5070.
- [521] A.I. Golovashkin, I.E. Leskina, G.P. Motulevich, A.A. Shubin, Sov. Phys. JETP 29 (1969) 27–34.
- [522] E.D. Palik, Handbook of Optical Constants of Solids, Academic Press, 1998.
- [523] S. Logothetidis, I. Alexandrou, S. Kokkou, Surf. Coat. Technol. 80 (1996) 66–71.
- [524] P.B. Johnson, R.W. Christy, Phys. Rev. B 6 (1972) 4370–4379.
- [525] M.J. Vasile, A.B. Emerson, F.A. Baiocchi, J. Vac. Sci. Technol. A 8 (1990) 99–105.
- [526] Y. Fukuda, F. Honda, J.W. Rabalais, Surf. Sci. 91 (1980) 165–174.
- [527] P. Blaha, K. Schwarz, G.K.H. Madsen, D. Kvasnicka, J. Luitz, K. WIEN2, An Augmented Plane Wave Local Orbitals Program for Calculating Crystal Properties, Techn. Universität, Wien, Austria, 2001.
- [528] J.P. Perdew, K. Burke, M. Ernzerhof, Phys. Rev. Lett. 77 (1996) 3865–3868.
- [529] W.A. Harrison, Electronic Structure and the Properties of Solids: The Physics of the Chemical Bond, Dover Publications, 2012.
- [530] V.P. Zhukov, V.A. Gubanov, O. Jepsen, N.E. Christensen, O.K. Andersen, J. Phys. Chem. Solids 49 (1988) 841–849.
- [531] J. Häglund, G. Grimvall, T. Jarlborg, A.F. Guillermet, Phys. Rev. B 43 (1991) 14400–14408.
- [532] A. Delin, O. Eriksson, R. Ahuja, B. Johansson, M.S.S. Brooks, T. Gasche, S. Auluck, J.M. Wills, Phys. Rev. B 54 (1996) 1673–1681.
- [533] A. Zaoui, B. Bouhafs, P. Ruterana, Mater. Chem. Phys. 91 (2005) 108–115.
- [534] W. Chen, J.Z. Jiang, J. Alloys Compd. 499 (2010) 243–254.
- [535] D.G. Sangiovanni, L. Hultman, V. Chirita, Acta Mater. 59 (2011) 2121–2134.
- [536] M.G. Brik, C.G. Ma, Comput. Mater. Sci. 51 (2012) 380–388.
- [537] B. Altintas, Physica C 487 (2013) 37–41.
- [538] H. Rached, D. Rached, S. Benalia, A.H. Reshak, M. Rabah, R. Khenata, S. Bin Omran, Mater. Chem. Phys. 143 (2013) 93–108.
- [539] M. Chauhan, D.C. Gupta, Int. J. Refract. Met. Hard Mater. 42 (2014) 77–90.
- [540] H. Klostermann, F. Fietzke, R. Labitzke, T. Modes, O. Zywitzki, Surf. Coat. Technol. 204 (2009) 1076–1080.
- [541] S.K. Gupta, S.D. Gupta, H.R. Soni, V. Mankad, P.K. Jha, Mater. Chem. Phys. 143 (2014) 503–513.
- [542] M. Kumar, N. Umezawa, S. Ishii, T. Nagao, ACS Photonics 3 (2016) 43–50.
- [543] J.P. Perdew, A. Ruzsinszky, G.I. Csonka, O.A. Vydrov, G.E. Scuseria, L.A. Constantin, X. Zhou, K. Burke, Phys. Rev. Lett. 100 (2008) 136406.
- [544] Y. Wang, J.P. Perdew, Phys. Rev. B 43 (1991) 8911–8916.
- [545] P. Giannozzi, S. Baroni, N. Bonini, M. Calandra, R. Car, C. Cavazzoni, D. Ceresoli, G.L. Chiarotti, M. Cococcioni, I. Dabo, A.D. Corso, S. de Gironcoli, S. Fabris, G. Fratesi, R. Gebauer, U. Gerstmann, C. Gougoussis, A. Kokalj, M. Lazzeri, L. Martin-Samos, N. Marzari, F. Mauri, R. Mazzarello, S. Paolini, A. Pasquarello, L. Paulatto, C. Sbraccia, S. Scandolo, G. Scialuzero, A.P. Seitsonen, A. Smogunov, P. Umari, R.M. Wentzcovitch, J. Phys.: Condens. Matter 21 (2009) 395502.
- [546] M.D. Segall, J.D.L. Philip, M.J. Probert, C.J. Pickard, P.J. Hasnip, S.J. Clark, M.C. Payne, J. Phys.: Condens. Matter 14 (2002) 2717.
- [547] X. Gonze, B. Amadon, P.-M. Anglade, J.-M. Beuken, F. Bottin, P. Boulanger, F. Bruneval, D. Caliste, R. Caracas, M. Côté, T. Deutsch, L. Genovese, Ph. Ghosez, M. Giantomassi, S. Goedecker, D.R. Hamann, P. Hermet, F. Jollet, G. Jomard, S. Leroux, M. Mancini, S. Mazevet, M.J.T. Oliveira, G. Onida, Y. Pouillon, T. Rangel, G.-M. Rignanese, D. Sangalli, R. Shaltaf, M. Torrent, M.J. Verstraete, G. Zerah, J.W. Zwanziger, Comput. Phys. Commun. 180 (2009) 2582–2615.
- [548] G. Kresse, J. Furthmüller, Phys. Rev. B 54 (1996) 11169–11186.
- [549] J.M. Soler, E. Artacho, J.D. Gale, A. Garcia, J. Junquera, P. Ordejon, D. Sanchez-Portal, J. Phys.: Condens. Matter 14 (2002) 2745–2779.
- [550] F. Wooten, Chapter 4 – free-electron metals, in: Optical Properties of Solids, Academic Press, 1972, pp. 85–107.
- [551] P. Patsalas, S. Logothetidis, J. Appl. Phys. 93 (2003) 4725–4734.
- [552] P.H. Mayrhofer, D. Music, J.M. Schneider, J. Appl. Phys. 100 (2006) 94906.
- [553] S.M. Aouadi, J. Appl. Phys. 99 (2006) 053507.
- [554] B. Alling, A.V. Ruban, A. Karimi, O.E. Peil, S.I. Simak, L. Hultman, I.A. Abrikosov, Phys. Rev. B 75 (2007) 045123.
- [555] B. Alling, A. Karimi, I.A. Abrikosov, Surf. Coat. Technol. 203 (2008) 883–886.
- [556] A. Hoerling, J. Sjöln, H. Willmann, T. Larsson, M. Odén, L. Hultman, Thin Solid Films 516 (2008) 6421–6431.
- [557] D.G. Sangiovanni, V. Chirita, L. Hultman, Phys. Rev. B 81 (2010) 104107.
- [558] K. Bouamama, P. Djemia, D. Faurie, G. Abadias, J. Alloys Compd. 536 (2012) S138–S142.
- [559] S. Kerdsonpanya, B. Alling, P. Eklund, J. Appl. Phys. 114 (2013) 73512.
- [560] B. Alling, Phys. Rev. B 89 (2014) 85112.
- [561] K. Bouamama, P. Djemia, M. Benhamida, J. Phys.: Conf. Ser. 640 (2015) 012022.
- [562] P. Ou, J. Wang, S. Shang, L. Chen, Y. Du, Z.-K. Liu, F. Zheng, Surf. Coat. Technol. 264 (2015) 41–48.
- [563] D.G. Sangiovanni, L. Hultman, V. Chirita, I. Petrov, J.E. Greene, Acta Mater. 103 (2016) 823–835.
- [564] Z. Gu, H. Huang, S. Zhang, X. Wang, J. Gao, J. Zhao, W. Zheng, C. Hu, Appl. Phys. Lett. 109 (2016) 232102.
- [565] M. Kumar, S. Ishii, N. Umezawa, T. Nagao, Opt. Mater. Express 6 (2016) 29–38.
- [566] G. Greczynski, S. Mráz, M. Hans, D. Primetzhofer, J. Lu, L. Hultman, J.M. Schneider, J. Appl. Phys. 121 (2017) 171907.
- [567] Z.T.Y. Liu, B.P. Burton, S.V. Khare, D. Gall, J. Phys. Condens. Matter 29 (2017) 035401.
- [568] L. Hedin, B.I. Lundqvist, J. Phys. C: Solid State Phys. 4 (1971) 2064–2083.
- [569] H. Tompkins, E.A. Haber, Handbook of Ellipsometry, William Andrew Publishing, New York, USA, 2005.
- [570] D.M. Roessler, Br. J. Appl. Phys. 16 (1965) 1119–1123.
- [571] F. Wooten, Optical Properties of Solids, Academic Press, 1972, pp. 15–41 Chapter 2.
- [572] S. Logothetidis, I. Alexandrou, A. Papadopoulos, J. Appl. Phys. 77 (1995) 1043–1047.
- [573] O.S. Heavens, Optical Properties of Thin Solid Films, Dover Publications, 1991.
- [574] K. Balasubramanian, S.V. Khare, D. Gall, Phys. Rev. B 94 (2016) 174111.
- [575] J.C. Ndukaife, V.M. Shalae, A. Boltasseva, Science 351 (2016) 334–335.
- [576] S. Feng, Phys. Rev. Lett. 108 (2012) 93904.
- [577] C. Hu, Z. Gu, J. Wang, K. Zhang, X. Zhang, M. Li, S. Zhang, X. Fan, W. Zheng, J. Phys. Chem. C 118 (2014) 20511–20520.
- [578] S.M. Aouadi, M. Debessai, J. Vac. Sci. Technol. A 22 (2004) 1975–1979.
- [579] B. Angélique, Z. Fadi, C. Joël, T.-G. Christine, T. Sauvage, T. Eric, J. Phys. D: Appl. Phys. 47 (2014) 475201.
- [580] T. Waechtler, B. Gruska, S. Zimmermann, S.E. Schulz, T. Gessner, Characterization of sputtered Ta and TaN films by spectroscopic ellipsometry, ICSICT 2006–8th International Conference on Solid-State and Integrated Circuit Technology (2006).
- [581] M. Tonouchi, Y. Sakaguchi, T. Kobayashi, J. Appl. Phys. 62 (1987) 961–966.
- [582] N. Hayashi, I.H. Murzin, I. Sakamoto, M. Ohkubo, Thin Solid Films 259 (1995) 146–149.
- [583] K. Inumaru, H. Okamoto, S. Yamanaka, J. Cryst. Growth (2002) 2050–2054.
- [584] R. Espiau De Lamaestre, Ph. Odier, J.-C. Villégier, Appl. Phys. Lett. 91 (2007) 232501.
- [585] Y. Duan, L. Qin, H. Liu, J. Phys. Condens. Matter. 28 (2016) 205403.
- [586] V. Mankad, S.K. Gupta, H.R. Soni, P.K. Jha, J. Therm. Anal. Calorim. 107 (2012) 45–48.
- [587] R.R. Palanichamy, G.S. Priyanga, A.J. Cinthia, A. Murugan, A.T. Meenaatci, K. Iyakutti, J. Mag. Mag. Mater. 346 (2013) 26–37.
- [588] M.G. Blaber, M.D. Arnold, M.J. Ford, J. Phys.: Condens. Matter 22 (2010) 143201.
- [589] S. Dellis, N. Kalfagiannis, S. Kassavetis, C. Baziotti, G.P. Dimitrakopoulos, D.C. Koutsogeorgis, P. Patsalas, J. Appl. Phys. 121 (2017) 103104.
- [590] W.L. Barnes, J. Opt. A: Pure Appl. Opt. 8 (2006) S87–S93.
- [591] A.M. Smith, M.C. Mancini, S. Nie, Nat. Nanotechnol. 4 (2009) 710–711.
- [592] T. Skauli, P.S. Kuo, K.L. Vodopyanov, T.J. Pinguet, O. Levi, L.A. Eyres, J.S. Harris, M.M. Fejer, B. Gerard, L. Becouarn, E. Lallier, J. Appl. Phys. 94 (2003) 6447–6455.
- [593] D.E. Aspnes, A.A. Studna, Phys. Rev. B 27 (1983) 985–1008.
- [594] P. Patsalas, Thin Solid Films 519 (2011) 3990–3996.
- [595] J. Kischkat, S. Peters, B. Gruska, M. Semtsiv, M. Chashnikova, M. Klinkmüller, O. Fedosenko, S. Machulik, A. Aleksandrova, G. Monastyrskiy, Y. Flores, W.T. Masselin, Appl. Opt. 51 (2012) 6789–6798.
- [596] A.M. Hofmeister, E. Keppel, A.K. Speck, Mon. Not. R. Astron. Soc. 345 (2003) 16–38.
- [597] H.R. Philipp, J. Electrochem. Soc. 120 (1973) 295–300.
- [598] Fiber optic telecommunication (module 1.8), M. Nick, C. Roychoudhuri (Eds.), Fundamentals of Photonics, SPIE the international society for optics and photonics, Bellingham-Washington, 2000.
- [599] S. Murai, K. Fujita, Y. Daido, R. Yasuhara, R. Kamakura, K. Tanaka, Opt. Express 24 (2016) 1143–1153.
- [600] M.A. Garcia, J. Phys. D: Appl. Phys. 44 (2011) 283001.
- [601] G. Lilley, M. Messner, K. Unterrainer, Opt. Mater. Express (2015) 2112.
- [602] A. Taflova, S.C. Hagness, Computational Electrodynamics: The Finite-Difference Time-Domain Method, Artech House, Incorporated, 2005.
- [603] J. Yguerabide, E.E. Yguerabide, Anal. Biochem. 262 (1998) 137–156.
- [604] C.R. Yonzon, D.A. Stuart, X. Zhang, A.D. McFarland, C.L. Haynes, R.P. Van Duyne, Talanta 67 (2005) 438–448.
- [605] A.J. Haes, L. Chang, W.L. Klein, R.P. Van Duyne, J. Am. Chem. Soc. 127 (2005) 2264–2271.
- [606] G. Raschke, S. Kowarik, T. Franzl, C. Sönnichsen, T.A. Klar, J. Feldmann, A. Nichtl, K. Kürzinger, Nano Lett. 3 (2003) 935–938.
- [607] K.M. Mayer, J.H. Hafner, Chem. Rev. 111 (2011) 3828–3857.
- [608] M. Moskovits, Rev. Mod. Phys. 57 (1985) 783–826.
- [609] C.L. Haynes, C.R. Yonzon, X. Zhang, R.P. Van Duyne, J. Raman Spectrosc. 36 (2005) 471–484.
- [610] Y. Fang, N.-H. Seong, D.D. Dlott, Science 321 (2008) 388–392.
- [611] J.F. Li, Y.F. Huang, Y. Ding, Z.L. Yang, S.B. Li, X.S. Zhou, F.R. Fan, W. Zhang, Z.Y. Zhou, D.Y. Wu, B. Ren, Z.L. Wang, Z.Q. Tian, Nature 464 (2010) 392–395.
- [612] S. Nie, S.R. Emory, Science 275 (1997) 1102–1106.
- [613] M.J. Beliatas, N.A. Martin, E.J. Leming, S.R.P. Silva, S.J. Henley, Langmuir 27 (2010) 1241–1244.
- [614] A. Stalmashonak, H. Graener, G. Seifert, Appl. Phys. Lett. 94 (2009) 193111.
- [615] N. Kalfagiannis, A. Siozios, D.V. Bellas, D. Toliopoulos, L. Bowen, N. Pliatsikas, W.M. Cranton, C. Kosmidis, D.C. Koutsogeorgis, E. Lidorikis, P. Patsalas, Nano-scale 8 (2016) 8236–8244.
- [616] C.C. Wang, S.A. Akbar, W. Chen, V.D. Patton, J. Mater. Sci. 30 (1995) 1627–1641.
- [617] P.R. Couchman, W.A. Jesser, Nature 269 (1977) 481–483.

- [618] Q. Jiang, S. Zhang, M. Zhao, *Mater. Chem. Phys.* 82 (2003) 225–227.
- [619] J.D. Jackson, *Classical Electrodynamics*, Wiley, New York, NY, 1999.
- [620] A. Alabastri, S. Tuccio, A. Giugni, A. Toma, C. Liberale, G. Das, F.D. Angelis, E.D. Fabrizio, R.P. Zaccaria, *Materials* 2013 (2013) 4879–4910.
- [621] K. Ujihara, *J. Appl. Phys.* 43 (1972) 2376–2383.
- [622] D. Chester, P. Bermel, J.D. Joannopoulos, M. Soljacic, I. Celanovic, *Opt. Express* 19 (2011) A245–A257.
- [623] A. Sakurai, H. Tanikawa, M. Yamada, *J. Quant. Spectrosc. Radiat. Transfer* 132 (2014) 80–89.
- [624] N.W. Ashcroft, N.D. Mermin, *Solid State Physics*, Holt, Rinehart and Winston, 1976.
- [625] C.Y. Ho, M.W. Ackerman, K.Y. Wu, T.N. Havill, R.H. Bogaard, R.A. Matula, S.G. Oh, H.M. James, *J. Phys. Chem. Ref. Data* 12 (1983) 183–322.
- [626] B.O. Johansson, J.E. Sundgren, J.E. Greene, A. Rockett, S.A. Barnett, *J. Vac. Sci. Technol. A* 3 (1985) 303–307.
- [627] B.W. Karr, D.G. Cahill, I. Petrov, J.E. Greene, *Phys. Rev. B* 61 (2000) 16137–16143.
- [628] F. Schedin, E. Lidorikis, A. Lombardo, V.G. Kravets, A.K. Geim, A.N. Grigorenko, K.S. Novoselov, A.C. Ferrari, *ACS Nano* 4 (2010) 5617–5626.